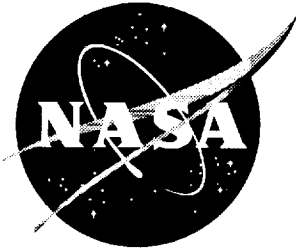


NASA/CR-1999-209528



# Multivariable Techniques for High-Speed Research Flight Control Systems

*Brett A. Newman*  
*Old Dominion University, Norfolk, Virginia*

---

December 1999

## The NASA STI Program Office . . . in Profile

Since its founding, NASA has been dedicated to the advancement of aeronautics and space science. The NASA Scientific and Technical Information (STI) Program Office plays a key part in helping NASA maintain this important role.

The NASA STI Program Office is operated by Langley Research Center, the lead center for NASA's scientific and technical information. The NASA STI Program Office provides access to the NASA STI Database, the largest collection of aeronautical and space science STI in the world. The Program Office is also NASA's institutional mechanism for disseminating the results of its research and development activities. These results are published by NASA in the NASA STI Report Series, which includes the following report types:

- **TECHNICAL PUBLICATION.** Reports of completed research or a major significant phase of research that present the results of NASA programs and include extensive data or theoretical analysis. Includes compilations of significant scientific and technical data and information deemed to be of continuing reference value. NASA counterpart of peer-reviewed formal professional papers, but having less stringent limitations on manuscript length and extent of graphic presentations.
- **TECHNICAL MEMORANDUM.** Scientific and technical findings that are preliminary or of specialized interest, e.g., quick release reports, working papers, and bibliographies that contain minimal annotation. Does not contain extensive analysis.
- **CONTRACTOR REPORT.** Scientific and technical findings by NASA-sponsored contractors and grantees.

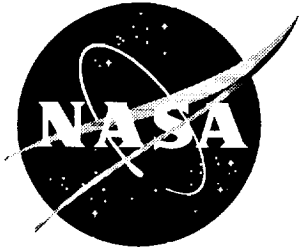
- **CONFERENCE PUBLICATION.** Collected papers from scientific and technical conferences, symposia, seminars, or other meetings sponsored or co-sponsored by NASA.
- **SPECIAL PUBLICATION.** Scientific, technical, or historical information from NASA programs, projects, and missions, often concerned with subjects having substantial public interest.
- **TECHNICAL TRANSLATION.** English-language translations of foreign scientific and technical material pertinent to NASA's mission.

Specialized services that complement the STI Program Office's diverse offerings include creating custom thesauri, building customized databases, organizing and publishing research results . . . even providing videos.

For more information about the NASA STI Program Office, see the following:

- Access the NASA STI Program Home Page at <http://www.sti.nasa.gov>
- Email your question via the Internet to [help@sti.nasa.gov](mailto:help@sti.nasa.gov)
- Fax your question to the NASA STI Help Desk at (301) 621-0134
- Telephone the NASA STI Help Desk at (301) 621-0390
- Write to:  
NASA STI Help Desk  
NASA Center for Aerospace Information  
7121 Standard Drive  
Hanover, MD 21076-1320

NASA/CR-1999-209528



# Multivariable Techniques for High-Speed Research Flight Control Systems

*Brett A. Newman*  
*Old Dominion University, Norfolk, Virginia*

National Aeronautics and  
Space Administration

Langley Research Center  
Hampton, Virginia 23681-2199

Prepared for Langley Research Center  
under Contract NAS1-19858

---

December 1999

---

Available from:

NASA Center for Aerospace Information (CASI)  
7121 Standard Drive  
Hanover, MD 21076-1320  
(301) 621-0390

National Technical Information Service (NTIS)  
5285 Port Royal Road  
Springfield, VA 22161-2171  
(703) 605-6000



# Table of Contents

	Page
I. Introduction.....	1
II. Aeroelastic Vehicle Modeling .....	6
A. Model Description.....	6
B. Model Comparison and Characteristics .....	12
C. Forward Vane Development.....	68
III. Assessment of Wykes Mode Suppression Logic .....	80
A. Review of and Comment on Original Wykes Logic .....	80
B. Wykes Logic Recast in Multi-Sensor/Single-Surface Framework.....	91
C. Wykes Logic Applied to HSCT.....	95
IV. Conventional Multi-Sensor/Multi-Surface Design Strategy.....	112
A. Summary of Design Strategy .....	112
B. Aeroelastic Suppression Loop .....	118
C. Coordination Crossfeed .....	130
D. Pitch Augmentation Loop .....	138
E. Command Shaping Prefilter.....	154
F. Additional Evaluation of Control Law .....	164
V. Forward Vane Sizing Requirements.....	216
A. Sizing Strategy Formulation .....	216
B. Closed-Loop Simulation Results .....	221
C. Discussion of Sizing Results.....	236
VI. Conclusions and Recommendations .....	241
References .....	244
Appendix A Statement of Work for NAS1-19858-93.....	247
Appendix B $M = 0.24 / h = 500 \text{ ft}$ Cycle 3.1a Model .....	249
Appendix C $M = 0.24 / h = 0 \text{ ft}$ Cycle 1/ISAC Model.....	261
Appendix D Estimation of Component Lift Curve Slopes .....	279

## List of Figures

	Page
1. Overall Airframe-Actuator Model .....	8
2. Overall Airframe-Gust Model.....	9
3. Ref. H HSCT Configuration.....	10
4. Frequency Response Comparison Of Appendix B & C Models For 358 in Pitch Rate To Stabilator Channel .....	15
5. Frequency Response Comparison Of Appendix B & C Models For 2,152 in Pitch Rate To Stabilator Channel .....	16
6. Frequency Response Comparison Of Appendix B & C Models For 358 in Pitch Rate To Elevator Channel.....	17
7. Frequency Response Comparison Of Appendix B & C Models For 2,152 in Pitch Rate To Elevator Channel.....	18
8. Frequency Response Comparison Of Appendix B & C Models For 358 in Pitch Rate To Trailing Edge 3 Channel .....	19
9. Frequency Response Comparison Of Appendix B & C Models For 2,152 in Pitch Rate To Trailing Edge 3 Channel .....	20
10. Frequency Response Comparison Of Appendix B & C Models For 358 in Vertical Acceleration To Stabilator Channel .....	21
11. Frequency Response Comparison Of Appendix B & C Models For 2,152 in Vertical Acceleration To Stabilator Channel .....	22
12. Frequency Response Comparison Of Appendix B & C Models For 358 in Vertical Acceleration To Elevator Channel.....	23
13. Frequency Response Comparison Of Appendix B & C Models For 2,152 in Vertical Acceleration To Elevator Channel.....	24
14. Frequency Response Comparison Of Appendix B & C Models For 358 in Vertical Acceleration To Trailing Edge 3 Channel .....	25
15. Frequency Response Comparison Of Appendix B & C Models For 2,152 in Vertical Acceleration To Trailing Edge 3 Channel .....	26
16. Frequency Response Of Appendix C Model For 400 in Pitch Rate To Elevator Channel.....	55
17. Frequency Response Of Appendix C Model For 1,850 in Pitch Rate To Elevator Channel.....	56
18. Frequency Response Of Appendix C Model For 3,460 in Pitch Rate To Elevator Channel.....	57

## List of Figures Continued

	Page
19. Frequency Response Of Appendix C Model For 400 in Pitch Rate To Vane Channel .....	58
20. Frequency Response Of Appendix C Model For 1,850 in Pitch Rate To Vane Channel .....	59
21. Frequency Response Of Appendix C Model For 3,460 in Pitch Rate To Vane Channel .....	60
22. Frequency Response Of Appendix C Model For 400 in Vertical Acceleration To Elevator Channel.....	61
23. Frequency Response Of Appendix C Model For 1,850 in Vertical Acceleration To Elevator Channel.....	62
24. Frequency Response Of Appendix C Model For 3,460 in Vertical Acceleration To Elevator Channel.....	63
25. Frequency Response Of Appendix C Model For 400 in Vertical Acceleration To Vane Channel .....	64
26. Frequency Response Of Appendix C Model For 1,850 in Vertical Acceleration To Vane Channel .....	65
27. Frequency Response Of Appendix C Model For 3,460 in Vertical Acceleration To Vane Channel .....	66
28. Structural Mode Shape Data - Mass Case M3A.....	67
29. Vane Geometry .....	69
30. HSCT Configuration With Vane.....	70
31. Vane Modeling Summary.....	71
32. Summary Of Stability Derivative Modifications .....	77
33. Summary Of Control Derivative Modifications .....	78
34. Original Wykes SMCS Architecture.....	81
35. Airframe $n_{qd}(s)$ Root Migration Paths Without Aerodynamic Coupling - Eq. (3.7).....	84
36. Closed-Loop $d(s)+kn_{qd}(s)$ Root Migration Paths Without Aerodynamic Coupling - Fig. 34 .....	85
37. Intermediate Root Migration Paths With Aerodynamic Coupling - Eq. (3.11).....	88
38. Airframe $d(s)$ Root Migration Paths With Aerodynamic Coupling - Eq. (3.12).....	89
39. Airframe $n_{\eta_2}(s)$ Root Migration Paths With Aerodynamic Coupling - Eq. (3.12).....	90
40. MS/SS Architectures Previously Analyzed.....	92
41. Wykes SMCS Logic Recast In MS/SS Framework.....	93

## List of Figures Continued

	Page
42. Parameterization Of The Blending Family .....	94
43. Evans Plot For 1,850 in Pitch Rate To Elevator .....	96
44. Bode Plot For 1,850 in Pitch Rate To Elevator, $k = -4.52$ rad/rad/s .....	98
45. Evans Plot For 3,460 in Pitch Rate To Elevator.....	100
46. Bode Plot For 3,460 in Pitch Rate To Elevator, $k = -4.27$ rad/rad/s.....	102
47. Lag-Lead And High Pass Blending With $k_{SMCS}/k_{SAS} = -0.25$ .....	104
48. Evans Plot For Blend Of Lag-Lead 1,850 in And High Pass 3,460 in Pitch Rate To Elevator, $k_{SMCS}/k_{SAS} = -0.25$ .....	105
49. Bode Plot For Blend Of Lag-Lead 1,850 in And High Pass 3,460 in Pitch Rate To Elevator, $k_{SMCS}/k_{SAS} = -0.25$ And $k = -4.52$ rad/rad/s.....	106
50. Lag-Lead And High Pass Blending With $k_{SMCS}/k_{SAS} = -0.75$ .....	107
51. Evans Plot For Blend Of Lag-Lead 1,850 in And High Pass 3,460 in Pitch Rate To Elevator, $k_{SMCS}/k_{SAS} = -0.75$ .....	108
52. Bode Plot For Blend Of Lag-Lead 1,850 in And High Pass 3,460 in Pitch Rate To Elevator, $k_{SMCS}/k_{SAS} = -0.75$ And $k = -4.52$ rad/rad/s.....	109
53. Numerator Root Locus For Lag-Lead 1,850 in And High Pass 3,460 in Pitch Rate To Elevator, $k_{SMCS}/k_{SAS} = -0.75$ .....	111
54. Multi-Sensor/Multi-Surface Control Architecture .....	115
55. "Mechanics" Of The MS/MS Flight Control System .....	117
56. Evans Plot For 400 in Pitch Rate To Vane With Static Compensation .....	119
57. Bode Plot For 400 in Pitch Rate To Vane With Static Compensation, $k_{11} = 2.33$ rad/rad/s.....	120
58. Evans Plot For 400 in Pitch Rate To Vane With Low Pass Filter.....	122
59. Bode Plot For 400 in Pitch Rate To Vane With Low Pass Filter, $k_{11} = 1.91$ rad/rad/s.....	123
60. Evans Plot For 400 in Pitch Rate To Vane With Phase Lead Filter .....	126
61. Bode Plot For 400 in Pitch Rate To Vane With Phase Lead Filter, $k_{11} = 4.66$ rad/rad/s.....	127
62. Evans Plot For 400 in Pitch Rate To Vane With Phase Lead And Notch Filter .....	128
63. Bode Plot For 400 in Pitch Rate To Vane With Phase Lead And Notch Filter, $k_{11} = 3.00$ rad/rad/s.....	129
64. Numerator Migration Plot For 400 in Pitch Rate To Elevator With Static Compensation.....	132

## List of Figures Continued

	Page
65. Numerator Migration Plot For 400 in Vertical Acceleration To Elevator With Static Compensation.....	133
66. Numerator Migration Plot For 400 in Pitch Rate To Elevator With Cliff Filter .....	136
67. Numerator Migration Plot For 400 in Vertical Acceleration To Elevator With Cliff Filter .....	137
68. Evans Plot For 1,850 in Pitch Rate To Elevator Without Filtering.....	140
69. Bode Plot For 1,850 in Pitch Rate To Elevator Without Filtering, $k_{22} = -3.07 \text{ rad/rad/s}$ .....	142
70. Control Anticipation & Omega-Tau vs. Damping For 1,850 in Pitch Rate To Elevator Without Filtering.....	148
71. Bode Plot For 1,850 in Pitch Rate To Elevator With Filtering, $k_{22} = -5.08 \text{ rad/rad/s}$ .....	149
72. Evans Plot For 1,850 in Pitch Rate To Elevator With Filtering .....	150
73. Closed-Loop 400 in Pitch Rate Time Response Due To 1 deg/s Command Without Prefilter.....	152
74. Closed-Loop 400 in Vertical Acceleration Time Response Due To 1 deg/s Command Without Prefilter.....	153
75. Closed-Loop 400 in Pitch Rate Time Response Due To 1 deg/s Command With Prefilter .....	156
76. Closed-Loop 400 in Vertical Acceleration Time Response Due To 1 deg/s Command With Prefilter .....	157
77. Closed-Loop 1,850 in Pitch Rate Time Response Due To 1 deg/s Command With Prefilter .....	158
78. Closed-Loop 1,850 in Vertical Acceleration Time Response Due To 1 deg/s Command With Prefilter .....	159
79. Closed-Loop 2,500 in Pitch Rate Time Response Due To 1 deg/s Command With Prefilter .....	160
80. Closed-Loop 2,500 in Vertical Acceleration Time Response Due To 1 deg/s Command With Prefilter .....	161
81. Closed-Loop 3,460 in Pitch Rate Time Response Due To 1 deg/s Command With Prefilter .....	162
82. Closed-Loop 3,460 in Vertical Acceleration Time Response Due To 1 deg/s Command With Prefilter .....	163

## List of Figures Continued

	Page
83. Equivalent Inner Loop Architecture.....	166
84. Bode Plot For Input 1 Break Point.....	168
85. Bode Plot For Input 2 Break Point.....	169
86. Bode Plot For Output 1 Break Point.....	170
87. Bode Plot For Output 2 Break Point.....	171
88. Inner Loop Architecture Expressed With Vector Notation .....	173
89. Singular Value Robustness Against Multi-Loop MIL-F-87242 Gain Requirement At Input.....	175
90. Singular Value Robustness Against Multi-Loop MIL-F-87242 Phase Requirement At Input.....	176
91. Singular Value Robustness Against Uniform Gain At Input.....	177
92. Singular Value Robustness Against Uniform Phase At Input .....	178
93. Singular Value Robustness Against Multi-Loop MIL-F-87242 Gain Requirement At Output.....	179
94. Singular Value Robustness Against Multi-Loop MIL-F-87242 Phase Requirement At Output.....	180
95. Singular Value Robustness Against Uniform Gain At Output.....	181
96. Singular Value Robustness Against Uniform Phase At Output.....	182
97. Inner Loop Architecture With Internal Parameter Variations.....	183
98. Singular Value Robustness Against Structural Damping Ratio.....	186
99. Singular Value Robustness Against Structural Natural Frequency.....	189
100. Singular Value Robustness Against Structural Mode Shape - Input And Output.....	192
101. Singular Value Robustness Against Structural Mode Shape - Internal .....	195
102. Singular Value Robustness Against Aerodynamic Control Effectiveness.....	198
103. Singular Value Robustness Against Aerodynamic Lift Curve Slope.....	201
104. Closed-Loop 400 in Pitch Rate To Stick Command Unscaled Frequency Response Comparison .....	208
105. Closed-Loop 400 in Pitch Rate To Stick Command Scaled Frequency Response Comparison .....	209
106. Frequency And Component Distribution For Ride Discomfort Index Integrand At 400 in .....	212
107. Vane Surface Area Upper And Lower Bounds.....	217
108. Vane Sizing Summary.....	219

## List of Figures Continued

	Page
109. Response Characteristics For Maneuver Command - Step.....	224
110. Response Characteristics For Maneuver Command - Sinusoid .....	226
111. Response Characteristics For Maneuver Command - Square Wave .....	228
112. Response Characteristics For Atmospheric Gust - Step.....	230
113. Response Characteristics For Atmospheric Gust - Sinusoid.....	232
114. Response Characteristics For Atmospheric Gust - Turbulence.....	234
115. Response Characteristics For Maneuver Command - Square Wave With Crossfeed Path Eliminated.....	239

## List of Tables

	Page
1. Poles Of Appendix C Model .....	29
2. Zeros Of Appendix C Model For 400 in Pitch Rate To Elevator Channel .....	31
3. Zeros Of Appendix C Model For 1,850 in Pitch Rate To Elevator Channel.....	33
4. Zeros Of Appendix C Model For 3,460 in Pitch Rate To Elevator Channel.....	35
5. Zeros Of Appendix C Model For 400 in Pitch Rate To Vane Channel.....	37
6. Zeros Of Appendix C Model For 1,850 in Pitch Rate To Vane Channel .....	39
7. Zeros Of Appendix C Model For 3,460 in Pitch Rate To Vane Channel .....	41
8. Zeros Of Appendix C Model For 400 in Vertical Acceleration To Elevator Channel.....	43
9. Zeros Of Appendix C Model For 1,850 in Vertical Acceleration To Elevator Channel .....	45
10. Zeros Of Appendix C Model For 3,460 in Vertical Acceleration To Elevator Channel .....	47
11. Zeros Of Appendix C Model For 400 in Vertical Acceleration To Vane Channel.....	49
12. Zeros Of Appendix C Model For 1,850 in Vertical Acceleration To Vane Channel .....	51
13. Zeros Of Appendix C Model For 3,460 in Vertical Acceleration To Vane Channel .....	53
14. System Characteristics With Gain Adjustment For 1,850 in Pitch Rate To Elevator Without Filtering .....	143
15. Design Summary Of 1,850 in Pitch Rate To Elevator With Filtering, $k_{22} = -5.08 \text{ rad/rad/s}$ .....	145
16. Closed-Loop Mode 1 & 2 Root Locations For 400 in Pitch Rate And Vertical Acceleration .....	154
17. Isolated Gain And Phase Margins.....	165
18. Nominal Structural Natural Frequencies .....	185
19. Summary Of Multivariable Stability Robustness .....	202
20. Estimated Flying Qualities Summary Of 400 in Closed-Loop Pitch Rate Dynamics With Prefilter .....	207
21. Estimated Ride Quality Of Closed-Loop Airframe .....	211
22. Vane Sizing Results For Unit Excitations.....	236
23. Vane Sizing Results For Calibrated Excitations .....	238



## Section I

### Introduction

This report describes the activities and findings conducted under contract NAS1-19858-93 with NASA Langley Research Center. Subject matter is the investigation of suitable multivariable flight control design methodologies and solutions for large, flexible high-speed vehicles. Specifically, methodologies are to address the inner control loops used for stabilization and augmentation of a highly coupled airframe system possibly involving rigid-body motion, structural vibrations, unsteady aerodynamics, and actuator dynamics. The flight control strategies must address basic specifications/requirements,<sup>1,2</sup> or clearly display the design tradeoffs to the flight control engineer. Design and analysis techniques considered in this body of work are both conventional-based<sup>3</sup> and contemporary-based.<sup>4,5</sup> The conventional-based schemes facilitate understanding into the "physics" and lead to simple, effective solutions that go a long way in implementation of a multiply redundant architecture requiring scheduling with flight condition and modification during test and development. On the other hand, the contemporary-based schemes provide powerful, efficient tools for closing multiple feedback loops in an integrated framework and allow assessment of the upper limits of achievable closed-loop stability and performance.

The vehicle of interest is the High-Speed Civil Transport (HSCT).<sup>6,7</sup> This vehicle is projected to have a pitch divergence due to the relaxation of static stability at subsonic speeds. Further, significant interaction between rigid-body and aeroelastic degrees of freedom is expected. Characteristics of this sort will, by necessity, require a set of initial feedback loops to correct for these deficiencies and bring the closed-loop vehicle system back to a level which is acceptable to the pilot and passengers. Functions of this inner loop flight control system (FCS) for HSCT will be to 1) artificially supply the stability inherently lacking in the airframe, 2) augment the key pilot/passenger centered responses to obtain crisp, well damped behavior, and 3) suppress

aeroelastic motions in all responses, all with minimal FCS architecture. The objectives of the contract work are to explore the possibilities for such an inner loop FCS.

This work is heavily dependent upon generation of representative airframe math models with the requisite fidelity, as well as modifications made to these math models representing hypothetical aerodynamic control surfaces. Section II presents two HSCT numerical models made available to the contractor.<sup>8,9</sup> The HSCT models were developed from a nonlinear simulation tool<sup>10,11</sup> at various stages in its development: Cycle 1 and Cycle 3.1a. Within this simulation tool, aerodynamic load predictions associated with structural vibration and unsteady aerodynamic coordinates are computed with the package Integrated Structures Aerodynamics and Controls (ISAC).<sup>12</sup> Comparisons of the HSCT models reveal good correlation for pitch rate and normal acceleration dynamics at several sensor locations when excited by elevator and stabilator inputs. In some sense, this result validates the current modeling process. More importantly, the correlations validate results and conclusions from previous flight control investigations.<sup>13</sup> Section II also describes the component build-up modeling procedure, and modifications made to the original stability and control derivatives, to represent effects from small aerodynamic vanes located on the forward fuselage. As will be shown, these vanes are crucial to the development of feasible inner loop FCS architectures.

The contract Statement of Work (see Appendix A) consisted of three distinct tasks contributing to the overall objective. These tasks include investigations of

1. Control benefits derived from small forward aerodynamic control surfaces  
(Conventional Multi-Sensor/Multi-Surface design strategies utilizing forward vanes),
2. Contemporary multivariable design strategies  
(Contemporary Multi-Sensor/Multi-Surface design strategies utilizing forward vanes), and
3. Controllability requirements for rigid and elastic responses  
(Sizing requirements for forward vanes).

In addition, it was felt prudent to re-examine the Multi-Sensor/Single-Surface structural mode suppression logic utilized by John Wykes/North American Rockwell for the XB-70, in a final attempt to avoid use of forward vanes.<sup>14-15</sup> These tasks are briefly outlined here before moving on to the dedicated chapters with detailed reporting of the activities. Due to limited resources and NASA/Industry program emphasis and scheduling, Task 2 was assigned low priority and postponed for future activities. This redistribution of effort does not imply contemporary techniques are of lesser importance, rather it reflects on current needs and realistic deliverables in the allotted contractual framework.

Section III describes the supplemental task of re-examining the Stability Augmentation System (SAS) and Structural Mode Control System (SMCS) logic utilized by John Wykes/North American Rockwell on the XB-70 program, in the context of HSCT. In the XB-70 program, significant strides were made in simultaneously suppressing aeroelastic vibrations and augmenting pitch characteristics with a single control input surface. If this success could be duplicated with HSCT, the need for configuration redesign with forward vanes would diminish. The Wykes control logic can be reinterpreted in the Multi-Sensor/Single-Surface framework previously considered in Ref. 13. In Ref. 13, studies utilized low pass/band pass and lag-lead/lead-lag blending filters with sensors located at 1,850 in and 2,500 in. The Wykes control law is equivalent to lag-lead/high pass blending of sensors located at 1,850 in and 3,460 in. When applied to HSCT, the Wykes control law is found to be unacceptable. The control logic destabilizes higher frequency aeroelastic modes due to neglected but significant mode slope terms and aerodynamic coupling terms. In addition, the lag-lead/high pass blending results in nonminimum phase characteristics which reduce the upper limit of usable loop gain. With this reduced upper limit, augmentation of pitch and aeroelastic dampings is restricted. Similar results were found in Ref. 13 for other Multi-Sensor/Single-Surface architectures. A Wykes SAS/SMCS control law with elevator only does not appear feasible for HSCT.

Previous analysis and synthesis of conventional Single-Sensor/Single-Surface (SS/SS) and Multi-Sensor/Single-Surface (MS/SS) FCS using the elevator indicate unacceptable design trades

between necessary bandwidth for low frequency pitch handling qualities and necessary attenuation for aeroelastic stability margins, as well as an inability to control cockpit motions.<sup>13</sup> Multi-Sensor/Multi-Surface (MS/MS) FCS architectures utilizing the elevator and wing trailing edge surfaces have also been considered.<sup>13</sup> Results indicate the wing trailing edge devices are not appropriate for the aeroelastic suppression role. Section IV describes the first task of revisiting this conventional MS/MS architecture using the elevator and hypothetical forward vanes, in order to assess their control benefits. The new control surfaces provide an attractive solution to the noted problems. Forward vanes significantly enlarge the tight design box by allowing separate loops dedicated to aeroelastic suppression and pitch augmentation functions, and provide enhanced control of cockpit motions. A MS/MS FCS utilizing forward vanes is offered as a feasible, baseline architecture for the inner loops. This architecture is relatively simple and tractable, yet is capable of achieving high levels of stability and performance, as evaluated by a mixture of criteria and requirements commonly used within the flight dynamics and control community (although applicability to aeroelastic vehicles has not been fully established, in some cases).

All analysis and synthesis utilizing the forward vanes are based upon the specific vane model described in Section II. This model represents a "first-cut" design based upon vane mounting location and vane-to-tail planform area ratios of other high-speed elastic vehicles. This specific vane may be undersized, or oversized, from such a preliminary assumption. Section V describes a vane sizing analysis that was undertaken to accomplish the third task. Analysis is based on closed-loop simulation results. The closed-loop design from Section IV is excited with both maneuver commands and atmospheric gusts, and the peak vane travel and rate activity are recorded. Based upon hardware travel limit and rate limit values, the necessary surface area to avoid saturation can be "reverse engineered" from the data. Surface area results can be scaled with input amplitude. Maneuver commands dominate the vane travel activity, while both maneuver commands and atmospheric gusts drive the peak rate activity. Large maneuver commands (such as go around, high alpha recovery, etc.) will most likely drive small vanes beyond the travel and rate limits. A critical design trade was uncovered in this study. The vane activity is approximately

halved with the elevator-to-vane crossfeed path absent from the baseline FCS in Section IV, but this signal path is necessary for crew station flying quality and ride quality performance.

## Section II

### Aeroelastic Vehicle Modeling

#### A. Model Description

Modeling of highly integrated HSCT class vehicles requires the flight dynamics engineer to return to the governing fundamental principles of rigid-body motion, structural vibrations, unsteady aerodynamics, etc. Revisiting these principles allows the relevant features to enter the early stages of the modeling process. The resulting models accurately capture the contributions from each discipline to the overall dynamic behavior, as well as the interaction between the disciplines. Refs. 12 and 16-19 describe such a process leading to nonlinear models, from which linear models can be extracted for use in control system design.

The linear models are represented in state space form as

$$\begin{aligned}\dot{x} &= Ax + Bu + B'\ddot{u} + B''\ddot{u} + B_d d \\ y &= Cx + Du + D'\dot{u} + D''\ddot{u} + D_d d\end{aligned}\tag{2.1}$$

In general, the state vector  $x$  consists of the rigid-body positions and velocities, generalized coordinates originating from the structural vibrations, and variables representing the unsteady aerodynamic degrees of freedom. Focusing on the longitudinal dynamics leads to

$$x = \begin{bmatrix} u & w & q & \theta & \dots \dot{\eta}_i \dots & \dots \eta_i \dots & \dots z_i \dots \end{bmatrix}^T\tag{2.2}$$

- $u$       - forward speed
- $w$       - downward speed
- $q$       - pitch rate
- $\theta$       - pitch angle
- $\eta_i$     - generalized coordinate for  $i^{\text{th}}$  aeroelastic mode
- $z_i$     -  $i^{\text{th}}$  unsteady aerodynamic state

Control inputs are denoted by  $u$  where

$$u = \begin{bmatrix} \delta_S & \delta_E & \delta_V & \dots \delta_{TEi} \dots \end{bmatrix}^T\tag{2.3}$$

- $\delta_S$     - stabilator deflection

- $\delta_E$  - elevator deflection
- $\delta_V$  - vane deflection
- $\delta_{TEi}$  -  $i$ th wing trailing edge symmetric deflection  
(TE1 is inboard most, TE4 is outboard most)

Further, disturbance inputs are denoted by  $d$  where

$$d = w_G \quad (2.4)$$

$w_G$  - vertical gust

Finally, responses of interest  $y$  include measured pitch rates and vertical accelerations throughout the vehicle,

$$y = \begin{bmatrix} \dots q_{x_s} \dots & \dots a_{z_{x_s}} \dots \end{bmatrix}^T \quad (2.5)$$

$q_{x_s}$  - pitch rate at structural axes location  $x_s$

$a_{z_{x_s}}$  - vertical acceleration at structural axes location  $x_s$

If unsteady aerodynamics are modeled, then surface deflection rates and accelerations become inputs leading to matrices  $B'$ ,  $B''$ ,  $D'$ , and  $D''$  as indicated in Eq. (2.1). To circumvent this noncausal behavior, and to model the actuation hardware dynamics, 3rd order actuator models are considered as a "front end" to the airframe model. Fig. 1 illustrates this feature with the elevator surface actuator. From Fig. 1, the elevator actuator model is

$$\delta_E(s) = \frac{p}{s+p} \frac{\omega^2}{s^2+2\zeta\omega s+\omega^2} \delta_{Ec}(s) \quad (2.6)$$

$$\begin{bmatrix} \delta_E \\ \dot{\delta}_E \\ \ddot{\delta}_E \end{bmatrix} = \begin{bmatrix} 0 & 1 & 0 \\ 0 & 0 & 1 \\ -p\omega^2 & -(p2\zeta\omega+\omega^2) & -(p+2\zeta\omega) \end{bmatrix} \begin{bmatrix} \delta_E \\ \dot{\delta}_E \\ \ddot{\delta}_E \end{bmatrix} + \begin{bmatrix} 0 \\ 0 \\ p\omega^2 \end{bmatrix} \delta_{Ec}$$

$$\begin{bmatrix} \delta_E \\ \dot{\delta}_E \\ \ddot{\delta}_E \end{bmatrix} = \begin{bmatrix} 1 & 0 & 0 \\ 0 & 1 & 0 \\ 0 & 0 & 1 \end{bmatrix} \begin{bmatrix} \delta_E \\ \dot{\delta}_E \\ \ddot{\delta}_E \end{bmatrix}$$

$p$  - actuator first order break frequency

$\zeta$  - actuator second order damping

$\omega$  - actuator second order natural frequency

Note  $G(s)$  represents the airframe transfer function matrix. Generalizing for all actuator hardware,  
or

$$\dot{x}_a = A_a x_a + B_a u_c \quad (2.7)$$

$$\begin{bmatrix} u \\ \dot{u} \\ \ddot{u} \end{bmatrix} = \begin{bmatrix} C_a \\ C'_a \\ C''_a \end{bmatrix} x_a$$

leads to the overall airframe-actuator model

$$\begin{bmatrix} \dot{x} \\ \dot{x}_a \end{bmatrix} = \begin{bmatrix} A & \hat{A} \\ 0 & A_a \end{bmatrix} \begin{bmatrix} x \\ x_a \end{bmatrix} + \begin{bmatrix} 0 & B_d \\ B_a & 0 \end{bmatrix} \begin{bmatrix} u_c \\ d \end{bmatrix}$$

$$y = \begin{bmatrix} C & \hat{C} \end{bmatrix} \begin{bmatrix} x \\ x_a \end{bmatrix} + \begin{bmatrix} 0 & D_d \end{bmatrix} \begin{bmatrix} u_c \\ d \end{bmatrix}$$

$$\begin{aligned} \hat{A} &= B C_a + B' C'_a + B'' C''_a \\ \hat{C} &= D C_a + D' C'_a + D'' C''_a \end{aligned} \quad (2.8)$$

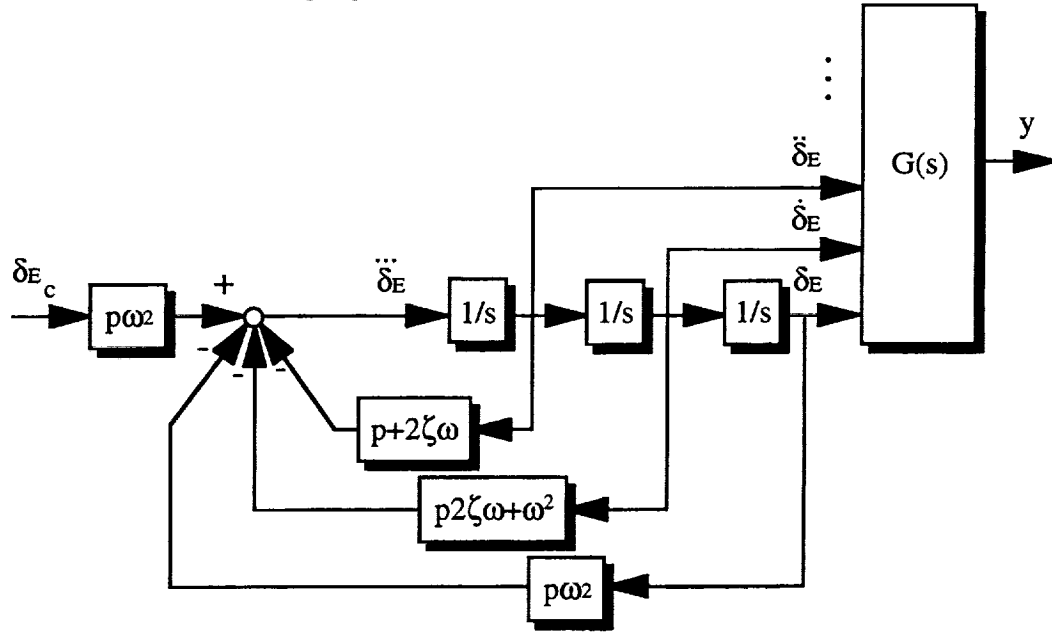


Figure 1. Overall Airframe-Actuator Model

In keeping with traditional analysis techniques, an approximate von Karman turbulence filter<sup>20</sup> excited by noise  $n$  is utilized to generate stochastic disturbance gust velocities, or

$$w_G(s) = \frac{k(s+z_1)(s+z_2)}{(s+p_1)(s+p_2)(s+p_3)} n(s) \quad (2.9)$$

$$\begin{bmatrix} \dot{w} \\ \ddot{w} \\ \ddot{w} \end{bmatrix} = \begin{bmatrix} 0 & 1 & 0 \\ 0 & 0 & 1 \\ -(p_1 p_2 p_3) & -(p_1 p_2 + p_2 p_3 + p_3 p_1) & -(p_1 + p_2 + p_3) \end{bmatrix} \begin{bmatrix} w \\ \dot{w} \\ \ddot{w} \end{bmatrix} + \begin{bmatrix} 0 \\ 0 \\ k z_1 z_2 \end{bmatrix} n$$



$$w_G = \begin{bmatrix} 1 & (z_1+z_2)/z_1z_2 & 1/z_1z_2 \end{bmatrix} \begin{bmatrix} w \\ \dot{w} \\ \ddot{w} \end{bmatrix}$$

$$k = 1.246 \sigma_{wG} (V_T/L)^{1/2} \quad z_1 = 0.3820 V_T/L \quad z_2 = 7.704 V_T/L$$

$$p_1 = 0.4801 V_T/L \quad p_2 = 1.215 V_T/L \quad p_3 = 11.14 V_T/L$$

$\sigma_{wG}$  - gust standard deviation  
 $L$  - gust characteristic length  
 $V_T$  - total flight speed

Fig. 2 illustrates this turbulence filter and its connection to the vehicle model. Generalizing the notation for the gust filter yields

$$\begin{aligned} \dot{x}_g &= A_g x_g + B_g n \\ d &= C_g x_g \end{aligned} \quad (2.10)$$

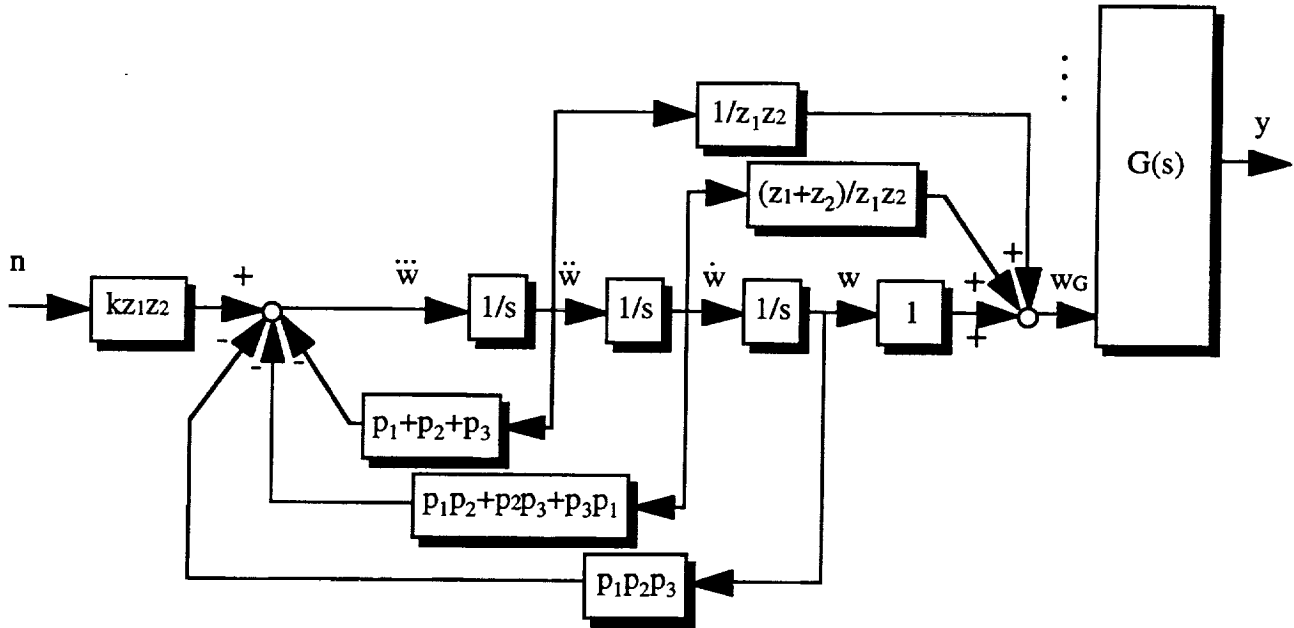


Figure 2. Overall Airframe-Gust Model

Two numerical models of the type discussed here were made available by NASA Langley for the Ref. H HSCT.<sup>8,9</sup> The baseline configuration is shown in Fig. 3. The vehicle consists of a long slender fuselage with a highly swept cranked delta wing and conventional aft tail. Wing and tail placement, in relation to the operational range of mass centers, results in relaxed pitch stability at low speeds. The low aspect ratio plate-like wing structure leads to complex vibrational shapes

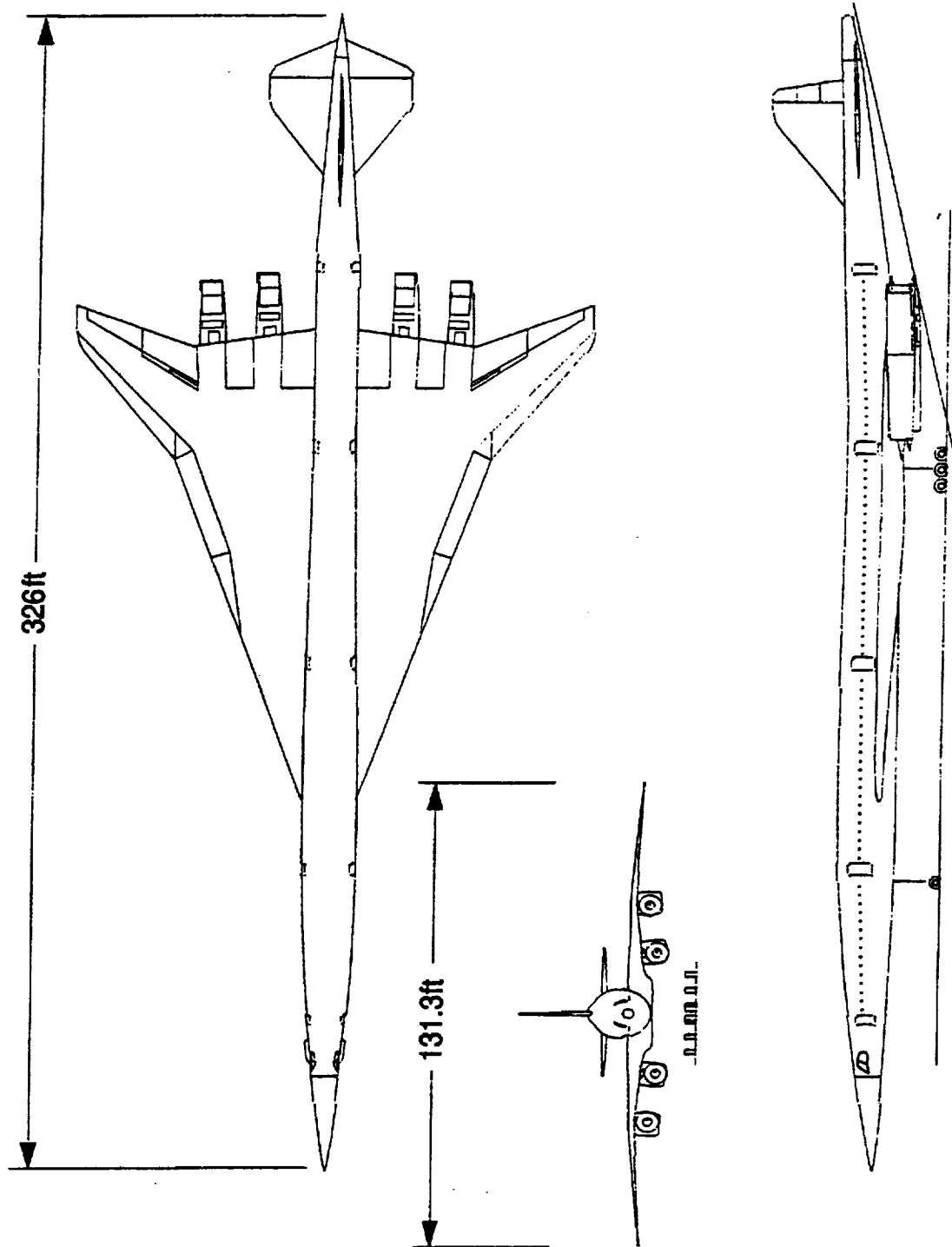


Figure 3. Ref. H HSCT Configuration

which do not resemble conventional modes of high-aspect ratio cantilevered surfaces. Note the forward crew station can be thought of as being cantilevered on the tip of a long elastic appendage.

Appendix B describes one of the NASA Langley numerical models which reflects the most current data available to the flight controls team. The Ref. H Cycle 3.1a Simulation<sup>11</sup> was utilized for model development. Internally, the Cycle 3.1a tool relies upon the package known as Integrated Structures Aerodynamics and Controls (ISAC).<sup>12</sup> This model contains the full set of rigid-body states, as well as 17 aeroelastic modes. No unsteady aerodynamic coordinates or gust inputs are included in this model. The model was supplied as an overall airframe-actuator package. However, the actuation model was modified to match characteristics in the Appendix C model. The Appendix B model corresponds to the following flight condition.

Source: NASA Langley (Appendix B)		
Trim Condition: Wings-Level, Level, Rectilinear Flight, Landing Approach Phase		
M = 0.24	h = 500 ft	W = 384,862 lbf (M3A)

Appendix C describes the other NASA Langley model. This model is essentially identical to the Appendix D model in Ref. 13, which was utilized heavily in previous flight control design studies. The only differences are 1) stability and control effects from forward vanes, 2) mode shape data covering the aft region of the airframe, 3) inclusion of the stabilator input, and 4) inclusion of vertical gust input. The model is an aggregate model fusing the forward speed degree of freedom stability and control derivatives from the rigid-body Ref. H Cycle 1 Simulation<sup>10</sup> with ISAC output data. At the time of construction, dynamic aeroelastic modeling capability was not available in the simulation tool. Due to the lack of a rigid-body forward speed degree of freedom in the ISAC models (i.e., essentially a short period approximation), manual fusion of the data was a necessary step. This procedure is discussed further in Section II-C of Ref. 13. The model includes 17 aeroelastic modes and 10 unsteady aerodynamic states. Also, the model was supplied as an overall airframe-actuator-gust package. The relevant flight condition data is listed below.

Source: NASA Langley (Appendix C)		
Trim Condition: Wings-Level, Level, Rectilinear Flight, Landing Approach Phase		
M = 0.24	h = 0 ft	W = 384,862 (M3A)

## **B. Model Comparison and Characteristics**

Modeling a highly elastic vehicle with unsteady air flow is a difficult task. Current procedures for generating such models are being expanded and refined. As wisdom should have it, initial analysis should compare/contrast similar models from independent sources to assess if they are in rough agreement, thereby invoking confidence in predictions of vehicle motions. On the other hand, if considerable differences do exist, the implication is to use caution when relying upon the model. Models in Appendix B and C are examined in this way. In terms of flight condition and modeling assumptions, the two models are very similar, thus allowing a valid comparison. Mach-Altitude parameters are nearly equivalent (500 ft altitude difference only). Both models utilize the same finite element structural data base (ELFINI 1080-892STR), and correspond to identical mass cases with mass coupling effects taken out. Further, actuation characteristics for all the aerodynamic surfaces are equivalent. Also, aerodynamic effects from close proximity to the ground are excluded in both models. Noted differences between the models include reliance upon separate aerodynamic data bases (Cycle 3 vs. Cycle 1 and different ISAC runs), and unsteady aerodynamic effects (quasi-static vs. true unsteady). At the time of analysis, the nonlinear simulation tool did not allow for unsteady aerodynamic states in the Appendix B model, precluding a more direct "item for item" comparison. Dependence upon characteristic deflection shapes also differ somewhat (discrete data vs. continuous data via polynomial fits). Polynomial fits to the discrete mode shape data can introduce small differences in the deflection and slope values associated with the higher frequency modes. However, the benefits of having smooth transfer function behavior during sensor placement studies far out weigh these costs. Finally, the models differ (a small effect) due to the presence of forward vanes in the Appendix C model.

Figs. 4-15 illustrate the frequency response characteristics of both models, for several types of measured responses at different locations, excited by various aerodynamic surface deflections. Measured responses include both pitch rate and vertical acceleration at the crew station (358 in) and center of mass (2,152 in). Excitation sources consist of the stabilator, elevator, and wing trailing edge deflections. In all stabilator and elevator driven responses (Figs. 4-7 and 10-

13), rigid-body and aeroelastic modes correlate well between one model and the other. Small differences at low frequencies (less than 3 rad/s), near the 3<sup>rd</sup> oscillatory and aperiodic slow and fast modes, are most likely associated with reliance upon different aerodynamic data bases and different ISAC runs. Another source for small differences in the vertical accelerations at very low frequencies is the term " $+g\sin(\Theta_0)\theta$ ". The Appendix B model includes this term, the Appendix C model does not. In the aeroelastic mode frequency region (more than 3 rad/s), small differences can be traced to dissimilar unsteady aerodynamic models and the use of smoothed mode shape data. Larger differences are seen between the two models at the high-end of the dynamic spectrum. This difference is most likely associated with the different ISAC runs having different convergence criteria. With control loop attenuation, these noted high frequency differences will not be of concern. In all wing trailing edge driven responses (Figs. 8-9 and 14-15), the aeroelastic mode correlation between the models breaks down beyond the 2<sup>nd</sup> aeroelastic mode (more than 13 rad/s). The source of this mismatch could possibly be due to early ISAC model development approximations such as utilization of fuselage centerline mode shapes, rather than outboard wing mode shapes, when computing control derivatives for the trailing edge surfaces. Without the necessary model data, further investigation can not take place. Wing trailing edge devices will not be utilized in feedback control studies here.

In general, very good agreement exists between the predicted dynamic characteristics of the two models for stabilator and elevator inputs. These correlations between the models in Appendix B and C validate, in some limited sense, the modeling process conducted in the nonlinear simulation tool, and in particular the linear model generation process. In other words, two separate modeling procedures yield the same dynamic characteristics. More importantly, high correlation of the aged model in Appendix C with the newer and updated characteristics in the Appendix B model validate conclusions and results from previous flight control investigations (which utilize the Appendix C model).<sup>13</sup> In this reference, the major conclusion, that single aft surface inner loop FCS architectures are not feasible, impacts overall configuration design and all major supporting disciplines. Results in Figs. 4-7 and 10-13 imply the "best available" modeling accuracy, as

reflected by the Appendix B model, for predicting airframe dynamic characteristics, can be reasonably approximated by conducting analyses with the Appendix C model. Therefore, further FCS investigations in this report will utilize the Appendix C model.

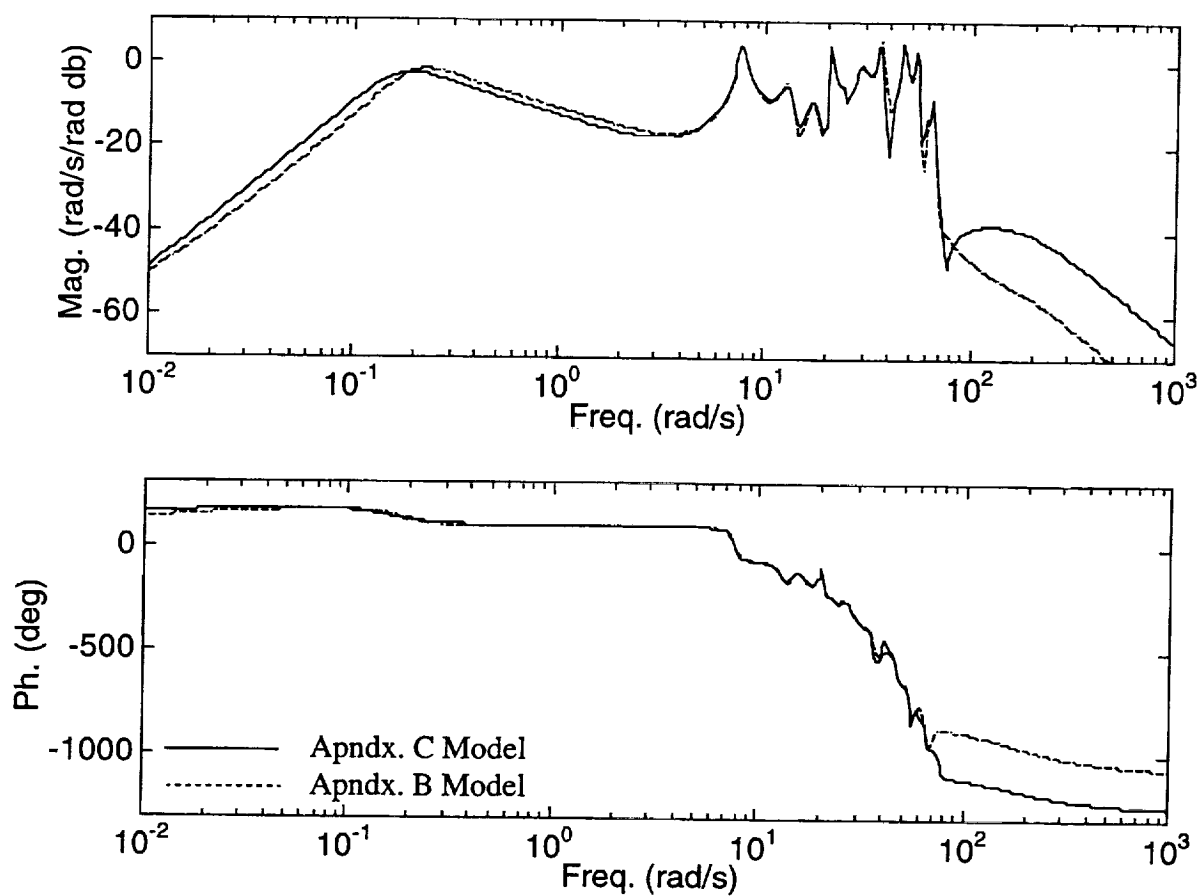


Figure 4. Frequency Response Comparison Of Appendix B & C Models  
For 358 in Pitch Rate To Stabilator Channel

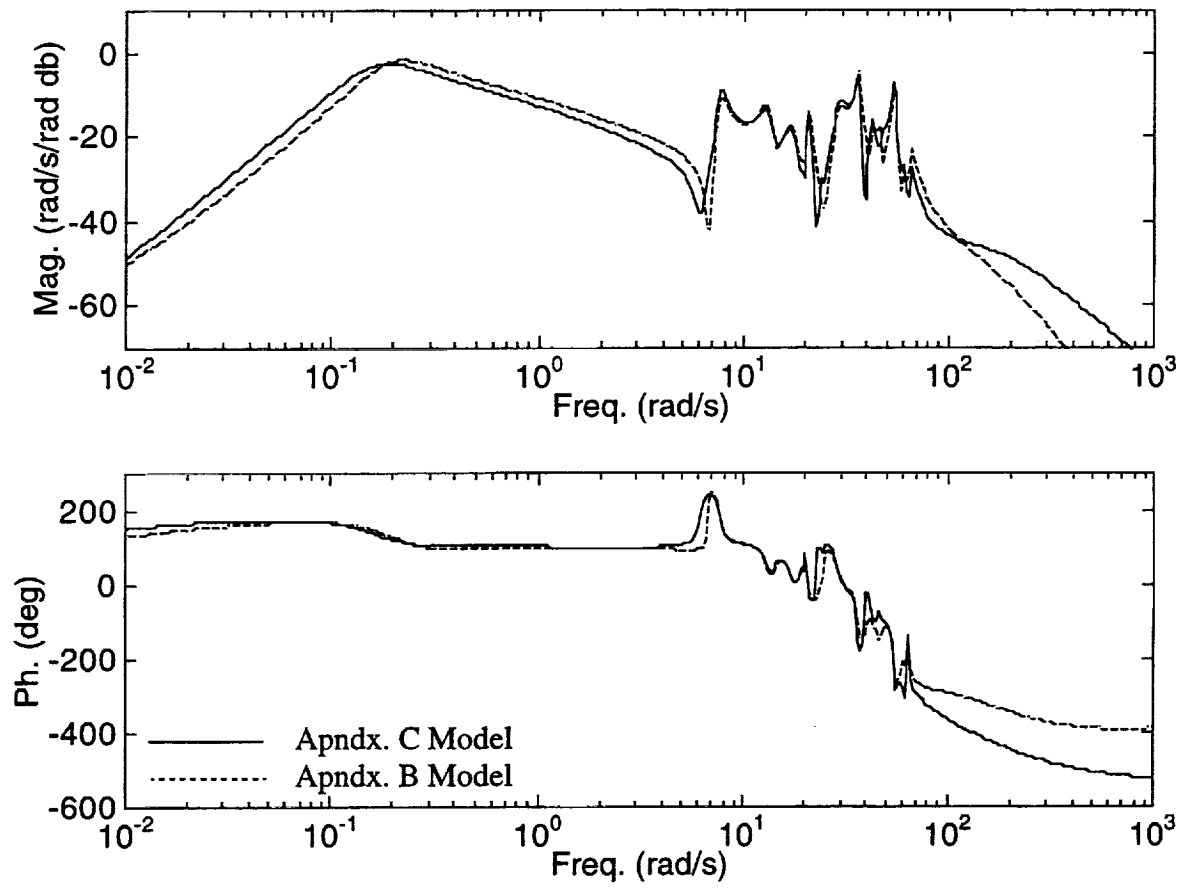


Figure 5. Frequency Response Comparison Of Appendix B & C Models  
For 2,152 in Pitch Rate To Stabilator Channel



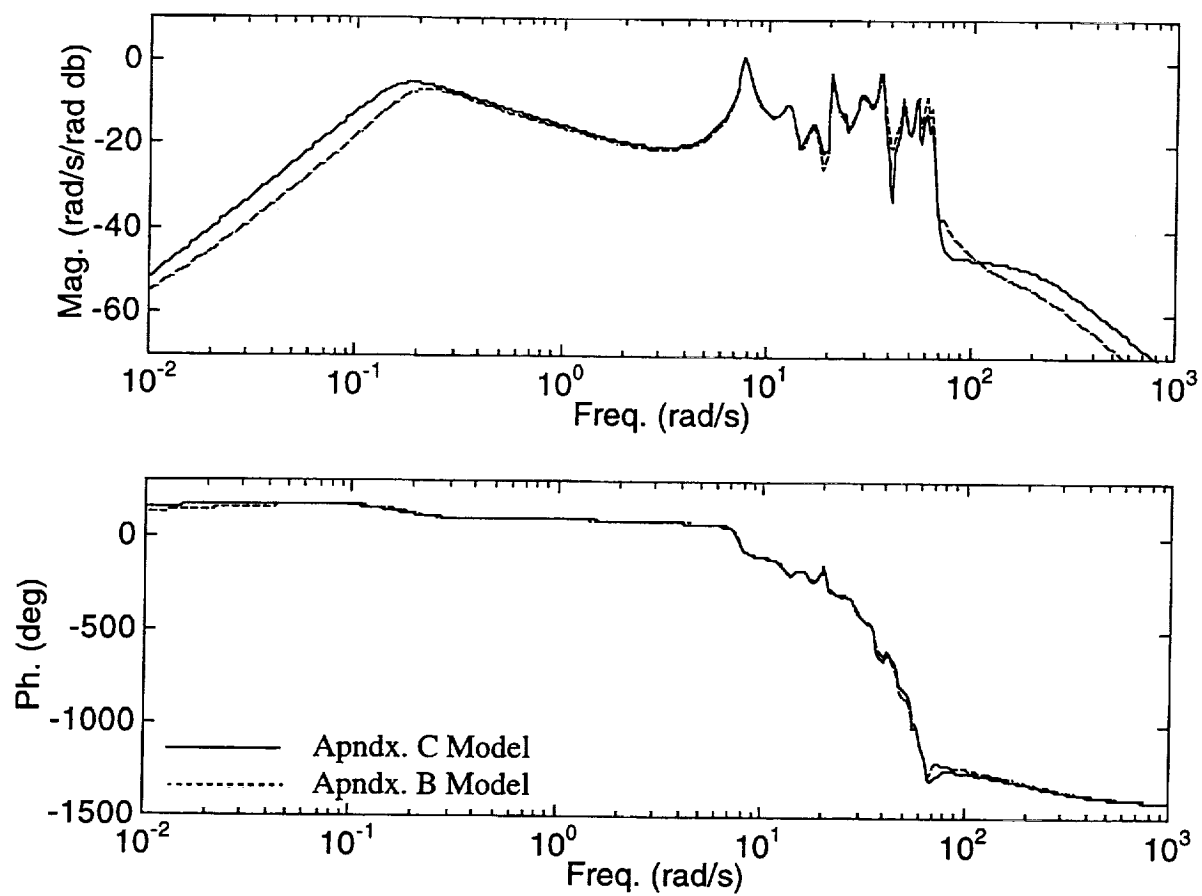


Figure 6. Frequency Response Comparison Of Appendix B & C Models  
For 358 in Pitch Rate To Elevator Channel

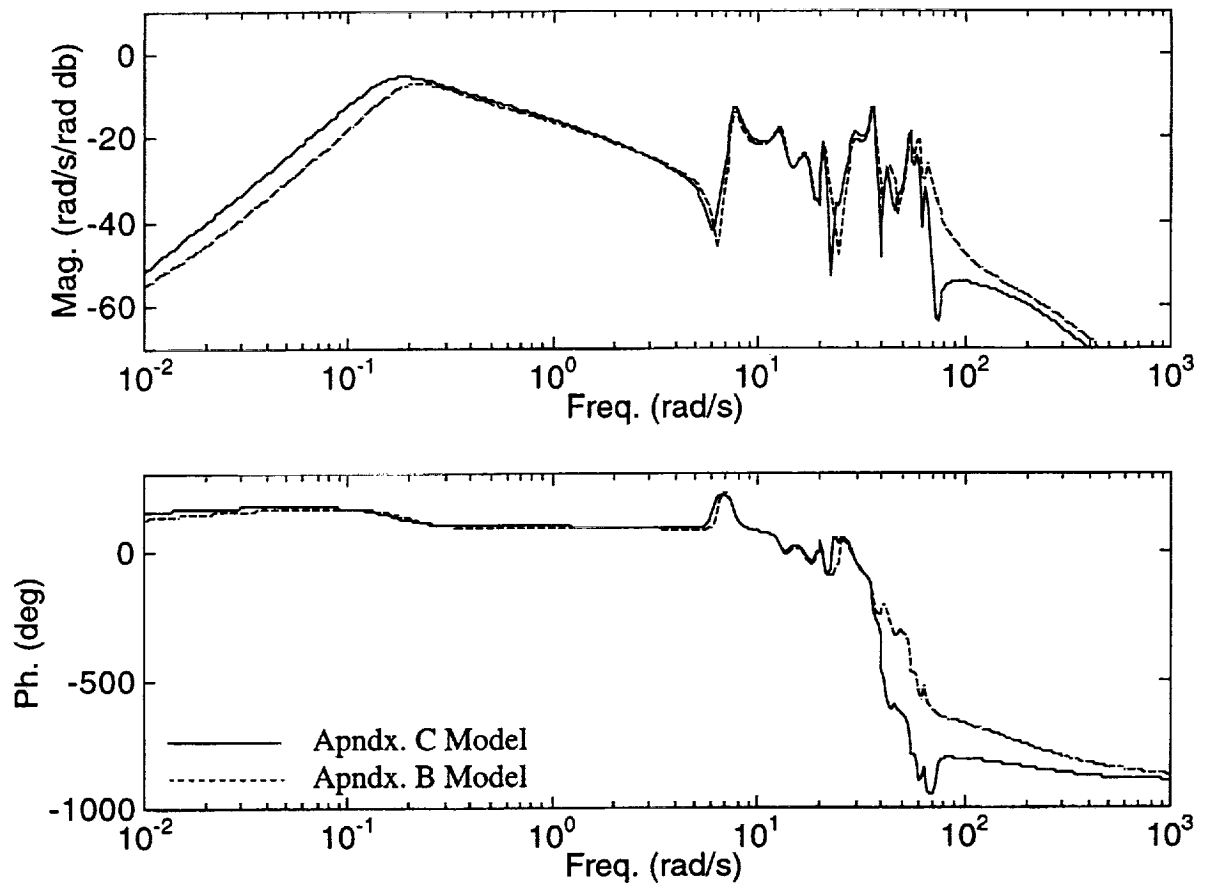


Figure 7. Frequency Response Comparison Of Appendix B & C Models  
For 2,152 in Pitch Rate To Elevator Channel

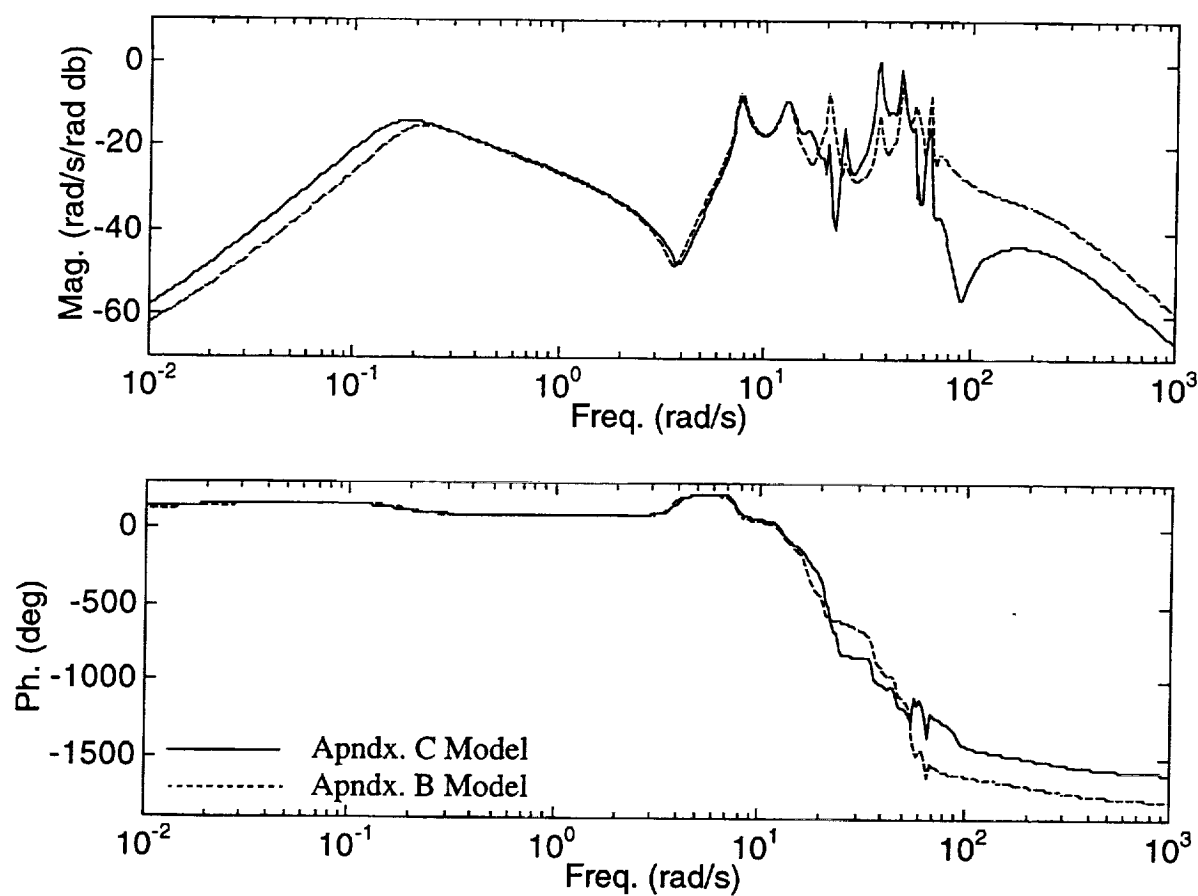


Figure 8. Frequency Response Comparison Of Appendix B & C Models  
For 358 in Pitch Rate To Trailing Edge 3 Channel

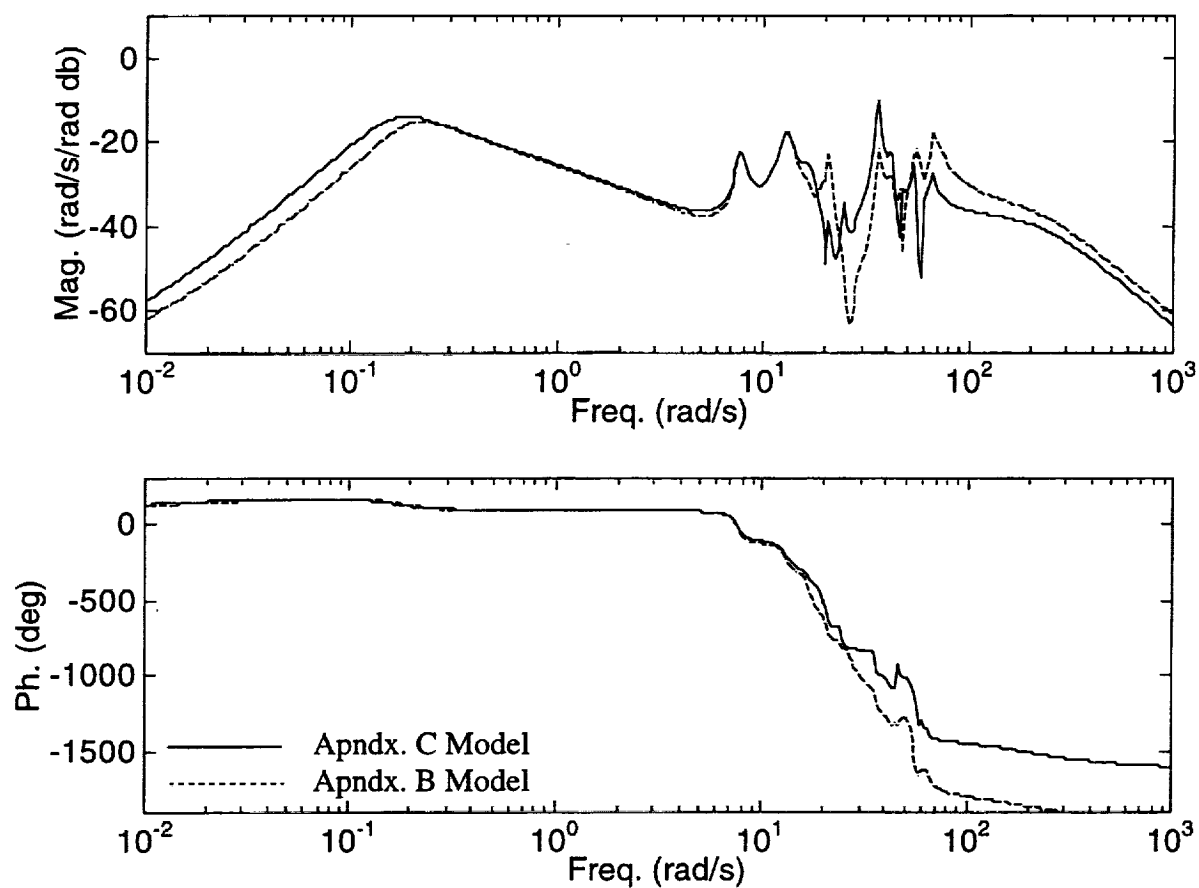


Figure 9. Frequency Response Comparison Of Appendix B & C Models  
For 2,152 in Pitch Rate To Trailing Edge 3 Channel

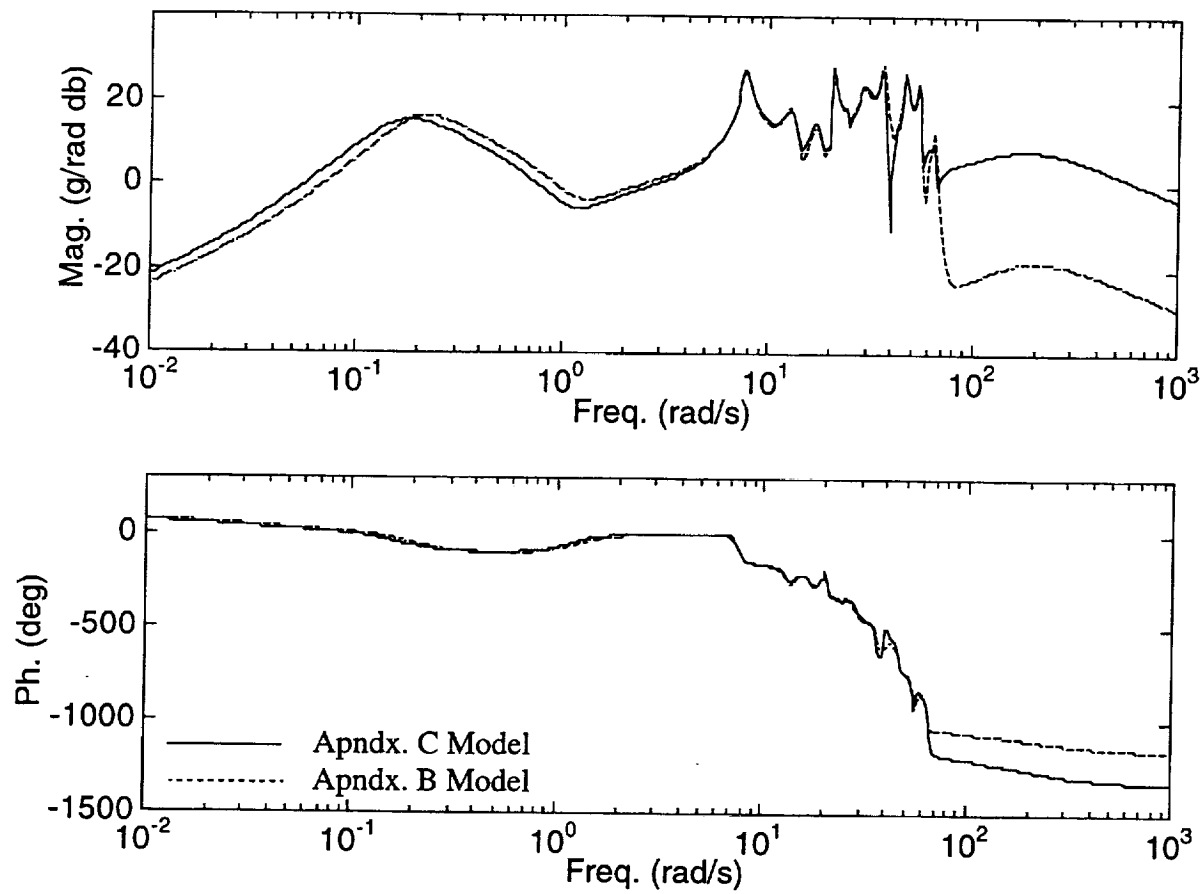


Figure 10. Frequency Response Comparison Of Appendix B & C Models  
For 358 in Vertical Acceleration To Stabilator Channel

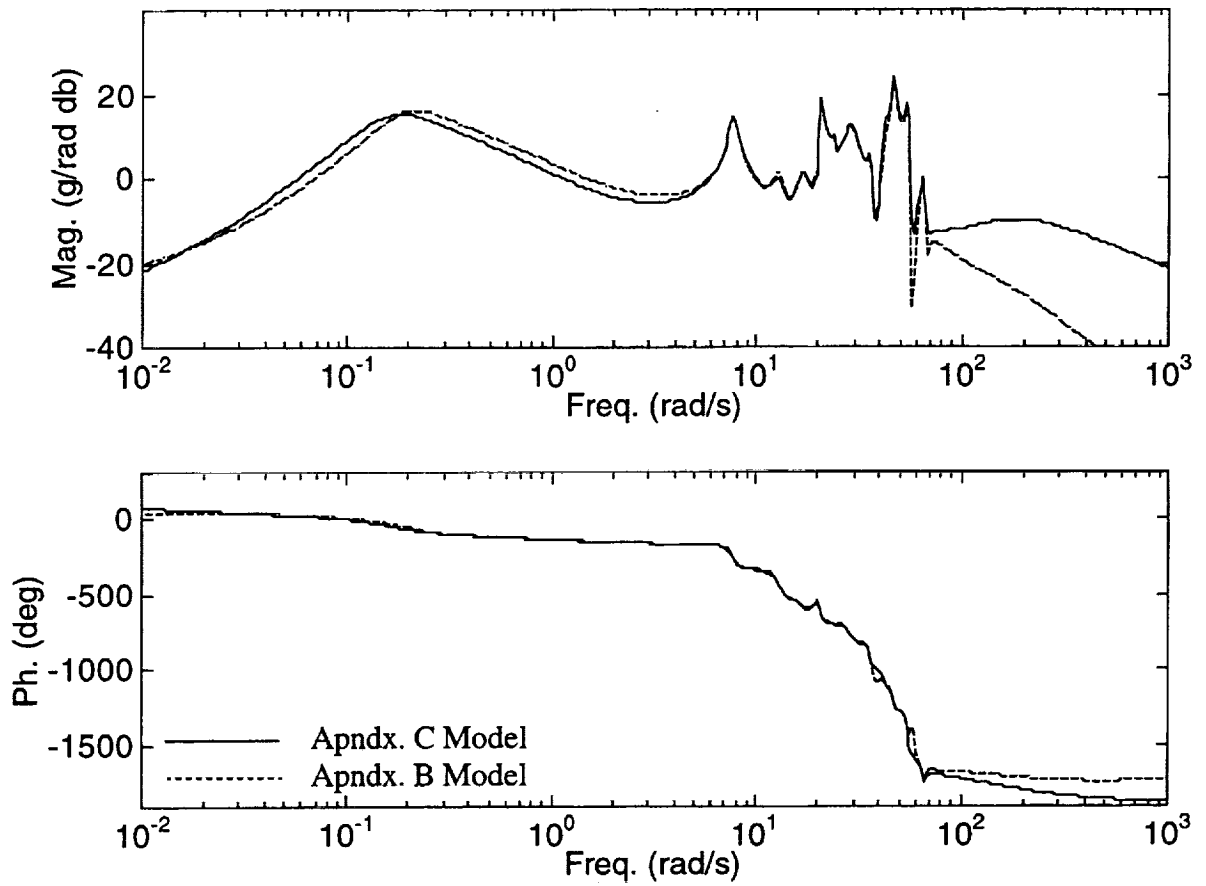


Figure 11. Frequency Response Comparison Of Appendix B & C Models  
 For 2,152 in Vertical Acceleration To Stabilator Channel

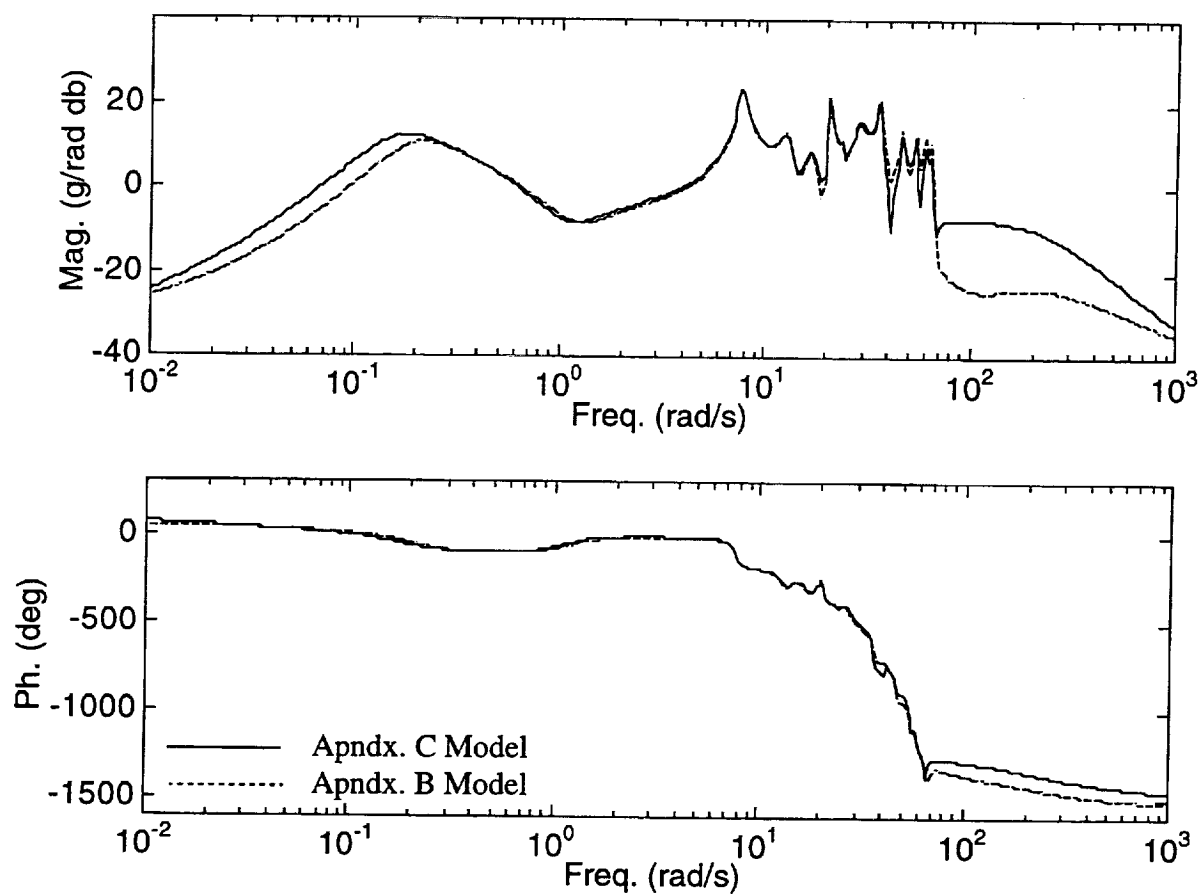


Figure 12. Frequency Response Comparison Of Appendix B & C Models  
For 358 in Vertical Acceleration To Elevator Channel

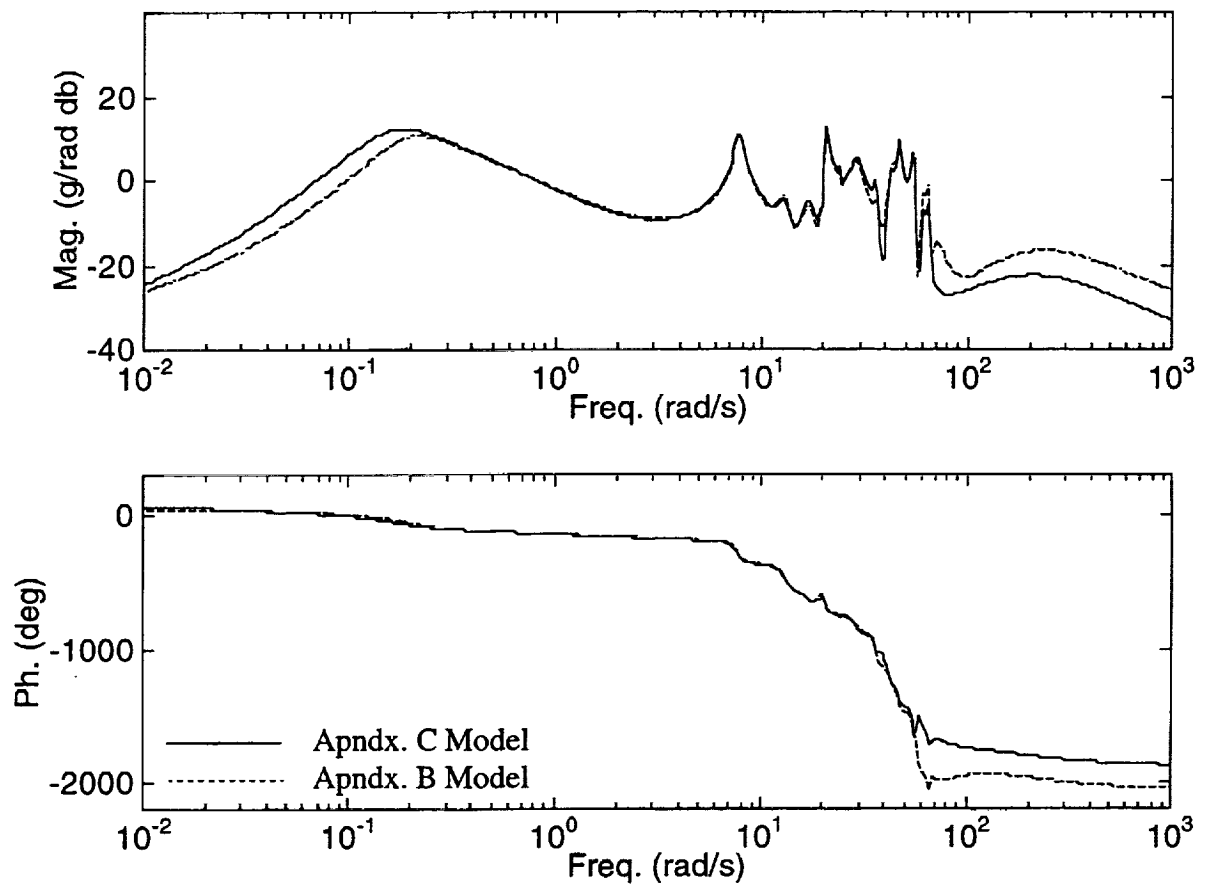


Figure 13. Frequency Response Comparison Of Appendix B & C Models  
For 2,152 in Vertical Acceleration To Elevator Channel



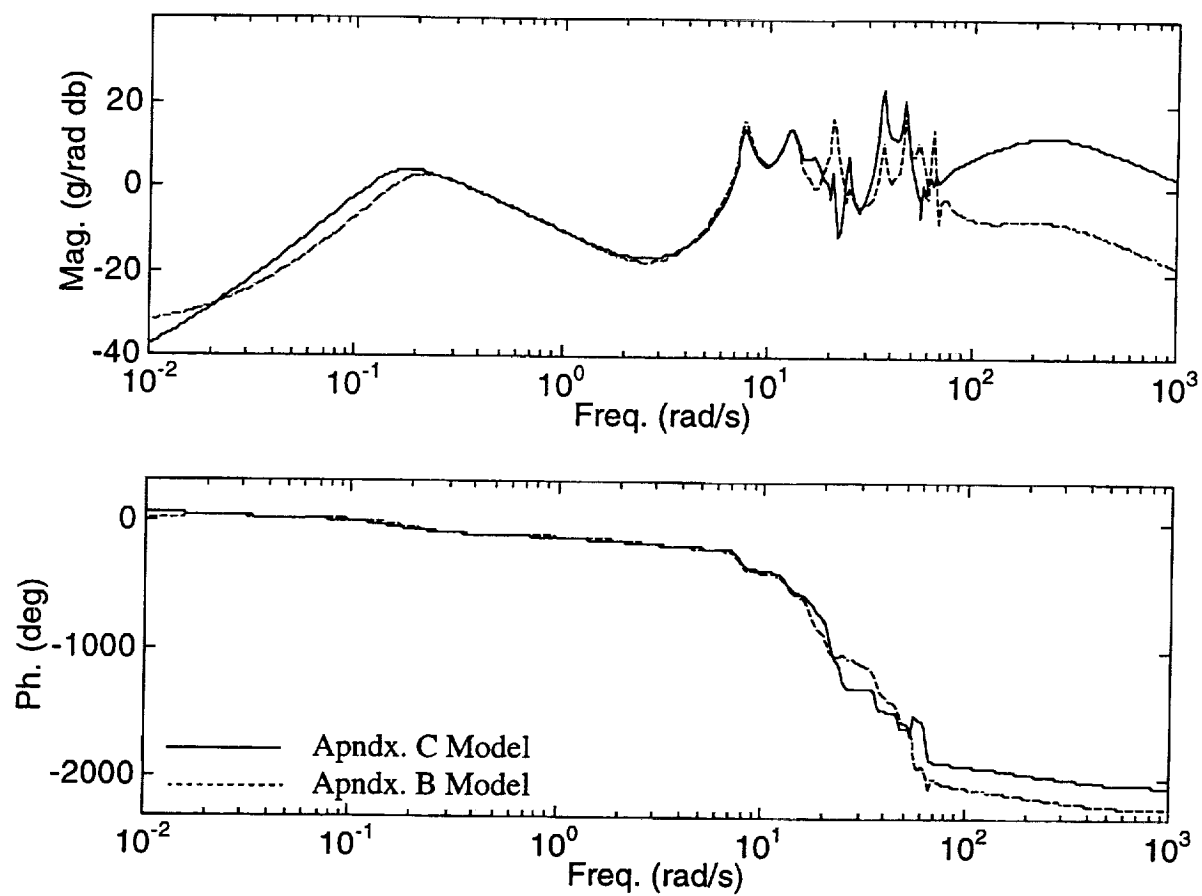


Figure 14. Frequency Response Comparison Of Appendix B & C Models  
For 358 in Vertical Acceleration To Trailing Edge 3 Channel

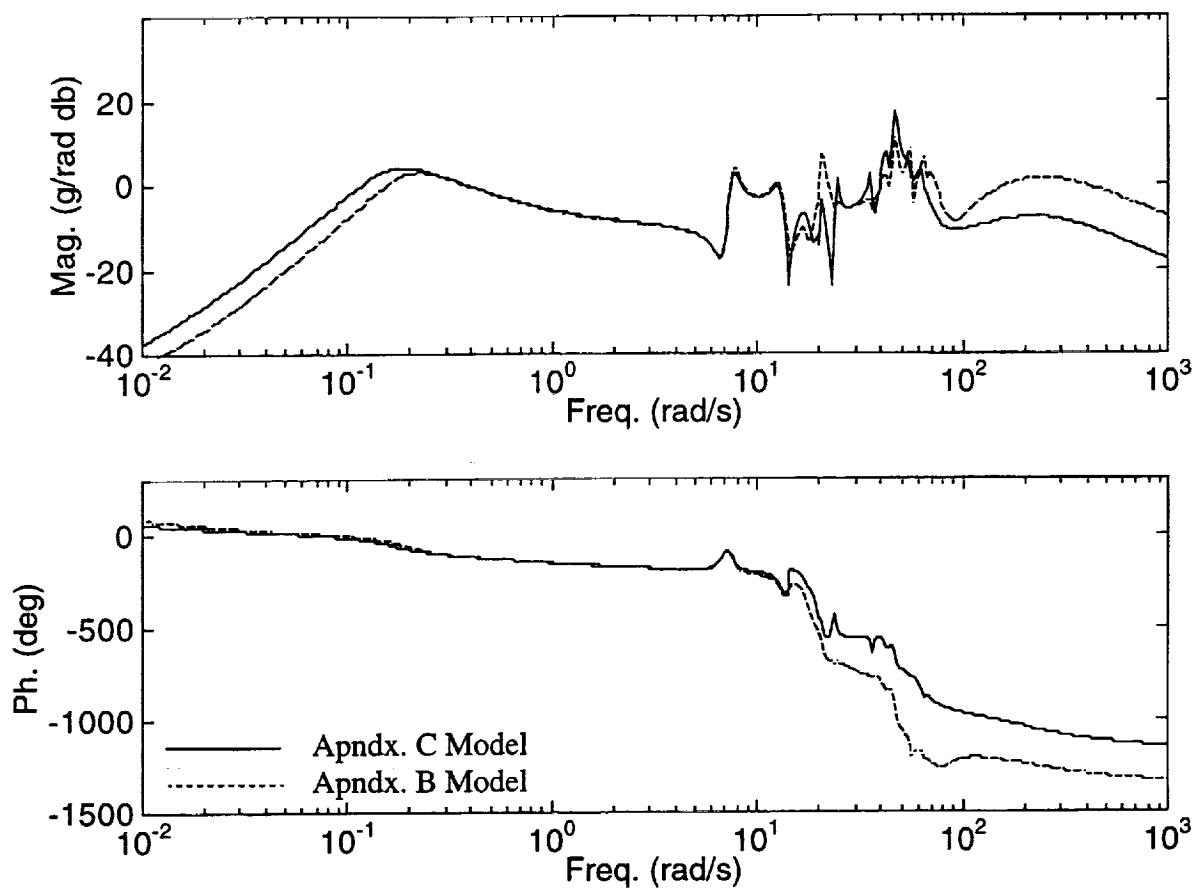


Figure 15. Frequency Response Comparison Of Appendix B & C Models  
For 2,152 in Vertical Acceleration To Trailing Edge 3 Channel

Dynamic characteristics associated with key transfer functions of the HSCT airframe that will appear later in control system design activities are discussed next. Tab. 1 lists the poles of the Appendix C airframe-actuator model. At this low-speed, low-altitude condition, the HSCT inherent pitch instability is clearly present. Rigid-body modes consist of the so called third oscillatory mode and two real axis modes, one fast and stable, the other slow and unstable. Aeroelastic mode frequencies include the 1<sup>st</sup> and 2<sup>nd</sup> mode values at 7.7 and 12.8 rad/s all the way up to a value of 65.1 rad/s for the 17<sup>th</sup> mode with unsteady aerodynamic modes throughout this frequency range. Damping ratios for the aeroelastic modes are extremely light (i.e., on the order of 0.1 or sometimes considerably less). Unsteady aerodynamic modes have reciprocal time constants ranging from 0.86 to 29.4 1/s.

Tabs. 2-13 contain the transfer function gains and zeros for measured pitch rate and vertical acceleration to elevator and vane, at three key locations along the fuselage centerline: 400, 1,850 and 3,460 in. These positions yield coverage over the vehicle length and correspond to the vane mounting point, the anti-node of the 1<sup>st</sup> aeroelastic mode, and the elevator hinge line. The crew station is only 3.5 ft removed from the vane mounting, therefore, response characteristics at 400 in will reflect what the pilot experiences. Figs. 16-27 show the corresponding frequency responses. Each set of factored numerators contain the rigid-body zeros  $1/\tau_{\theta_1}$  and  $1/\tau_{\theta_2}$  for pitch rate, rigid-body zeros  $1/\tau_{az_1}$ ,  $1/\tau_{az_2}$ ,  $1/\tau_{az_3}$ , and  $1/\tau_{az_4}$  for vertical acceleration (or complex conjugate equivalents), a pair of zeros for every aeroelastic mode, and a zero for every unsteady aerodynamic mode. In addition, two zeros having their origin from the noncausal input terms  $B'\dot{u}$  and  $B''\ddot{u}$  in Eq. (2.1) are present, and canceling zeros associated with the other channel actuators.

In general, observe from the frequency responses and tabular data how the aeroelastic modes excite the sensors at different frequencies, as the sensor mounting location is varied along the fuselage. Aeroelastic contamination of all responses is clearly seen. The 1<sup>st</sup> aeroelastic zeros essentially cancel the 1<sup>st</sup> aeroelastic poles when the rate gyro is located at 1,850 in. At 400 in, the 1<sup>st</sup> aeroelastic zeros of the pitch rate to vane transfer function are minimum phase, have complex root structure, and are located directly below the 1<sup>st</sup> aeroelastic poles (i.e., collocated

actuator/sensor pair). On the other hand, at 400 in for pitch rate to elevator, the 1<sup>st</sup> aeroelastic zeros consist of real roots with one located in the right-half plane (i.e., an extreme non-collocated actuator/sensor pair). These trends and others can be correlated with the structural vibration mode shapes for the fuselage centerline shown in Fig. 28.  $x_s$  and  $z_s$  denote typical structural axes with  $x_s$  pointing aft,  $z_s$  pointing up, and origin located at the nose.

In Tabs. 2-13, note the zeros associated with unsteady aerodynamic modes are always located close to the pole. These unsteady aerodynamic dipoles with "tight" structure do not appear to significantly impact the dynamics, other than introducing small phase variations. The most significant impact from unsteady aerodynamics comes into play through the noncausal zeros associated with the  $B'\dot{u}$  and  $B''\ddot{u}$  terms. These noncausal zeros are primarily determined by the quadratic term  $B''s^2+B's+B$ . These roots lie well inside the actuator bandwidth (compare Tabs. 1 and 2), and amplify the aeroelastic frequency region due to a lack of actuator attenuation until higher frequencies. This feature is more easily recognized graphically. Typically with aeroelastic models, attenuation characteristics are a gradual (-20 db/dec) roll off due to the fundamental rigid-body physics of rate-to-force transfers, with superimposed aeroelastic peaks and troughs. In Fig. 16, the -20 db/dec attenuation behavior is missing in the 10 to 100 rad/s frequency range due to the noncausal zeros. This behavior leads to large aeroelastic peak values.

Table 1. Poles Of Appendix C Model				
Root Location (1/s)	Freq. (rad/s)	Damping (-)	Description	
-7.9137e-02+ 1.4458e-01i	1.6482e-01	4.8013e-01	Mid Period (3rd Osc)	
-7.9137e-02- 1.4458e-01i	1.6482e-01	4.8013e-01	Mid Period (3rd Osc)	
1.7766e-01	1.7766e-01	-1.0000e+00	Slow	
-6.6819e-01	6.6819e-01	1.0000e+00	Fast	
-8.5519e-01	8.5519e-01	1.0000e+00	Unsteady Aero 1	
-1.3592e+00	1.3592e+00	1.0000e+00	Unsteady Aero 2	
-4.2577e+00	4.2577e+00	1.0000e+00	Unsteady Aero 3	
-3.4547e-01+ 7.6804e+00i	7.6881e+00	4.4935e-02	Aeroelastic 1	
-3.4547e-01- 7.6804e+00i	7.6881e+00	4.4935e-02	Aeroelastic 1	
-8.3170e+00	8.3170e+00	1.0000e+00	Unsteady Aero 4	
-9.3213e+00+ 3.2228e-01i	9.3269e+00	9.9940e-01	Unsteady Aero 5	
-9.3213e+00- 3.2228e-01i	9.3269e+00	9.9940e-01	Unsteady Aero 6	
-1.1150e+01	1.1150e+01	1.0000e+00	Unsteady Aero 7	
-7.5590e-01+ 1.2783e+01i	1.2806e+01	5.9028e-02	Aeroelastic 2	
-7.5590e-01- 1.2783e+01i	1.2806e+01	5.9028e-02	Aeroelastic 2	
-1.3487e+01	1.3487e+01	1.0000e+00	Unsteady Aero 8	
-1.0920e+00+ 1.6934e+01i	1.6969e+01	6.4353e-02	Aeroelastic 3	
-1.0920e+00- 1.6934e+01i	1.6969e+01	6.4353e-02	Aeroelastic 3	
-1.8717e-01+ 1.7264e+01i	1.7265e+01	1.0841e-02	Aeroelastic 4	
-1.8717e-01- 1.7264e+01i	1.7265e+01	1.0841e-02	Aeroelastic 4	
-1.8306e+01	1.8306e+01	1.0000e+00	Unsteady Aero 9	
-1.9000e+01	1.9000e+01	1.0000e+00	Stabilator Actuator	
-3.1204e-01+ 1.9563e+01i	1.9565e+01	1.5949e-02	Aeroelastic 5	
-3.1204e-01- 1.9563e+01i	1.9565e+01	1.5949e-02	Aeroelastic 5	
-2.0000e+01	2.0000e+01	1.0000e+00	Trailing Edge 1 Actuator	
-2.8716e-01+ 2.0829e+01i	2.0831e+01	1.3785e-02	Aeroelastic 6	
-2.8716e-01- 2.0829e+01i	2.0831e+01	1.3785e-02	Aeroelastic 6	
-2.1000e+01	2.1000e+01	1.0000e+00	Trailing Edge 2 Actuator	
-2.2000e+01	2.2000e+01	1.0000e+00	Elevator Actuator	
-2.2000e+01	2.2000e+01	1.0000e+00	Vane Actuator	
-2.3000e+01	2.3000e+01	1.0000e+00	Trailing Edge 3 Actuator	
-2.4000e+01	2.4000e+01	1.0000e+00	Trailing Edge 4 Actuator	
-3.1140e-01+ 2.4273e+01i	2.4275e+01	1.2828e-02	Aeroelastic 7	
-3.1140e-01- 2.4273e+01i	2.4275e+01	1.2828e-02	Aeroelastic 7	
-1.9558e+00+ 2.9246e+01i	2.9311e+01	6.6726e-02	Aeroelastic 8	
-1.9558e+00- 2.9246e+01i	2.9311e+01	6.6726e-02	Aeroelastic 8	
-2.9351e+01	2.9351e+01	1.0000e+00	Unsteady Aero 10	
-3.5782e-01+ 3.5652e+01i	3.5654e+01	1.0036e-02	Aeroelastic 9	
-3.5782e-01- 3.5652e+01i	3.5654e+01	1.0036e-02	Aeroelastic 9	
-9.1268e-01+ 4.2395e+01i	4.2405e+01	2.1523e-02	Aeroelastic 10	
-9.1268e-01- 4.2395e+01i	4.2405e+01	2.1523e-02	Aeroelastic 10	
-6.9489e-01+ 4.6602e+01i	4.6607e+01	1.4909e-02	Aeroelastic 11	
-6.9489e-01- 4.6602e+01i	4.6607e+01	1.4909e-02	Aeroelastic 11	
-9.0245e-01+ 5.3631e+01i	5.3639e+01	1.6825e-02	Aeroelastic 12	
-9.0245e-01- 5.3631e+01i	5.3639e+01	1.6825e-02	Aeroelastic 12	
-7.4053e-01+ 5.6048e+01i	5.6053e+01	1.3211e-02	Aeroelastic 13	
-7.4053e-01- 5.6048e+01i	5.6053e+01	1.3211e-02	Aeroelastic 13	
-8.8368e-01+ 6.0401e+01i	6.0407e+01	1.4629e-02	Aeroelastic 14	
-8.8368e-01- 6.0401e+01i	6.0407e+01	1.4629e-02	Aeroelastic 14	
-3.2257e+00+ 6.1401e+01i	6.1486e+01	5.2462e-02	Aeroelastic 15	
-3.2257e+00- 6.1401e+01i	6.1486e+01	5.2462e-02	Aeroelastic 15	
-8.4990e-01+ 6.2380e+01i	6.2386e+01	1.3623e-02	Aeroelastic 16	
-8.4990e-01- 6.2380e+01i	6.2386e+01	1.3623e-02	Aeroelastic 16	
-7.2400e-01+ 6.5083e+01i	6.5087e+01	1.1124e-02	Aeroelastic 17	
-7.2400e-01- 6.5083e+01i	6.5087e+01	1.1124e-02	Aeroelastic 17	

Table 1. Continued				
-1.3435e+02+	1.3435e+02i	1.9000e+02	7.0710e-01	Stabilator Actuator
-1.3435e+02-	1.3435e+02i	1.9000e+02	7.0710e-01	Stabilator Actuator
-1.4142e+02+	1.4142e+02i	2.0000e+02	7.0710e-01	Trailing Edge 1 Actuator
-1.4142e+02-	1.4142e+02i	2.0000e+02	7.0710e-01	Trailing Edge 1 Actuator
-1.4849e+02+	1.4849e+02i	2.1000e+02	7.0710e-01	Trailing Edge 2 Actuator
-1.4849e+02-	1.4849e+02i	2.1000e+02	7.0710e-01	Trailing Edge 2 Actuator
-1.5556e+02+	1.5556e+02i	2.2000e+02	7.0710e-01	Elevator Actuator
-1.5556e+02-	1.5556e+02i	2.2000e+02	7.0710e-01	Elevator Actuator
-1.5556e+02+	1.5556e+02i	2.2000e+02	7.0710e-01	Vane Actuator
-1.5556e+02-	1.5556e+02i	2.2000e+02	7.0710e-01	Vane Actuator
-1.6263e+02+	1.6263e+02i	2.3000e+02	7.0710e-01	Trailing Edge 3 Actuator
-1.6263e+02-	1.6263e+02i	2.3000e+02	7.0710e-01	Trailing Edge 3 Actuator
-1.6970e+02+	1.6970e+02i	2.4000e+02	7.0710e-01	Trailing Edge 4 Actuator
-1.6970e+02-	1.6970e+02i	2.4000e+02	7.0710e-01	Trailing Edge 4 Actuator

Table 2. Zeros Of Appendix C Model For 400 in Pitch Rate To Elevator Channel			
Gain = -2.1345e+02 rad/s/rad			
Root Location (1/s)	Freq. (rad/s)	Damping (-)	Description
0	0	1.0000e+00	Pitch "Rate"
-4.2957e-03	4.2957e-03	1.0000e+00	Tau Theta 1
-4.8215e-01	4.8215e-01	1.0000e+00	Tau Theta 2
-7.3580e-01	7.3580e-01	1.0000e+00	Unsteady Aero 1
-1.3602e+00	1.3602e+00	1.0000e+00	Unsteady Aero 2
-4.8325e+00+ 1.5792e-01i	4.8351e+00	9.9947e-01	Unsteady Aero 3
-4.8325e+00- 1.5792e-01i	4.8351e+00	9.9947e-01	Aeroelastic 1
5.5433e+00	5.5433e+00	-1.0000e+00	Aeroelastic 1
-8.2182e+00	8.2182e+00	1.0000e+00	Unsteady Aero 4
-8.9847e+00+ 2.1916e+00i	9.2482e+00	9.7151e-01	Unsteady Aero 5
-8.9847e+00- 2.1916e+00i	9.2482e+00	9.7151e-01	Unsteady Aero 6
-1.0823e+01	1.0823e+01	1.0000e+00	Unsteady Aero 7
-1.1706e+01+ 7.5449e+00i	1.3927e+01	8.4053e-01	Unsteady Aero 8
-1.1706e+01- 7.5449e+00i	1.3927e+01	8.4053e-01	Noncausal Rate
-1.1881e+00+ 1.4138e+01i	1.4188e+01	8.3741e-02	Aeroelastic 2
-1.1881e+00- 1.4138e+01i	1.4188e+01	8.3741e-02	Aeroelastic 2
-1.5980e+01	1.5980e+01	1.0000e+00	Unsteady Aero 9
-1.7269e-01+ 1.7262e+01i	1.7263e+01	1.0004e-02	Aeroelastic 3
-1.7269e-01- 1.7262e+01i	1.7263e+01	1.0004e-02	Aeroelastic 3
-7.1568e-01+ 1.8841e+01i	1.8855e+01	3.7958e-02	Aeroelastic 4
-7.1568e-01- 1.8841e+01i	1.8855e+01	3.7958e-02	Aeroelastic 4
-1.9000e+01	1.9000e+01	1.0000e+00	Stabilator Actuator
-2.0480e-01+ 1.9696e+01i	1.9697e+01	1.0397e-02	Aeroelastic 5
-2.0480e-01- 1.9696e+01i	1.9697e+01	1.0397e-02	Aeroelastic 5
-2.0000e+01	2.0000e+01	1.0000e+00	Trailing Edge 1 Actuator
-2.1000e+01	2.1000e+01	1.0000e+00	Trailing Edge 2 Actuator
-2.2000e+01	2.2000e+01	1.0000e+00	Vane Actuator
-2.3000e+01	2.3000e+01	1.0000e+00	Trailing Edge 3 Actuator
-2.4000e+01	2.4000e+01	1.0000e+00	Trailing Edge 4 Actuator
-1.1586e+01+ 2.1164e+01i	2.4128e+01	4.8021e-01	Aeroelastic 6
-1.1586e+01- 2.1164e+01i	2.4128e+01	4.8021e-01	Aeroelastic 6
-2.9159e-01+ 2.4423e+01i	2.4425e+01	1.1938e-02	Aeroelastic 7
-2.9159e-01- 2.4423e+01i	2.4425e+01	1.1938e-02	Aeroelastic 7
2.2906e+01+ 1.3520e+01i	2.6598e+01	-8.6118e-01	Aeroelastic 8
2.2906e+01- 1.3520e+01i	2.6598e+01	-8.6118e-01	Aeroelastic 8
-3.0907e+01	3.0907e+01	1.0000e+00	Unsteady Aero 10
8.1385e+00+ 4.0372e+01i	4.1184e+01	-1.9761e-01	Aeroelastic 9
8.1385e+00- 4.0372e+01i	4.1184e+01	-1.9761e-01	Aeroelastic 9
-6.8058e-01+ 4.1583e+01i	4.1589e+01	1.6365e-02	Aeroelastic 10
-6.8058e-01- 4.1583e+01i	4.1589e+01	1.6365e-02	Aeroelastic 10
-5.6056e+00+ 4.4476e+01i	4.4828e+01	1.2505e-01	Aeroelastic 11
-5.6056e+00- 4.4476e+01i	4.4828e+01	1.2505e-01	Aeroelastic 11
-6.9744e-01+ 5.6411e+01i	5.6416e+01	1.2363e-02	Aeroelastic 12
-6.9744e-01- 5.6411e+01i	5.6416e+01	1.2363e-02	Aeroelastic 12
-8.7376e+00+ 5.5985e+01i	5.6663e+01	1.5420e-01	Aeroelastic 13
-8.7376e+00- 5.5985e+01i	5.6663e+01	1.5420e-01	Aeroelastic 13
5.7633e+01	5.7633e+01	-1.0000e+00	Noncausal Acceleration
7.5621e+00+ 5.8873e+01i	5.9357e+01	-1.2740e-01	Aeroelastic 14
7.5621e+00- 5.8873e+01i	5.9357e+01	-1.2740e-01	Aeroelastic 14
-3.6777e+00+ 6.1330e+01i	6.1441e+01	5.9857e-02	Aeroelastic 15
-3.6777e+00- 6.1330e+01i	6.1441e+01	5.9857e-02	Aeroelastic 15
-8.4996e-01+ 6.2328e+01i	6.2334e+01	1.3636e-02	Aeroelastic 16
-8.4996e-01- 6.2328e+01i	6.2334e+01	1.3636e-02	Aeroelastic 16
-3.5423e+00+ 6.9037e+01i	6.9128e+01	5.1242e-02	Aeroelastic 17

Table 2. Continued				
-3.5423e+00-	6.9037e+01i	6.9128e+01	5.1242e-02	Aeroelastic 17
-1.3435e+02+	1.3435e+02i	1.9000e+02	7.0710e-01	Stabilator Actuator
-1.3435e+02-	1.3435e+02i	1.9000e+02	7.0710e-01	Stabilator Actuator
-1.4142e+02+	1.4142e+02i	2.0000e+02	7.0710e-01	Trailing Edge 1 Actuator
-1.4142e+02-	1.4142e+02i	2.0000e+02	7.0710e-01	Trailing Edge 1 Actuator
-1.4849e+02+	1.4849e+02i	2.1000e+02	7.0710e-01	Trailing Edge 2 Actuator
-1.4849e+02-	1.4849e+02i	2.1000e+02	7.0710e-01	Trailing Edge 2 Actuator
-1.5556e+02+	1.5556e+02i	2.2000e+02	7.0710e-01	Vane Actuator
-1.5556e+02-	1.5556e+02i	2.2000e+02	7.0710e-01	Vane Actuator
-1.6263e+02+	1.6263e+02i	2.3000e+02	7.0710e-01	Trailing Edge 3 Actuator
-1.6263e+02-	1.6263e+02i	2.3000e+02	7.0710e-01	Trailing Edge 3 Actuator
-1.6970e+02+	1.6970e+02i	2.4000e+02	7.0710e-01	Trailing Edge 4 Actuator
-1.6970e+02-	1.6970e+02i	2.4000e+02	7.0710e-01	Trailing Edge 4 Actuator



Table 3. Zeros Of Appendix C Model For 1,850 in Pitch Rate To Elevator Channel			
Gain = 1.8707e+01 rad/s/rad			
Root Location (1/s)	Freq. (rad/s)	Damping (-)	Description
0	0	1.0000e+00	Pitch "Rate"
-4.6378e-03	4.6378e-03	1.0000e+00	Tau Theta 1
-4.7774e-01	4.7774e-01	1.0000e+00	Tau Theta 2
-7.3042e-01	7.3042e-01	1.0000e+00	Unsteady Aero 1
-1.3598e+00	1.3598e+00	1.0000e+00	Unsteady Aero 2
-4.3275e+00	4.3275e+00	1.0000e+00	Unsteady Aero 3
-7.3185e+00	7.3185e+00	1.0000e+00	Unsteady Aero 4
-2.2041e-01+ 7.5144e+00i	7.5176e+00	2.9319e-02	Aeroelastic 1
-2.2041e-01- 7.5144e+00i	7.5176e+00	2.9319e-02	Aeroelastic 1
-8.6014e+00	8.6014e+00	1.0000e+00	Unsteady Aero 5
-9.4612e+00	9.4612e+00	1.0000e+00	Unsteady Aero 6
-1.1112e+01	1.1112e+01	1.0000e+00	Unsteady Aero 7
-1.2277e+00+ 1.4031e+01i	1.4085e+01	8.7166e-02	Aeroelastic 2
-1.2277e+00- 1.4031e+01i	1.4085e+01	8.7166e-02	Aeroelastic 2
-1.4714e+01	1.4714e+01	1.0000e+00	Unsteady Aero 8
-1.7252e-01+ 1.7263e+01i	1.7264e+01	9.9928e-03	Aeroelastic 4
-1.7252e-01- 1.7263e+01i	1.7264e+01	9.9928e-03	Aeroelastic 4
-1.4168e+01+ 1.1515e+01i	1.8258e+01	7.7602e-01	Unsteady Aero 9
-1.4168e+01- 1.1515e+01i	1.8258e+01	7.7602e-01	Aeroelastic 3
1.8609e+01	1.8609e+01	-1.0000e+00	Aeroelastic 3
-6.8532e-01+ 1.8882e+01i	1.8894e+01	3.6271e-02	Aeroelastic 5
-6.8532e-01- 1.8882e+01i	1.8894e+01	3.6271e-02	Aeroelastic 5
-1.9000e+01	1.9000e+01	1.0000e+00	Stabilator Actuator
-1.9770e-01+ 1.9704e+01i	1.9705e+01	1.0033e-02	Aeroelastic 6
-1.9770e-01- 1.9704e+01i	1.9705e+01	1.0033e-02	Aeroelastic 6
-1.9872e+01	1.9872e+01	1.0000e+00	Unsteady Aero 10
-2.0000e+01	2.0000e+01	1.0000e+00	Trailing Edge 1 Actuator
-2.1000e+01	2.1000e+01	1.0000e+00	Trailing Edge 2 Actuator
-2.2000e+01	2.2000e+01	1.0000e+00	Vane Actuator
-2.3000e+01	2.3000e+01	1.0000e+00	Trailing Edge 3 Actuator
-2.4000e+01	2.4000e+01	1.0000e+00	Trailing Edge 4 Actuator
-3.0152e-01+ 2.4409e+01i	2.4411e+01	1.2352e-02	Aeroelastic 7
-3.0152e-01- 2.4409e+01i	2.4411e+01	1.2352e-02	Aeroelastic 7
-3.4877e-01+ 3.0789e+01i	3.0791e+01	1.1327e-02	Aeroelastic 8
-3.4877e-01- 3.0789e+01i	3.0791e+01	1.1327e-02	Aeroelastic 8
-6.1879e-01+ 4.1244e+01i	4.1249e+01	1.5001e-02	Aeroelastic 10
-6.1879e-01- 4.1244e+01i	4.1249e+01	1.5001e-02	Aeroelastic 10
1.1303e+01+ 4.4748e+01i	4.6153e+01	-2.4490e-01	Aeroelastic 11
1.1303e+01- 4.4748e+01i	4.6153e+01	-2.4490e-01	Aeroelastic 11
-6.7012e+00+ 4.7043e+01i	4.7518e+01	1.4102e-01	Aeroelastic 12
-6.7012e+00- 4.7043e+01i	4.7518e+01	1.4102e-01	Aeroelastic 12
-4.4525e+01+ 2.3808e+01i	5.0491e+01	8.8184e-01	Aeroelastic 9
-4.4525e+01- 2.3808e+01i	5.0491e+01	8.8184e-01	Aeroelastic 9
-6.9670e-01+ 5.6408e+01i	5.6413e+01	1.2350e-02	Aeroelastic 13
-6.9670e-01- 5.6408e+01i	5.6413e+01	1.2350e-02	Aeroelastic 13
-5.8057e-01+ 5.8379e+01i	5.8382e+01	9.9443e-03	Aeroelastic 14
-5.8057e-01- 5.8379e+01i	5.8382e+01	9.9443e-03	Aeroelastic 14
-3.6590e+00+ 6.1051e+01i	6.1161e+01	5.9826e-02	Aeroelastic 15
-3.6590e+00- 6.1051e+01i	6.1161e+01	5.9826e-02	Aeroelastic 15
-8.4107e-01+ 6.2334e+01i	6.2340e+01	1.3492e-02	Aeroelastic 18
-8.4107e-01- 6.2334e+01i	6.2340e+01	1.3492e-02	Aeroelastic 16
-1.2648e+00+ 6.7467e+01i	6.7478e+01	1.8744e-02	Aeroelastic 17
-1.2648e+00- 6.7467e+01i	6.7478e+01	1.8744e-02	Aeroelastic 17
4.0838e+01+ 8.7425e+01i	9.6493e+01	-4.2323e-01	Noncausal Rate

Table 3. Continued				
4.0838e+01-	8.7425e+01i	9.6493e+01	-4.2323e-01	Noncausal Acceleration
-1.3435e+02+	1.3435e+02i	1.9000e+02	7.0710e-01	Stabilator Actuator
-1.3435e+02-	1.3435e+02i	1.9000e+02	7.0710e-01	Stabilator Actuator
-1.4142e+02+	1.4142e+02i	2.0000e+02	7.0710e-01	Trailing Edge 1 Actuator
-1.4142e+02-	1.4142e+02i	2.0000e+02	7.0710e-01	Trailing Edge 1 Actuator
-1.4849e+02+	1.4849e+02i	2.1000e+02	7.0710e-01	Trailing Edge 2 Actuator
-1.4849e+02-	1.4849e+02i	2.1000e+02	7.0710e-01	Trailing Edge 2 Actuator
-1.5556e+02+	1.5556e+02i	2.2000e+02	7.0710e-01	Vane Actuator
-1.5556e+02-	1.5556e+02i	2.2000e+02	7.0710e-01	Vane Actuator
-1.6263e+02+	1.6263e+02i	2.3000e+02	7.0710e-01	Trailing Edge 3 Actuator
-1.6263e+02-	1.6263e+02i	2.3000e+02	7.0710e-01	Trailing Edge 3 Actuator
-1.6970e+02+	1.6970e+02i	2.4000e+02	7.0710e-01	Trailing Edge 4 Actuator
-1.6970e+02-	1.6970e+02i	2.4000e+02	7.0710e-01	Trailing Edge 4 Actuator

Table 4. Zeros Of Appendix C Model For 3,460 in Pitch Rate To Elevator Channel			
Gain = -2.0283e+03 rad/s/rad			
Root Location (1/s)	Freq. (rad/s)	Damping (-)	Description
0	0	1.0000e+00	-
-4.9135e-03	4.9135e-03	1.0000e+00	-
-4.7327e-01	4.7327e-01	1.0000e+00	-
-7.2387e-01	7.2387e-01	1.0000e+00	-
-1.3595e+00	1.3595e+00	1.0000e+00	-
-1.5970e-01+ 3.2064e+00i	3.2104e+00	4.9744e-02	-
-1.5970e-01- 3.2064e+00i	3.2104e+00	4.9744e-02	-
-4.2406e+00	4.2406e+00	1.0000e+00	-
-8.4480e+00+ 2.7789e-01i	8.4526e+00	9.9946e-01	-
-8.4480e+00- 2.7789e-01i	8.4526e+00	9.9946e-01	-
-8.7277e-02+ 1.0558e+01i	1.0558e+01	8.2663e-03	-
-8.7277e-02- 1.0558e+01i	1.0558e+01	8.2663e-03	-
-1.0646e+01	1.0646e+01	1.0000e+00	-
-1.1058e+01	1.1058e+01	1.0000e+00	-
-1.2817e+01	1.2817e+01	1.0000e+00	-
-1.0171e+00+ 1.4219e+01i	1.4255e+01	7.1350e-02	-
-1.0171e+00- 1.4219e+01i	1.4255e+01	7.1350e-02	-
-1.7247e-01+ 1.7257e+01i	1.7257e+01	9.9942e-03	-
-1.7247e-01- 1.7257e+01i	1.7257e+01	9.9942e-03	-
-1.8035e+01	1.8035e+01	1.0000e+00	-
-6.5305e-01+ 1.8246e+01i	1.8258e+01	3.5768e-02	-
-6.5305e-01- 1.8246e+01i	1.8258e+01	3.5768e-02	-
-1.9128e+01	1.9128e+01	1.0000e+00	-
-2.4464e-01+ 1.9600e+01i	1.9602e+01	1.2480e-02	-
-2.4464e-01- 1.9600e+01i	1.9602e+01	1.2480e-02	-
-1.9752e+01	1.9752e+01	1.0000e+00	-
-2.1526e+01+ 1.3992e-01i	2.1527e+01	9.9998e-01	-
-2.1526e+01- 1.3992e-01i	2.1527e+01	9.9998e-01	-
-1.4866e-01+ 2.1679e+01i	2.1679e+01	6.8571e-03	-
-1.4866e-01- 2.1679e+01i	2.1679e+01	6.8571e-03	-
-2.3110e+01	2.3110e+01	1.0000e+00	-
-2.3978e+01	2.3978e+01	1.0000e+00	-
-3.1078e-01+ 2.4282e+01i	2.4284e+01	1.2798e-02	-
-3.1078e-01- 2.4282e+01i	2.4284e+01	1.2798e-02	-
-3.5407e+01+ 1.1873e+00i	3.5427e+01	9.9944e-01	-
-3.5407e+01- 1.1873e+00i	3.5427e+01	9.9944e-01	-
-1.6288e-01+ 3.5894e+01i	3.5895e+01	4.5377e-03	-
-1.6288e-01- 3.5894e+01i	3.5895e+01	4.5377e-03	-
-9.2871e-01+ 4.4226e+01i	4.4236e+01	2.0995e-02	-
-9.2871e-01- 4.4226e+01i	4.4236e+01	2.0995e-02	-
3.9494e+00+ 4.8414e+01i	4.8575e+01	-8.1306e-02	-
3.9494e+00- 4.8414e+01i	4.8575e+01	-8.1306e-02	-
-3.9299e+00+ 4.9008e+01i	4.9166e+01	7.9933e-02	-
-3.9299e+00- 4.9008e+01i	4.9166e+01	7.9933e-02	-
-5.8349e-01+ 5.5417e+01i	5.5420e+01	1.0529e-02	-
-5.8349e-01- 5.5417e+01i	5.5420e+01	1.0529e-02	-
-7.7748e-01+ 5.8947e+01i	5.8952e+01	1.3188e-02	-
-7.7748e-01- 5.8947e+01i	5.8952e+01	1.3188e-02	-
-3.4479e+00+ 6.1260e+01i	6.1357e+01	5.6194e-02	-
-3.4479e+00- 6.1260e+01i	6.1357e+01	5.6194e-02	-
-8.3462e-01+ 6.2375e+01i	6.2380e+01	1.3380e-02	-
-8.3462e-01- 6.2375e+01i	6.2380e+01	1.3380e-02	-
-6.4431e-01+ 6.4570e+01i	6.4574e+01	9.9779e-03	-
-6.4431e-01- 6.4570e+01i	6.4574e+01	9.9779e-03	-

Table 4. Continued				
-7.4749e+01		7.4749e+01	1.0000e+00	-
-1.3435e+02+	1.3435e+02i	1.9000e+02	7.0710e-01	-
-1.3435e+02-	1.3435e+02i	1.9000e+02	7.0710e-01	-
-1.4142e+02+	1.4142e+02i	2.0000e+02	7.0710e-01	-
-1.4142e+02-	1.4142e+02i	2.0000e+02	7.0710e-01	-
-1.4849e+02+	1.4849e+02i	2.1000e+02	7.0710e-01	-
-1.4849e+02-	1.4849e+02i	2.1000e+02	7.0710e-01	-
-1.5556e+02+	1.5556e+02i	2.2000e+02	7.0710e-01	-
-1.5556e+02-	1.5556e+02i	2.2000e+02	7.0710e-01	-
-1.6263e+02+	1.6263e+02i	2.3000e+02	7.0710e-01	-
-1.6263e+02-	1.6263e+02i	2.3000e+02	7.0710e-01	-
-1.6970e+02+	1.6970e+02i	2.4000e+02	7.0710e-01	-
-1.6970e+02-	1.6970e+02i	2.4000e+02	7.0710e-01	-

Table 5. Zeros Of Appendix C Model For 400 in Pitch Rate To Vane Channel

Gain = 4.7673e+06 rad/s/rad

Root Location (1/s)	Freq. (rad/s)	Damping (-)	Description
0	0	1.0000e+00	Pitch "Rate"
-3.3139e-03	3.3139e-03	1.0000e+00	Tau Theta 1
-4.6652e-01	4.6652e-01	1.0000e+00	Tau Theta 2
-7.3330e-01	7.3330e-01	1.0000e+00	Unsteady Aero 1
-1.3576e+00	1.3576e+00	1.0000e+00	Unsteady Aero 2
-1.6974e-01+ 2.1432e+00i	2.1500e+00	7.8952e-02	Aeroelastic 1
-1.6974e-01- 2.1432e+00i	2.1500e+00	7.8952e-02	Aeroelastic 1
-4.2202e+00	4.2202e+00	1.0000e+00	Unsteady Aero 3
-8.2740e+00	8.2740e+00	1.0000e+00	Unsteady Aero 4
-9.1709e+00	9.1709e+00	1.0000e+00	Unsteady Aero 5
-9.4719e+00	9.4719e+00	1.0000e+00	Unsteady Aero 6
-5.8408e-01+ 1.0983e+01i	1.0998e+01	5.3107e-02	Aeroelastic 2
-5.8408e-01- 1.0983e+01i	1.0998e+01	5.3107e-02	Aeroelastic 2
-1.1230e+01	1.1230e+01	1.0000e+00	Unsteady Aero 7
-1.3542e+01	1.3542e+01	1.0000e+00	Unsteady Aero 8
-9.7380e-01+ 1.5187e+01i	1.5218e+01	6.3991e-02	Aeroelastic 3
-9.7380e-01- 1.5187e+01i	1.5218e+01	6.3991e-02	Aeroelastic 3
-1.7335e-01+ 1.7264e+01i	1.7265e+01	1.0040e-02	Aeroelastic 4
-1.7335e-01- 1.7264e+01i	1.7265e+01	1.0040e-02	Aeroelastic 4
-6.9425e-01+ 1.8286e+01i	1.8299e+01	3.7940e-02	Aeroelastic 5
-6.9425e-01- 1.8286e+01i	1.8299e+01	3.7940e-02	Aeroelastic 5
-1.8854e+01	1.8854e+01	1.0000e+00	Unsteady Aero 9
-1.9000e+01	1.9000e+01	1.0000e+00	Stabilator Actuator
-2.3977e-01+ 1.9644e+01i	1.9646e+01	1.2205e-02	Aeroelastic 6
-2.3977e-01- 1.9644e+01i	1.9646e+01	1.2205e-02	Aeroelastic 6
-2.0000e+01	2.0000e+01	1.0000e+00	Trailing Edge 1 Actuator
-2.1000e+01	2.1000e+01	1.0000e+00	Trailing Edge 2 Actuator
-2.2000e+01	2.2000e+01	1.0000e+00	Elevator Actuator
-2.3000e+01	2.3000e+01	1.0000e+00	Trailing Edge 3 Actuator
-3.5589e-01+ 2.3196e+01i	2.3199e+01	1.5341e-02	Aeroelastic 7
-3.5589e-01- 2.3196e+01i	2.3199e+01	1.5341e-02	Aeroelastic 7
-2.4000e+01	2.4000e+01	1.0000e+00	Trailing Edge 4 Actuator
-1.5387e+00+ 2.8611e+01i	2.8653e+01	5.3702e-02	Aeroelastic 8
-1.5387e+00- 2.8611e+01i	2.8653e+01	5.3702e-02	Aeroelastic 8
-2.9338e+01	2.9338e+01	1.0000e+00	Unsteady Aero 10
-7.9676e-01+ 3.1663e+01i	3.1673e+01	2.5156e-02	Aeroelastic 9
-7.9676e-01- 3.1663e+01i	3.1673e+01	2.5156e-02	Aeroelastic 9
-9.1811e-01+ 4.2355e+01i	4.2365e+01	2.1671e-02	Aeroelastic 10
-9.1811e-01- 4.2355e+01i	4.2365e+01	2.1671e-02	Aeroelastic 10
-5.6739e-01+ 4.4740e+01i	4.4743e+01	1.2681e-02	Aeroelastic 11
-5.6739e-01- 4.4740e+01i	4.4743e+01	1.2681e-02	Aeroelastic 11
-8.7159e-01+ 5.2862e+01i	5.2869e+01	1.6486e-02	Aeroelastic 12
-8.7159e-01- 5.2862e+01i	5.2869e+01	1.6486e-02	Aeroelastic 12
-7.8541e-01+ 5.5918e+01i	5.5924e+01	1.4044e-02	Aeroelastic 13
-7.8541e-01- 5.5918e+01i	5.5924e+01	1.4044e-02	Aeroelastic 13
-7.8138e-01+ 5.8897e+01i	5.8902e+01	1.3266e-02	Aeroelastic 14
-7.8138e-01- 5.8897e+01i	5.8902e+01	1.3266e-02	Aeroelastic 14
-3.2789e+00+ 6.1390e+01i	6.1478e+01	5.3335e-02	Aeroelastic 15
-3.2789e+00- 6.1390e+01i	6.1478e+01	5.3335e-02	Aeroelastic 15
-7.6298e-01+ 6.2299e+01i	6.2303e+01	1.2246e-02	Aeroelastic 16
-7.6298e-01- 6.2299e+01i	6.2303e+01	1.2246e-02	Aeroelastic 16
-8.3436e-01+ 6.4451e+01i	6.4457e+01	1.2944e-02	Aeroelastic 17
-8.3436e-01- 6.4451e+01i	6.4457e+01	1.2944e-02	Aeroelastic 17
-1.3435e+02+ 1.3435e+02i	1.9000e+02	7.0710e-01	Stabilator Actuator

Table 5. Continued				
-1.3435e+02-	1.3435e+02i	1.9000e+02	7.0710e-01	Stabilator Actuator
-1.4142e+02+	1.4142e+02i	2.0000e+02	7.0710e-01	Trailing Edge 1 Actuator
-1.4142e+02-	1.4142e+02i	2.0000e+02	7.0710e-01	Trailing Edge 1 Actuator
-1.4849e+02+	1.4849e+02i	2.1000e+02	7.0710e-01	Trailing Edge 2 Actuator
-1.4849e+02-	1.4849e+02i	2.1000e+02	7.0710e-01	Trailing Edge 2 Actuator
-1.5556e+02+	1.5556e+02i	2.2000e+02	7.0710e-01	Elevator Actuator
-1.5556e+02-	1.5556e+02i	2.2000e+02	7.0710e-01	Elevator Actuator
-1.6263e+02+	1.6263e+02i	2.3000e+02	7.0710e-01	Trailing Edge 3 Actuator
-1.6263e+02-	1.6263e+02i	2.3000e+02	7.0710e-01	Trailing Edge 3 Actuator
-1.6970e+02+	1.6970e+02i	2.4000e+02	7.0710e-01	Trailing Edge 4 Actuator
-1.6970e+02-	1.6970e+02i	2.4000e+02	7.0710e-01	Trailing Edge 4 Actuator

Table 6. Zeros Of Appendix C Model For 1,850 in Pitch Rate To Vane Channel

Gain = -1.0114e+05 rad/s/rad			
Root Location (1/s)	Freq. (rad/s)	Damping (-)	Description
0	0	1.0000e+00	Pitch "Rate"
-5.8897e-03	5.8897e-03	1.0000e+00	Tau Theta 1
-4.4322e-01	4.4322e-01	1.0000e+00	Tau Theta 2
-7.2421e-01	7.2421e-01	1.0000e+00	Unsteady Aero 1
-1.3578e+00	1.3578e+00	1.0000e+00	Unsteady Aero 2
-4.1466e+00	4.1466e+00	1.0000e+00	Unsteady Aero 3
-5.3080e-01+ 7.9075e+00i	7.9253e+00	6.6975e-02	Aeroelastic 1
-5.3080e-01- 7.9075e+00i	7.9253e+00	6.6975e-02	Aeroelastic 1
-8.1343e+00+ 9.3030e-01i	8.1874e+00	9.9352e-01	Unsteady Aero 4
-8.1343e+00- 9.3030e-01i	8.1874e+00	9.9352e-01	Unsteady Aero 5
-9.9182e+00+ 7.6790e-02i	9.9185e+00	9.9997e-01	Unsteady Aero 6
-9.9182e+00- 7.6790e-02i	9.9185e+00	9.9997e-01	Aeroelastic 2
1.0023e+01	1.0023e+01	-1.0000e+00	Aeroelastic 2
-1.1308e+01	1.1308e+01	1.0000e+00	Unsteady Aero 7
-1.3738e+01	1.3738e+01	1.0000e+00	Unsteady Aero 8
-1.1039e+00+ 1.4258e+01i	1.4301e+01	7.7192e-02	Aeroelastic 3
-1.1039e+00- 1.4258e+01i	1.4301e+01	7.7192e-02	Aeroelastic 3
-1.7316e-01+ 1.7263e+01i	1.7263e+01	1.0030e-02	Aeroelastic 4
-1.7316e-01- 1.7263e+01i	1.7263e+01	1.0030e-02	Aeroelastic 4
-7.7741e-01+ 1.8299e+01i	1.8315e+01	4.2447e-02	Aeroelastic 5
-7.7741e-01- 1.8299e+01i	1.8315e+01	4.2447e-02	Aeroelastic 5
-1.8644e+01	1.8644e+01	1.0000e+00	Unsteady Aero 9
-2.3388e-01+ 1.9656e+01i	1.9657e+01	1.1898e-02	Aeroelastic 6
-2.3388e-01- 1.9656e+01i	1.9657e+01	1.1898e-02	Aeroelastic 6
-1.9000e+01	1.9000e+01	1.0000e+00	Stabilator Actuator
-2.0000e+01	2.0000e+01	1.0000e+00	Trailing Edge 1 Actuator
-2.1000e+01	2.1000e+01	1.0000e+00	Trailing Edge 2 Actuator
-2.2000e+01	2.2000e+01	1.0000e+00	Elevator Actuator
-3.4935e-01+ 2.3577e+01i	2.3580e+01	1.4816e-02	Aeroelastic 7
-3.4935e-01- 2.3577e+01i	2.3580e+01	1.4816e-02	Aeroelastic 7
-2.3000e+01	2.3000e+01	1.0000e+00	Trailing Edge 3 Actuator
-2.4000e+01	2.4000e+01	1.0000e+00	Trailing Edge 4 Actuator
-2.0295e+00+ 2.9157e+01i	2.9227e+01	6.9440e-02	Aeroelastic 8
-2.0295e+00- 2.9157e+01i	2.9227e+01	6.9440e-02	Aeroelastic 8
-2.9561e+01	2.9561e+01	1.0000e+00	Unsteady Aero 10
-4.4544e-01+ 3.9346e+01i	3.9349e+01	1.1320e-02	Aeroelastic 9
-4.4544e-01- 3.9346e+01i	3.9349e+01	1.1320e-02	Aeroelastic 9
-8.8010e-01+ 4.2514e+01i	4.2523e+01	2.0697e-02	Aeroelastic 10
-8.8010e-01- 4.2514e+01i	4.2523e+01	2.0697e-02	Aeroelastic 10
-9.4895e-01+ 5.2453e+01i	5.2461e+01	1.8089e-02	Aeroelastic 11
-9.4895e-01- 5.2453e+01i	5.2461e+01	1.8089e-02	Aeroelastic 11
-7.8428e-01+ 5.5973e+01i	5.5978e+01	1.4010e-02	Aeroelastic 12
-7.8428e-01- 5.5973e+01i	5.5978e+01	1.4010e-02	Aeroelastic 12
-2.9875e+00+ 6.1274e+01i	6.1347e+01	4.8699e-02	Aeroelastic 13
-2.9875e+00- 6.1274e+01i	6.1347e+01	4.8699e-02	Aeroelastic 13
-8.3789e-01+ 6.1761e+01i	6.1766e+01	1.3565e-02	Aeroelastic 14
-8.3789e-01- 6.1761e+01i	6.1766e+01	1.3565e-02	Aeroelastic 14
-1.3981e+00+ 6.2873e+01i	6.2888e+01	2.2231e-02	Aeroelastic 15
-1.3981e+00- 6.2873e+01i	6.2888e+01	2.2231e-02	Aeroelastic 15
-1.1198e+01+ 6.8650e+01i	6.9557e+01	1.6099e-01	Aeroelastic 16
-1.1198e+01- 6.8650e+01i	6.9557e+01	1.6099e-01	Aeroelastic 16
9.4640e+00+ 6.9112e+01i	6.9757e+01	-1.3567e-01	Aeroelastic 17
9.4640e+00- 6.9112e+01i	6.9757e+01	-1.3567e-01	Aeroelastic 17
-1.3435e+02+ 1.3435e+02i	1.9000e+02	7.0710e-01	Stabilator Actuator

Table 6. Continued				
-1.3435e+02-	1.3435e+02i	1.9000e+02	7.0710e-01	Stabilator Actuator
-1.4142e+02+	1.4142e+02i	2.0000e+02	7.0710e-01	Trailing Edge 1 Actuator
-1.4142e+02-	1.4142e+02i	2.0000e+02	7.0710e-01	Trailing Edge 1 Actuator
-1.4849e+02+	1.4849e+02i	2.1000e+02	7.0710e-01	Trailing Edge 2 Actuator
-1.4849e+02-	1.4849e+02i	2.1000e+02	7.0710e-01	Trailing Edge 2 Actuator
-1.5556e+02+	1.5556e+02i	2.2000e+02	7.0710e-01	Elevator Actuator
-1.5556e+02-	1.5556e+02i	2.2000e+02	7.0710e-01	Elevator Actuator
-1.6263e+02+	1.6263e+02i	2.3000e+02	7.0710e-01	Trailing Edge 3 Actuator
-1.6263e+02-	1.6263e+02i	2.3000e+02	7.0710e-01	Trailing Edge 3 Actuator
-1.6970e+02+	1.6970e+02i	2.4000e+02	7.0710e-01	Trailing Edge 4 Actuator
-1.6970e+02-	1.6970e+02i	2.4000e+02	7.0710e-01	Trailing Edge 4 Actuator



Table 7. Zeros Of Appendix C Model For 3,460 in Pitch Rate To Vane Channel

Gain = -8.7033e+04 rad/s/rad			
Root Location (1/s)	Freq. (rad/s)	Damping (-)	Description
0	0	1.0000e+00	-
-7.4858e-03	7.4858e-03	1.0000e+00	-
-4.2794e-01	4.2794e-01	1.0000e+00	-
-7.1636e-01	7.1636e-01	1.0000e+00	-
-1.3583e+00	1.3583e+00	1.0000e+00	-
-4.3347e+00+ 3.8391e-01i	4.3516e+00	9.9610e-01	-
-4.3347e+00- 3.8391e-01i	4.3516e+00	9.9610e-01	-
4.8353e+00	4.8353e+00	-1.0000e+00	-
-8.6186e+00	8.6186e+00	1.0000e+00	-
-9.5966e+00+ 1.5892e+00i	9.7273e+00	9.8656e-01	-
-9.5966e+00- 1.5892e+00i	9.7273e+00	9.8656e-01	-
-1.1234e+01	1.1234e+01	1.0000e+00	-
-1.2946e+01	1.2946e+01	1.0000e+00	-
-1.2364e+00+ 1.4013e+01i	1.4067e+01	8.7892e-02	-
-1.2364e+00- 1.4013e+01i	1.4067e+01	8.7892e-02	-
-1.6332e+01	1.6332e+01	1.0000e+00	-
-1.7346e-01+ 1.7262e+01i	1.7263e+01	1.0048e-02	-
-1.7346e-01- 1.7262e+01i	1.7263e+01	1.0048e-02	-
-7.7301e-01+ 1.8672e+01i	1.8688e+01	4.1365e-02	-
-7.7301e-01- 1.8672e+01i	1.8688e+01	4.1365e-02	-
-1.9276e+01+ 4.4104e-01i	1.9281e+01	9.9974e-01	-
-1.9276e+01- 4.4104e-01i	1.9281e+01	9.9974e-01	-
-2.1396e-01+ 1.9690e+01i	1.9691e+01	1.0866e-02	-
-2.1396e-01- 1.9690e+01i	1.9691e+01	1.0866e-02	-
-2.1554e+01+ 8.8990e-01i	2.1573e+01	9.9915e-01	-
-2.1554e+01- 8.8990e-01i	2.1573e+01	9.9915e-01	-
-2.3676e+01+ 6.7014e-02i	2.3676e+01	1.0000e+00	-
-2.3676e+01- 6.7014e-02i	2.3676e+01	1.0000e+00	-
-3.4488e-01+ 2.4429e+01i	2.4432e+01	1.4116e-02	-
-3.4488e-01- 2.4429e+01i	2.4432e+01	1.4116e-02	-
1.5449e+01+ 2.1453e+01i	2.6436e+01	-5.8437e-01	-
1.5449e+01- 2.1453e+01i	2.6436e+01	-5.8437e-01	-
-1.5327e+01+ 2.1753e+01i	2.6610e+01	5.7597e-01	-
-1.5327e+01- 2.1753e+01i	2.6610e+01	5.7597e-01	-
-2.9778e+01	2.9778e+01	1.0000e+00	-
-2.2172e+00+ 3.3092e+01i	3.3166e+01	6.6852e-02	-
-2.2172e+00- 3.3092e+01i	3.3166e+01	6.6852e-02	-
-9.0747e-01+ 4.1976e+01i	4.1986e+01	2.1614e-02	-
-9.0747e-01- 4.1976e+01i	4.1986e+01	2.1614e-02	-
-9.3167e-01+ 5.1790e+01i	5.1799e+01	1.7986e-02	-
-9.3167e-01- 5.1790e+01i	5.1799e+01	1.7986e-02	-
-7.2913e-01+ 5.6576e+01i	5.6581e+01	1.2887e-02	-
-7.2913e-01- 5.6576e+01i	5.6581e+01	1.2887e-02	-
-1.4811e+01+ 5.7947e+01i	5.9810e+01	2.4763e-01	-
-1.4811e+01- 5.7947e+01i	5.9810e+01	2.4763e-01	-
-3.2853e+00+ 6.1186e+01i	6.1274e+01	5.3616e-02	-
-3.2853e+00- 6.1186e+01i	6.1274e+01	5.3616e-02	-
-7.7845e-01+ 6.2420e+01i	6.2425e+01	1.2470e-02	-
-7.7845e-01- 6.2420e+01i	6.2425e+01	1.2470e-02	-
1.6669e+01+ 6.1058e+01i	6.3292e+01	-2.6337e-01	-
1.6669e+01- 6.1058e+01i	6.3292e+01	-2.6337e-01	-
2.1926e+00+ 7.2660e+01i	7.2693e+01	-3.0162e-02	-
2.1926e+00- 7.2660e+01i	7.2693e+01	-3.0162e-02	-
-1.3435e+02+ 1.3435e+02i	1.9000e+02	7.0710e-01	-

Table 7. Continued				
-1.3435e+02-	1.3435e+02i	1.9000e+02	7.0710e-01	-
-1.4142e+02+	1.4142e+02i	2.0000e+02	7.0710e-01	-
-1.4142e+02-	1.4142e+02i	2.0000e+02	7.0710e-01	-
-1.4849e+02+	1.4849e+02i	2.1000e+02	7.0710e-01	-
-1.4849e+02-	1.4849e+02i	2.1000e+02	7.0710e-01	-
-1.5556e+02+	1.5556e+02i	2.2000e+02	7.0710e-01	-
-1.5556e+02-	1.5556e+02i	2.2000e+02	7.0710e-01	-
-1.6263e+02+	1.6263e+02i	2.3000e+02	7.0710e-01	-
-1.6263e+02-	1.6263e+02i	2.3000e+02	7.0710e-01	-
-1.6970e+02+	1.6970e+02i	2.4000e+02	7.0710e-01	-
-1.6970e+02-	1.6970e+02i	2.4000e+02	7.0710e-01	-

Table 8. Zeros Of Appendix C Model For 400 in Vertical Acceleration To Elevator Channel

Gain = -2.7221e+02 ft/s<sup>2</sup>/rad

Root Location (1/s)	Freq. (rad/s)	Damping (-)	Description
0	0	1.0000e+00	-
2.8141e-02	2.8141e-02	-1.0000e+00	-
-6.5819e-01	6.5819e-01	1.0000e+00	-
-4.2680e-01+ 1.0391e+00i	1.1233e+00	3.7994e-01	-
-4.2680e-01- 1.0391e+00i	1.1233e+00	3.7994e-01	-
-1.3576e+00	1.3576e+00	1.0000e+00	-
-4.1873e+00	4.1873e+00	1.0000e+00	-
-6.8167e+00	6.8167e+00	1.0000e+00	-
-8.1987e+00	8.1987e+00	1.0000e+00	-
-1.0709e+01	1.0709e+01	1.0000e+00	-
-1.0778e+01+ 2.8160e+00i	1.1140e+01	9.6752e-01	-
-1.0778e+01- 2.8160e+00i	1.1140e+01	9.6752e-01	-
1.2035e+01	1.2035e+01	-1.0000e+00	-
-1.0692e+01+ 8.9173e+00i	1.3922e+01	7.6795e-01	-
-1.0692e+01- 8.9173e+00i	1.3922e+01	7.6795e-01	-
-1.1979e+00+ 1.4149e+01i	1.4200e+01	8.4357e-02	-
-1.1979e+00- 1.4149e+01i	1.4200e+01	8.4357e-02	-
-1.6154e+01	1.6154e+01	1.0000e+00	-
-1.7283e-01+ 1.7263e+01i	1.7263e+01	1.0011e-02	-
-1.7283e-01- 1.7263e+01i	1.7263e+01	1.0011e-02	-
-7.2877e-01+ 1.8871e+01i	1.8885e+01	3.8590e-02	-
-7.2877e-01- 1.8871e+01i	1.8885e+01	3.8590e-02	-
-1.9000e+01	1.9000e+01	1.0000e+00	-
-2.0823e-01+ 1.9702e+01i	1.9703e+01	1.0568e-02	-
-2.0823e-01- 1.9702e+01i	1.9703e+01	1.0568e-02	-
-2.0000e+01	2.0000e+01	1.0000e+00	-
-2.0999e+01	2.0999e+01	1.0000e+00	-
1.5952e+01+ 1.5076e+01i	2.1949e+01	-7.2678e-01	-
1.5952e+01- 1.5076e+01i	2.1949e+01	-7.2678e-01	-
-2.2001e+01	2.2001e+01	1.0000e+00	-
-2.3001e+01	2.3001e+01	1.0000e+00	-
-2.4001e+01	2.4001e+01	1.0000e+00	-
-2.7952e-01+ 2.4414e+01i	2.4415e+01	1.1449e-02	-
-2.7952e-01- 2.4414e+01i	2.4415e+01	1.1449e-02	-
-9.1251e+00+ 2.3142e+01i	2.4876e+01	3.6682e-01	-
-9.1251e+00- 2.3142e+01i	2.4876e+01	3.6682e-01	-
-3.3857e+01	3.3857e+01	1.0000e+00	-
3.4622e+00+ 3.7807e+01i	3.7965e+01	-9.1193e-02	-
3.4622e+00- 3.7807e+01i	3.7965e+01	-9.1193e-02	-
-3.5137e-01+ 4.1913e+01i	4.1915e+01	8.3829e-03	-
-3.5137e-01- 4.1913e+01i	4.1915e+01	8.3829e-03	-
-2.6411e+00+ 4.5281e+01i	4.5358e+01	5.8229e-02	-
-2.6411e+00- 4.5281e+01i	4.5358e+01	5.8229e-02	-
1.2798e+00+ 5.6126e+01i	5.6140e+01	-2.2796e-02	-
1.2798e+00- 5.6126e+01i	5.6140e+01	-2.2796e-02	-
-1.9557e+00+ 5.6439e+01i	5.6473e+01	3.4630e-02	-
-1.9557e+00- 5.6439e+01i	5.6473e+01	3.4630e-02	-
-1.0494e+00+ 5.7782e+01i	5.7792e+01	1.8158e-02	-
-1.0494e+00- 5.7782e+01i	5.7792e+01	1.8158e-02	-
-3.4058e+00+ 6.1666e+01i	6.1760e+01	5.5145e-02	-
-3.4058e+00- 6.1666e+01i	6.1760e+01	5.5145e-02	-
-8.5624e-01+ 6.2343e+01i	6.2349e+01	1.3733e-02	-
-8.5624e-01- 6.2343e+01i	6.2349e+01	1.3733e-02	-
-7.9946e-01+ 6.6205e+01i	6.6210e+01	1.2075e-02	-

Table 8. Continued				
-7.9946e-01-	6.6205e+01i	6.6210e+01	1.2075e-02	-
-1.3435e+02+	1.3435e+02i	1.9000e+02	7.0710e-01	-
-1.3435e+02-	1.3435e+02i	1.9000e+02	7.0710e-01	-
-1.4142e+02+	1.4142e+02i	2.0000e+02	7.0710e-01	-
-1.4142e+02-	1.4142e+02i	2.0000e+02	7.0710e-01	-
-1.4849e+02+	1.4849e+02i	2.1000e+02	7.0710e-01	-
-1.4849e+02-	1.4849e+02i	2.1000e+02	7.0710e-01	-
-1.5556e+02+	1.5556e+02i	2.2000e+02	7.0710e-01	-
-1.5556e+02-	1.5556e+02i	2.2000e+02	7.0710e-01	-
-1.6263e+02+	1.6263e+02i	2.3000e+02	7.0710e-01	-
-1.6263e+02-	1.6263e+02i	2.3000e+02	7.0710e-01	-
-1.6970e+02+	1.6970e+02i	2.4000e+02	7.0710e-01	-
-1.6970e+02-	1.6970e+02i	2.4000e+02	7.0710e-01	-
-2.1977e+03		2.1977e+03	1.0000e+00	-

Table 9. Zeros Of Appendix C Model For 1,850 in Vertical Acceleration To Elevator Channel  
Gain = 4.1678e+02 ft/s<sup>2</sup>/rad

Root Location (1/s)	Freq. (rad/s)	Damping (-)	Description
0	0	1.0000e+00	-
2.8583e-02	2.8583e-02	-1.0000e+00	-
-6.4979e-01	6.4979e-01	1.0000e+00	-
-1.3543e+00	1.3543e+00	1.0000e+00	-
-2.6731e+00	2.6731e+00	1.0000e+00	-
2.6570e+00+ 2.7515e+00i	3.8250e+00	-6.9465e-01	-
2.6570e+00- 2.7515e+00i	3.8250e+00	-6.9465e-01	-
-3.8479e+00+ 1.9085e+00i	4.2952e+00	8.9586e-01	-
-3.8479e+00- 1.9085e+00i	4.2952e+00	8.9586e-01	-
-8.3750e+00+ 7.0143e-01i	8.4043e+00	9.9651e-01	-
-8.3750e+00- 7.0143e-01i	8.4043e+00	9.9651e-01	-
-1.1044e+01+ 4.9147e-01i	1.1055e+01	9.9901e-01	-
-1.1044e+01- 4.9147e-01i	1.1055e+01	9.9901e-01	-
-1.3887e+00+ 1.4743e+01i	1.4809e+01	9.3778e-02	-
-1.3887e+00- 1.4743e+01i	1.4809e+01	9.3778e-02	-
-1.3873e+01+ 8.8758e+00i	1.6469e+01	8.4235e-01	-
-1.3873e+01- 8.8758e+00i	1.6469e+01	8.4235e-01	-
-1.7334e-01+ 1.7261e+01i	1.7262e+01	1.0042e-02	-
-1.7334e-01- 1.7261e+01i	1.7262e+01	1.0042e-02	-
-1.7557e+01	1.7557e+01	1.0000e+00	-
-1.8996e+01	1.8996e+01	1.0000e+00	-
1.0835e+00+ 1.8987e+01i	1.9018e+01	-5.6971e-02	-
1.0835e+00- 1.8987e+01i	1.9018e+01	-5.6971e-02	-
-1.4395e+00+ 1.9328e+01i	1.9381e+01	7.4273e-02	-
-1.4395e+00- 1.9328e+01i	1.9381e+01	7.4273e-02	-
-2.5923e-01+ 1.9634e+01i	1.9636e+01	1.3202e-02	-
-2.5923e-01- 1.9634e+01i	1.9636e+01	1.3202e-02	-
-2.0014e+01	2.0014e+01	1.0000e+00	-
-2.0980e+01	2.0980e+01	1.0000e+00	-
-2.2015e+01	2.2015e+01	1.0000e+00	-
-2.2995e+01	2.2995e+01	1.0000e+00	-
-2.4001e+01	2.4001e+01	1.0000e+00	-
-2.9927e-01+ 2.4438e+01i	2.4440e+01	1.2245e-02	-
-2.9927e-01- 2.4438e+01i	2.4440e+01	1.2245e-02	-
-2.9460e+01	2.9460e+01	1.0000e+00	-
-2.8137e+00+ 4.2076e+01i	4.2170e+01	6.6724e-02	-
-2.8137e+00- 4.2076e+01i	4.2170e+01	6.6724e-02	-
9.4830e-01+ 4.3830e+01i	4.3840e+01	-2.1631e-02	-
9.4830e-01- 4.3830e+01i	4.3840e+01	-2.1631e-02	-
9.7969e+00+ 4.4541e+01i	4.5606e+01	-2.1482e-01	-
9.7969e+00- 4.4541e+01i	4.5606e+01	-2.1482e-01	-
-4.9144e+00+ 4.5883e+01i	4.6145e+01	1.0650e-01	-
-4.9144e+00- 4.5883e+01i	4.6145e+01	1.0650e-01	-
5.3740e+01	5.3740e+01	-1.0000e+00	-
-7.1092e-01+ 5.6392e+01i	5.6396e+01	1.2606e-02	-
-7.1092e-01- 5.6392e+01i	5.6396e+01	1.2606e-02	-
-5.7376e+01	5.7376e+01	1.0000e+00	-
-3.5922e+00+ 6.1227e+01i	6.1332e+01	5.8569e-02	-
-3.5922e+00- 6.1227e+01i	6.1332e+01	5.8569e-02	-
-8.2971e-01+ 6.2326e+01i	6.2331e+01	1.3311e-02	-
-8.2971e-01- 6.2326e+01i	6.2331e+01	1.3311e-02	-
-6.8153e-01+ 6.3081e+01i	6.3085e+01	1.0803e-02	-
-6.8153e-01- 6.3081e+01i	6.3085e+01	1.0803e-02	-
-8.8967e+00+ 7.3147e+01i	7.3686e+01	1.2074e-01	-

Table 9. Continued				
-8.8967e+00-	7.3147e+01i	7.3686e+01	1.2074e-01	-
1.4421e+02		1.4421e+02	-1.0000e+00	-
-1.3435e+02+	1.3435e+02i	1.9000e+02	7.0710e-01	-
-1.3435e+02-	1.3435e+02i	1.9000e+02	7.0710e-01	-
-1.4142e+02+	1.4142e+02i	2.0000e+02	7.0710e-01	-
-1.4142e+02-	1.4142e+02i	2.0000e+02	7.0710e-01	-
-1.4849e+02+	1.4849e+02i	2.1000e+02	7.0710e-01	-
-1.4849e+02-	1.4849e+02i	2.1000e+02	7.0710e-01	-
-1.5556e+02+	1.5556e+02i	2.2000e+02	7.0710e-01	-
-1.5556e+02-	1.5556e+02i	2.2000e+02	7.0710e-01	-
-1.6263e+02+	1.6263e+02i	2.3000e+02	7.0710e-01	-
-1.6263e+02-	1.6263e+02i	2.3000e+02	7.0710e-01	-
-1.6970e+02+	1.6970e+02i	2.4000e+02	7.0710e-01	-
-1.6970e+02-	1.6970e+02i	2.4000e+02	7.0710e-01	-

Table 10. Zeros Of Appendix C Model For 3,460 in Vertical Acceleration To Elevator Channel  
Gain = -4.7630e+04 ft/s<sup>2</sup>/rad

Root Location (1/s)	Freq. (rad/s)	Damping (-)	Description
0	0	1.0000e+00	-
2.9119e-02	2.9119e-02	-1.0000e+00	-
-6.3989e-01	6.3989e-01	1.0000e+00	-
7.8598e-01	7.8598e-01	-1.0000e+00	-
-1.1694e+00	1.1694e+00	1.0000e+00	-
-1.3669e+00	1.3669e+00	1.0000e+00	-
-4.3328e+00	4.3328e+00	1.0000e+00	-
-2.5960e-01+ 4.9448e+00i	4.9516e+00	5.2427e-02	-
-2.5960e-01- 4.9448e+00i	4.9516e+00	5.2427e-02	-
-8.3225e+00+ 8.9255e-02i	8.3230e+00	9.9994e-01	-
-8.3225e+00- 8.9255e-02i	8.3230e+00	9.9994e-01	-
-1.0314e+01	1.0314e+01	1.0000e+00	-
-1.1198e+01	1.1198e+01	1.0000e+00	-
-3.5672e-01+ 1.1791e+01i	1.1796e+01	3.0240e-02	-
-3.5672e-01- 1.1791e+01i	1.1796e+01	3.0240e-02	-
-1.2942e+01	1.2942e+01	1.0000e+00	-
-1.1789e+00+ 1.5827e+01i	1.5871e+01	7.4282e-02	-
-1.1789e+00- 1.5827e+01i	1.5871e+01	7.4282e-02	-
-1.7752e-01+ 1.7268e+01i	1.7268e+01	1.0280e-02	-
-1.7752e-01- 1.7268e+01i	1.7268e+01	1.0280e-02	-
-1.8048e+01	1.8048e+01	1.0000e+00	-
-1.9024e+01	1.9024e+01	1.0000e+00	-
-4.1523e-01+ 1.9484e+01i	1.9489e+01	2.1306e-02	-
-4.1523e-01- 1.9484e+01i	1.9489e+01	2.1306e-02	-
-1.9948e+01	1.9948e+01	1.0000e+00	-
-2.1381e-01+ 2.0099e+01i	2.0100e+01	1.0637e-02	-
-2.1381e-01- 2.0099e+01i	2.0100e+01	1.0637e-02	-
-2.1068e+01	2.1068e+01	1.0000e+00	-
-2.1947e+01	2.1947e+01	1.0000e+00	-
-2.3022e+01	2.3022e+01	1.0000e+00	-
-2.3997e+01	2.3997e+01	1.0000e+00	-
-3.0124e-01+ 2.4214e+01i	2.4216e+01	1.2440e-02	-
-3.0124e-01- 2.4214e+01i	2.4216e+01	1.2440e-02	-
-3.5416e-01+ 2.4936e+01i	2.4938e+01	1.4201e-02	-
-3.5416e-01- 2.4936e+01i	2.4938e+01	1.4201e-02	-
-3.4326e+01	3.4326e+01	1.0000e+00	-
-1.9588e-01+ 3.6283e+01i	3.6283e+01	5.3988e-03	-
-1.9588e-01- 3.6283e+01i	3.6283e+01	5.3988e-03	-
-1.0383e+00+ 4.4917e+01i	4.4929e+01	2.3111e-02	-
-1.0383e+00- 4.4917e+01i	4.4929e+01	2.3111e-02	-
-5.4531e+00+ 4.8488e+01i	4.8794e+01	1.1176e-01	-
-5.4531e+00- 4.8488e+01i	4.8794e+01	1.1176e-01	-
5.7963e+00+ 4.8633e+01i	4.8978e+01	-1.1835e-01	-
5.7963e+00- 4.8633e+01i	4.8978e+01	-1.1835e-01	-
-4.6655e+01+ 2.6440e+01i	5.3627e+01	8.7001e-01	-
-4.6655e+01- 2.6440e+01i	5.3627e+01	8.7001e-01	-
-5.8572e-01+ 5.5390e+01i	5.5393e+01	1.0574e-02	-
-5.8572e-01- 5.5390e+01i	5.5393e+01	1.0574e-02	-
-7.9841e-01+ 5.8967e+01i	5.8973e+01	1.3539e-02	-
-7.9841e-01- 5.8967e+01i	5.8973e+01	1.3539e-02	-
-3.4317e+00+ 6.1268e+01i	6.1364e+01	5.5924e-02	-
-3.4317e+00- 6.1268e+01i	6.1364e+01	5.5924e-02	-
-8.3454e-01+ 6.2375e+01i	6.2381e+01	1.3378e-02	-
-8.3454e-01- 6.2375e+01i	6.2381e+01	1.3378e-02	-

Table 10. Continued				
-6.5819e-01+	6.4598e+01i	6.4601e+01	1.0188e-02	-
-6.5819e-01-	6.4598e+01i	6.4601e+01	1.0188e-02	-
-1.3435e+02+	1.3435e+02i	1.9000e+02	7.0710e-01	-
-1.3435e+02-	1.3435e+02i	1.9000e+02	7.0710e-01	-
-1.4142e+02+	1.4142e+02i	2.0000e+02	7.0710e-01	-
-1.4142e+02-	1.4142e+02i	2.0000e+02	7.0710e-01	-
-1.4849e+02+	1.4849e+02i	2.1000e+02	7.0710e-01	-
-1.4849e+02-	1.4849e+02i	2.1000e+02	7.0710e-01	-
-1.5556e+02+	1.5556e+02i	2.2000e+02	7.0710e-01	-
-1.5556e+02-	1.5556e+02i	2.2000e+02	7.0710e-01	-
-1.6263e+02+	1.6263e+02i	2.3000e+02	7.0710e-01	-
-1.6263e+02-	1.6263e+02i	2.3000e+02	7.0710e-01	-
-1.6970e+02+	1.6970e+02i	2.4000e+02	7.0710e-01	-
-1.6970e+02-	1.6970e+02i	2.4000e+02	7.0710e-01	-



Table 11. Zeros Of Appendix C Model For 400 in Vertical Acceleration To Vane Channel			
Gain = -1.1449e+08 ft/s <sup>2</sup> /rad			
Root Location (1/s)	Freq. (rad/s)	Damping (-)	Description
0	0	1.0000e+00	-
3.0288e-02	3.0288e-02	-1.0000e+00	-
-6.5797e-01	6.5797e-01	1.0000e+00	-
-3.5405e-01+ 8.4868e-01i	9.1957e-01	3.8501e-01	-
-3.5405e-01- 8.4868e-01i	9.1957e-01	3.8501e-01	-
-1.3617e+00	1.3617e+00	1.0000e+00	-
-1.8699e-01+ 3.7613e+00i	3.7660e+00	4.9652e-02	-
-1.8699e-01- 3.7613e+00i	3.7660e+00	4.9652e-02	-
-4.2833e+00	4.2833e+00	1.0000e+00	-
-8.2366e+00	8.2366e+00	1.0000e+00	-
-9.0232e+00	9.0232e+00	1.0000e+00	-
-9.5754e+00	9.5754e+00	1.0000e+00	-
-1.1242e+01	1.1242e+01	1.0000e+00	-
-6.8811e-01+ 1.1874e+01i	1.1894e+01	5.7853e-02	-
-6.8811e-01- 1.1874e+01i	1.1894e+01	5.7853e-02	-
-1.3531e+01	1.3531e+01	1.0000e+00	-
-1.1220e+00+ 1.6234e+01i	1.6273e+01	6.8946e-02	-
-1.1220e+00- 1.6234e+01i	1.6273e+01	6.8946e-02	-
-1.8133e-01+ 1.7270e+01i	1.7271e+01	1.0500e-02	-
-1.8133e-01- 1.7270e+01i	1.7271e+01	1.0500e-02	-
-1.8889e+01	1.8889e+01	1.0000e+00	-
-1.9084e+01	1.9084e+01	1.0000e+00	-
-4.7644e-01+ 1.9255e+01i	1.9261e+01	2.4736e-02	-
-4.7644e-01- 1.9255e+01i	1.9261e+01	2.4736e-02	-
-1.9882e-01+ 1.9819e+01i	1.9820e+01	1.0031e-02	-
-1.9882e-01- 1.9819e+01i	1.9820e+01	1.0031e-02	-
-1.9966e+01	1.9966e+01	1.0000e+00	-
-2.1029e+01	2.1029e+01	1.0000e+00	-
-2.1982e+01	2.1982e+01	1.0000e+00	-
-2.3007e+01	2.3007e+01	1.0000e+00	-
-3.2989e-01+ 2.3711e+01i	2.3713e+01	1.3912e-02	-
-3.2989e-01- 2.3711e+01i	2.3713e+01	1.3912e-02	-
-2.4000e+01	2.4000e+01	1.0000e+00	-
-1.8381e+00+ 2.9033e+01i	2.9091e+01	6.3183e-02	-
-1.8381e+00- 2.9033e+01i	2.9091e+01	6.3183e-02	-
-2.9319e+01	2.9319e+01	1.0000e+00	-
-5.2959e-01+ 3.4214e+01i	3.4218e+01	1.5477e-02	-
-5.2959e-01- 3.4214e+01i	3.4218e+01	1.5477e-02	-
-9.1753e-01+ 4.2387e+01i	4.2397e+01	2.1641e-02	-
-9.1753e-01- 4.2387e+01i	4.2397e+01	2.1641e-02	-
-6.5603e-01+ 4.6162e+01i	4.6166e+01	1.4210e-02	-
-6.5603e-01- 4.6162e+01i	4.6166e+01	1.4210e-02	-
-9.0926e-01+ 5.3517e+01i	5.3524e+01	1.6988e-02	-
-9.0926e-01- 5.3517e+01i	5.3524e+01	1.6988e-02	-
-7.4626e-01+ 5.6027e+01i	5.6032e+01	1.3318e-02	-
-7.4626e-01- 5.6027e+01i	5.6032e+01	1.3318e-02	-
-8.7183e-01+ 6.0194e+01i	6.0201e+01	1.4482e-02	-
-8.7183e-01- 6.0194e+01i	6.0201e+01	1.4482e-02	-
-3.2372e+00+ 6.1411e+01i	6.1497e+01	5.2640e-02	-
-3.2372e+00- 6.1411e+01i	6.1497e+01	5.2640e-02	-
-8.3211e-01+ 6.2361e+01i	6.2367e+01	1.3342e-02	-
-8.3211e-01- 6.2361e+01i	6.2367e+01	1.3342e-02	-
-7.4028e-01+ 6.4952e+01i	6.4956e+01	1.1397e-02	-
-7.4028e-01- 6.4952e+01i	6.4956e+01	1.1397e-02	-

Table 11. Continued				
-1.3435e+02+	1.3435e+02i	1.9000e+02	7.0710e-01	-
-1.3435e+02-	1.3435e+02i	1.9000e+02	7.0710e-01	-
-1.4142e+02+	1.4142e+02i	2.0000e+02	7.0710e-01	-
-1.4142e+02-	1.4142e+02i	2.0000e+02	7.0710e-01	-
-1.4849e+02+	1.4849e+02i	2.1000e+02	7.0710e-01	-
-1.4849e+02-	1.4849e+02i	2.1000e+02	7.0710e-01	-
-1.5556e+02+	1.5556e+02i	2.2000e+02	7.0710e-01	-
-1.5556e+02-	1.5556e+02i	2.2000e+02	7.0710e-01	-
-1.6263e+02+	1.6263e+02i	2.3000e+02	7.0710e-01	-
-1.6263e+02-	1.6263e+02i	2.3000e+02	7.0710e-01	-
-1.6970e+02+	1.6970e+02i	2.4000e+02	7.0710e-01	-
-1.6970e+02-	1.6970e+02i	2.4000e+02	7.0710e-01	-

Table 12. Zeros Of Appendix C Model For 1,850 in Vertical Acceleration To Vane Channel  
Gain = 4.1381e+06 ft/s<sup>2</sup>/rad

Root Location (1/s)	Freq. (rad/s)	Damping (-)	Description
0	0	1.0000e+00	-
3.0796e-02	3.0796e-02	-1.0000e+00	-
-6.4906e-01	6.4906e-01	1.0000e+00	-
-1.3655e+00	1.3655e+00	1.0000e+00	-
-4.6747e-01+ 1.5489e+00i	1.6179e+00	2.8894e-01	-
-4.6747e-01- 1.5489e+00i	1.6179e+00	2.8894e-01	-
-4.3712e+00+ 1.1292e+00i	4.5147e+00	9.6822e-01	-
-4.3712e+00- 1.1292e+00i	4.5147e+00	9.6822e-01	-
5.7079e+00	5.7079e+00	-1.0000e+00	-
-8.7026e+00	8.7026e+00	1.0000e+00	-
-9.5564e+00+ 8.1969e-01i	9.5915e+00	9.9634e-01	-
-9.5564e+00- 8.1969e-01i	9.5915e+00	9.9634e-01	-
-1.1263e+01	1.1263e+01	1.0000e+00	-
-8.0603e-01+ 1.1445e+01i	1.1473e+01	7.0253e-02	-
-8.0603e-01- 1.1445e+01i	1.1473e+01	7.0253e-02	-
-1.3651e+01	1.3651e+01	1.0000e+00	-
-1.2638e+00+ 1.6703e+01i	1.6751e+01	7.5444e-02	-
-1.2638e+00- 1.6703e+01i	1.6751e+01	7.5444e-02	-
-1.8474e-01+ 1.7266e+01i	1.7267e+01	1.0699e-02	-
-1.8474e-01- 1.7266e+01i	1.7267e+01	1.0699e-02	-
-1.8733e+01	1.8733e+01	1.0000e+00	-
-1.9001e+01	1.9001e+01	1.0000e+00	-
-3.0507e-01+ 1.9575e+01i	1.9577e+01	1.5583e-02	-
-3.0507e-01- 1.9575e+01i	1.9577e+01	1.5583e-02	-
-1.9995e+01	1.9995e+01	1.0000e+00	-
-2.1009e+01	2.1009e+01	1.0000e+00	-
-3.5986e-01+ 2.1410e+01i	2.1413e+01	1.6806e-02	-
-3.5986e-01- 2.1410e+01i	2.1413e+01	1.6806e-02	-
-2.1991e+01	2.1991e+01	1.0000e+00	-
-2.3006e+01	2.3006e+01	1.0000e+00	-
-2.3999e+01	2.3999e+01	1.0000e+00	-
-4.1818e-01+ 2.5738e+01i	2.5741e+01	1.6246e-02	-
-4.1818e-01- 2.5738e+01i	2.5741e+01	1.6246e-02	-
-2.9350e+01	2.9350e+01	1.0000e+00	-
-1.8446e+00+ 2.9947e+01i	3.0003e+01	6.1478e-02	-
-1.8446e+00- 2.9947e+01i	3.0003e+01	6.1478e-02	-
-9.1895e-01+ 4.2422e+01i	4.2432e+01	2.1657e-02	-
-9.1895e-01- 4.2422e+01i	4.2432e+01	2.1657e-02	-
-9.3715e-01+ 4.7993e+01i	4.8002e+01	1.9523e-02	-
-9.3715e-01- 4.7993e+01i	4.8002e+01	1.9523e-02	-
-1.6170e+01+ 5.1722e+01i	5.4191e+01	2.9839e-01	-
-1.6170e+01- 5.1722e+01i	5.4191e+01	2.9839e-01	-
1.5907e+01+ 5.2752e+01i	5.5098e+01	-2.8871e-01	-
1.5907e+01- 5.2752e+01i	5.5098e+01	-2.8871e-01	-
-9.8295e-01+ 5.5499e+01i	5.5507e+01	1.7708e-02	-
-9.8295e-01- 5.5499e+01i	5.5507e+01	1.7708e-02	-
-7.8327e-01+ 5.7572e+01i	5.7577e+01	1.3604e-02	-
-7.8327e-01- 5.7572e+01i	5.7577e+01	1.3604e-02	-
-3.3305e+00+ 6.1438e+01i	6.1528e+01	5.4129e-02	-
-3.3305e+00- 6.1438e+01i	6.1528e+01	5.4129e-02	-
-8.0793e-01+ 6.2360e+01i	6.2365e+01	1.2955e-02	-
-8.0793e-01- 6.2360e+01i	6.2365e+01	1.2955e-02	-
-5.4590e-01+ 6.7212e+01i	6.7214e+01	8.1218e-03	-
-5.4590e-01- 6.7212e+01i	6.7214e+01	8.1218e-03	-

Table 12. Continued				
-1.3435e+02+	1.3435e+02i	1.9000e+02	7.0710e-01	-
-1.3435e+02-	1.3435e+02i	1.9000e+02	7.0710e-01	-
-1.4142e+02+	1.4142e+02i	2.0000e+02	7.0710e-01	-
-1.4142e+02-	1.4142e+02i	2.0000e+02	7.0710e-01	-
-1.4849e+02+	1.4849e+02i	2.1000e+02	7.0710e-01	-
-1.4849e+02-	1.4849e+02i	2.1000e+02	7.0710e-01	-
-1.5556e+02+	1.5556e+02i	2.2000e+02	7.0710e-01	-
-1.5556e+02-	1.5556e+02i	2.2000e+02	7.0710e-01	-
-1.6263e+02+	1.6263e+02i	2.3000e+02	7.0710e-01	-
-1.6263e+02-	1.6263e+02i	2.3000e+02	7.0710e-01	-
-1.6970e+02+	1.6970e+02i	2.4000e+02	7.0710e-01	-
-1.6970e+02-	1.6970e+02i	2.4000e+02	7.0710e-01	-

Table 13. Zeros Of Appendix C Model For 3,460 in Vertical Acceleration To Vane Channel			
Gain = -7.7040e+06 ft/s^2/rad			
Root Location (1/s)	Freq. (rad/s)	Damping (-)	Description
0	0	1.0000e+00	-
3.1449e-02	3.1449e-02	-1.0000e+00	-
-6.3766e-01	6.3766e-01	1.0000e+00	-
1.0518e+00	1.0518e+00	-1.0000e+00	-
-1.3765e+00+ 7.2361e-02i	1.3784e+00	9.9862e-01	-
-1.3765e+00- 7.2361e-02i	1.3784e+00	9.9862e-01	-
-3.7560e+00	3.7560e+00	1.0000e+00	-
5.8962e+00	5.8962e+00	-1.0000e+00	-
-6.1385e+00	6.1385e+00	1.0000e+00	-
-8.3526e+00	8.3526e+00	1.0000e+00	-
-9.6928e+00+ 1.6130e+00i	9.8261e+00	9.8643e-01	-
-9.6928e+00- 1.6130e+00i	9.8261e+00	9.8643e-01	-
-1.1071e+01	1.1071e+01	1.0000e+00	-
-1.3098e+01	1.3098e+01	1.0000e+00	-
-1.2120e+00+ 1.4118e+01i	1.4170e+01	8.5535e-02	-
-1.2120e+00- 1.4118e+01i	1.4170e+01	8.5535e-02	-
-1.6628e+01	1.6628e+01	1.0000e+00	-
-1.7340e-01+ 1.7262e+01i	1.7263e+01	1.0045e-02	-
-1.7340e-01- 1.7262e+01i	1.7263e+01	1.0045e-02	-
-7.5721e-01+ 1.8654e+01i	1.8669e+01	4.0560e-02	-
-7.5721e-01- 1.8654e+01i	1.8669e+01	4.0560e-02	-
-1.8999e+01	1.8999e+01	1.0000e+00	-
-2.1367e-01+ 1.9685e+01i	1.9686e+01	1.0854e-02	-
-2.1367e-01- 1.9685e+01i	1.9686e+01	1.0854e-02	-
-2.0002e+01	2.0002e+01	1.0000e+00	-
-2.0998e+01	2.0998e+01	1.0000e+00	-
-2.2000e+01	2.2000e+01	1.0000e+00	-
-2.3002e+01	2.3002e+01	1.0000e+00	-
-2.4000e+01	2.4000e+01	1.0000e+00	-
-3.6037e-01+ 2.4479e+01i	2.4481e+01	1.4720e-02	-
-3.6037e-01- 2.4479e+01i	2.4481e+01	1.4720e-02	-
-1.0870e+01+ 2.4768e+01i	2.7048e+01	4.0187e-01	-
-1.0870e+01- 2.4768e+01i	2.7048e+01	4.0187e-01	-
1.0929e+01+ 2.5099e+01i	2.7375e+01	-3.9925e-01	-
1.0929e+01- 2.5099e+01i	2.7375e+01	-3.9925e-01	-
-2.9881e+01	2.9881e+01	1.0000e+00	-
-2.0788e+00+ 3.1234e+01i	3.1303e+01	6.6409e-02	-
-2.0788e+00- 3.1234e+01i	3.1303e+01	6.6409e-02	-
-9.1714e-01+ 4.1970e+01i	4.1980e+01	2.1847e-02	-
-9.1714e-01- 4.1970e+01i	4.1980e+01	2.1847e-02	-
-9.1751e-01+ 5.1169e+01i	5.1177e+01	1.7928e-02	-
-9.1751e-01- 5.1169e+01i	5.1177e+01	1.7928e-02	-
-7.2960e-01+ 5.6666e+01i	5.6671e+01	1.2874e-02	-
-7.2960e-01- 5.6666e+01i	5.6671e+01	1.2874e-02	-
-9.2873e+00+ 5.6050e+01i	5.6814e+01	1.6347e-01	-
-9.2873e+00- 5.6050e+01i	5.6814e+01	1.6347e-01	-
8.9230e+00+ 5.6264e+01i	5.6967e+01	-1.5663e-01	-
8.9230e+00- 5.6264e+01i	5.6967e+01	-1.5663e-01	-
-3.2882e+00+ 6.1217e+01i	6.1305e+01	5.3637e-02	-
-3.2882e+00- 6.1217e+01i	6.1305e+01	5.3637e-02	-
-7.8271e-01+ 6.2420e+01i	6.2425e+01	1.2538e-02	-
-7.8271e-01- 6.2420e+01i	6.2425e+01	1.2538e-02	-
-1.6643e-01+ 6.8400e+01i	6.8401e+01	2.4332e-03	-
-1.6643e-01- 6.8400e+01i	6.8401e+01	2.4332e-03	-

Table 13. Continued				
-1.3435e+02+	1.3435e+02i	1.9000e+02	7.0710e-01	-
-1.3435e+02-	1.3435e+02i	1.9000e+02	7.0710e-01	-
-1.4142e+02+	1.4142e+02i	2.0000e+02	7.0710e-01	-
-1.4142e+02-	1.4142e+02i	2.0000e+02	7.0710e-01	-
-1.4849e+02+	1.4849e+02i	2.1000e+02	7.0710e-01	-
-1.4849e+02-	1.4849e+02i	2.1000e+02	7.0710e-01	-
-1.5556e+02+	1.5556e+02i	2.2000e+02	7.0710e-01	-
-1.5556e+02-	1.5556e+02i	2.2000e+02	7.0710e-01	-
-1.6263e+02+	1.6263e+02i	2.3000e+02	7.0710e-01	-
-1.6263e+02-	1.6263e+02i	2.3000e+02	7.0710e-01	-
-1.6970e+02+	1.6970e+02i	2.4000e+02	7.0710e-01	-
-1.6970e+02-	1.6970e+02i	2.4000e+02	7.0710e-01	-

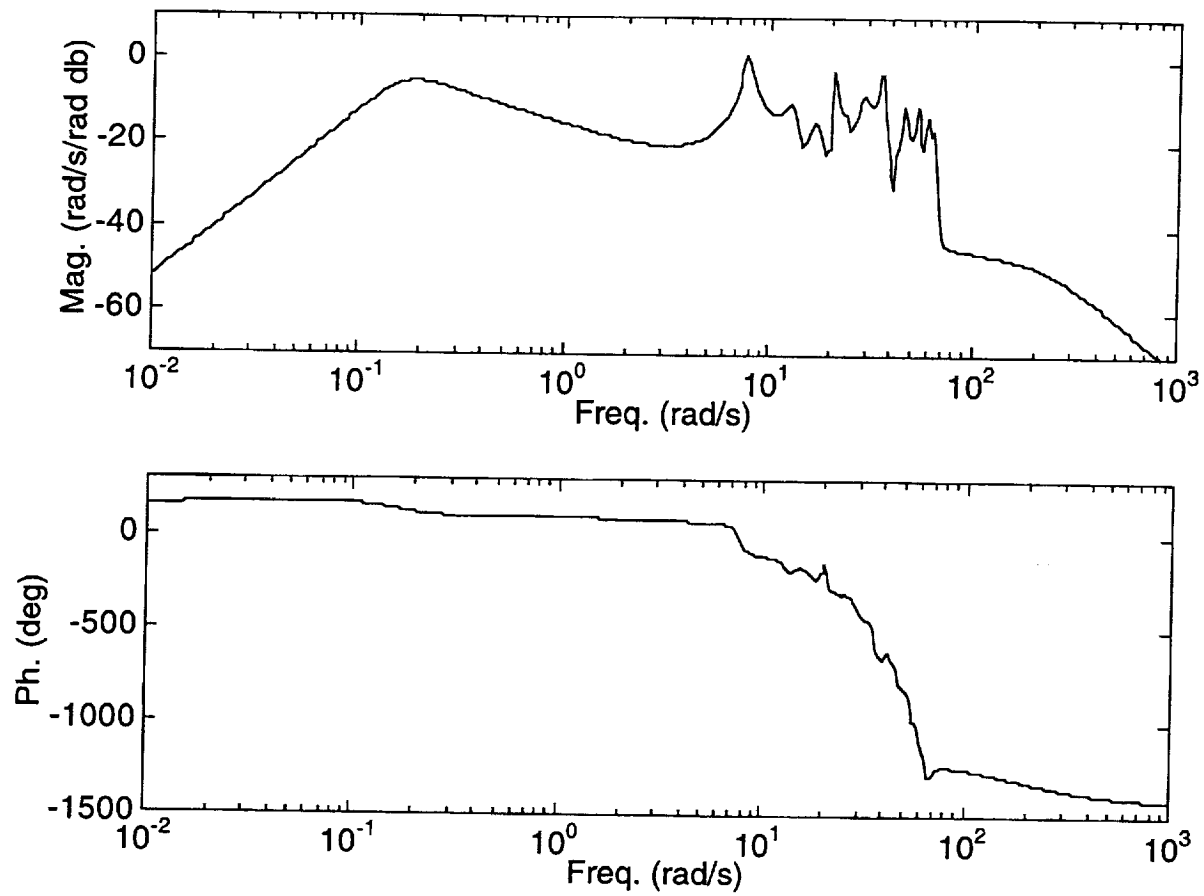


Figure 16. Frequency Response Of Appendix C Model  
For 400 in Pitch Rate To Elevator Channel

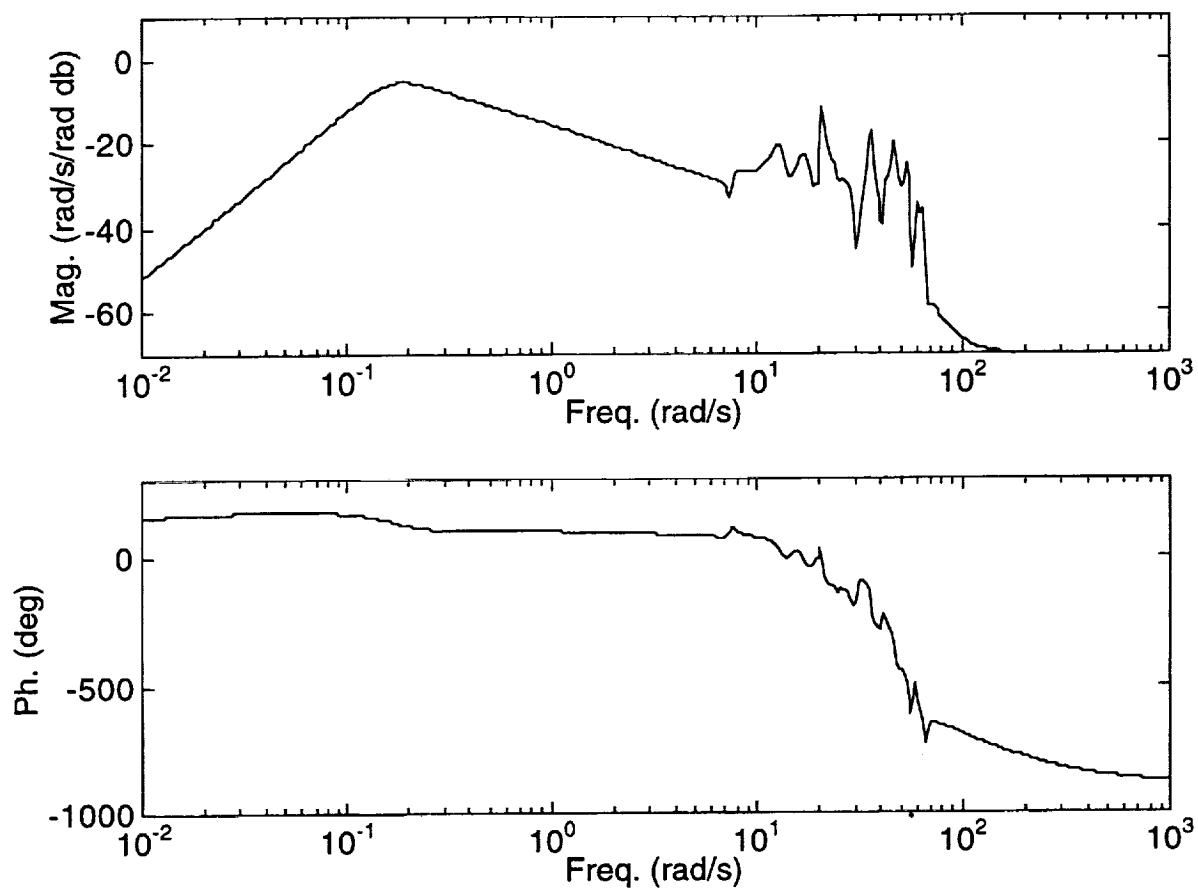


Figure 17. Frequency Response Of Appendix C Model  
For 1,850 in Pitch Rate To Elevator Channel



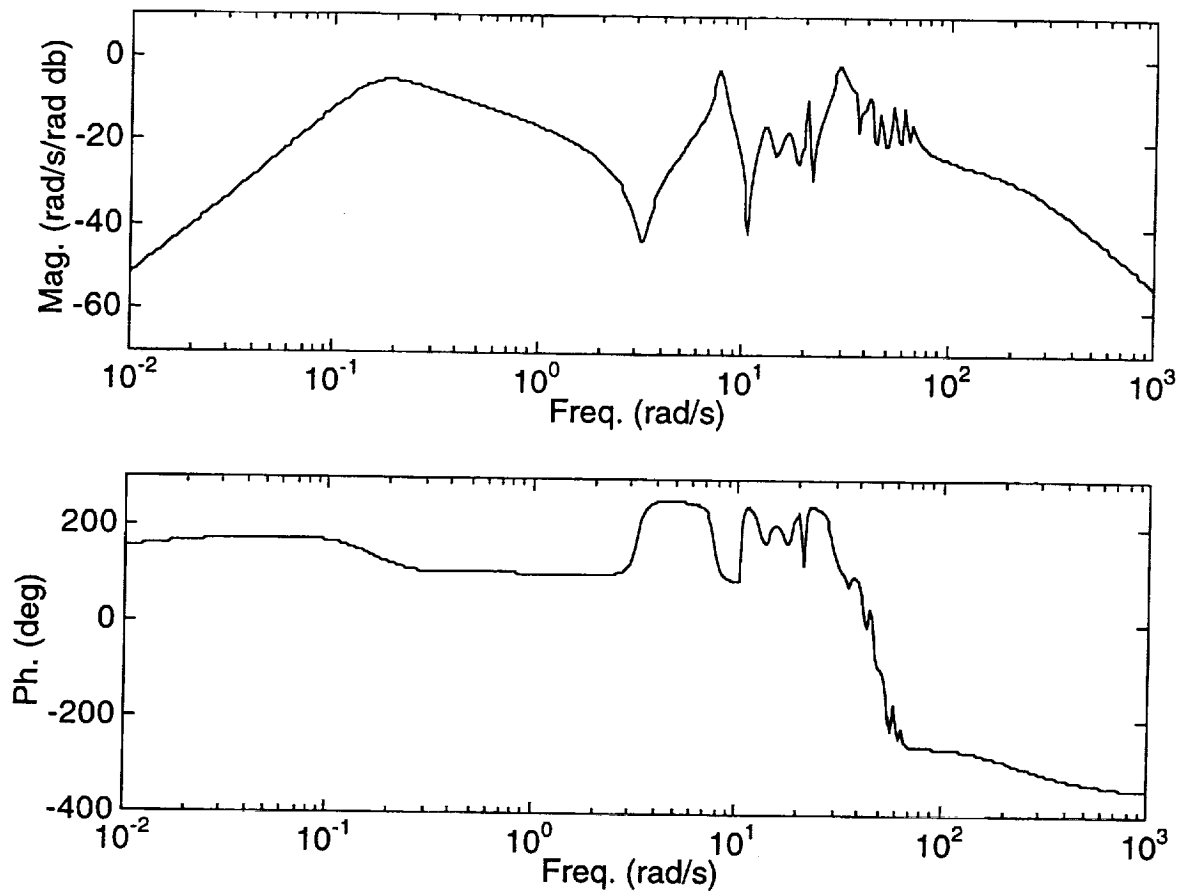


Figure 18. Frequency Response Of Appendix C Model  
For 3,460 in Pitch Rate To Elevator Channel

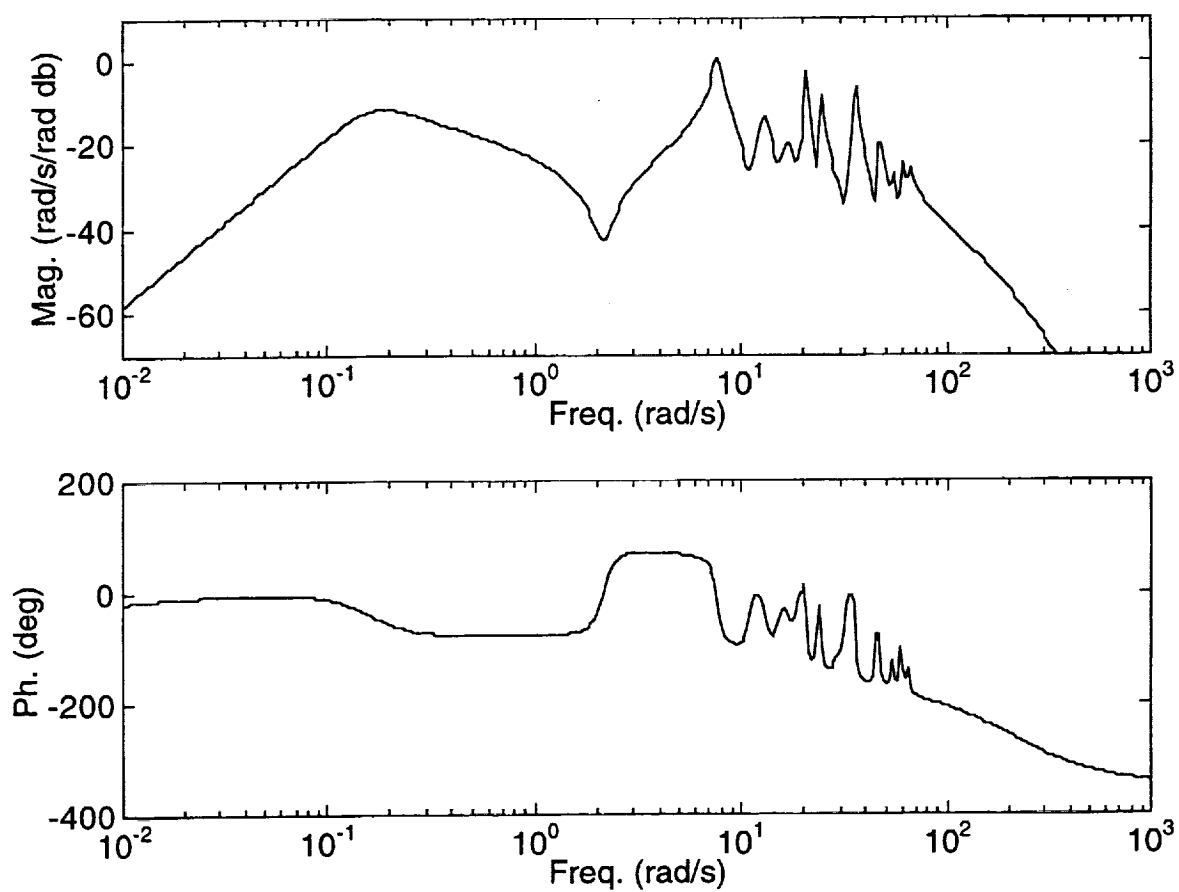


Figure 19. Frequency Response Of Appendix C Model  
For 400 in Pitch Rate To Vane Channel

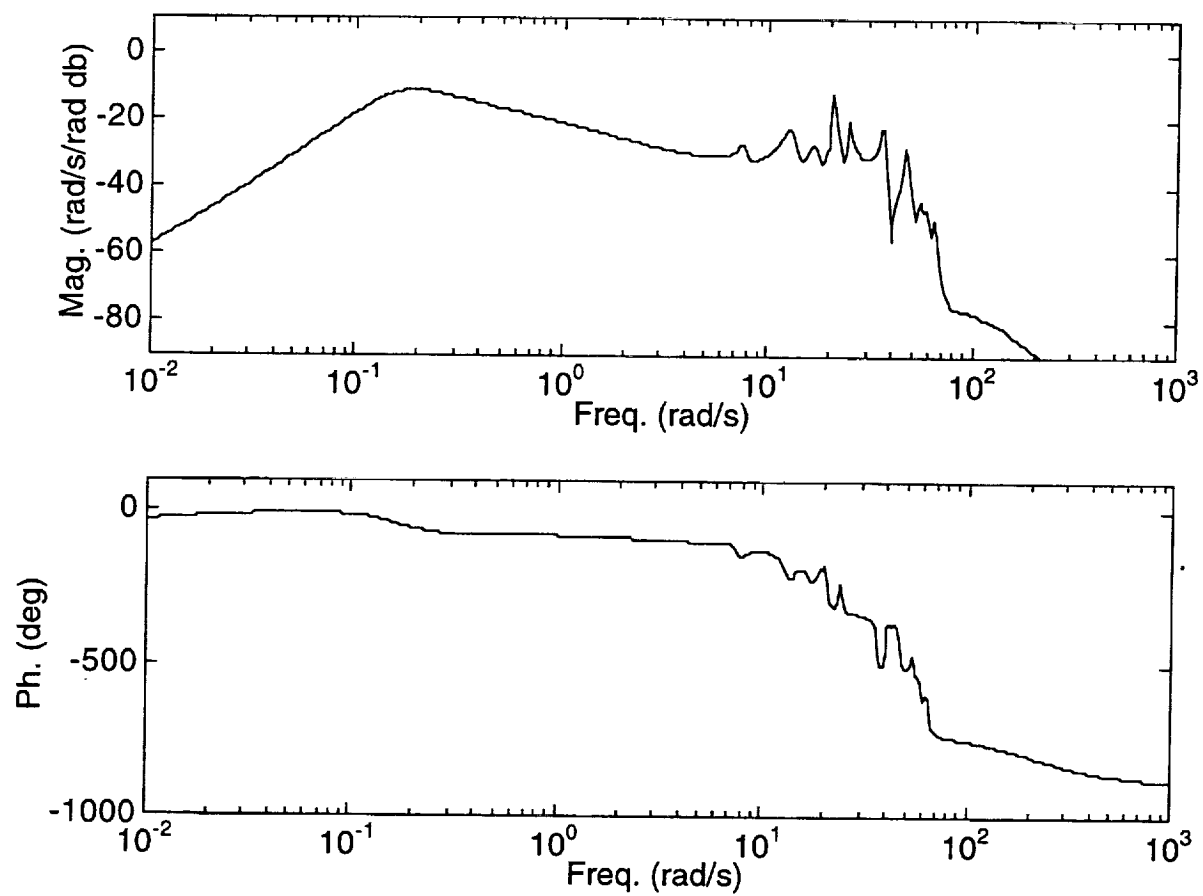


Figure 20. Frequency Response Of Appendix C Model  
For 1,850 in Pitch Rate To Vane Channel

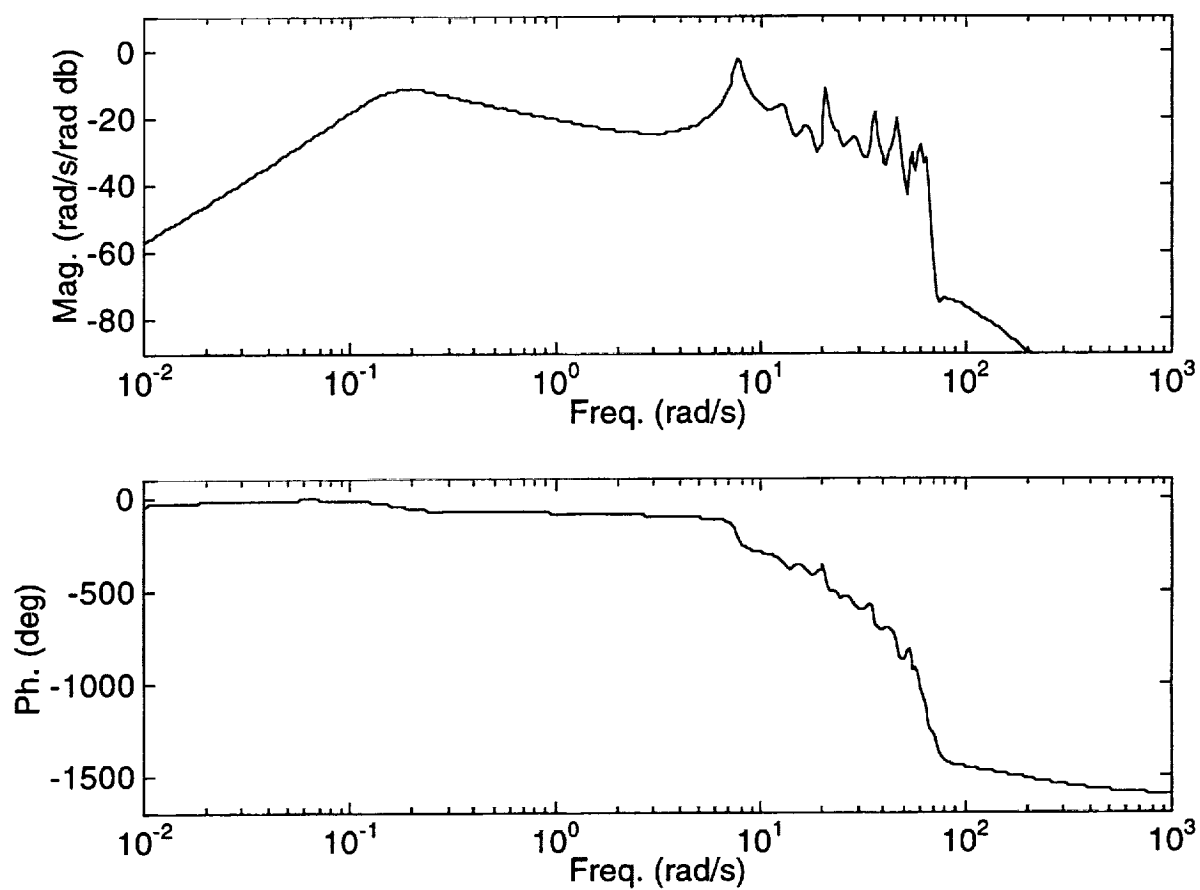


Figure 21. Frequency Response Of Appendix C Model  
For 3,460 in Pitch Rate To Vane Channel

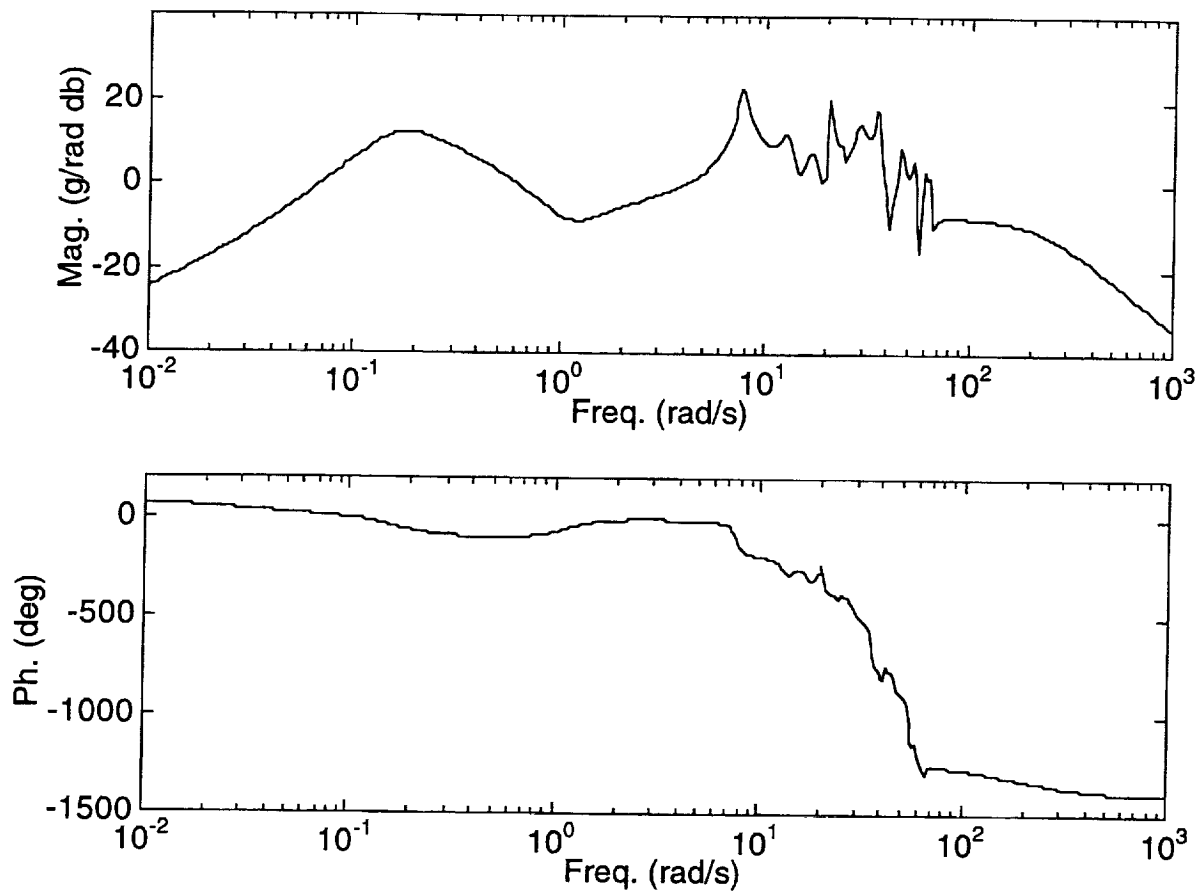


Figure 22. Frequency Response Of Appendix C Model  
For 400 in Vertical Acceleration To Elevator Channel

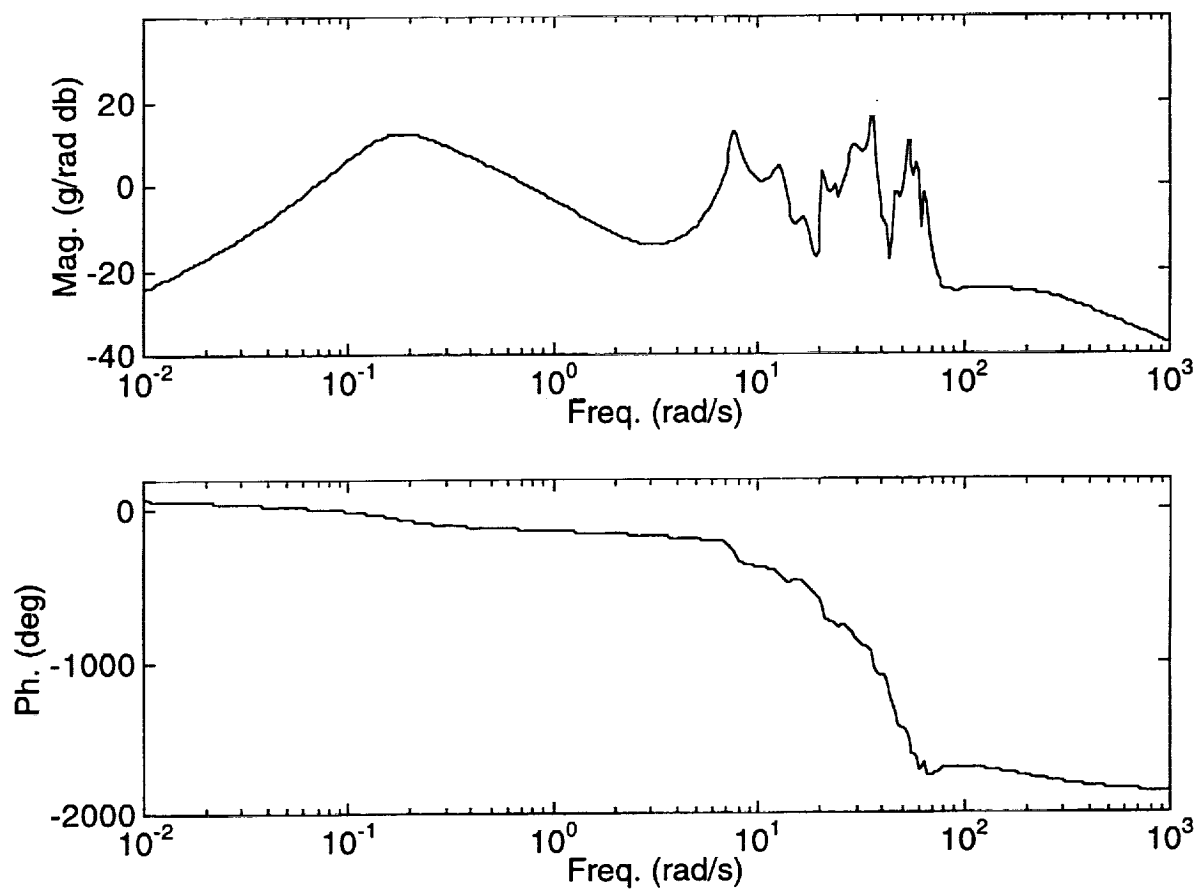


Figure 23. Frequency Response Of Appendix C Model  
For 1,850 in Vertical Acceleration To Elevator Channel

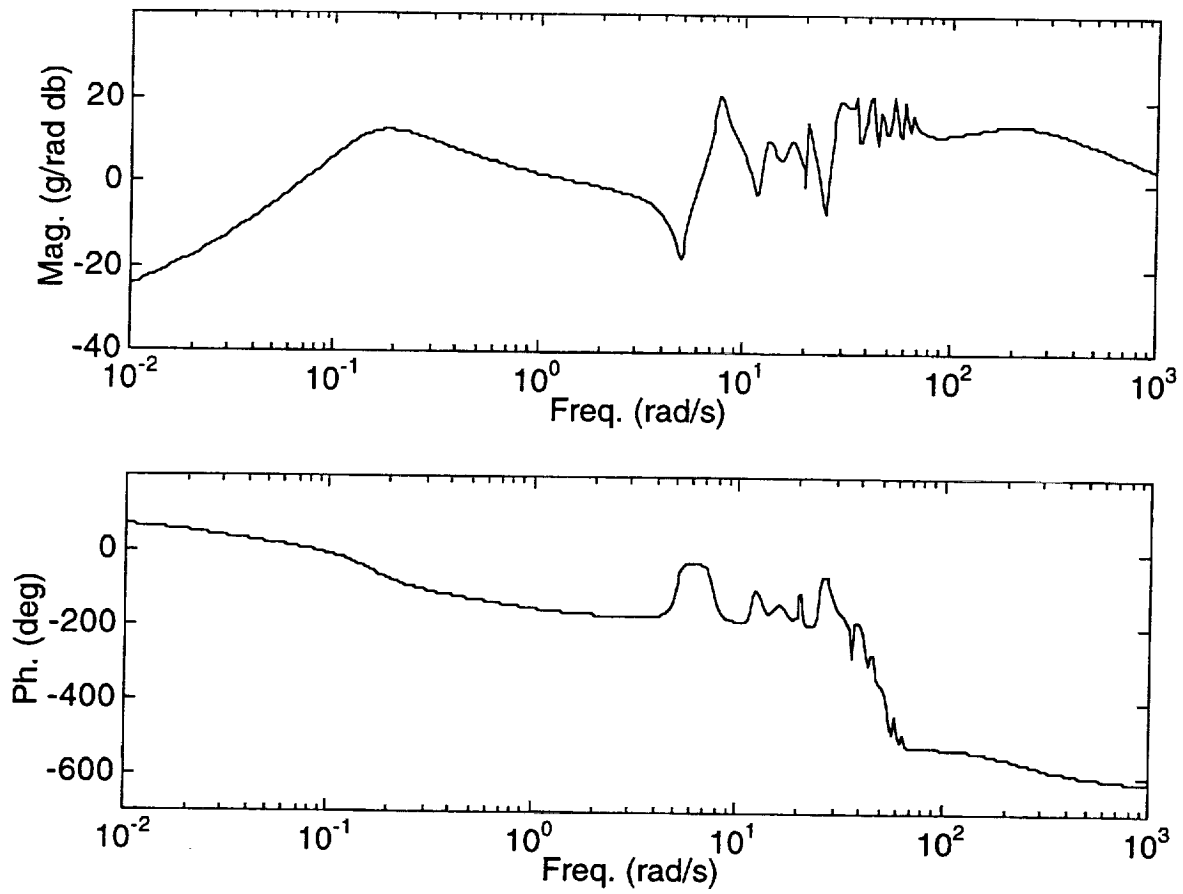


Figure 24. Frequency Response Of Appendix C Model  
For 3,460 in Vertical Acceleration To Elevator Channel

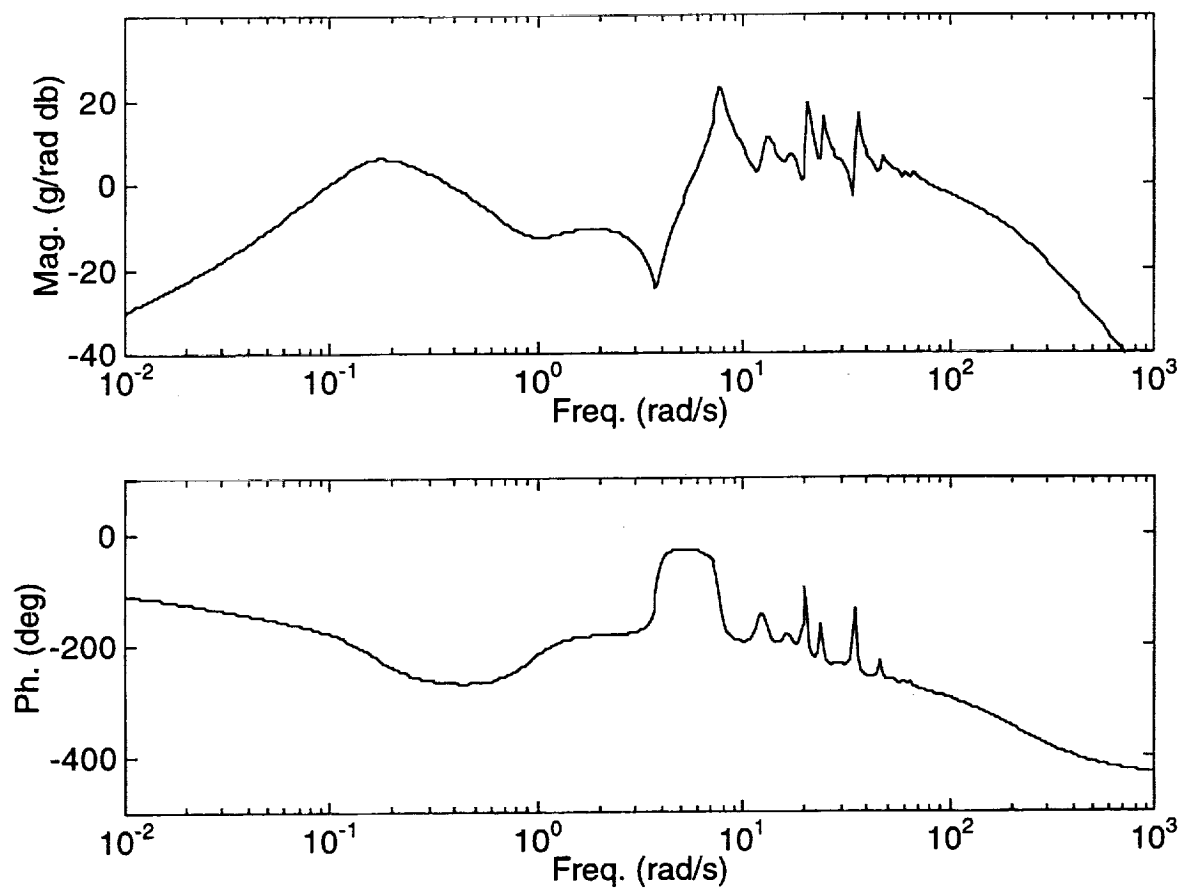


Figure 25. Frequency Response Of Appendix C Model  
For 400 in Vertical Acceleration To Vane Channel



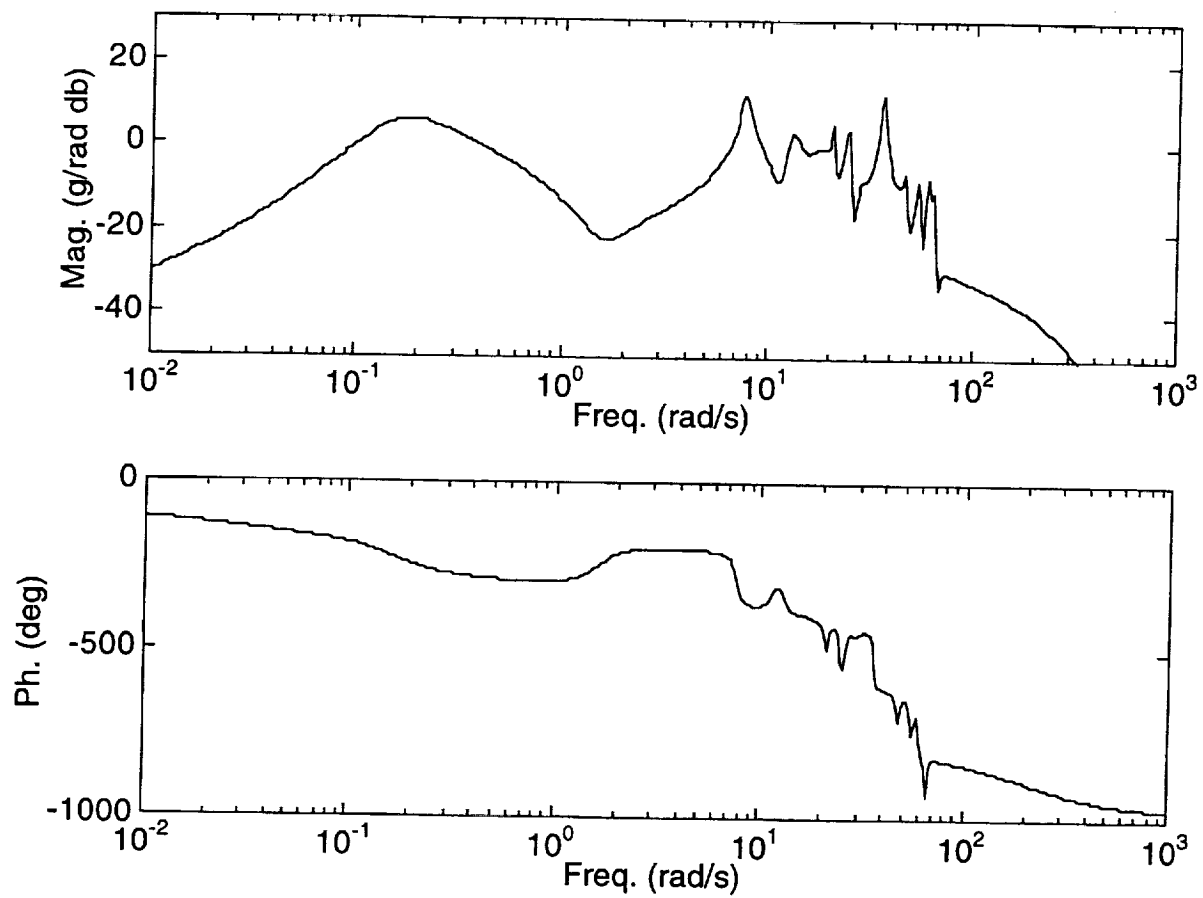


Figure 26. Frequency Response Of Appendix C Model  
For 1,850 in Vertical Acceleration To Vane Channel

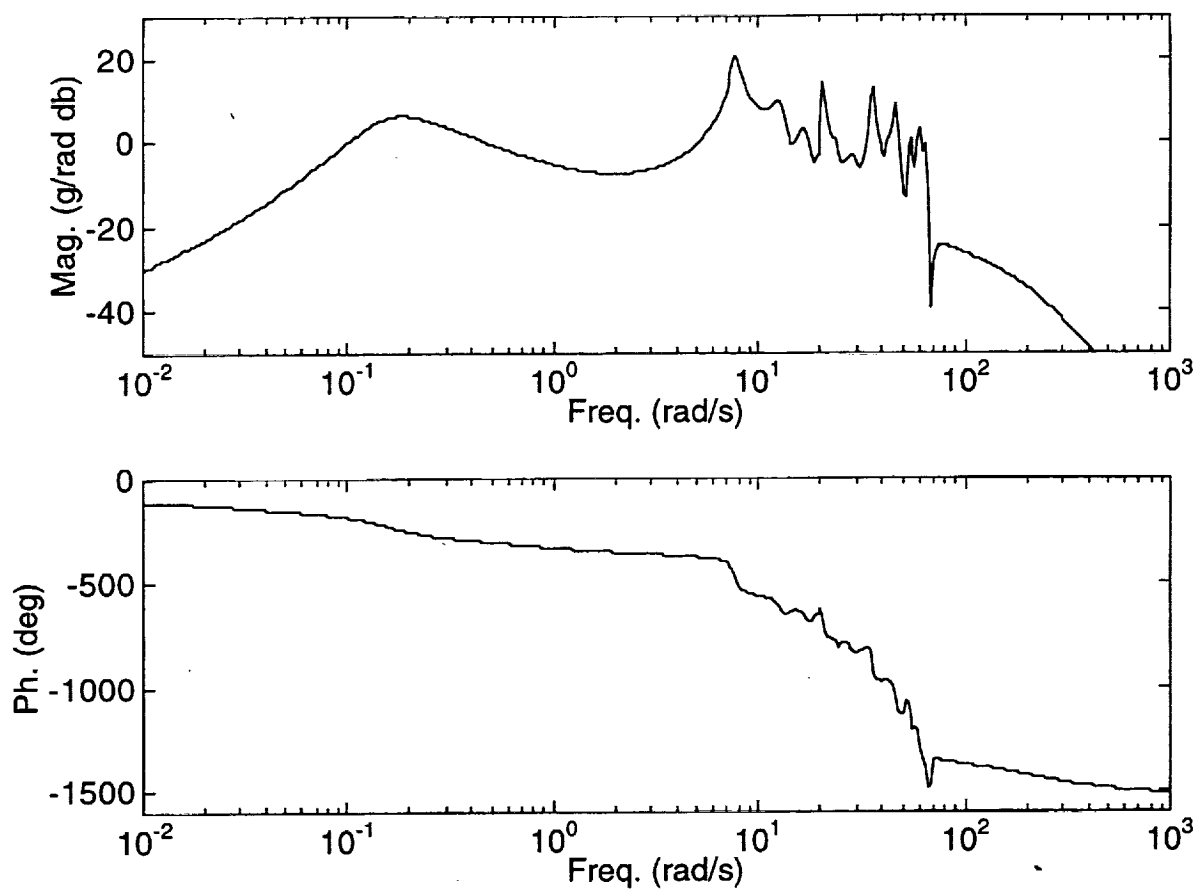


Figure 27. Frequency Response Of Appendix C Model  
For 3,460 in Vertical Acceleration To Vane Channel

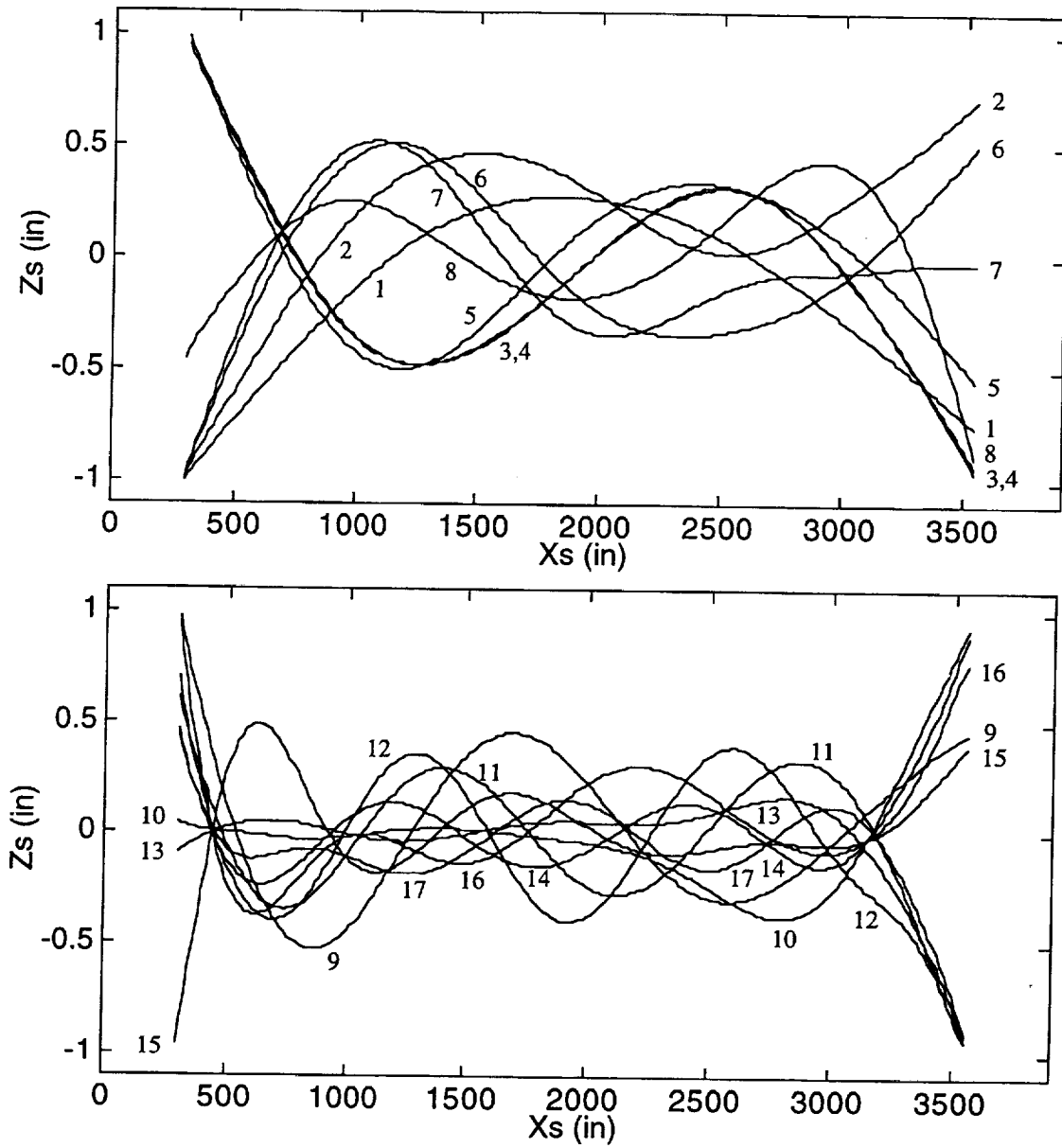


Figure 28. Structural Mode Shape Data - Mass Case M3A

### C. Forward Vane Development

Due to the predicted infeasibility of aft tail only inner loop FCS architectures, alternate means to elicit the necessary control forces to damp structural vibrations and augment pitch motions were considered. Based on the demonstrated potential of other similar vehicles, attention has focused on utilization of small forward vanes as alternate/additional control surfaces. The current HSCT configuration does not have an ability to generate control loads near the forward fuselage. Therefore, inclusion of hypothetical forward lifting surfaces, and their effects upon the existing vehicle math model characteristics, to fulfill such a role has been undertaken. To avoid burdens associated with high-fidelity modeling techniques utilized by the nonlinear simulation tool and ISAC, and to allow a relatively quick investigation to probe the benefits and/or deficiencies of the candidate vane surfaces, a "first cut" modeling procedure is utilized and discussed next.

Figs. 29-30 indicate the vane geometry and its appearance on the HSCT configuration. The vane planform is a scaled version of the horizontal tail shape. Exposed surface area is  $\bar{S}_V = 177.5 \text{ ft}^2$ , which is 2.5% of the wing reference area and 25.26% of the horizontal tail exposed area. Mean aerodynamic chord and span, based on exposed area, are  $\bar{c}_V = 12.94 \text{ ft}$  and  $\bar{b}_V = 15.58 \text{ ft}$ , respectively, giving an aspect ratio of  $A_V = 1.367$ . Leading and trailing edge sweep angles are  $\Lambda_{LEV} = 54.23 \text{ deg}$  and  $\Lambda_{TEV} = -25.55 \text{ deg}$ . The quarter chord point, along the mean aerodynamic chord, is mounted to the fuselage at station 400 in, just aft of the crew station. Other geometric data is indicated in Fig. 29.

The original Cycle 1/ISAC model from Appendix D in Ref. 13 serves as the backbone, to which vane effects are added by a first order, component build-up procedure making use of empirical lifting surface predictions and structural vibration characteristics. Ref. 17 provides the basic foundation for such a procedure. The vane is taken to be a rigid massless surface, and any effects on the structural model, in terms of vehicle mass and rotational inertias and modal vibration characteristics, are neglected. Further, the vane panel is assumed to be very thin with symmetric upper and lower surface profiles. The vane will be an all flying surface with rotation about the mean aerodynamic quarter chord point. Only vane lift is accounted for, vane pitch moment

$\bar{S}_V = 177.50 \text{ ft}^2$  (based on exposed area)

$\bar{c}_V = 12.94 \text{ ft}$  (based on exposed area)

$\bar{b}_V = 15.58 \text{ ft}$  (based on exposed area)

$A_V = 1.367$

$\Lambda_{LE_V} = 54.23 \text{ deg}$

$\Lambda_{TE_V} = -25.55 \text{ deg}$

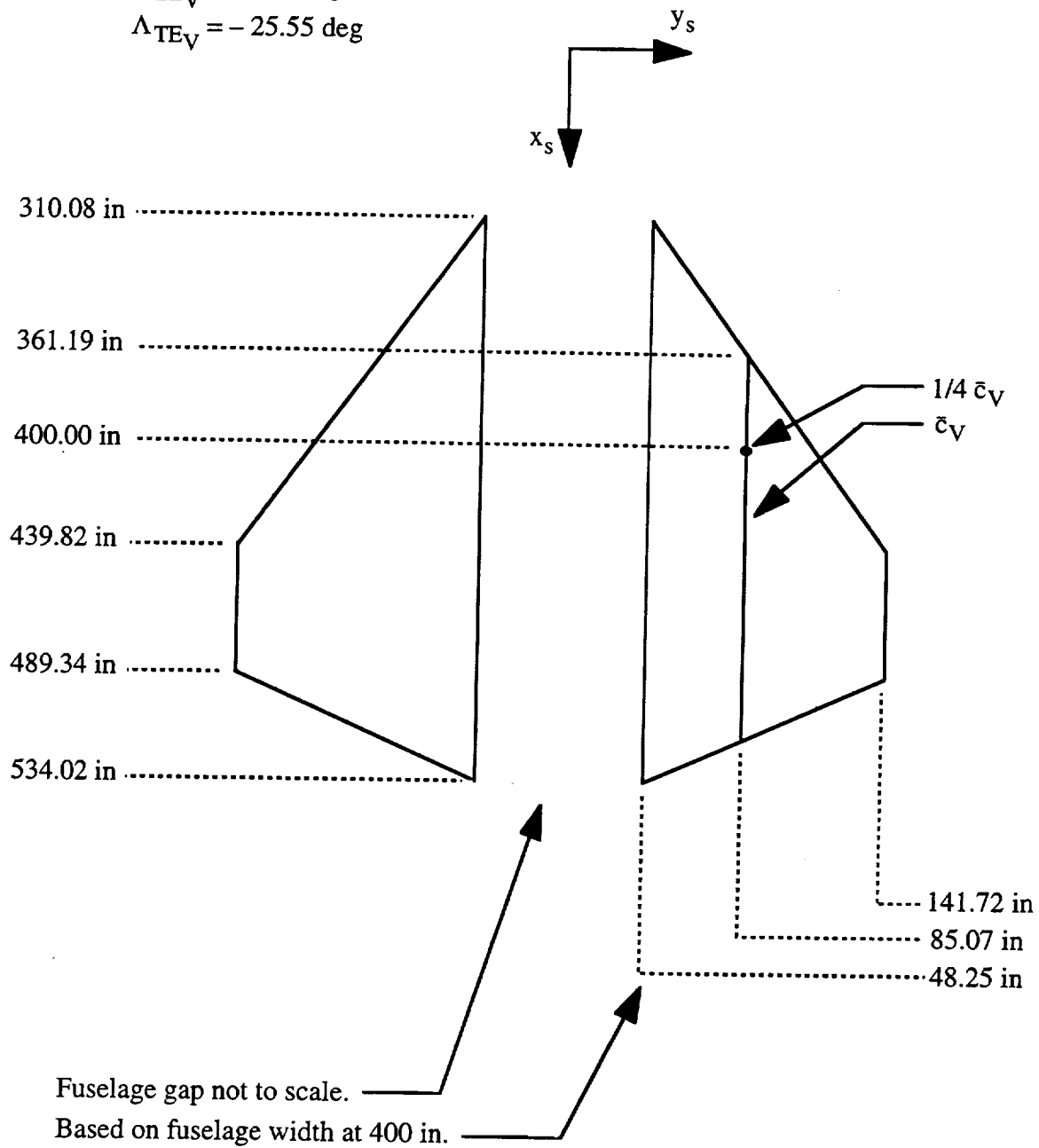


Figure 29. Vane Geometry

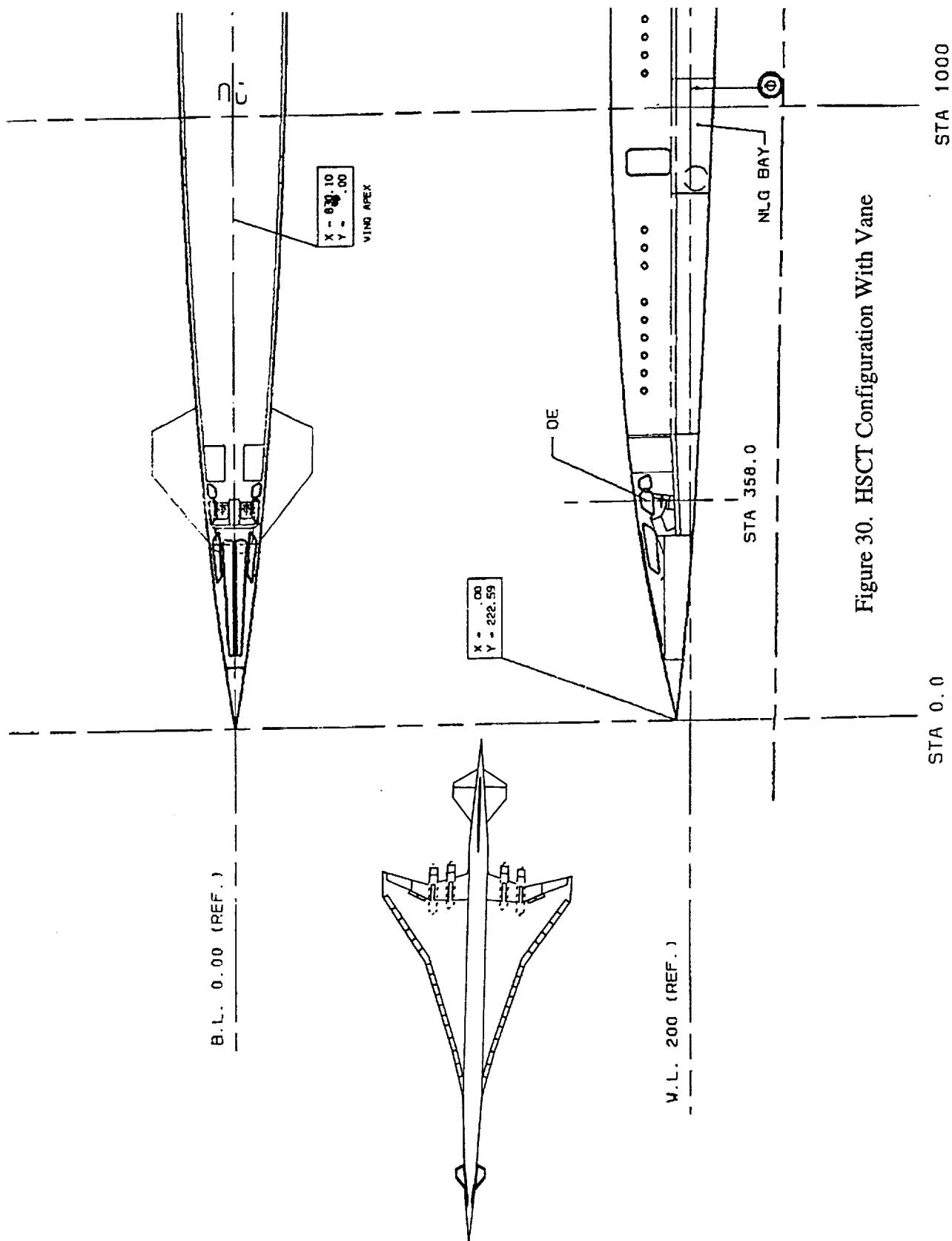
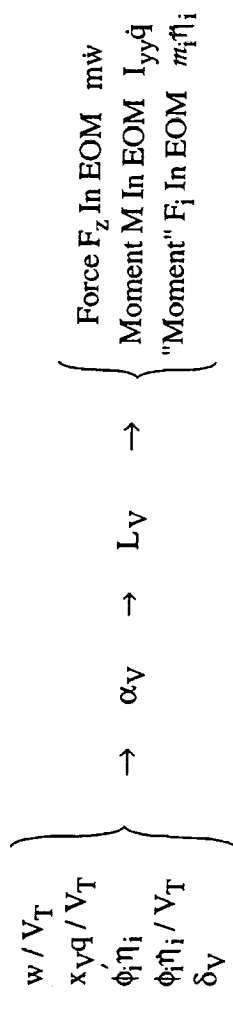


Figure 30. HSCT Configuration With Vane



## Insertion of Lift into Equation of Motion

**Figure 31. Vane Modeling Summary**

about the rotation line is taken as zero and drag forces are neglected. Interference effects from the vane on downstream components are also ignored. The vane normal load is allowed to excite rigid-body and structural degrees of freedom, but not the unsteady aerodynamic states. New control derivatives arising from the vane, as well as vane contributions to the existing vehicle stability derivatives, are considered in the modeling procedure (i.e., modifications to the original state space A and B matrices in Eq. (2.1) are considered).

The vane modeling procedure is summarized in Fig. 31. Generation of vane angle of attack ( $\alpha_v$ ) originates from several sources: rigid-body plunge rate ( $w/V_T$ ), rigid-body pitch rate ( $x_v q/V_T$ ), structural pitch ( $\phi_i' \eta_i$ ), structural plunge rate ( $\phi_i \dot{\eta}_i/V_T$ ), and control deflection ( $\delta_v$ ). The parameters  $x_v$ ,  $\phi_i$  and  $\phi_i'$  denote the body x axis vane location, the  $i^{\text{th}}$  mode shape, and the  $i^{\text{th}}$  mode slope. The local angle of attack results in the vane lift force ( $L^V$ ), which is approximated as a pure body axis vertical force. The lift force is estimated from a common quasi-static empirical formula<sup>21</sup> for the vane lift curve slope coefficient, or

$$L^V = \bar{q} S_V C_L^V \quad C_L^V = C_{L_\alpha}^V \alpha_v$$

$$C_{L_\alpha}^V = \frac{2\pi A_V}{2 + \left[ \frac{A_V^2 \beta^2}{\kappa^2} \left( 1 + \frac{\tan^2 \Lambda_{1/2c}}{\beta^2} \right) + 4 \right]^{1/2}} \quad (2.11)$$

$$\beta = (1 - M^2)^{1/2} \quad \kappa = \frac{c_{l_\alpha}^V}{2\pi}$$

$$\alpha_v = \frac{w}{V_T} - \frac{x_v q}{V_T} - \phi_i' \eta_i - \frac{\phi_i \dot{\eta}_i}{V_T} + \delta_v$$

In Eq. (2.11),  $\bar{q}$  denotes dynamic pressure,  $M$  denotes Mach number,  $C_{L_\alpha}^V$  denotes the vane surface lift curve slope coefficient, and  $c_{l_\alpha}^V$  denotes the vane section lift curve slope coefficient (taken as  $2\pi$  here). Finally, as indicated in Fig. 31, the vane lift force effect is inserted into the governing rigid and structural equations of motion, in particular the  $w$ ,  $q$ , and  $\eta_i$  kinetic equations.

Analytically, the affected equations of motion are

$$\begin{aligned} \dot{w} &= \dots + Z_w w + Z_q q + \sum_i Z_{\eta_i} \eta_i + \sum_i Z_{\dot{\eta}_i} \dot{\eta}_i + Z_{\delta_v} \delta_v + \dots \\ \dot{q} &= \dots + M_w w + M_q q + \sum_i M_{\eta_i} \eta_i + \sum_i M_{\dot{\eta}_i} \dot{\eta}_i + M_{\delta_v} \delta_v + \dots \end{aligned} \quad (2.12)$$



$$\eta_i = \dots + F_{i_w} w + F_{i_q} q + \sum_j F_{i_{\eta_j}} \eta_j + \sum_j F_{i_{\dot{\eta}_j}} \dot{\eta}_j + F_{i_{\delta_V}} \delta_V + \dots$$

Parameters of interest in Eq. (2.12) are the rigid and aeroelastic stability and control derivatives  $Z_k$ ,  $M_k$ ,  $F_{i_k}$  with  $k = w, q, \eta_j, \dot{\eta}_j, \delta_V$ . Other terms appear in these equations of motion but are not explicitly shown. Only stability derivatives explicitly appearing in Eq. (2.12) are modified to account for effects from the vane (i.e., existing baseline values appearing in Appendix D in Ref. 13 are adjusted leading to the values listed in Appendix C). The vane control derivatives appearing in Eq. (2.12) are new terms. In addition to these equations, the vane actuator equations, similar to that shown in Eq. (2.6), are appended to the vehicle math model.

The dimensional derivatives in Eq. (2.12) are defined as

$$\begin{aligned} Z_w &= \frac{\bar{q} \bar{S}}{m V_T} C_{Z_w} & M_w &= \frac{\bar{q} \bar{S} \bar{c}}{I_{yy} V_T} C_{M_w} & F_{i_w} &= \frac{\bar{q} \bar{S} \bar{c}}{m_i V_T} C_{i_w} \\ Z_q &= \frac{\bar{q} \bar{S} \bar{c}}{2m V_T} C_{Z_q} & M_q &= \frac{\bar{q} \bar{S} \bar{c}^2}{2I_{yy} V_T} C_{M_q} & F_{i_q} &= \frac{\bar{q} \bar{S} \bar{c}^2}{2m_i V_T} C_{i_q} \\ Z_{\eta_i} &= \frac{\bar{q} \bar{S}}{m} C_{Z_{\eta_i}} & M_{\eta_i} &= \frac{\bar{q} \bar{S} \bar{c}}{I_{yy}} C_{M_{\eta_i}} & F_{i_{\eta_j}} &= \frac{\bar{q} \bar{S} \bar{c}}{m_i} C_{i_{\eta_j}} \\ Z_{\dot{\eta}_i} &= \frac{\bar{q} \bar{S} \bar{c}}{2m V_T} C_{Z_{\dot{\eta}_i}} & M_{\dot{\eta}_i} &= \frac{\bar{q} \bar{S} \bar{c}^2}{2I_{yy} V_T} C_{M_{\dot{\eta}_i}} & F_{i_{\dot{\eta}_j}} &= \frac{\bar{q} \bar{S} \bar{c}^2}{2m_i V_T} C_{i_{\dot{\eta}_j}} \\ Z_{\delta_V} &= \frac{\bar{q} \bar{S}}{m} C_{Z_{\delta_V}} & M_{\delta_V} &= \frac{\bar{q} \bar{S} \bar{c}}{I_{yy}} C_{M_{\delta_V}} & F_{i_{\delta_V}} &= \frac{\bar{q} \bar{S} \bar{c}}{m_i} C_{i_{\delta_V}} \end{aligned} \quad (2.13)$$

In these definitions,  $m$  and  $I_{yy}$  denote the vehicle mass and pitch moment of inertia,  $m_i$  denotes the structural vibration modal masses,  $\bar{S}$  denotes the vehicle reference area, and  $\bar{c}$  denotes the vehicle reference chord. Further,  $C_{Z_k}$ ,  $C_{M_k}$ ,  $C_{i_k}$  with  $k = w, q, \eta_j, \dot{\eta}_j, \delta_V$  represent the stability and control derivatives in coefficient or nondimensional form, or

$$\begin{aligned} C_{Z_w} &= \frac{\partial C_Z}{\partial (w/V_T)} & C_{M_w} &= \frac{\partial C_M}{\partial (w/V_T)} & C_{i_w} &= \frac{\partial C_i}{\partial (w/V_T)} \\ C_{Z_q} &= \frac{\partial C_Z}{\partial (\bar{c}q/2V_T)} & C_{M_q} &= \frac{\partial C_M}{\partial (\bar{c}q/2V_T)} & C_{i_q} &= \frac{\partial C_i}{\partial (\bar{c}q/2V_T)} \\ C_{Z_{\eta_i}} &= \frac{\partial C_Z}{\partial \eta_i} & C_{M_{\eta_i}} &= \frac{\partial C_M}{\partial \eta_i} & C_{i_{\eta_j}} &= \frac{\partial C_i}{\partial \eta_j} \end{aligned} \quad (2.14)$$

$$\begin{aligned}
C_{Z\eta_i} &= \frac{\partial C_Z}{\partial (\bar{c}\eta_i/2V_T)} & C_{M\eta_i} &= \frac{\partial C_M}{\partial (\bar{c}\eta_i/2V_T)} & C_{i\eta_j} &= \frac{\partial C_i}{\partial (\bar{c}\eta_j/2V_T)} \\
C_{Z\delta_V} &= \frac{\partial C_Z}{\partial \delta_V} & C_{M\delta_V} &= \frac{\partial C_M}{\partial \delta_V} & C_{i\delta_V} &= \frac{\partial C_i}{\partial \delta_V}
\end{aligned}$$

Changes in dynamic pressure with respect to vertical speed variations are deemed small and neglected in Eq. (2.13) for this flight condition.

Using a component build-up procedure, the vehicle aerodynamic body z axis force ( $F_Z$ ) and pitch moment ( $M$ ), and the generalized force for each structural mode ( $F_i$ ), have contributions from the body (B), wing (W), horizontal tail (H), and vane (V), or

$$\begin{aligned}
F_Z &= F_Z^B + F_Z^W + F_Z^H + F_Z^V \\
M &= M^B + M^W + M^H + M^V \\
F_i &= F_i^B + F_i^W + F_i^H + F_i^V
\end{aligned} \tag{2.15}$$

Dividing through by the vehicle reference area and reference chord in Eq. (2.15) yields

$$\begin{aligned}
C_Z &= \frac{\bar{S}_B}{\bar{S}} C_Z^B + \frac{\bar{S}_W}{\bar{S}} C_Z^W + \frac{\bar{S}_H}{\bar{S}} C_Z^H + \frac{\bar{S}_V}{\bar{S}} C_Z^V \\
C_M &= \frac{\bar{S}_B \bar{c}_B}{\bar{S} \bar{c}} C_M^B + \frac{\bar{S}_W \bar{c}_W}{\bar{S} \bar{c}} C_M^W + \frac{\bar{S}_H \bar{c}_H}{\bar{S} \bar{c}} C_M^H + \frac{\bar{S}_V \bar{c}_V}{\bar{S} \bar{c}} C_M^V \\
C_i &= \frac{\bar{S}_B \bar{c}_B}{\bar{S} \bar{c}} C_i^B + \frac{\bar{S}_W \bar{c}_W}{\bar{S} \bar{c}} C_i^W + \frac{\bar{S}_H \bar{c}_H}{\bar{S} \bar{c}} C_i^H + \frac{\bar{S}_V \bar{c}_V}{\bar{S} \bar{c}} C_i^V
\end{aligned} \tag{2.16}$$

where the notation is clear from previous definitions. Finally, the nondimensional derivatives in component form are

$$\begin{aligned}
C_{Z_k} &= \frac{\bar{S}_B}{\bar{S}} C_{Z_k}^B + \frac{\bar{S}_W}{\bar{S}} C_{Z_k}^W + \frac{\bar{S}_H}{\bar{S}} C_{Z_k}^H + \frac{\bar{S}_V}{\bar{S}} C_{Z_k}^V \\
C_{M_k} &= \frac{\bar{S}_B \bar{c}_B}{\bar{S} \bar{c}} C_{M_k}^B + \frac{\bar{S}_W \bar{c}_W}{\bar{S} \bar{c}} C_{M_k}^W + \frac{\bar{S}_H \bar{c}_H}{\bar{S} \bar{c}} C_{M_k}^H + \frac{\bar{S}_V \bar{c}_V}{\bar{S} \bar{c}} C_{M_k}^V \\
C_{i_k} &= \frac{\bar{S}_B \bar{c}_B}{\bar{S} \bar{c}} C_{i_k}^B + \frac{\bar{S}_W \bar{c}_W}{\bar{S} \bar{c}} C_{i_k}^W + \frac{\bar{S}_H \bar{c}_H}{\bar{S} \bar{c}} C_{i_k}^H + \frac{\bar{S}_V \bar{c}_V}{\bar{S} \bar{c}} C_{i_k}^V
\end{aligned} \tag{2.17}$$

where  $k = w, q, \eta_j, \delta_V$ . The terms associated with the vane in Eq. (2.17) represent the new contributions which are added to the baseline values (i.e., the body, wing, and horizontal tail terms).

Starting with the vane model in Eq. (2.11), the vane aerodynamic coefficients are

$$\begin{aligned}
C_Z^V &= -C_{L\alpha}^V \left( \frac{w}{V_T} - \frac{x_{Vq}}{V_T} - \phi_i' \eta_i - \frac{\phi_i \eta_i}{V_T} + \delta_V \right) \\
C_M^V &= \frac{x_V}{\bar{c}_V} C_{L\alpha}^V \left( \frac{w}{V_T} - \frac{x_{Vq}}{V_T} - \phi_i' \eta_i - \frac{\phi_i \eta_i}{V_T} + \delta_V \right) \\
C_i^V &= \frac{\phi_i}{\bar{c}_V} C_{L\alpha}^V \left( \frac{w}{V_T} - \frac{x_{Vq}}{V_T} - \phi_i' \eta_i - \frac{\phi_i \eta_i}{V_T} + \delta_V \right)
\end{aligned} \tag{2.18}$$

Taking the appropriate partial derivatives indicated in Eq. (2.14) yields the nondimensional derivatives

$$\begin{aligned}
C_{Z_w}^V &= -C_{L\alpha}^V & C_{M_w}^V &= \frac{x_V}{\bar{c}_V} C_{L\alpha}^V & C_{i_w}^V &= \frac{\phi_i}{\bar{c}_V} C_{L\alpha}^V \\
C_{Z_q}^V &= 2 \frac{x_V}{\bar{c}} C_{L\alpha}^V & C_{M_q}^V &= -2 \frac{x_V^2}{\bar{c}_V \bar{c}} C_{L\alpha}^V & C_{i_q}^V &= -2 \frac{x_V \phi_i}{\bar{c}_V \bar{c}} C_{L\alpha}^V \\
C_{Z_{\eta_i}}^V &= \phi_i' C_{L\alpha}^V & C_{M_{\eta_i}}^V &= -\phi_i' \frac{x_V}{\bar{c}_V} C_{L\alpha}^V & C_{i_{\eta_j}}^V &= -\phi_j' \frac{\phi_i}{\bar{c}_V} C_{L\alpha}^V \\
C_{Z_{\eta_i}}^V &= 2 \frac{\phi_i}{\bar{c}} C_{L\alpha}^V & C_{M_{\eta_i}}^V &= -2 \frac{x_V \phi_i}{\bar{c}_V \bar{c}} C_{L\alpha}^V & C_{i_{\eta_j}}^V &= -2 \frac{\phi_i \phi_j}{\bar{c}_V \bar{c}} C_{L\alpha}^V \\
C_{Z_{\delta_V}}^V &= -C_{L\alpha}^V & C_{M_{\delta_V}}^V &= \frac{x_V}{\bar{c}_V} C_{L\alpha}^V & C_{i_{\delta_V}}^V &= \frac{\phi_i}{\bar{c}_V} C_{L\alpha}^V
\end{aligned} \tag{2.19}$$

In summary, after inserting numerical values into Eq. (2.19) for the vane component nondimensional derivatives, back substitution is utilized with Eqs. (2.17), (2.13), and (2.12) to fold the vane characteristics into the overall vehicle dynamic stability and control characteristics.

To assess the impact from the control vanes, Fig. 32 lists the percent change in the modified elements of the state space A matrix. Recall that some matrix elements are not pure aerodynamic stability derivatives, as one might conclude from Eq. (2.12), but rather are a combination of stability derivatives, speed terms from Coriolis accelerations, and structural compliance terms. Note some of the percent change values are extremely large due to a near zero original value. Fig. 33 lists similar information for the elements of the state space B matrix (which are all pure aerodynamic control derivatives). Since the vane control derivatives are new terms, percentage values can not be computed. Thus, elevator terms are shown for comparison.

To understand and "validate" the model adjustments from the vane, consider several of the terms in Fig. 32, along with the geometry indicated in Fig. 31 and the characteristic deflection

shapes in Fig. 28. First consider  $Z_w$  and  $M_w$ . With a positive perturbation in  $w$ , the vane force is directed up, and the resulting change in  $Z_w$  is negative (-1%), while that for  $M_w$  is positive (+2%) since the vane is forward of the mass center. Next consider the terms  $U+Z_q$  and  $M_q$  where  $U$  is defined in Appendix C. A positive perturbation in  $q$  leads to a down vane load. Consequently,  $U+Z_q$  experiences a positive change (+1%) and  $M_q$  a negative one (-168%, down load at the nose). Note  $M_q$  experiences the largest change among these four terms. This large increase is traced to the  $M_q$  dependence on the square of the lever arm ( $x_V^2$  in Eq. (2.19)), while the other terms are only proportional to  $x_V$  or 1. As an additional observation, the original relaxed stability mode (from Tab. 15 in Ref. 13) is located at +0.134 1/s in the complex plane, while the corresponding value from Tab. 1 in this report is +0.178 1/s. The destabilizing effect of the vane is thus apparent.

Now consider several stability derivatives associated with rigid-elastic coupling through aerodynamic means. Assuming a positive perturbation in  $\eta_3$  (structural nose up pitch, see Fig. 28), the vane load will be directed up, leading to a negative change in  $Z_{\eta_3}$  (-6%). On the other hand, for a positive perturbation in  $\eta_3$  (structural up plunge), the vane load is pointed down and  $M_{\eta_3}$  experiences a negative change (-21%). For a positive perturbation in  $w$ , the vane load is up and this deflects the 3<sup>rd</sup> mode shape in a positive sense (see Fig. 28), thus  $F_{3_w}$  undergoes a positive change (+4%). Finally, a positive perturbation in  $q$  yields a downward vane load inducing a negative change in  $F_{3_q}$  (-143%). This last effect is relatively large since  $F_{3_q}$  is proportional to the long moment arm and large modal deflection near the vehicle nose ( $x_V$  and  $\phi_3$ , see Eq. (2.19)).

As for control derivatives, consider the data in Fig. 33. Positive vane deflection leads to an up load and negative  $Z_{\delta_V}$  and positive  $M_{\delta_V}$  since the vane is forward of the mass center. Up load also deflects the 3<sup>rd</sup> mode shape in the positive direction leading to positive  $F_{3_{\delta_V}}$ . Data in Fig. 33 indicates vane plunge authority is of the same order of magnitude as that for elevator. Even though the vane is a much smaller surface relative to the horizontal tail, this observation can be traced to the vane being an all flying surface, while the elevator is only about 1/3 of the horizontal tail chord. Pitch authority is also roughly equivalent for the two inputs. Again, even though the vane surface area is much smaller, the lever arm for the vane is significantly larger when compared to the aft tail.

$$\text{Percent Change of A Matrix Elements} \left( \frac{A_{ij_{\text{new}}} - A_{ij_{\text{old}}}}{|A_{ij_{\text{old}}}|} \times 100 \right)$$

		$\dot{\eta}_i$																	$\eta_i$																			
w	q	1	2	3	4	5	6	7	8	9	10	11	12	13	14	15	16	17	1	2	3	4	5	6	7	8	9	10	11	12	13	14	15	16	17			
-1	1	-18	-2	4	2	2	-20	-11	-0	0	10	1	26	-0	3	-0	0	0	5	2	-6	-3	-24	2	2	0	-0	-0	-3	-1	0	-4	2	-0	-2			
2	-168	84	14	-21	-12	-13	289	62	0	-1	-1	-2	-10	2	-7	1	-0	-1	-239	-46	1237	60	37	-174	-39	-0	1	0	214	3	-1	4	-5	0	6			
1	31	90	-87	-9	41	62	10	-28	-41	-3	17	1	7	3	-1	11	-3	1	7	1	12	-29	-17	-52	12	9	60	-23	-2	-6	-6	1	-20	11	-5	-8		
2	-10	24	-15	-3	2	2	2	-276	-8	-1	2	0	2	5	-0	9	-1	0	1	57	0	-6	-5	-24	9	24	2	-2	-0	-2	-67	1	-5	1	-1	-2		
3	4	-143	132	3	-1	-1	-1	15	17	1	-2	-0	-2	-2	0	-1	10	-0	-0	-21	-4	0	11	5	-20	-25	-1	2	0	4	9	-1	3	-1	0	2		
4	4	-381	229	3	-1	-0	-1	14	14	1	-2	-0	-2	-2	0	-1	3	-0	-0	-22	-4	38	0	5	-22	-39	-1	2	0	4	8	-1	3	-1	0	1		
5	5	-9	11	2	-1	-1	-0	10	4	1	-3	-0	-1	-4	0	-1	1	-0	-0	-22	-3	3	2	0	-3	-4	-5	3	0	2	11	-0	4	-1	0	1		
6	-35	13	-19	-15	5	5	4	-9	-16	-7	33	9	5	4	-1	23	-11	1	2	69	11	-4	-4	-24	0	6	4	-15	-1	-7	-29	1	-35	15	-1	-4		
7	-16	19	-33	-31	108	50	9	-24	-4	-27	7	1	7	166	-2	5	-1	4	6	69	23	-8	-7	-26	7	0	44	-18	-1	-35	-51	3	-58	6	-6	-26		
8	-58	18	-50	-9	4	4	6	-4	-144	-0	1	0	0	0	-0	1	-3	4	2	17	8	-8	-7	-9	24	7	0	-5	-2	-4	-1	0	-9	10	-11	-24		
9	16	-27	90	5	-49	-335	-30	51	22	2	-24	-3	-2	-3	2	-4	0	-0	-7	-41	-6	21	9	8	-18	-10	-1	0	0	2	13	-1	17	-3	1	9		
10	0	-1	8	1	-0	-0	-1	1	1	1	0	-0	-6	-0	0	-0	0	-0	-1	-1	-0	0	0	0	0	-0	-0	0	0	0	0	0	0	0	0	0		
11	3	-9	12	3	-11	-8	-8	22	7	20	-69	-1	-1	-1	1	-1	0	-0	-4	-16	-4	6	4	3	-16	-4	-1	2	1	0	1	-0	2	-0	5	1		
12	1	-4	23	3	-4	-3	-10	7	7	0	-1	-0	-1	-0	0	-1	6	-0	-2	-38	-3	3	3	96	-21	-2	-0	1	0	1	0	-0	2	-1	0	2		
13	-4	1	-2	-0	1	1	0	-2	-1	-0	0	1	0	-0	1	-0	0	-1	-0	-0	-1	-0	-0	1	0	0	-0	-0	-0	-0	0	0	0	-0	-1	0		
14	24	-9	43	8	-3	-3	-3	21	8	0	-2	-2	-3	-4	0	-0	0	-0	-4	-8	-4	4	3	2	-11	-9	-0	2	0	3	1	-0	0	-0	0	-1		
15	-4	18	-125	-1	1	1	1	-2	-7	-1	1	0	2	0	-0	0	-0	0	9	93	-8	-43	-2	398	3	2	-1	-0	-0	-1	0	-0	0	-0	0	-2		
16	1	-3	3	1	-0	-0	-0	1	2	3	-1	-0	-1	-1	0	-6	0	-0	-3	-0	0	0	0	0	-1	-1	1	0	3	0	-0	1	-0	0	0			
17	7	-7	6	5	-1	-1	-1	6	9	1	-1	-0	-3	-2	0	-1	15	-0	-0	-13	-1	1	1	1	1	-2	-1	6	0	2	2	-1	1	-1	0			

Figure 32. Summary Of Stability Derivative Modifications

Actual Values  
Units: ft , s , rad

		$\delta_E$	$\delta_V$
	w	-2.1582e+00	-2.4285e+00
	q	-7.0595e-02	9.6527e-02
$\eta_i$	1	-4.0604e+03	-3.7183e+03
	2	2.5850e+03	-1.9350e+03
	3	-2.0286e+03	1.4492e+03
	4	-6.8974e+02	4.6036e+02
	5	-3.4643e+02	3.5372e+02
	6	1.8715e+03	-1.9682e+03
	7	-1.9086e+02	-1.5374e+03
	8	-1.0736e+04	-8.2493e+02
	9	-1.8711e+03	1.8122e+03
	10	-3.1457e+02	5.4043e+01
	11	-1.0017e+03	9.1599e+02
	12	1.8563e+03	4.1833e+02
	13	1.7076e+03	-1.0465e+02
	14	-5.9616e+02	5.1265e+02
	15	1.5631e-01	-1.8079e+02
	16	-9.1487e+01	2.1740e+02
	17	-7.2696e+01	3.7251e+02

Figure 33. Summary Of Control Derivative Modifications

These results "validate" the math model adjustments made to account for the vane, in the sense that each term has undergone a numerical change which possesses the correct sign, the correct magnitude, and can be tied back to the "physics". However, the fidelity of the vane model is only as good as the underlying theory, which is to first order here. Therefore, the Appendix C model characteristics will be utilized to explore new inner loop FCS architectures and control benefits offered by the vanes with these comments in mind.

## Section III

### Assessment of Wykes Mode Suppression Logic

#### A. Review of and Comment on Original Wykes Logic

Upon reflection of the demonstrated achievements of John Wykes/North American Rockwell in connection with structural mode suppression logic for the XB-70 vehicle,<sup>14,15</sup> efforts were put forth in this contract to re-examine these control strategies in the context of HSCT. Significant mode suppression accomplishments, including flight test validation of control law performance, were achieved in the XB-70 program. In particular, SMCS architectures, based on aft control incorporating two sensors, one collocated with the aerodynamic surface input, were highly successful. In light of these observations, and considering the potential impact on configuration selection and program decision making (i.e., aft tail only or aft tail supplemented with forward vanes), it was felt prudent to investigate and apply the Wykes control logic to HSCT.

In Refs. 14-15, aft control consisted of symmetric elevon deflections in the absence of a conventional tail. It is important to note the XB-70 canard was not utilized in the SMCS architectures. Other XB-70 features to keep in mind are 1) at low speeds the airframe is statically stable, 2) the rigid-body/aeroelastic modal frequency separation is approximately 10 rad/s, and 3) four structural modes exist in the frequency region below 30 rad/s. In comparison, HSCT is a considerably more modally dense and flexible vehicle (eight modes below 30 rad/s and rigid-elastic frequency separation of 6.5 rad/s). Further, the HSCT airframe has relaxed stability at low speeds. In its era, the XB-70 presented a difficult flight dynamics/structural vibration control problem, however, the HSCT configuration presents a significantly more difficult control challenge.

The Wykes SAS/SMCS XB-70 control logic, as it would be directly applied to the HSCT in its original form, is illustrated in Fig. 34. The pitch SAS loop utilizes proportional-integral (PI) compensation in the feedback path with the forward path block consisting of static compensation.



This loop is closed on the forward sensor signal (1,850 in). The SMCS loop incorporates pure gain in a feedback block which is excited by a forward sensor/tail sensor difference signal. The tail sensor is collocated with the control input and would correspond to the elevator hinge line (3,460 in) in the HSCT application. With the forward and tail rate gyro signals expressed as

$$\begin{aligned} q_{1850} &= q - \sum_i \phi_i'(1850) \dot{\eta}_i \\ q_{3460} &= q - \sum_i \phi_i'(3460) \dot{\eta}_i \end{aligned} \quad (3.1)$$

the differenced SMCS feedback signal  $q_d$  is

$$q_d = \sum_i \{ \phi_i'(3460) - \phi_i'(1850) \} \dot{\eta}_i \quad (3.2)$$

In essence, this feedback signal is devoid of rigid-body content and represents the difference between the structural pitch rates at the tail and forward sensor locations.

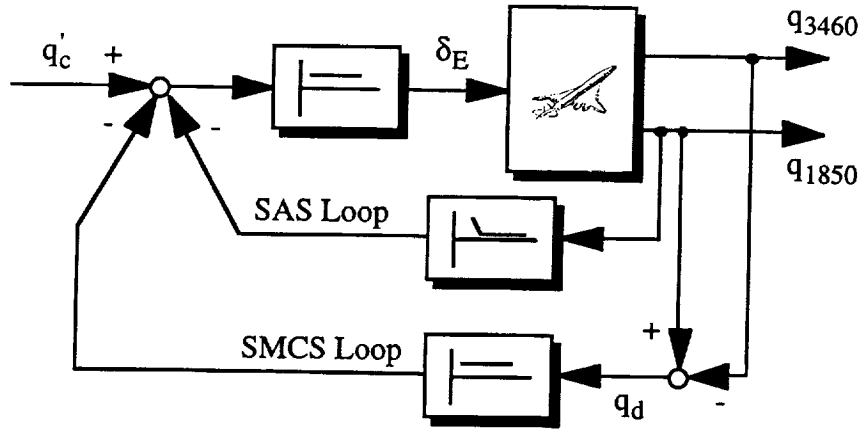


Figure 34. Original Wykes SMCS Architecture

To demonstrate why the Wykes SMCS logic is effective, to determine the conditions under which the logic can be expected to succeed, and to identify when the logic may fail, consider the polynomial matrix representation of the vehicle dynamics in Eq. (3.3), assuming two aeroelastic modes are present, the forward speed degree of freedom is negligible, and there are no actuator dynamics.

$$\underbrace{\begin{bmatrix} s - Z_w & -(U + Z_q)s & -Z_{\dot{\eta}_1}s - Z_{\eta_1} & -Z_{\dot{\eta}_2}s - Z_{\eta_2} \\ -M_w & s^2 - M_q s & -M_{\dot{\eta}_1}s - M_{\eta_1} & -M_{\dot{\eta}_2}s - M_{\eta_2} \\ -F_{1w} & -F_{1q}s & s^2 + (2\zeta_1\omega_1 - F_{1\dot{\eta}_1})s + (\omega_1^2 - F_{1\eta_1}) & -F_{1\dot{\eta}_2}s - F_{1\eta_2} \\ -F_{2w} & -F_{2q}s & -F_{2\dot{\eta}_1}s - F_{2\eta_1} & s^2 + (2\zeta_2\omega_2 - F_{2\dot{\eta}_2})s + (\omega_2^2 - F_{2\eta_2}) \end{bmatrix}}_{P(s)} \begin{bmatrix} w(s) \\ q(s) \\ \eta_1(s) \\ \eta_2(s) \end{bmatrix} = \begin{bmatrix} Z_{\delta_E} \\ M_{\delta_E} \\ F_{1\delta_E} \\ F_{2\delta_E} \end{bmatrix} \delta_E(s) \quad (3.3)$$

The  $q_d/\delta_E$  transfer function can be derived from Eq. (3.3) using linear algebra concepts, or

$$\frac{q_d(s)}{\delta_E(s)} = \frac{n_{q_d}(s)}{d(s)} = \frac{\{\phi'_1(3460) - \phi'_1(1850)\}n_{\dot{\eta}_1}(s) + \{\phi'_2(3460) - \phi'_2(1850)\}n_{\dot{\eta}_2}(s)}{d(s)} \quad (3.4)$$

$$d(s) = \det P(s)$$

$$n_{\dot{\eta}_i}(s) = s \det P_{i+2}(s) | Q(s)$$

In Eq. (3.4),  $P_{i+2}(s) | Q(s)$  denotes the matrix  $P(s)$  with the  $i+2$  column replaced with  $Q(s)$ . This transfer function represents the set of dynamics around which the SMCS logic is closed.

In the special case with no aerodynamic coupling ( $F_{1w} = F_{1q} = 0$ ,  $Z_{\eta_i} = Z_{\dot{\eta}_i} = 0$ ,  $M_{\eta_i} = M_{\dot{\eta}_i} = 0$ ,  $F_{1\eta_j} = F_{1\dot{\eta}_j} = 0$  for  $j \neq i$ ), numerator and denominator polynomials are listed in Eq. (3.5).

$$\begin{aligned} d(s) = & s \{ s^2 + (-Z_w - M_q)s + Z_w M_q - M_w(U + Z_q) \} \\ & \times \{ s^2 + (2\zeta_1\omega_1 - F_{1\dot{\eta}_1})s + (\omega_1^2 - F_{1\eta_1}) \} \{ s^2 + (2\zeta_2\omega_2 - F_{2\dot{\eta}_2})s + (\omega_2^2 - F_{2\eta_2}) \} \end{aligned} \quad (3.5)$$

$$n_{\dot{\eta}_1}(s) = F_{1\delta_E} s^2 \{ s^2 + (-Z_w - M_q)s + Z_w M_q - M_w(U + Z_q) \} \{ s^2 + (2\zeta_2\omega_2 - F_{2\dot{\eta}_2})s + (\omega_2^2 - F_{2\eta_2}) \}$$

$$n_{\dot{\eta}_2}(s) = F_{2\delta_E} s^2 \{ s^2 + (-Z_w - M_q)s + Z_w M_q - M_w(U + Z_q) \} \{ s^2 + (2\zeta_1\omega_1 - F_{1\dot{\eta}_1})s + (\omega_1^2 - F_{1\eta_1}) \}$$

In this case, the  $q_d/\delta_E$  transfer function describes pure aerodynamically damped/stiffened vibrational motion, or

$$\frac{q_d(s)}{\delta_E(s)} = \frac{s\{s^2 + (-Z_w - M_q)s + Z_w M_q - M_w(U + Z_q)\}}{\{s^2 + (-Z_w - M_q)s + Z_w M_q - M_w(U + Z_q)\}} \quad (3.6)$$

$$\times \frac{[\{\phi_1'(3460) - \phi_1'(1850)\}F_{1\delta_E}\{s^2 + (2\zeta_2\omega_2 - F_{2\eta_2})s + (\omega_2^2 - F_{2\eta_2})\} + \{\phi_2'(3460) - \phi_2'(1850)\}F_{2\delta_E}\{s^2 + (2\zeta_1\omega_1 - F_{1\eta_1})s + (\omega_1^2 - F_{1\eta_1})\}]}{\{s^2 + (2\zeta_1\omega_1 - F_{1\eta_1})s + (\omega_1^2 - F_{1\eta_1})\}\{s^2 + (2\zeta_2\omega_2 - F_{2\eta_2})s + (\omega_2^2 - F_{2\eta_2})\}}$$

With the short period poles exactly canceled by an identical factor in the numerator, the transfer function consists of two complex conjugate zeros and one zero at the origin, divided by the 1<sup>st</sup> and 2<sup>nd</sup> aeroelastic modes.

The sensor location and generalized force characteristics inherent to the Wykes SMCS feedback signal  $q_d$  in Eq. (3.2) strongly influences the location of the complex conjugate zeros in Eq. (3.6). Root locus concepts can be utilized to assess and understand this relationship. From Eq. (3.6), the complex conjugate zeros are governed by the equation

$$1 + \frac{\{\phi_1'(3460) - \phi_1'(1850)\}F_{1\delta_E}\{s^2 + (2\zeta_2\omega_2 - F_{2\eta_2})s + (\omega_2^2 - F_{2\eta_2})\}}{\{\phi_2'(3460) - \phi_2'(1850)\}F_{2\delta_E}\{s^2 + (2\zeta_1\omega_1 - F_{1\eta_1})s + (\omega_1^2 - F_{1\eta_1})\}} = 0 \quad (3.7)$$

With Eq. (3.7), these zeros can be thought of as originating from the 1<sup>st</sup> aeroelastic mode root locations and transitioning towards the 2<sup>nd</sup> aeroelastic mode root locations as the parameter  $\{\phi_1'(3460) - \phi_1'(1850)\}F_{1\delta_E} / \{\phi_2'(3460) - \phi_2'(1850)\}F_{2\delta_E}$  is increased. An illustration of this root migration is given in Fig. 35. If the 1<sup>st</sup> and 2<sup>nd</sup> aeroelastic modes are lightly damped, and the varying parameter is positive, utilization of basic root locus sketching rules indicate a departure angle (for the  $+j\omega$  root) of approximately  $+90$  deg. The migration paths are nearly vertical straight paths.

With these results, the effectiveness of the Wykes SMCS logic becomes clear. Consider closing the SMCS loop indicated in Fig. 34 around the  $q_d/\delta_E$  transfer in Eq. (3.6). Augmentation of the structural modes is shown in Fig. 36. Damping of both aeroelastic modes is increased as the 1<sup>st</sup> mode roots migrate towards the zero at the origin, and the 2<sup>nd</sup> mode roots migrate towards the

complex conjugate zeros. The effectiveness of this loop is due to the interlaced pole-zero pattern along the imaginary axis, which leads to +180 deg departure angles from the open-loop root locations. This basic effect was discovered and exploited over 30 years ago.

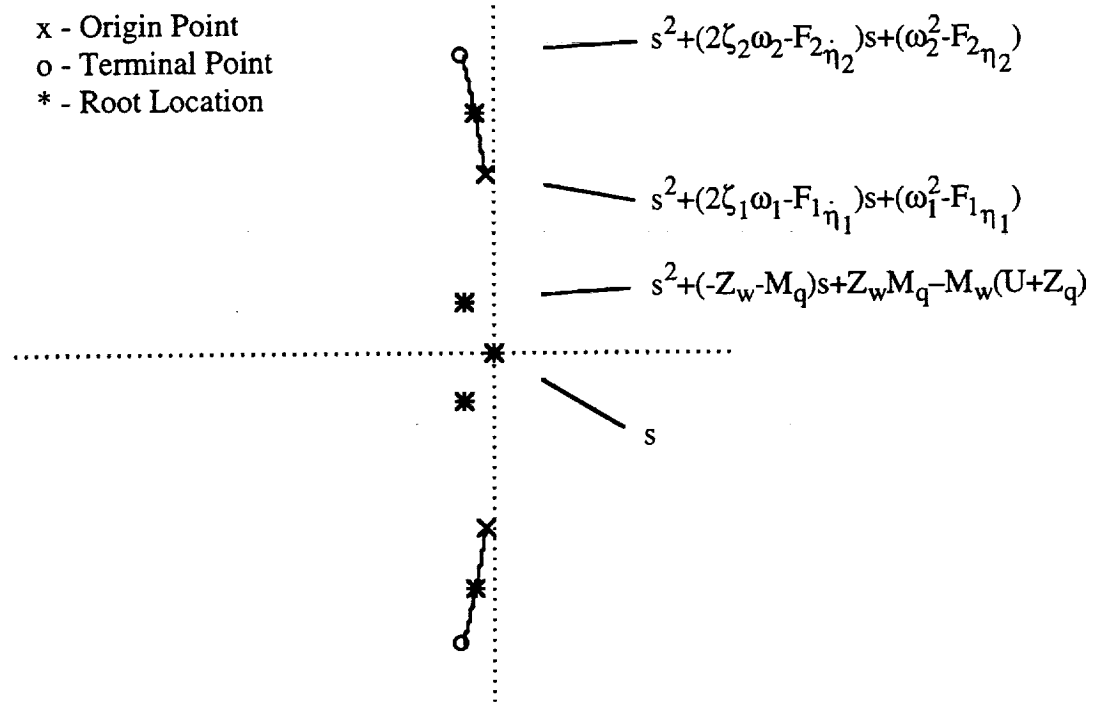


Figure 35. Airframe  $n_{qd}(s)$  Root Migration Paths  
Without Aerodynamic Coupling – Eq. (3.7)

The key to the pole-zero interlacing pattern in Fig. 36 is the collocated sensor-surface pair and associated likelihood the parameter  $\{\phi_1'(3460) - \phi_1'(1850)\} F_{1\delta_E} / \{\phi_2'(3460) - \phi_2'(1850)\} F_{2\delta_E}$  will be of positive sign. It is also important to note the numerator structure in Eq. (3.6) results from signal differencing as shown in Fig. 34. Referring back to the structure in Eqs. (2.13)-(2.19) for aeroelastic control derivatives,  $F_{1\delta_E}$  and  $F_{2\delta_E}$  are given by

$$F_{1\delta_E} = \frac{\bar{q} \bar{S}_H \phi_1(3460) C_{L\delta_E}^H}{m_1} \quad (3.8)$$

$$F_{2\delta_E} = \frac{\bar{q} \bar{S}_H \phi_2(3460) C_{L\delta_E}^H}{m_2}$$

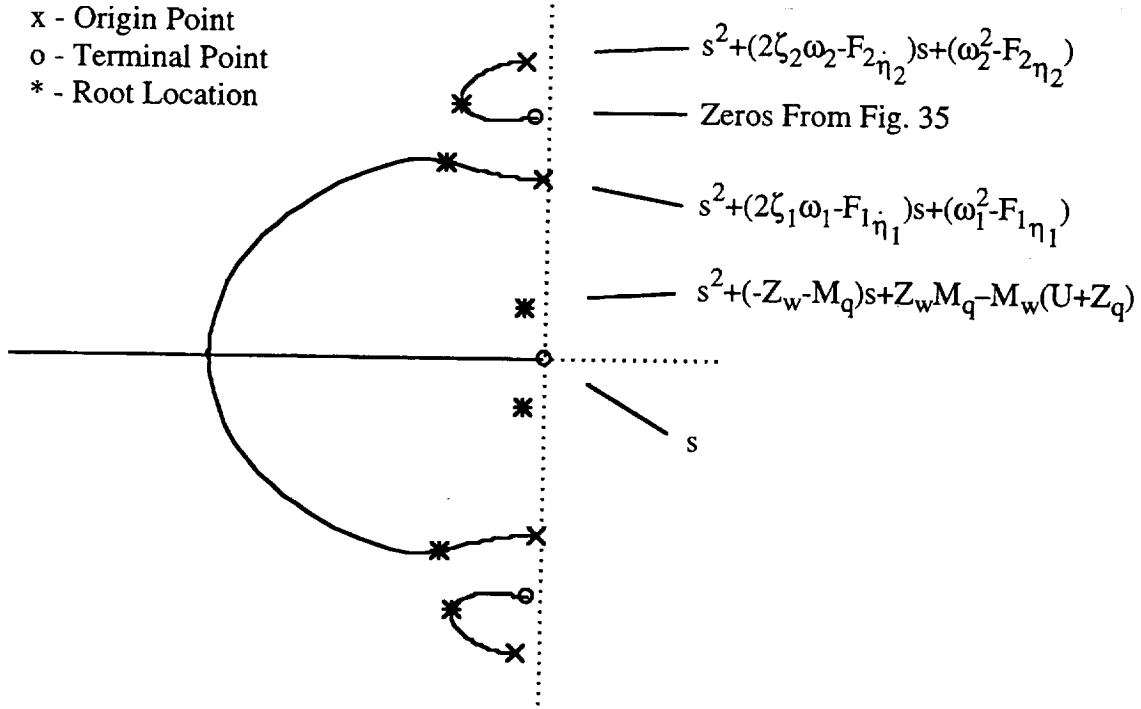


Figure 36. Closed – Loop  $d(s) + kn_{qd}(s)$  Root Migration Paths  
Without Aerodynamic Coupling – Fig. 34

Eq. (3.7) thus becomes

$$1 + \frac{\{\phi_1'(3460) - \phi_1'(1850)\} \frac{\phi_1(3460)}{m_1} \{s^2 + (2\zeta_2\omega_2 - F_2\eta_2)s + (\omega_2^2 - F_2\eta_2)\}}{\{\phi_2'(3460) - \phi_2'(1850)\} \frac{\phi_2(3460)}{m_2} \{s^2 + (2\zeta_1\omega_1 - F_1\eta_1)s + (\omega_1^2 - F_1\eta_1)\}} = 0 \quad (3.9)$$

Assuming the mode slopes at 1,850 in are small, the parameter is composed of the paired products  $\phi_i'\phi_i$  at the same fuselage station. At forward and aft regions along the vehicle centerline, the modal slope and deflection values are of the same sign leading to a positive parameter value. At other locations this may not be the case, but is of little hindrance since SMCS surfaces will be located forward or aft to maximize control leverage on the modes. Recalling the HSCT modal deflection data in Fig. 28,  $\phi_i'(3460)$  and  $\phi_i(3460)$  are of the same sign for the eight modes displayed. This slope-deflection parameter mismatch issue can be avoided if acceleration-based feedback signals are utilized (i.e.,  $\phi_i\phi_i$ ). In this case, however, rigid-body content in the feedback signal can not be fully eliminated by the differencing scheme in Fig. 34.

If the mode slope values in Eq. (3.9) at 3,460 in dominate the values at 1,850 in, the root locus parameter will be positive. One path to this result is to locate the second feedback sensor near the mid fuselage stations where slopes are minimal, such as at the anti-node of the 1<sup>st</sup> aeroelastic mode (1,850 in). However, for a vehicle with many significant modes, this sensor will pick-up the structural rotations of the higher frequency modes. The consequences are the pole-zero interlaced pattern along the imaginary axis will be perturbed, destroying the effectiveness of the Wykes SMCS logic in augmenting aeroelastic mode dampings. In this case, aeroelastic mode zeros can be out of sequence along the imaginary axis, they can be significantly offset from the vertical structure, and they can even present nonminimum phase characteristics. Based on these observations, one conclusion drawn is the Wykes SMCS logic, as implemented in Fig. 34, may not be effective in augmenting all aeroelastic modes, and in fact may destabilize some of the modes, when applied to a vehicle characterized as modally dense.

As a footnote, one means to avoid the parameter structure  $\{\phi_i'(\text{tail}) - \phi_i'(\text{fore})\} \phi_i(\text{tail})$  in Eq. (3.9) is simply to implement a SMCS loop without differencing two signals. In other words, use a collocated sensor and surface, dropping the second sensor. This strategy has been utilized in the control architectures presented in Section IV, and is very effective. The feedback signal will inherently have rigid-body content and can be used to an advantage in some cases, such as simultaneous stabilization of rigid-body pitch instabilities, for example.

The above development has all been under the assumption of no aerodynamic coupling. Strong aerodynamic coupling effects are another mechanism which can dilute the attractiveness of the Wykes SMCS logic. To demonstrate these effects, return to the vehicle model in Eq. (3.3). For ease of demonstration, consider a case with, not full, but limited aerodynamic coupling where  $F_{1q}$  is the main, but not only, parameter of interest. Assuming aeroelastic-to-rigid coupling is present ( $Z_{\eta_i}, Z_{\dot{\eta}_i}, M_{\eta_i}, M_{\dot{\eta}_i} \neq 0$ ), partial rigid to elastic coupling is present ( $F_{i_w} = F_{2q} = 0, F_{1q} \neq 0$ ), and no elastic to elastic coupling ( $F_{i\eta_j} = F_{i\dot{\eta}_j} = 0$  for  $j \neq i$ ), the numerator and denominator polynomials in Eq. (3.4) are

$$d(s) = s\{s^2 + (-Z_w - M_q)s + Z_w M_q - M_w(U + Z_q)\} \quad (3.10)$$

$$\times \{s^2 + (2\zeta_1 \omega_1 - F_{1\dot{\eta}_1})s + (\omega_1^2 - F_{1\eta_1})\} \{s^2 + (2\zeta_2 \omega_2 - F_{2\dot{\eta}_2})s + (\omega_2^2 - F_{2\eta_2})\}$$

$$- F_{1q} s \{M_{\dot{\eta}_1}(s - Z_w)(s + \frac{M_{\eta_1}}{M_{\dot{\eta}_1}}) + M_w Z_{\dot{\eta}_1}(s + \frac{Z_{\eta_1}}{Z_{\dot{\eta}_1}})\} \{s^2 + (2\zeta_2 \omega_2 - F_{2\dot{\eta}_2})s + (\omega_2^2 - F_{2\eta_2})\}$$

$$n_{\dot{\eta}_1}(s) = F_{1\delta_E} s^2 \{s^2 + (-Z_w - M_q)s + Z_w M_q - M_w(U + Z_q)\} \{s^2 + (2\zeta_2 \omega_2 - F_{2\dot{\eta}_2})s + (\omega_2^2 - F_{2\eta_2})\}$$

$$+ F_{1q} s^2 \{[M_{\delta_E}(s - Z_w) + M_w Z_{\delta_E}] \{s^2 + (2\zeta_2 \omega_2 - F_{2\dot{\eta}_2})s + (\omega_2^2 - F_{2\eta_2})\}$$

$$- F_{2\delta_E} \{M_{\dot{\eta}_2}(s - Z_w)(s + \frac{M_{\eta_2}}{M_{\dot{\eta}_2}}) + M_w Z_{\dot{\eta}_2}(s + \frac{Z_{\eta_2}}{Z_{\dot{\eta}_2}})\}]$$

$$n_{\dot{\eta}_2}(s) = F_{2\delta_E} s^2 \{s^2 + (-Z_w - M_q)s + Z_w M_q - M_w(U + Z_q)\} \{s^2 + (2\zeta_1 \omega_1 - F_{1\dot{\eta}_1})s + (\omega_1^2 - F_{1\eta_1})\}$$

$$- F_{1q} s^2 [F_{2\delta_E} \{M_{\dot{\eta}_1}(s - Z_w)(s + \frac{M_{\eta_1}}{M_{\dot{\eta}_1}}) + M_w Z_{\dot{\eta}_1}(s + \frac{Z_{\eta_1}}{Z_{\dot{\eta}_1}})\}]$$

In this quasi-general case, the dynamics are considerably more complicated.

Root locus concepts can again be utilized to assess and understand aerodynamic coupling effects on the transfer function factors. For example, to investigate the effect of aerodynamic coupling upon the vehicle poles, consider  $d(s)$  in Eq. (3.10). Fundamentally, the question here is "How does the 2nd term containing  $F_{1q}$  affect the roots of the 1st term?" A subset of the roots of the second term alone are given by

$$1 + M_w \frac{Z_{\dot{\eta}_1}}{M_{\dot{\eta}_1}} \frac{(s + \frac{Z_{\eta_1}}{Z_{\dot{\eta}_1}})}{(s - Z_w)(s + \frac{M_{\eta_1}}{M_{\dot{\eta}_1}})} = 0 \quad (3.11)$$

and Fig. 37 shows an example migration with variations in  $M_w$ . With  $F_{1q}$  as the main aerodynamic coupling parameter of interest, a subset of the vehicle poles are thus governed by

x - Origin Point  
o - Terminal Point  
\* - Root Location

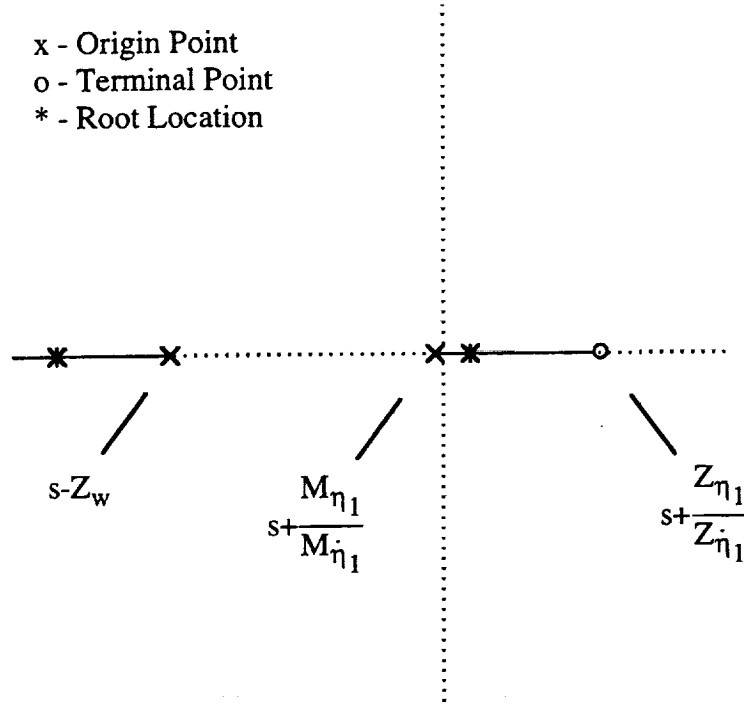


Figure 37. Intermediate Root Migration Paths  
With Aerodynamic Coupling - Eq. (3.11)

$$1 - F_{1q} \frac{M_{\dot{\eta}_1}(s - Z_w)(s + \frac{M_{\eta_1}}{M_{\dot{\eta}_1}}) + M_w Z_{\dot{\eta}_1}(s + \frac{Z_{\eta_1}}{Z_{\dot{\eta}_1}})}{\{s^2 + (-Z_w - M_q)s + Z_w M_q - M_w(U + Z_q)\} \{s^2 + (2\zeta_1 \omega_1 - F_{1\dot{\eta}_1})s + (\omega_1^2 - F_{1\eta_1})\}} = 0 \quad (3.12)$$

and Fig. 38 shows an example migration with variations in  $F_{1q}$ . Observations from Fig. 38 and Eqs. (3.11)-(3.12) are the short period poles lose damping due to the presence of coupling, specifically along the path  $q \rightarrow F_{1q} \rightarrow \eta_1 \rightarrow M_{\eta_1} \rightarrow q$  ( $F_{1q} M_{\eta_1}$ ), and for the same reason the 1<sup>st</sup> aeroelastic poles gain damping. Of more importance here is the effect on the interlaced pole-zero pattern. The root locations displayed in Fig. 38 will become new originating points for the root migration paths displayed in Fig. 36. Near imaginary axis migration contours can be highly sensitive to the originating points, and may be altered in an unfavorable manner. These alterations may significantly influence how individual modes are augmented.

This type of analysis can be conducted for the numerators as well. Observe the second term involving  $F_{1q}$  appearing in  $n_{\eta_2}(s)$  in Eq. (3.10). This term has identical factors as those found in the expression for  $d(s)$ . Therefore, Eq. (3.11) and Fig. 37 are also applicable for



determining the intermediate roots of this 2nd term as  $M_w$  is adjusted. When the 1st and 2nd terms of  $n_{\eta_2}(s)$  are combined, Eq. (3.12) also becomes applicable for assessing how the roots of  $n_{\eta_2}(s)$  are affected by the aerodynamic coupling term  $F_{1q}$ . These effects are shown in Fig. 39. Finally, the root locations displayed in Fig. 39 will become new originating points for the root migration paths displayed in Fig. 35. Undesirable impacts upon the interlaced pole-zero pattern are again possible. This example has concentrated on a single aerodynamic coupling term  $F_{1q}$ . Many other coupling terms are present in the full vehicle dynamic model. These aerodynamic coupling terms, and the physical mechanisms they represent, provide abundant means to alter and distort the interlaced pole-zero pattern of the simplified case. When the SMCS loop is closed on such a transfer function, there may be several aeroelastic modes which are destabilized. Therefore, a second conclusion drawn is the Wykes SMCS logic illustrated in Fig. 34 may not be effective when applied to a vehicle exhibiting strong aerodynamic coupling effects.

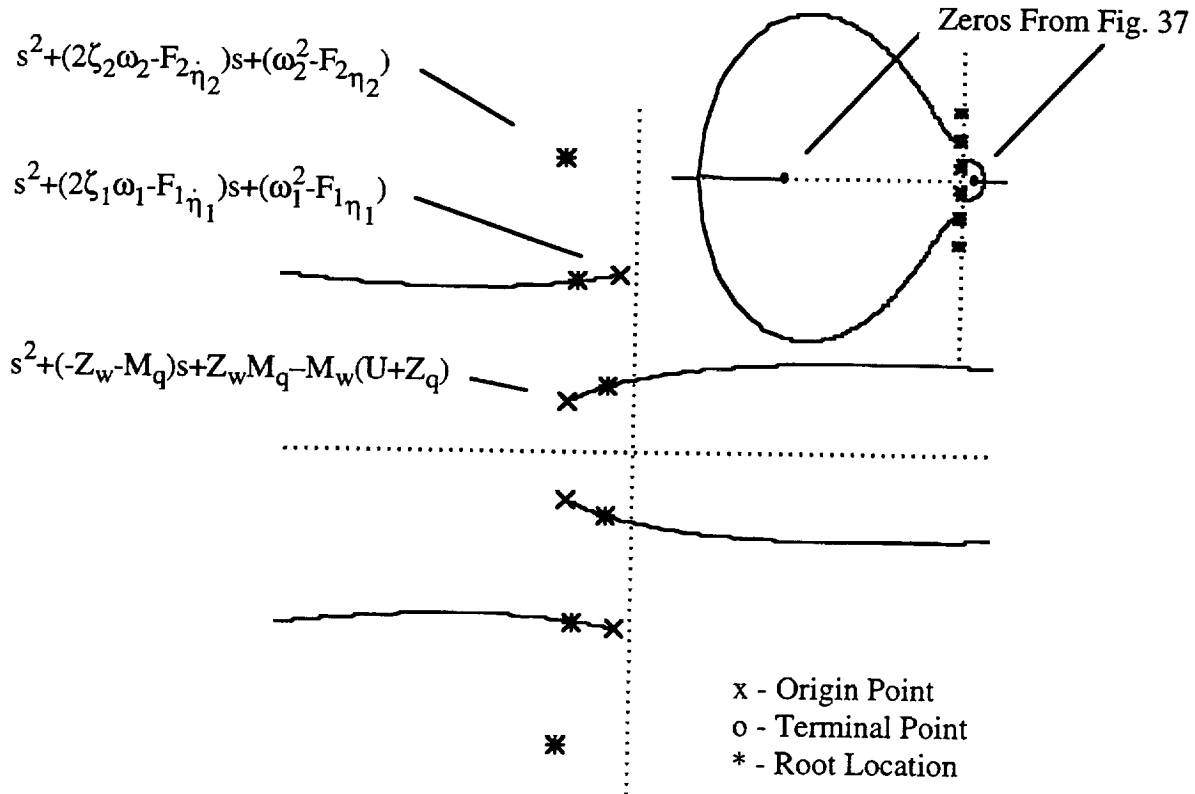


Figure 38. Airframe  $d(s)$  Root Migration Paths  
With Aerodynamic Coupling - Eq. (3.12)

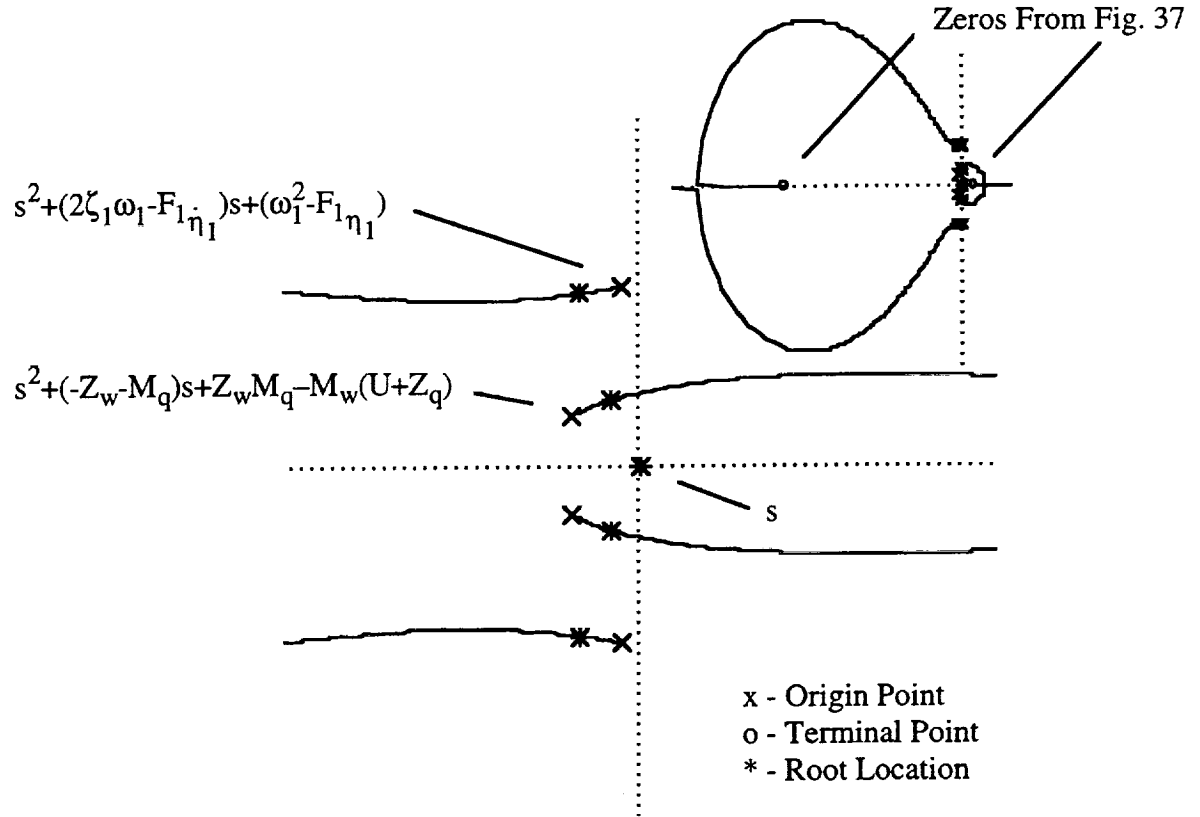


Figure 39. Airframe  $n_{\eta_2}(s)$  Root Migration Paths  
With Aerodynamic Coupling – Eq. (3.12)

Other sources of potential breakdown in the Wykes aeroelastic damping behavior of Fig. 36, which are absent from the example dynamics in Eq. (3.3), include actuator dynamics and unsteady aerodynamics. These dynamics appear as additional poles and zeros along the real axis in Fig. 36. Although no direct impact occurs on the imaginary axis interlacing pattern, these additional modes can profoundly influence the departure angles near this axis. If the actuation hardware is of poor quality, or the transient airflow behavior is significant, feedback destabilization effects can result from these sources.

## B. Wykes Logic Recast in Multi-Sensor/Single-Surface Framework

Ref. 13 examined in detail the feasibility of an aft tail only inner loop FCS architecture for HSCT. Results strongly indicated this architecture lacked ability to meet requirements associated with simultaneous augmentation of pitch motions and suppression of aeroelastic vibrations. Further, this architecture did not provide sufficient control of crew station motions. Fig. 40 indicates the MS/SS architectures that were considered in Ref. 13. In these studies, the forward path compensator block consisted of PI logic acting on a blended pitch rate signal. This PI compensation exudes an effective means for stabilizing the relaxed stability mode and providing a conventional, well-damped pitch mode. In addition, this compensation leads to a pitch rate command response type system. The feedback blocks serve as blending filters to exploit the desirable characteristics of the low frequency forward sensor signal (1,850 in) and the higher frequency characteristics of the aft sensor signal (2,500 in, fore and aft refer to location relative to the mass center at 2,152 in). Therefore, low-pass/band-pass and lag-lead/lead-lag filters were considered for these blocks, as indicated in Fig. 40. The forward and aft sensor locations were judiciously chosen to eliminate, or minimize, certain undesirable aeroelastic contamination effects in the feedback signal. Closed-loop results for these systems can be found in Ref. 13.

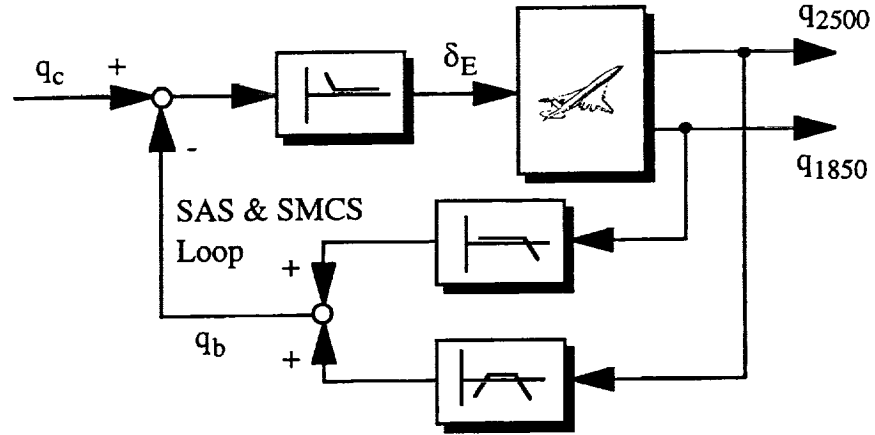
The Wykes SAS/SMCS XB-70 control logic, in the original form as displayed in Fig. 34, can be reformulated in terms of an equivalent MS/SS architecture, similar to that of Fig. 40. Block diagram manipulations can be used to convert the system in Fig. 34 to the MS/SS structure in Fig. 40. Here, algebraic manipulation of the feedback law will be utilized to generate the same result. In reference to Fig. 34, denote the feedforward, SAS, and SMCS compensation blocks as

$$\begin{aligned} K_{FF}(s) &= k_{FF} & , & & k_{FF} > 0 \\ K_{SAS}(s) &= k_{SAS} \frac{(s + z_{SAS})}{s} & , & & k_{SAS} < 0 \\ K_{SMCS}(s) &= k_{SMCS} & , & & k_{SMCS} > 0 \end{aligned} \quad (3.13)$$

The control law used to drive elevator deflection is

$$\delta_E(s) = K_{FF}(s) \{ q_c'(s) - K_{SAS}(s) q_{1850}(s) - K_{SMCS}(s) [q_{1850}(s) - q_{3460}(s)] \} \quad (3.14)$$

### MS/SS Architecture With Low Pass & Band Pass Blending



### MS/SS Architecture With Lag-Lead & Lead-Lag Blending

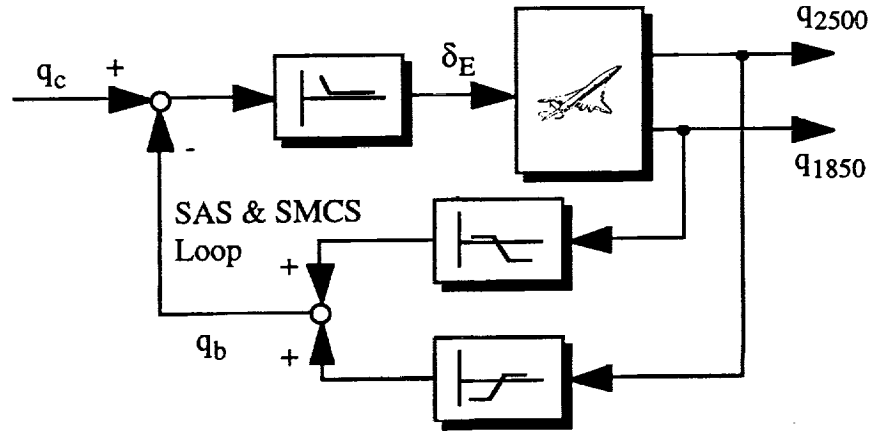


Figure 40. MS/SS Architectures Previously Analyzed

Factoring out the PI compensation term  $K_{SAS}(s)$  for the forward path yields

$$\begin{aligned} \delta_E(s) = & K_{FF}(s)K_{SAS}(s)\left\{\frac{1}{K_{SAS}(s)}q'_c(s)\right. \\ & \left.- q_{1850}(s) - \frac{1}{K_{SAS}(s)}K_{SMCS}(s)[q_{1850}(s) - q_{3460}(s)]\right\} \end{aligned} \quad (3.15)$$

Eq. (3.15) has a direct one to one correlation with the MS/SS architecture. Let  $q_c$  be the new command signal,  $K(s)$  the forward path compensator, and  $H_1(s)$  and  $H_2(s)$  the blending filters, or

$$q_c(s) = \frac{1}{K_{SAS}(s)} q'_c(s)$$

$$K(s) = K_{FF}(s)K_{SAS}(s) = k_{FF}k_{SAS} \frac{(s + z_{SAS})}{s} = k \frac{(s + z)}{s} \quad (3.16)$$

$$H_1(s) = 1 + \frac{1}{K_{SAS}(s)} K_{SMCS}(s) = (1 + \frac{k_{SMCS}}{k_{SAS}}) \frac{(s + z_{SAS}/\{1 + \frac{k_{SMCS}}{k_{SAS}}\})}{(s + z_{SAS})} = h_1 \frac{(s + z_1)}{(s + p_1)}$$

$$H_2(s) = -\frac{1}{K_{SAS}(s)} K_{SMCS}(s) = -\frac{k_{SMCS}}{k_{SAS}} \frac{s}{(s + z_{SAS})} = h_2 \frac{s}{(s + p_2)}$$

where  $p_1 = p_2 = z$ . The final architecture is indicated in Fig. 41 where explicit actuator dynamics  $A(s)$  are re-introduced.

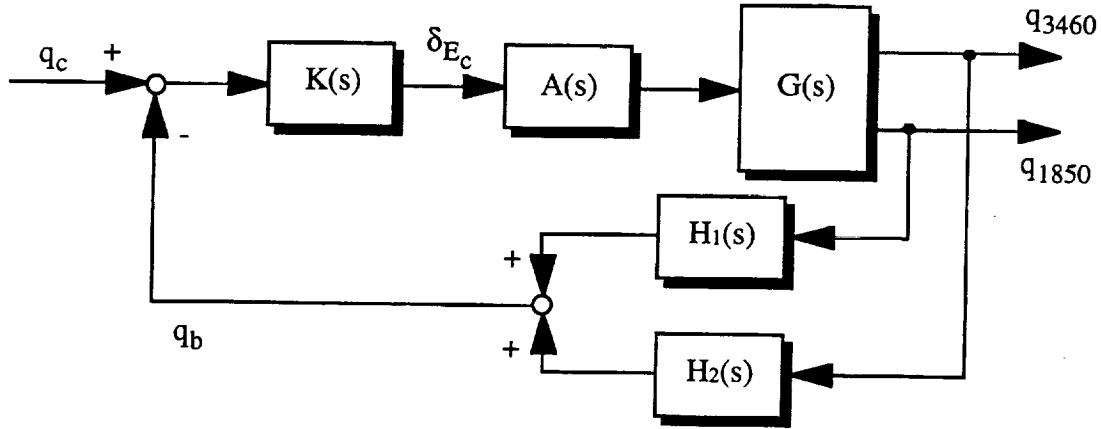


Figure 41. Wykes SMCS Logic Recast In MS/SS Framework

This control logic is efficiently parameterized by three variables: the PI zero location (which also corresponds to the blending filter poles)  $z_{SAS} = z = p_1 = p_2$ , the forward path gain  $k_{FF}k_{SAS} = k$ , and the key ratio between the strengths of the SMCS and SAS loops  $k_{SMCS}/k_{SAS}$ . For specified values of  $z$  and  $k$ , a family of blending functions is parameterized over the range  $-1 \leq k_{SMCS}/k_{SAS} \leq 0$ . Fig. 42 illustrates this parameterization. For  $k_{SMCS}/k_{SAS} = 0$ ,  $H_1(s)$  becomes all pass,  $H_2(s)$  becomes no pass and only SAS functions are extracted from the control architecture. With  $k_{SMCS}/k_{SAS} = -1$ ,  $H_1(s)$  is low pass,  $H_2(s)$  is high pass and both SAS and SMCS functions of equal strength are implemented. At intermediate values of  $k_{SMCS}/k_{SAS}$ , the SAS function is not fully attenuated at high frequency (lag-lead) and the SMCS function operates at reduced levels of strength or intensity (high pass with dc levels below 0 db).

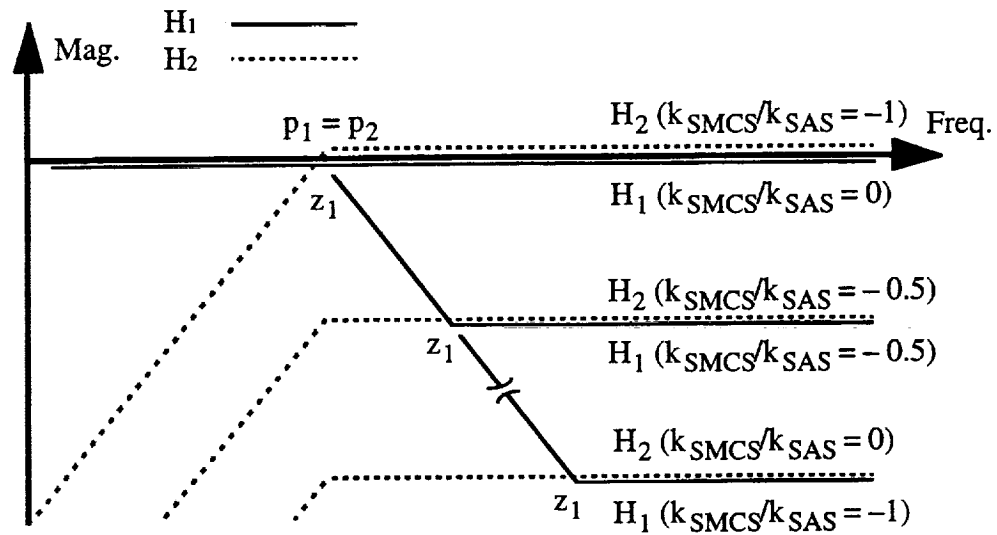


Figure 42. Parameterization Of The Blending Family

The Wykes SMCS logic thus equates to lag-lead and high pass blending of the two feedback signals when formulated in the MS/SS architecture. This type of blending strategy was not discussed in Ref. 13. Further, utilization of the tail sensor signal was not reported on in Ref. 13. The reasoning for this will become clear in Section III-C. Attention will now be focused on applying this reformulated Wykes SMCS logic to the HSCT vehicle.

### C. Wykes Logic Applied to HSCT

In this subsection, the reformulated Wykes controller is applied to the HSCT vehicle. Therefore, reconsider the MS/SS architecture depicted in Fig. 41, and the dynamic blocks given by Eq. (3.16). The methodology behind the reformulated Wykes SAS/SMCS control law is to blend the beneficial characteristics of the forward and tail sensor signals, and avoid any undesirable features that may be inherent within these signals, specifically utilizing lag-lead and high pass filtering. With the filter structures specified a priori, the only remaining task is to determine acceptable values for the break points and gains in  $K(s)$ ,  $H_1(s)$ , and  $H_2(s)$ . However, to better understand the inherent characteristics within the forward and tail feedback signals which are to be blended, initial consideration will focus on each feedback signal separately.

By taking  $h_1 = 1$ ,  $z_1 = p_1$ , and  $h_2 = 0$  in Eq. (3.16), the MS/SS system becomes a SS/SS system with  $q_{1850}$  as the feedback signal. The Evans plot for such a system is shown in Fig. 43 with  $z = 2$  1/s. Observe how the unstable real axis pole is driven into  $1/\tau_{\theta 1}$ , which resides slightly in the left-half plane, and how the mid period mode moves out to become the dominant pitch mode with potential for high levels of damping. By utilizing the sensor at the anti-node of mode 1, the 1<sup>st</sup> aeroelastic poles are accompanied with nearby zeros, effectively canceling this mode in the signal as it travels around the loop, regardless of the loop gain. At the higher frequency aeroelastic modes, the 1,850 in location is not conducive to a good feedback signal. Note the 1,850 in rate gyro leads to "out of phase" pick-up of the 2<sup>nd</sup>, 3<sup>rd</sup>, and 6<sup>th</sup> modes. As the loop gain is increased, these modes lose damping and foretell hard instabilities. These characteristics noted in Fig. 43 correlate with the mode slopes in Fig. 28.

The closed-loop poles in Fig. 43 are highlighted for a compensator gain value of  $k = -4.52$  rad/rad/s. Fig. 44 shows the corresponding Bode plot for this gain. The real axis instability is just stabilized, as indicated by the dc gain of 0 db in Fig. 44 and the closed-loop pole at the origin in Fig. 43. The rigid-body gain crossover point (see Fig. 44) is not sufficient to meet pitch damping, frequency, and phase margin requirements. Also note from the Bode the aeroelastic peak occurring at 20 rad/s, which corresponds to mode 6. This peak just touches the 0 db level with a

corresponding phase value near  $-180$  deg. At this loop gain value, the 6<sup>th</sup> mode has violated the 8 db/60 deg stability margin requirements, and is on the verge of instability (see mode 6 on the  $j\omega$  axis in Fig. 43). The unacceptable trades noted here between low frequency flying qualities and aeroelastic stability margins were also observed in Ref. 13.

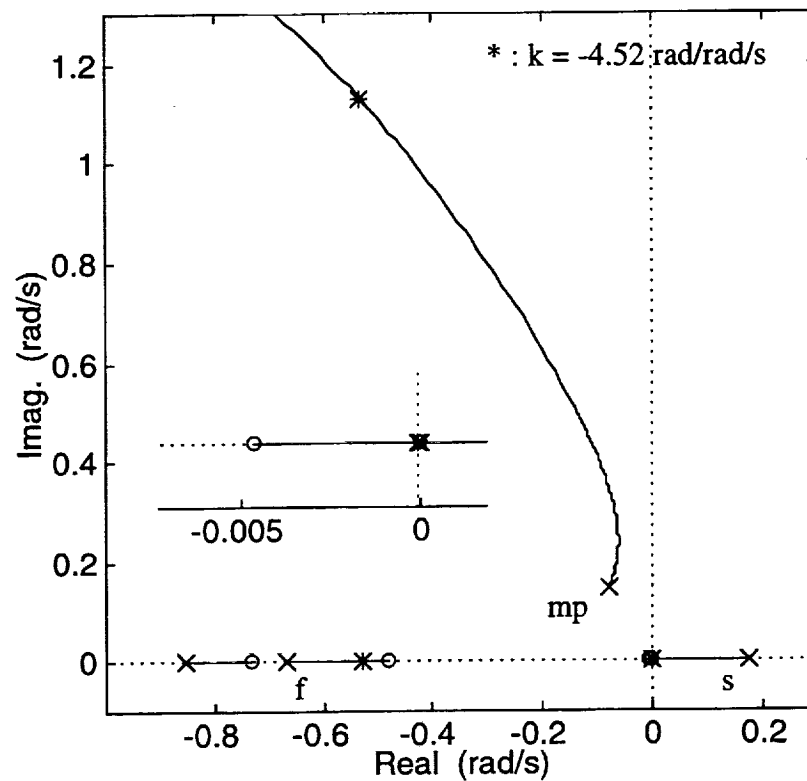


Figure 43. Evans Plot For 1,850 in Pitch Rate To Elevator



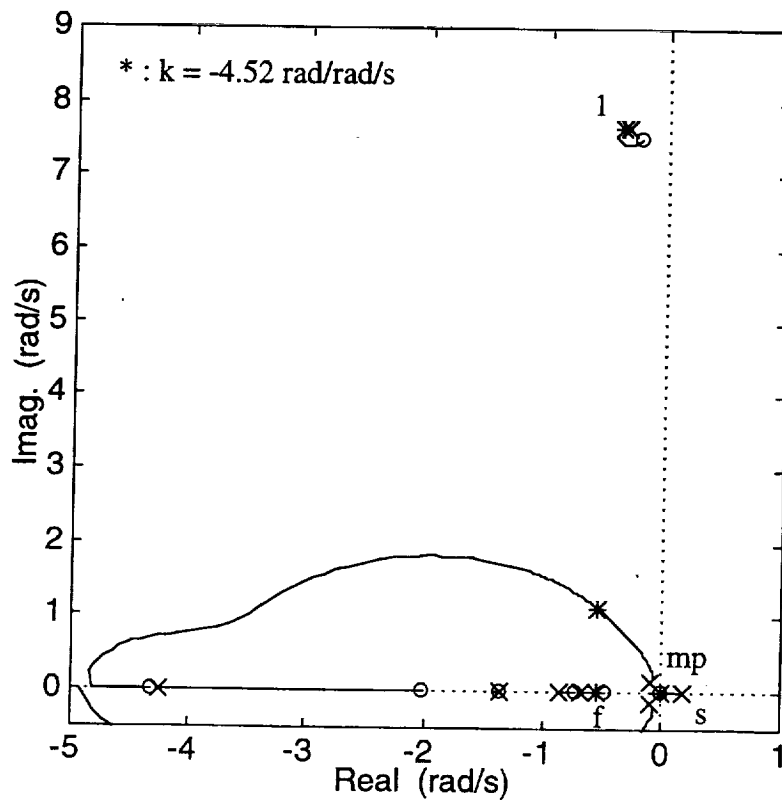
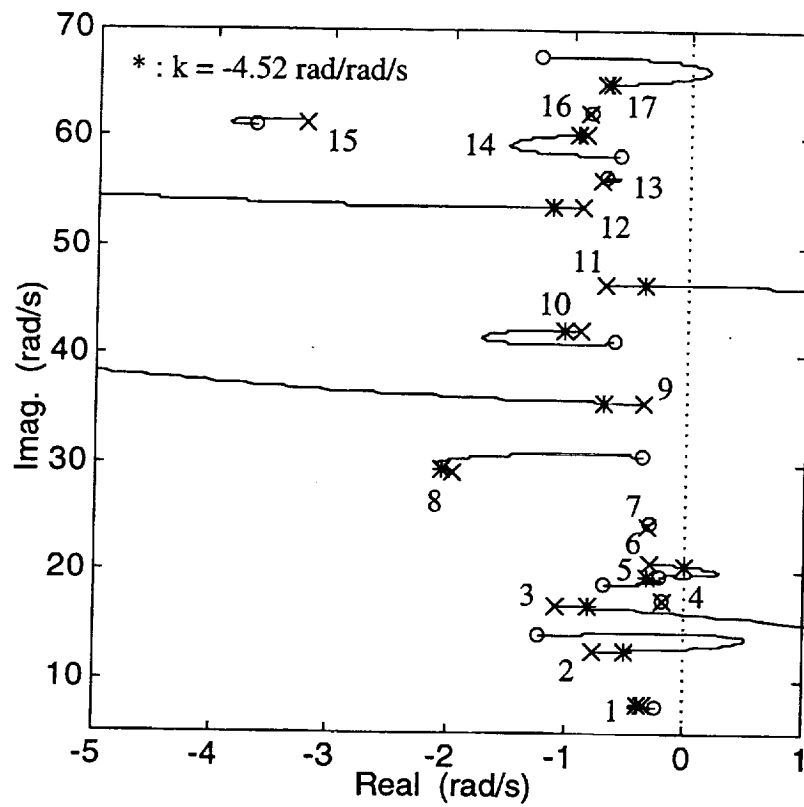


Figure 43. Continued

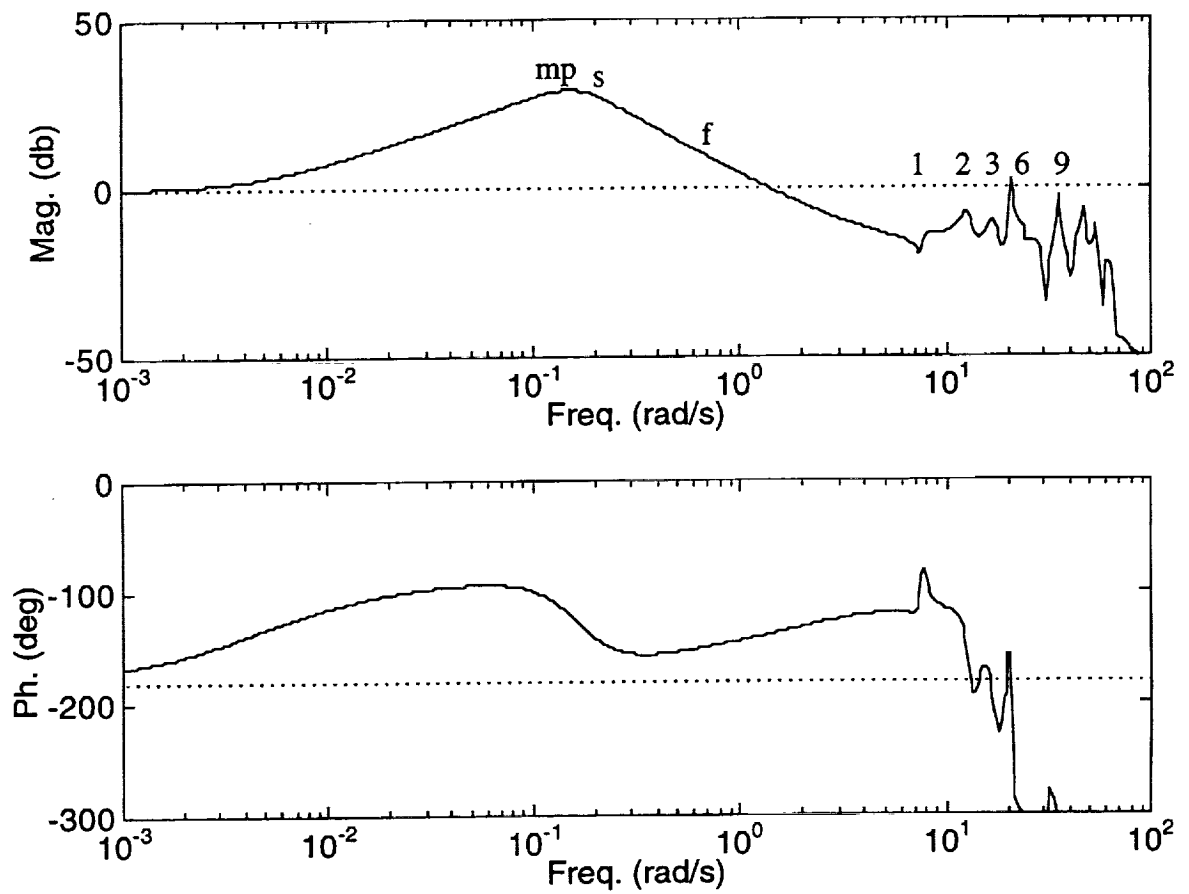


Figure 44. Bode Plot For 1,850 in Pitch Rate To Elevator,  
 $k = -4.52$  rad/rad/s

Now consider only the tail signal  $q_{3460}$  by taking  $h_2 = 1$ ,  $p_2 = 0$ , and  $h_1 = 0$  in Eq. (3.16). The Evans plot for this signal, again with  $z = 2$  1/s, is shown in Fig. 45. Due to the collocated rate gyro and surface, each aeroelastic mode up to mode 9 is now accompanied by an associated pair of zeros forming an approximate interlaced pattern. These modes are stabilized and their dampings are favorably augmented, or are unaffected, as the loop gain is increased. Note the 1<sup>st</sup> aeroelastic dipole structure has opened up considerably allowing the potential for increased damping. However, due to aerodynamic coupling, modes 10-11 are destabilized (examination of the modal data indicates  $\phi_i \phi_i'$  are of the same sign for modes 10-11). At lower frequencies, the unstable real axis pole again moves into  $1/\tau_{\theta 1}$ , and the mid period mode moves out to become the dominant pitch mode. However, with the tail sensor, the mid period mode does not wrap around the compensator zero ( $-2$  1/s in Fig. 45) towards the real axis, but moves instead towards a pair of complex conjugate zeros located near the imaginary axis. Note the limited amount of damping that can be added to the mid period mode due to the loci initially moving out radially from the origin.

The closed-loop poles in Fig. 45 are highlighted for a value of compensator gain  $k = -4.27$  rad/rad/s. Fig. 46 shows the corresponding Bode plot for this gain. The real axis instability is again just stabilized (dc gain of 0 db in Fig. 46 and closed-loop pole at the origin in Fig. 45). Rigid-body gain crossover must be increased to meet pitch damping, frequency, and phase margin requirements. From the Bode, the 1<sup>st</sup> aeroelastic peak occurring at 7.7 rad/s is well above the 0 db level, but an ample phase buffer from -180 deg is present at this frequency. Here, modes 1-9 are phase stable (i.e., the loop transfer pierces the unit circle, but away from -180 deg). This feature corresponds to the -180 deg departure angles seen in the Evans plot. In contrast, with  $k = -4.27$  rad/rad/s, the 10<sup>th</sup> and 11<sup>th</sup> aeroelastic modes are just destabilized. The peaks just touch the 0 db level with a corresponding phase value near -180 deg.

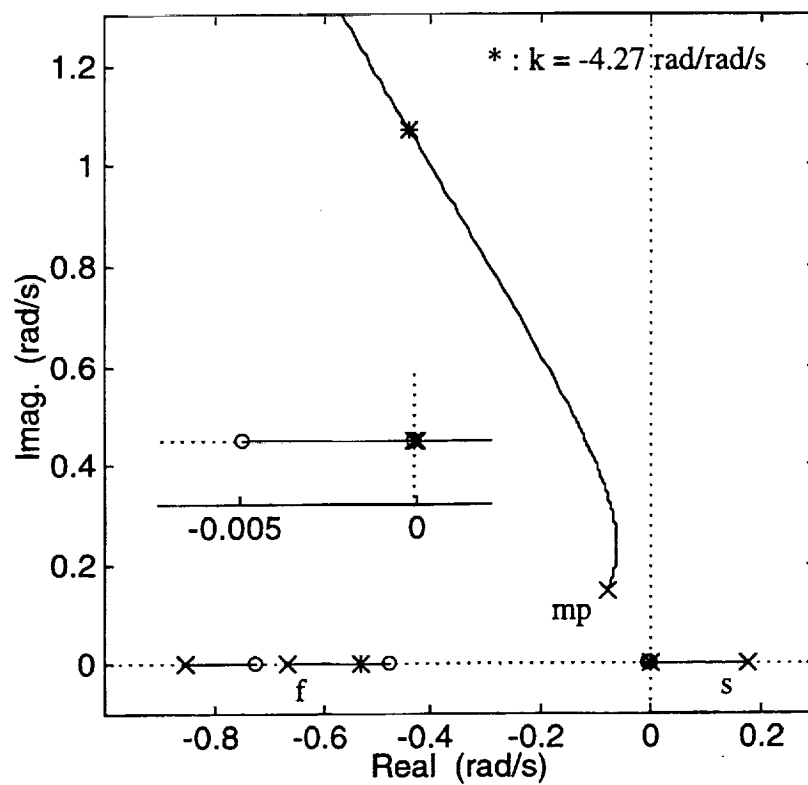


Figure 45. Evans Plot For 3,460 in Pitch Rate To Elevator

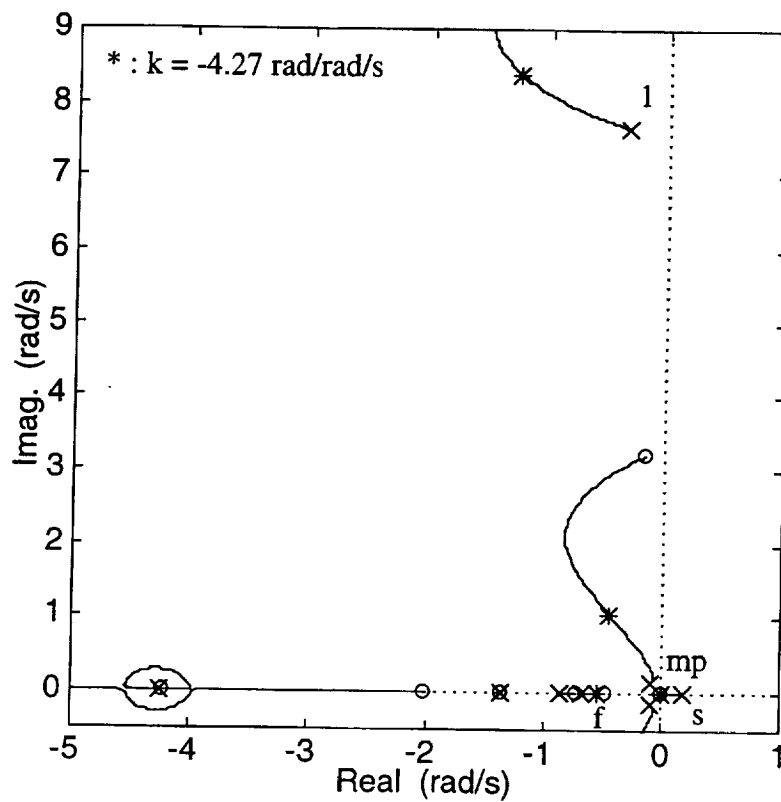
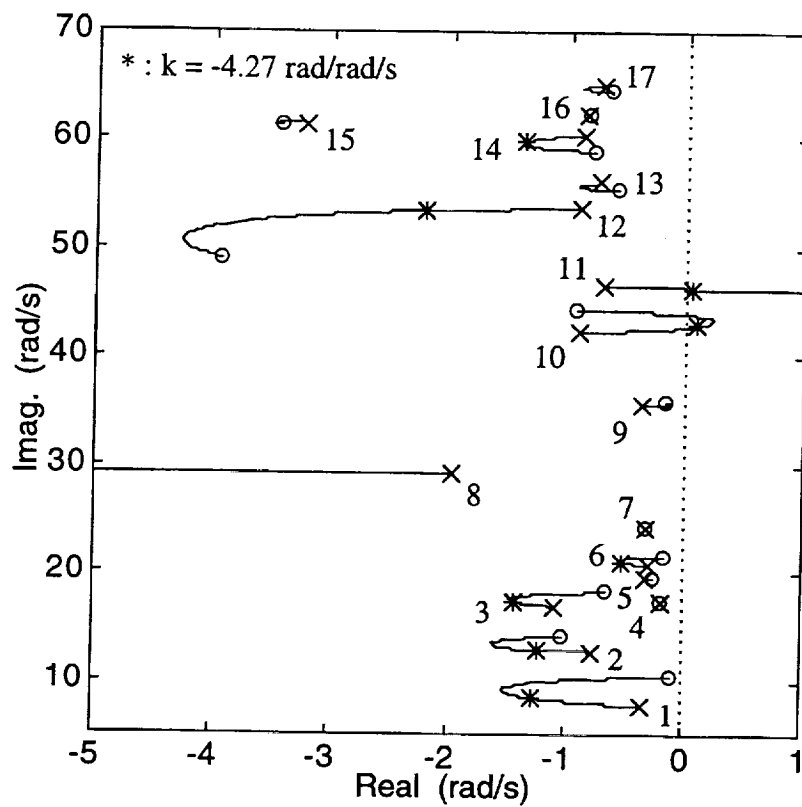


Figure 45. Continued

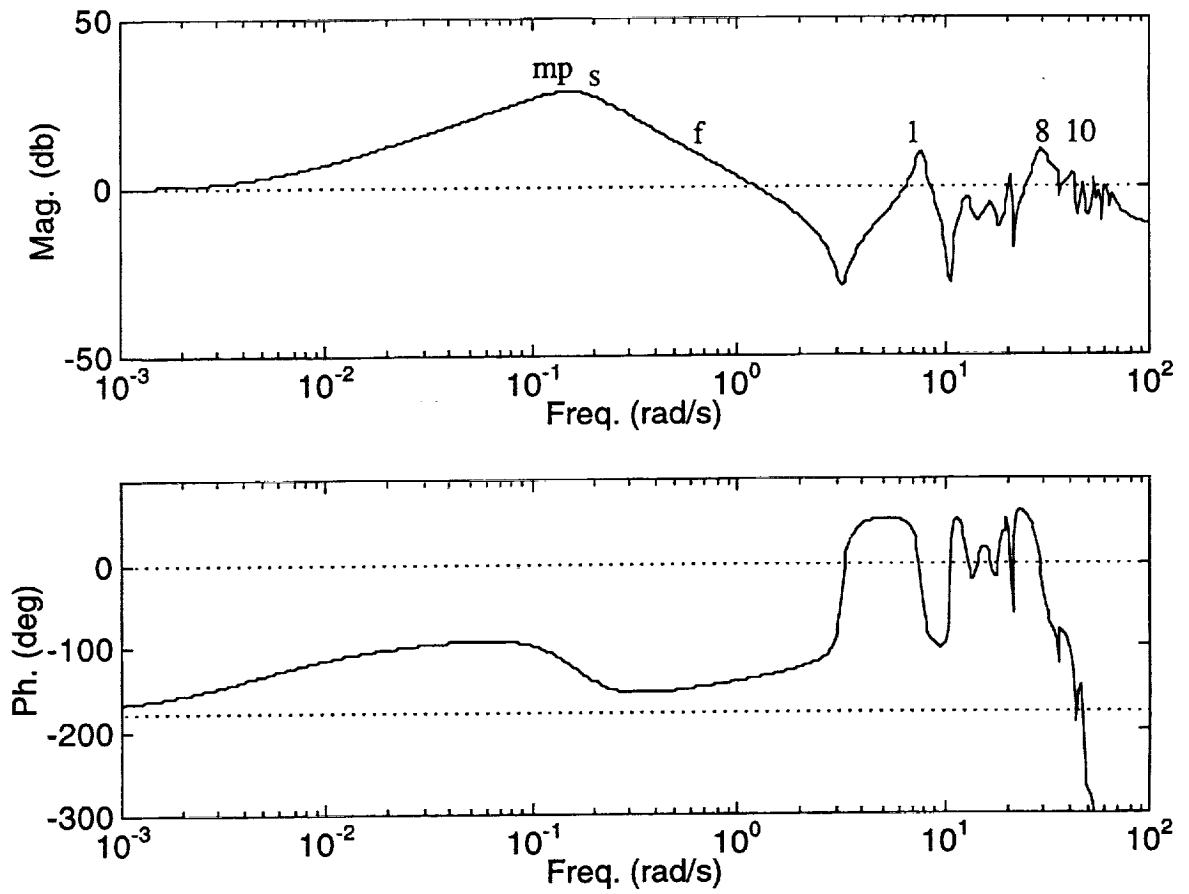


Figure 46. Bode Plot For 3,460 in Pitch Rate To Elevator,  
 $k = -4.27$  rad/rad/s

Tradeoff relationships between forward and tail sensor utilization are quite clear. With the forward sensor, desirable low frequency characteristics below 5 rad/s include relaxed stability stabilization and pitch damping augmentation, while above this frequency undesirable aeroelastic control effects result (mode 1 is invariant and modes 2, 3 and 6 are destabilized). An opposite trend occurs with the tail sensor. Below 5 rad/s, limited pitch damping augmentation is present, while above this frequency aeroelastic modes are augmented with higher damping and are phase stabilized, until 45 rad/s is reached (modes 10-11). Therefore, in the HSCT application, below 5 rad/s the 1,850 in sensor signal will be weighted higher, and above 5 rad/s the 3,460 in sensor signal will be weighted more heavily.

First consider the case where the level of SMCS strength is 25% of that for SAS ( $k_{SMCS}/k_{SAS} = -0.25$ ,  $z = 2 \text{ 1/s}$ ). Fig. 47 shows the blending logic as a function of frequency where  $H_1(s)$  and  $H_2(s)$  are

$$H_1(s) = 0.75 \frac{(s+2.67)}{(s+2)} \quad H_2(s) = 0.25 \frac{s}{(s+2)} \quad (3.17)$$

The Wykes control logic, in terms of the Evans behavior, is shown in Fig. 48. Results are consistent with the control design strategy, but several undesirable characteristics are noted. For frequencies below 5 rad/s, the closed-loop dynamics correlate with the forward SS/SS features in Fig. 43. A conventional, well damped rigid pitch mode is present. However, with a SMCS-to-SAS ratio of only 1-to-4, augmentation of the aeroelastic modes appears similar to Fig. 43 and is unlike that in Fig. 45. Aeroelastic modes 2 and 11 show hard instabilities. The only exception here is mode 1 which shows high potential for increased damping. Unfortunately, this high damping can not be realized because the blending strategy has pushed the mode 1 zeros into the right-half plane, reducing the usable loop gain. To show this, consider the Bode response in Fig. 49 for a gain of  $k = -4.52 \text{ rad/rad/s}$ , which just stabilizes the relaxed stability mode. Nonminimum phase zeros result in a 180 deg phase loss when contrasted with Fig. 46, where the phase "hangs on" until a higher frequency value. To avoid compromise of aeroelastic stability margins, loop gain must remain low.

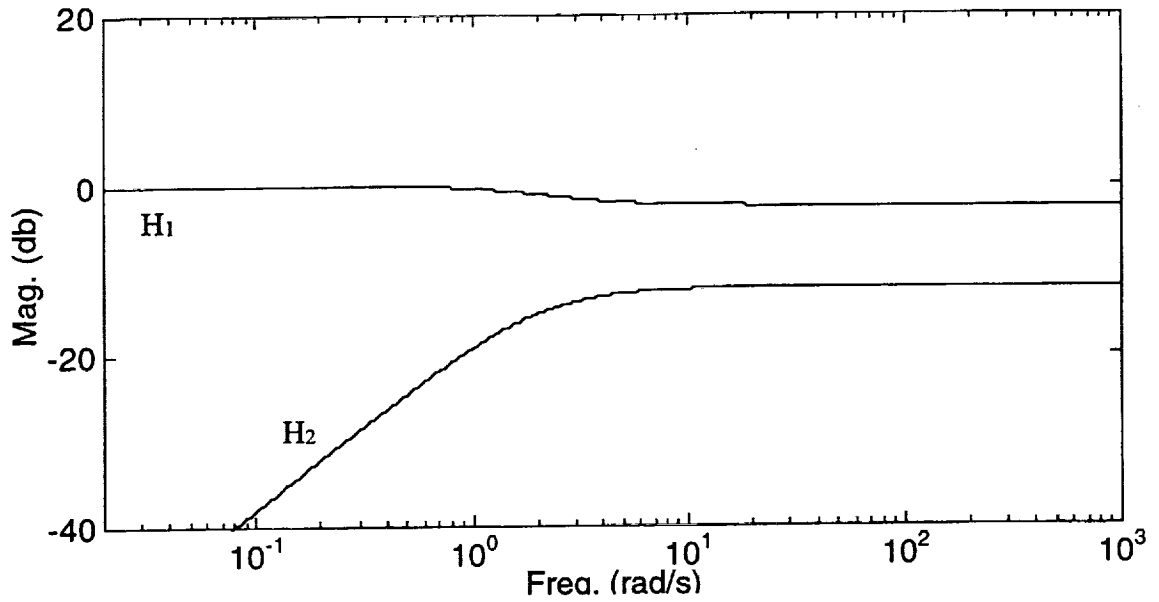


Figure 47. Lag-Lead And High Pass Blending With  $k_{SMCS}/k_{SAS} = -0.25$

To remedy this situation, consider a case where the level of SMCS strength is 75% of that for SAS ( $k_{SMCS}/k_{SAS} = -0.75$ ,  $z = 2 \text{ 1/s}$ ). The blending filters  $H_1(s)$  and  $H_2(s)$  are

$$H_1(s) = 0.25 \frac{(s+8)}{(s+2)} \quad H_2(s) = 0.75 \frac{s}{(s+2)} \quad (3.18)$$

and Fig. 50 illustrates the frequency responses. The Evans behavior is shown in Fig. 51. Results are again consistent with what is asked of the control design strategy, but several troublesome features appear. Above 5 rad/s, the closed-loop dynamics correlate with the tail SS/SS features in Fig. 45. Modes 1-9 are either augmented with higher damping, or are unaffected. A significant difference from Fig. 45, however, is the nonminimum phase characteristics associated with some of the modes, again introduced by the blending logic. Recall that aerodynamic coupling influences the instabilities associated with modes 10-11 and is inherent in the 3,460 in feedback signal. Now, with a SMCS-to-SAS ratio of 3-to-4, augmentation of the pitch mode appears similar to Fig. 45 and is unlike that in Fig. 43. The pitch mode migrates towards a pair of complex conjugate zeros located near the imaginary axis. This migration path limits the amount of pitch damping that can be achieved. The Bode response for a gain  $k = -4.52 \text{ rad/rad/s}$  is given in Fig. 52. Nonminimum phaseness again prevents higher loop gain values.



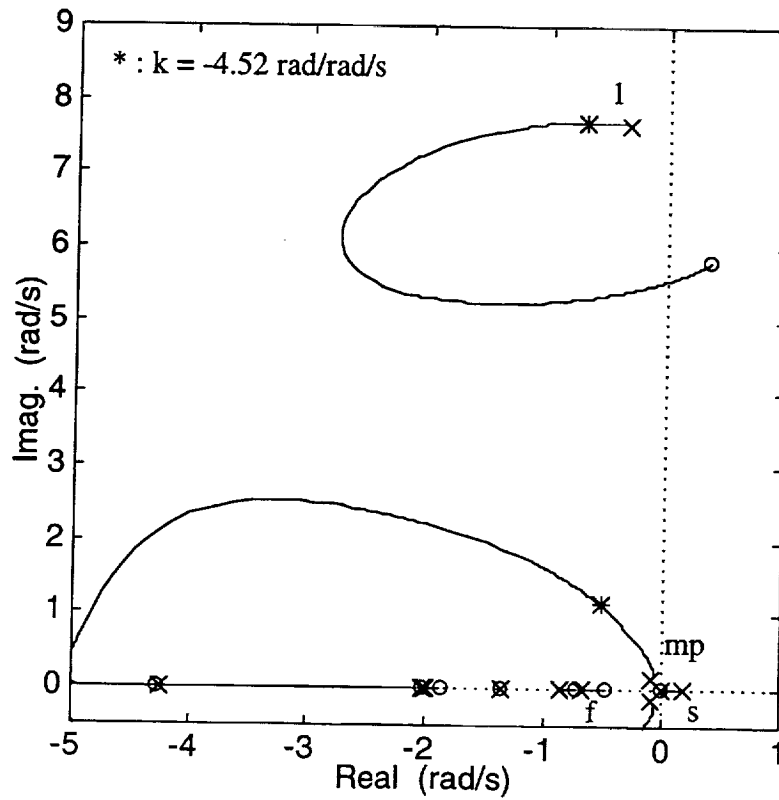
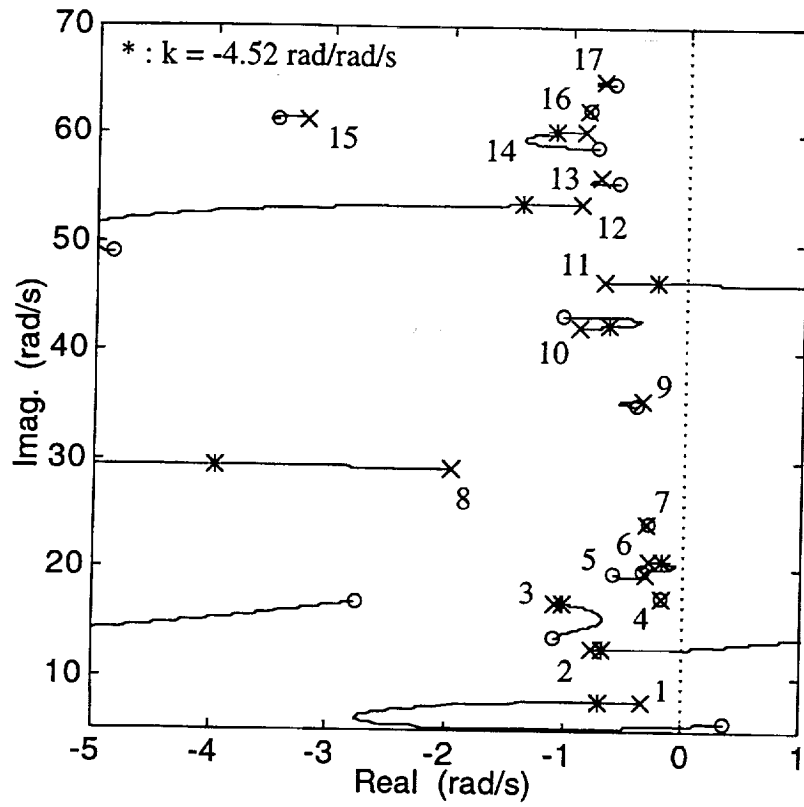


Figure 48. Evans Plot For Blend Of Lag-Lead 1,850 in  
And High Pass 3,460 in Pitch Rate To Elevator,  
 $k_{SMCS}/k_{SAS} = -0.25$

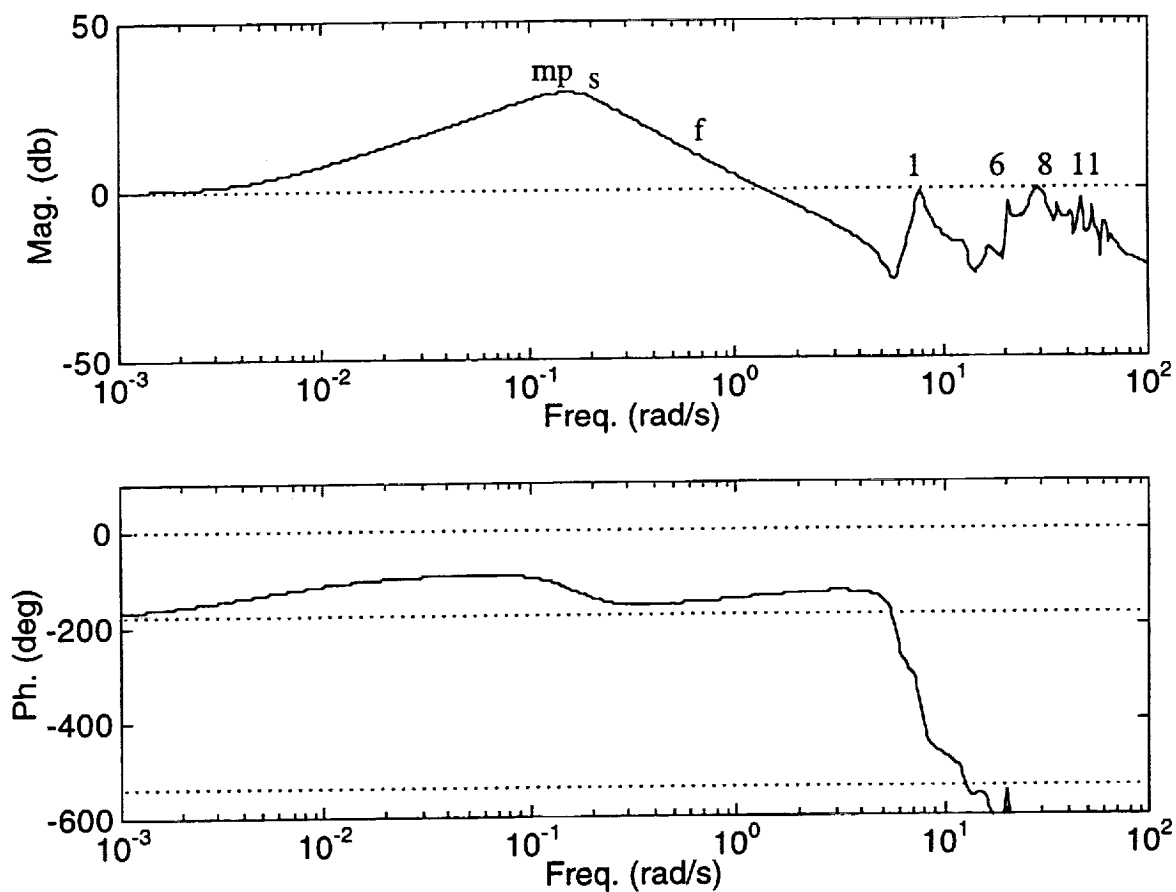


Figure 49. Bode Plot For Blend Of Lag-Lead 1,850 in  
And High Pass 3,460 in Pitch Rate To Elevator,  
 $k_{SMCS}/k_{SAS} = -0.25$  And  $k = -4.52$  rad/rad/s

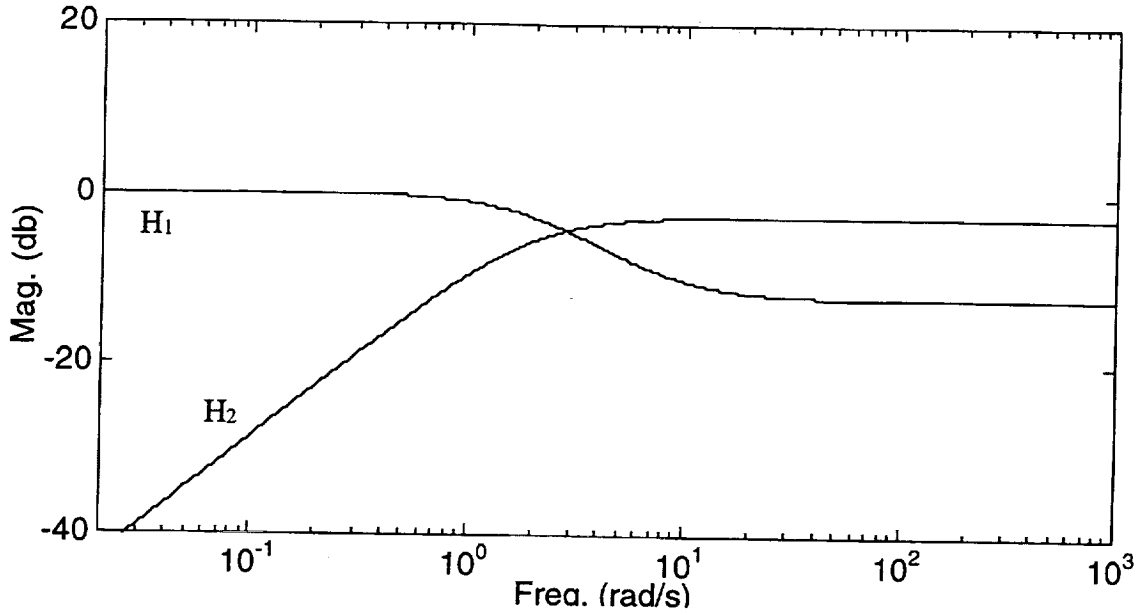


Figure 50. Lag-Lead And High Pass Blending With  $k_{SMCS}/k_{SAS} = -0.75$

The above results for the lag-lead/high pass blending strategy are flawed due to the observed nonminimum phase behavior and is discussed next. The numerator dynamics of the  $q_b/\delta_E$  transfer function in Fig. 41 consist of the addition of two terms originating from the two feedback signals. The relative strength of the two channels determines the final zeros according to the root locus

$$1 + \frac{h_2}{h_1} \frac{s}{(s+z_1)} \frac{n_{q3460}(s)}{n_{q1850}(s)} = 0 \quad (3.19)$$

where  $n_{q1850}(s)$  and  $n_{q3460}(s)$  denote vehicle numerator polynomials and  $h_2/h_1$  plays the role of a parameterization variable. Blending filters introduce the factor  $s/(s+z_1)$ . For  $h_2/h_1 = 0$ , Eq. (3.19) indicates the  $q_b/\delta_E$  zeros are coincident with the  $q_{1850}/\delta_E$  zeros and  $s = -z_1$ . For a large value of  $h_2/h_1$ , the  $q_b/\delta_E$  zeros tend towards the  $q_{3460}/\delta_E$  zeros and  $s = 0$ . At intermediate values for  $h_2/h_1$ , the zeros migrate according to the conventional rules. Fig. 53 shows this numerator root locus for the  $k_{SMCS}/k_{SAS} = -0.75$  design in Fig. 51, as an example. The behavior for  $k_{SMCS}/k_{SAS} = -0.25$  is similar. In transitioning from the root locations of  $n_{q1850}(s)$  to those of  $n_{q3460}(s)$ , the mode 1 zeros depart into the right-half plane leading to the nonminimum phase behavior.

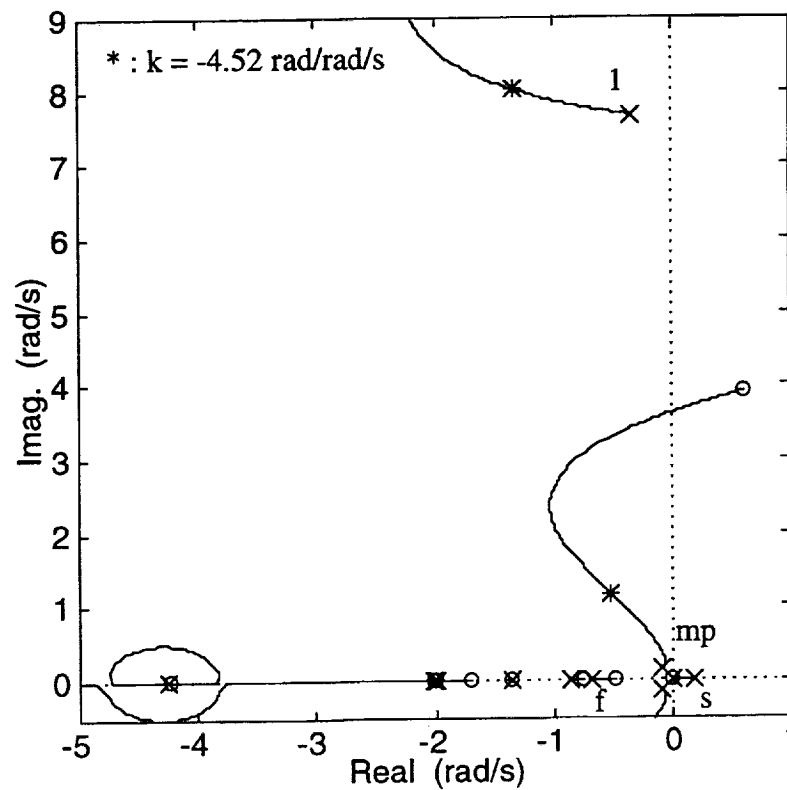
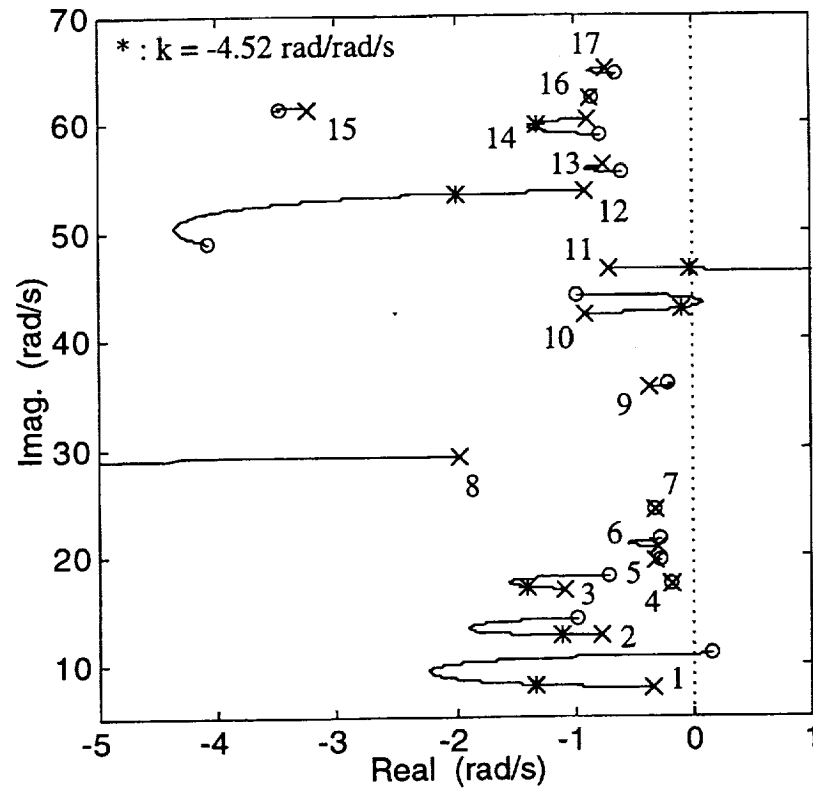


Figure 51. Evans Plot For Blend Of Lag-Lead 1,850 in  
And High Pass 3,460 in Pitch Rate To Elevator,  
 $k_{SMCS}/k_{SAS} = -0.75$

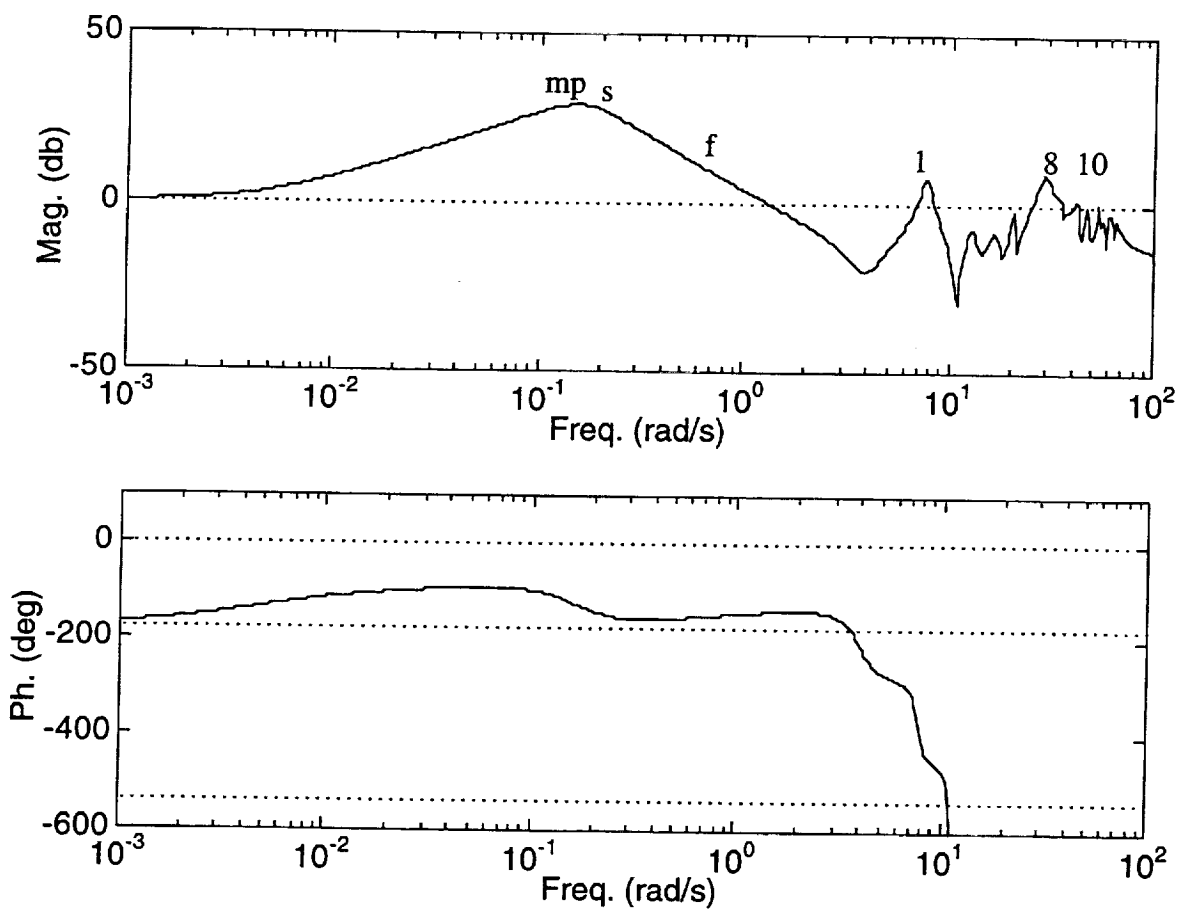


Figure 52. Bode Plot For Blend Of Lag-Lead 1,850 in  
And High Pass 3,460 in Pitch Rate To Elevator,  
 $k_{SMCS}/k_{SAS} = -0.75$  And  $k = -4.52$  rad/rad/s

Consider the angle of departure relationship as applied to mode 1 in Eq. (3.19) and Fig. 53. Let  $\theta_1$  represent the phase angle of factor  $s+Z_1$  contained within  $n_{q1850}(s)$  where  $Z_1$  represents the aeroelastic mode 1 zero with imaginary part greater than zero. From Tab. 6,  $Z_1 = -0.53 + j7.9$  1/s. For a test point very near  $Z_1$ , this relationship is

$$\theta_1 = \angle(s) - \angle(s+8) + \angle(n_{q3460}) - \angle(n'_{q1850}) - (2i+1)\pi \quad (3.20)$$

In Eq. (3.20),  $n'_{q1850}(s)$  denotes  $n_{q1850}(s)$  with the factor  $s+Z_1$  removed and  $i$  represents an integer. With  $s = Z_1$ , the  $s/(s+8)$  factor results in an additional contribution of 47 deg of phase to the departure angle from zero  $Z_1$ . Without this contribution, the initial migration would point down towards the origin, avoiding the right-half plane and nonminimum phase behavior.

The mode 1 nonminimum phase characteristic is due to the width of the high pass filter differentiator and final break frequency of the lag-lead filter. Insertion of the zero at the origin "pushes" the mode 1 loci out into the right-half plane. The lag-lead/high pass blending strategy is fundamentally flawed. Ref. 13 indicated low pass/band pass strategies exhibited similar tendencies and showed how lag-lead/lead-lag filtering provided a more gradual transition of the rate gyro signals. Utilization of lag-lead and lead-lag blending with the forward and tail sensors is not considered here.

Based on the above investigations, the contractor feels the aft tail only Wykes SMCS architecture is not feasible for the highly elastic HSCT airframe. This conclusion is based on two main observations: 1) aerodynamic coupling terms are of such strength that fundamental assumptions associated with the original Wykes paradigm are not valid for this airframe, and 2) lag-lead/high pass blending results in an excessively abrupt transition from forward to tail sensors and manifests itself in the form of nonminimum phase characteristics. A highly elastic and unstable airframe configuration with aft tail control only places unrealistic constraints on the flight controls discipline, and program planning should be modified accordingly.

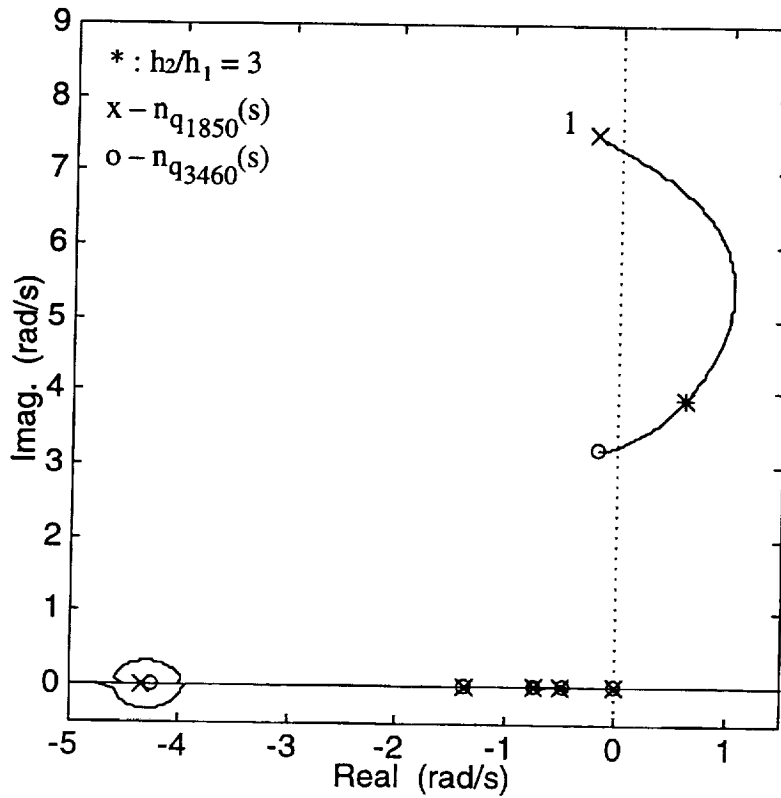
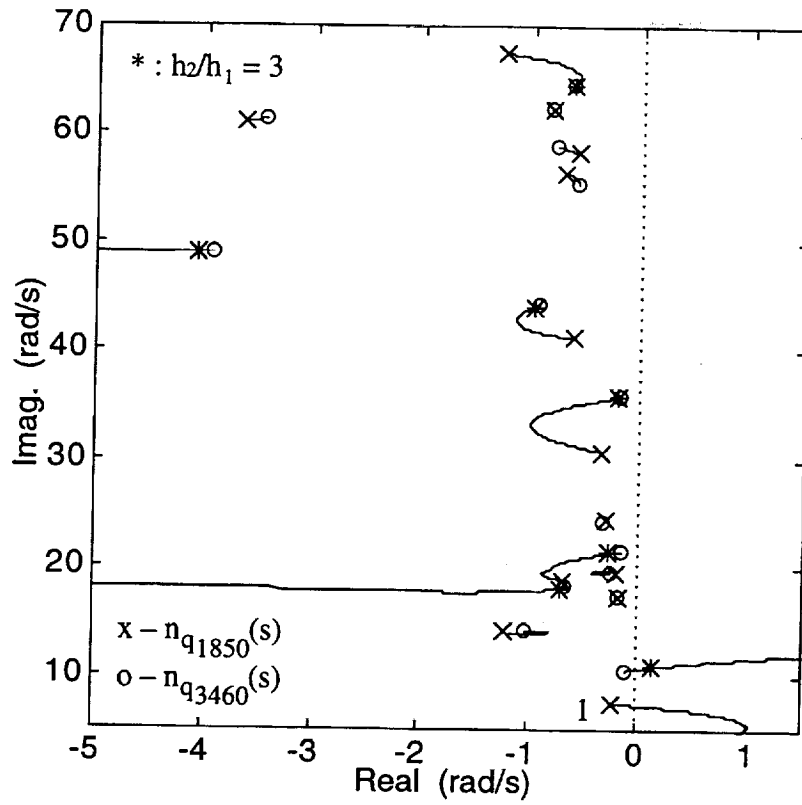


Figure 53. Numerator Root Locus For Lag-Lead 1,850 in And High Pass 3,460 in Pitch Rate To Elevator,  $k_{SMCS}/k_{SAS} = -0.75$

## Section IV

### Conventional Multi-Sensor/Multi-Surface Design Strategy

#### A. Summary of Design Strategy

The objectives of the inner loop FCS are to 1) artificially supply the stability inherently lacking in the airframe, 2) augment the key pilot/passenger centered responses in accordance with relevant flying quality metrics, and 3) suppress aeroelastic motions in the responses. The feasibility of achieving these goals with SS/SS and MS/SS architectures have been thoroughly explored in Ref. 13 and Section III of this report. The main conclusion from these investigations is architectures based on a single loop incorporating aft tail control and utilizing one sensor, or possibly several blended sensors, does not provide sufficient design freedom to satisfy closed-loop requirements. Trades between pitch augmentation/low frequency flying qualities and aeroelastic augmentation/high frequency stability margins are unacceptable. Further, aft tail control lacks sufficient capacity to tailor motions at the crew station. For a highly flexible HSCT vehicle, the inner loop FCS will, in all likelihood, require multiple, integrated feedback loops.

With this background, consider the MS/MS feedback architecture shown in Fig. 54. In Fig. 54,  $y_1(s)$  and  $y_2(s)$  denote two rate gyro feedback signals, perhaps representing near cockpit ( $y_1$ ) and near mass center ( $y_2$ ) pitch rate responses. The command input  $u_{2c}(s)$  represents aft tail control (elevator command,  $\delta_{E_c}$ ) previously used in the design studies of Ref. 13 and Section III of this report. The additional, new input available for control is  $u_{1c}(s)$  and will correspond to the forward vane commands ( $\delta_{V_c}$ ) described in Section II-C. Note the second input allows an additional feedback loop, as well as a crossfeed. Only one crossfeed is considered here. These additional design freedoms are exploited as discussed next. Also in Fig. 54,  $P_i(s)$  and  $K_{ij}(s)$  denote prefilter and compensation transfer functions, and  $A_i(s)$  represents actuator dynamics. The signal  $y_3(s)$  represents additional responses of interest not directly controlled, such as normal



acceleration or pitch rate at locations other than the cockpit or mass center (or possibly acceleration at the cockpit and mass center).

Control design efforts consist of four steps: 1) closure of the  $y_1/u_{1c}$  loop, 2) insertion of the  $u_{2c}$ -to- $u_{1c}$  crossfeed, 3) closure of the  $y_2/u_{2c}$  loop, and 4) insertion of the  $y_{2c}$  command shaping filter. The  $y_1/u_{1c}$  loop plays the role of a SMCS loop and hence is dedicated to aeroelastic suppression. The  $y_2/u_{2c}$  loop fulfills the role of a SAS loop and is primarily responsible for pitch augmentation. The  $u_{2c}$ -to- $u_{1c}$  crossfeed provides coordinated operation between the two feedback loops. Finally, the  $y_{2c}$  prefilter provides selected frequency screening of the command signal to improve response characteristics. Conventional frequency domain concepts are used in a sequential process<sup>3,22,23</sup> to construct these loops.

From Fig. 54, the vehicle model is

$$\begin{bmatrix} y_1 \\ y_2 \\ y_3 \end{bmatrix} = \begin{bmatrix} G_{11}A_1 & G_{12}A_2 \\ G_{21}A_1 & G_{22}A_2 \\ G_{31}A_1 & G_{32}A_2 \end{bmatrix} \begin{bmatrix} u_{1c} \\ u_{2c} \end{bmatrix} \quad (4.1)$$

Using the structure indicated in Fig. 54, consider closing the  $y_1/u_{1c}$  loop first. The control law is

$$u_{1c} = K_{11}(y_{1c} - y_1) \quad (4.2)$$

and the resulting intermediate system is

$$\begin{aligned} y_1 &= \frac{K_{11}G_{11}A_1}{1+K_{11}G_{11}A_1} y_{1c} + \frac{G_{12}A_2}{1+K_{11}G_{11}A_1} u_{2c} \\ y_2 &= \frac{K_{11}G_{21}A_1}{1+K_{11}G_{11}A_1} y_{1c} + \frac{G_{22}A_2 + K_{11}\tilde{G}_{1-2}A_1A_2}{1+K_{11}G_{11}A_1} u_{2c} \\ y_3 &= \frac{K_{11}G_{31}A_1}{1+K_{11}G_{11}A_1} y_{1c} + \frac{G_{32}A_2 + K_{11}\tilde{G}_{1-3}A_1A_2}{1+K_{11}G_{11}A_1} u_{2c} \\ \tilde{G}_{1-2} &= G_{11}G_{22} - G_{12}G_{21} \quad , \quad \tilde{G}_{1-3} = G_{11}G_{32} - G_{12}G_{31} \end{aligned} \quad (4.3)$$

where  $\tilde{G}_{i-j}$  denotes the vehicle coupling transfer functions.<sup>3</sup> As part of the synthesis, the loop transfer  $K_{11}G_{11}A_1$  is utilized to generate Evans and Bode traces. Selection of an angular rate sensor mounted very close to the forward vane would tend to elicit the highly sought pole-zero interlaced pattern of Section III for aeroelastic damping augmentation. Aerodynamic coupling effects should be less a factor, when compared with results in Section III, since the vane is located

well forward of the wing and body, thus minimizing interference effects, and the vane structure will be relatively stiff in comparison to the wing.

Before closing the  $y_2/u_{2c}$  SAS loop, note the coupling that exists between these two channels in Eq. (4.3) (i.e.,  $G_{12}$  and  $G_{21}$ ). If this coupling is significant but ignored in the design, the loops can not be expected to operate in a harmonious manner. To provide this synchronous behavior with coupling present, a  $u_{2c}$ -to- $u_{1c}$  crossfeed is considered, or

$$y_{1c} = K_{cf} u_{2c} \quad (4.4)$$

This signal path leads to a second intermediate system

$$\begin{aligned} y_1 &= \frac{G_{12}A_2 + K_{cf}K_{11}G_{11}A_1}{1 + K_{11}G_{11}A_1} u_{2c} \\ y_2 &= \frac{G_{22}A_2 + K_{11}\tilde{G}_{1-2}A_1A_2 + K_{cf}K_{11}G_{21}A_1}{1 + K_{11}G_{11}A_1} u_{2c} \\ y_3 &= \frac{G_{32}A_2 + K_{11}\tilde{G}_{1-3}A_1A_2 + K_{cf}K_{11}G_{31}A_1}{1 + K_{11}G_{11}A_1} u_{2c} \end{aligned} \quad (4.5)$$

Introduction of the crossfeed fundamentally alters the transfer function numerator characteristics in Eq. (4.5).  $K_{cf}(s)$  can be used to reduce excitation and participation of troublesome aeroelastic modes in both the  $y_1$  and  $y_3$  responses from the input  $u_{2c}$ . Sensor placement for response  $y_2$  can be relied upon to eliminate the most significant mode (mode 1) from this response, leaving the crossfeed to address responses  $y_1$  and  $y_3$ . Migration paths for the numerator roots of interest in Eq. (4.5) are based on the functions  $K_{cf}\{K_{11}G_{11}A_1\}/\{G_{12}A_2\}$  and  $K_{cf}\{K_{11}G_{31}A_1\}/\{G_{32}A_2 + K_{11}\tilde{G}_{1-3}A_1A_2\}$ .

Finally, the  $y_2/u_{2c}$  loop is closed, or

$$u_{2c} = K_{22}(y_{2c} - y_2) \quad (4.6)$$

With this loop closed, the augmented system is

$$\begin{aligned} y_1 &= \frac{K_{22}(G_{12}A_2 + K_{cf}K_{11}G_{11}A_1)}{1 + K_{11}G_{11}A_1 + K_{22}\{G_{22}A_2 + K_{11}\tilde{G}_{1-2}A_1A_2 + K_{cf}K_{11}G_{21}A_1\}} y_{2c} \\ y_2 &= \frac{K_{22}\{G_{22}A_2 + K_{11}\tilde{G}_{1-2}A_1A_2 + K_{cf}K_{11}G_{21}A_1\}}{1 + K_{11}G_{11}A_1 + K_{22}\{G_{22}A_2 + K_{11}\tilde{G}_{1-2}A_1A_2 + K_{cf}K_{11}G_{21}A_1\}} y_{2c} \\ y_3 &= \frac{K_{22}\{G_{32}A_2 + K_{11}\tilde{G}_{1-3}A_1A_2 + K_{cf}K_{11}G_{31}A_1\}}{1 + K_{11}G_{11}A_1 + K_{22}\{G_{22}A_2 + K_{11}\tilde{G}_{1-2}A_1A_2 + K_{cf}K_{11}G_{21}A_1\}} y_{2c} \end{aligned} \quad (4.7)$$

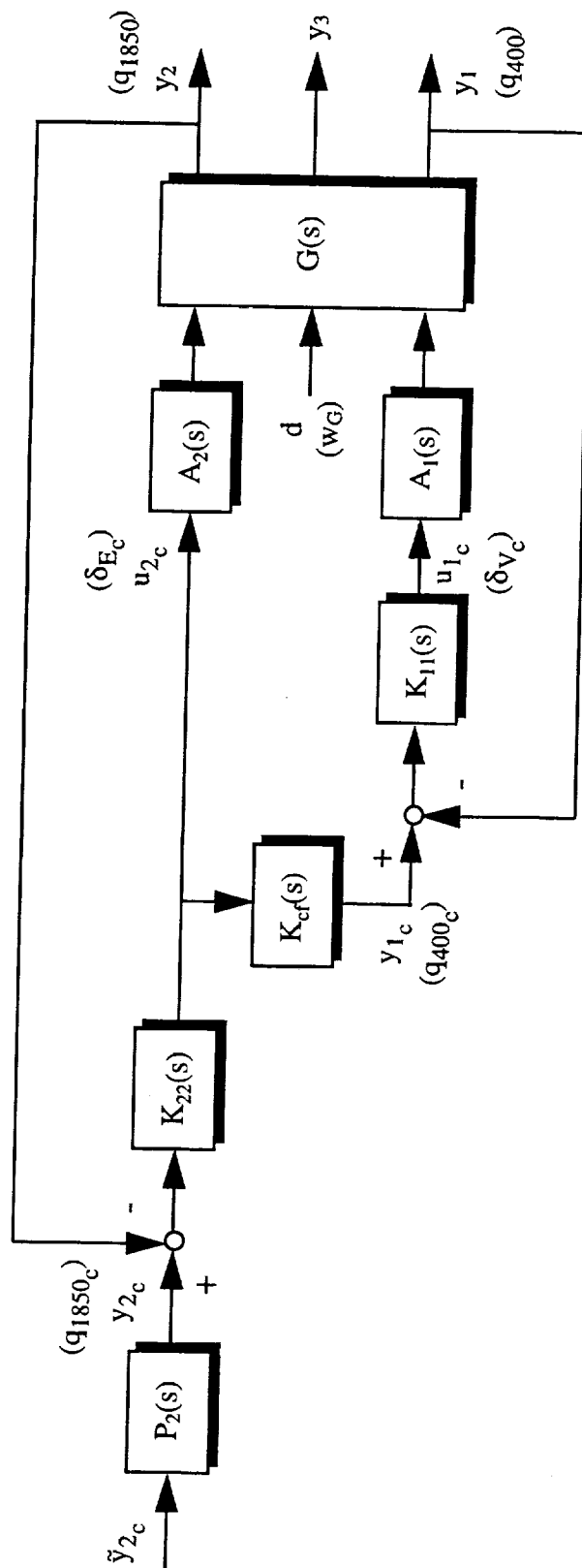


Figure 54. Multi-Sensor/Multi-Surface Control Architecture

The loop transfer  $K_{22}(G_{22}A_2 + K_{11}\tilde{G}_{1-2}A_1A_2 + K_{cf}K_{11}G_{21}A_1)/(1 + K_{11}G_{11}A_1)$  would determine the basic Evans and Bode characteristics during selection of gain and compensation logic for  $K_{22}(s)$ . Sensor placement near the anti-node of the 1<sup>st</sup> structural mode would tend to provide acceptable transfer function dynamic features for pitch stabilization and augmentation.

If deemed necessary, the  $y_{2c}$  prefilter can be considered, or

$$y_{2c} = P_2 \tilde{y}_{2c} \quad (4.8)$$

In this case, the final augmented system is

$$\begin{aligned} y_1 &= \frac{P_2 K_{22}(G_{12}A_2 + K_{cf}K_{11}G_{11}A_1)}{1 + K_{11}G_{11}A_1 + K_{22}\{G_{22}A_2 + K_{11}\tilde{G}_{1-2}A_1A_2 + K_{cf}K_{11}G_{21}A_1\}} \tilde{y}_{2c} \\ y_2 &= \frac{P_2 K_{22}\{G_{22}A_2 + K_{11}\tilde{G}_{1-2}A_1A_2 + K_{cf}K_{11}G_{21}A_1\}}{1 + K_{11}G_{11}A_1 + K_{22}\{G_{22}A_2 + K_{11}\tilde{G}_{1-2}A_1A_2 + K_{cf}K_{11}G_{21}A_1\}} \tilde{y}_{2c} \\ y_3 &= \frac{P_2 K_{22}\{G_{32}A_2 + K_{11}\tilde{G}_{1-3}A_1A_2 + K_{cf}K_{11}G_{31}A_1\}}{1 + K_{11}G_{11}A_1 + K_{22}\{G_{22}A_2 + K_{11}\tilde{G}_{1-2}A_1A_2 + K_{cf}K_{11}G_{21}A_1\}} \tilde{y}_{2c} \end{aligned} \quad (4.9)$$

This filter can be relied on to screen specific frequency content from the command signal in order to further reduce any residual oscillations that remain in the closed-loop system under stick commands, or possibly to "speed-up" the response quickness by providing lead action. This filter is not a substitute for the feedback loops, and only provides mild changes to the system characteristics. The prefilter will do nothing to alter response characteristics originating from other input sources such as atmospheric turbulence.

This feedback strategy corresponds to the "mechanics" illustrated in Fig. 55 and discussed below. If the application is to the HSCT model in Appendix C,  $u_{1c}$  and  $u_{2c}$  would correspond to  $u_{1c} = \delta_{V_c}$  and  $u_{2c} = \delta_{E_c}$ , and appropriate sensor locations would be  $y_1 = q_{400}$  and  $y_2 = q_{1850}$ . Suppose the pilot commands a nose down pitch motion with command signal  $q_{1850c}$ . Initial elevator deflection will be down with rigid rotation indicated in the figure. The  $q_{1850}/\delta_{E_c}$  loop will stabilize this motion and provide good handling qualities. The initial up tail force will excite the aeroelastic dynamics and mode 1 will initially deform as shown. The  $\delta_{E_c}$ -to- $\delta_{V_c}$  crossfeed will lead to initial trailing edge up deflection for the vane. This coordination hinders aeroelastic excitations from  $\delta_{E_c}$  inputs. Superimposed on top of this two-surface deflection strategy, the

$q_{400}/\delta_{V_c}$  loop acts to dampen aeroelastic motions that are inevitably excited, possibly from gust disturbances. The following sections describe in detail each of the four design steps.

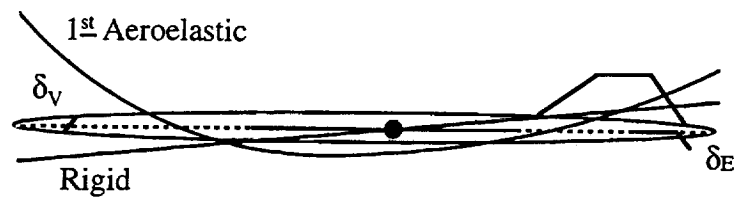


Figure 55. "Mechanics" Of The MS/MS Flight Control System

## B. Aeroelastic Suppression Loop

Consider the Evans plot behavior shown in Fig. 56 for the closed-loop poles corresponding to Eq. (4.3) using static compensation (i.e.,  $K_{11}(s) = k_{11}$ ). Recall only the  $q_{400}/\delta_V$  loop is closed here. Observe the approximate pole-zero interlaced behavior associated with this channel. Departure angles for nearly every aeroelastic mode are near the optimum 180 deg value. Significant potential exists to damp many of the modes. Only the highest frequency structural mode is potentially destabilized. Also note the relaxed stability mode tends to be stabilized by this loop, easing the required bandwidth in the pitch augmentation loop yet to be considered. After many loop closure attempts described in Ref. 13 and Section III of this report, a channel with significant design leverage for mode suppression has been identified.

The closed-loop poles in Fig. 56 are highlighted for a compensator gain value of  $k_{11} = 2.33$  rad/rad/s. Fig. 57 shows the corresponding Bode plot for this gain value. Observe how the system phase remains above -180 deg out to a frequency near 70 rad/s providing a buffer from possible instability due to modeling errors. For this design model, the phase buffer is not quite sufficient, however, to exploit the full potential of this mode control loop. For the indicated gain value, mode 9 lies just above the 0 db level and bumps into the 60 deg phase margin requirement set forth in Refs. 1-2. This restricts the upper limit of usable loop gain and prevents further augmentation of modes 1-2. Several design options incorporating dynamic compensation are considered next to overcome this restriction.

A cautious, low-gain option is to attenuate mode 9 with a low pass filter, inserted somewhere in the region of 10-20 rad/s. With this attenuation strategy, the loop gain can be increased to further augment modes 1-2. Considering the high number of modes in the 10-40 rad/s region in Fig. 56, it is highly unlikely insertion of a low pass filter can be accomplished without impacting the phase characteristics. Selecting a break point of 20 rad/s, the low-gain option compensator is

$$K_{11}(s) = k_{11} \frac{20}{(s+20)} \quad (4.10)$$

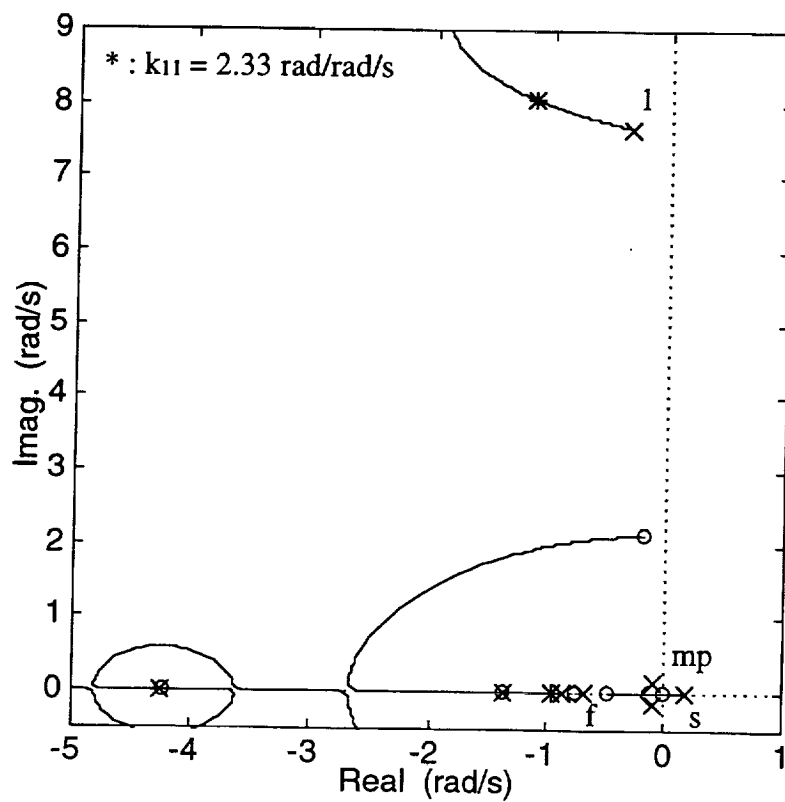
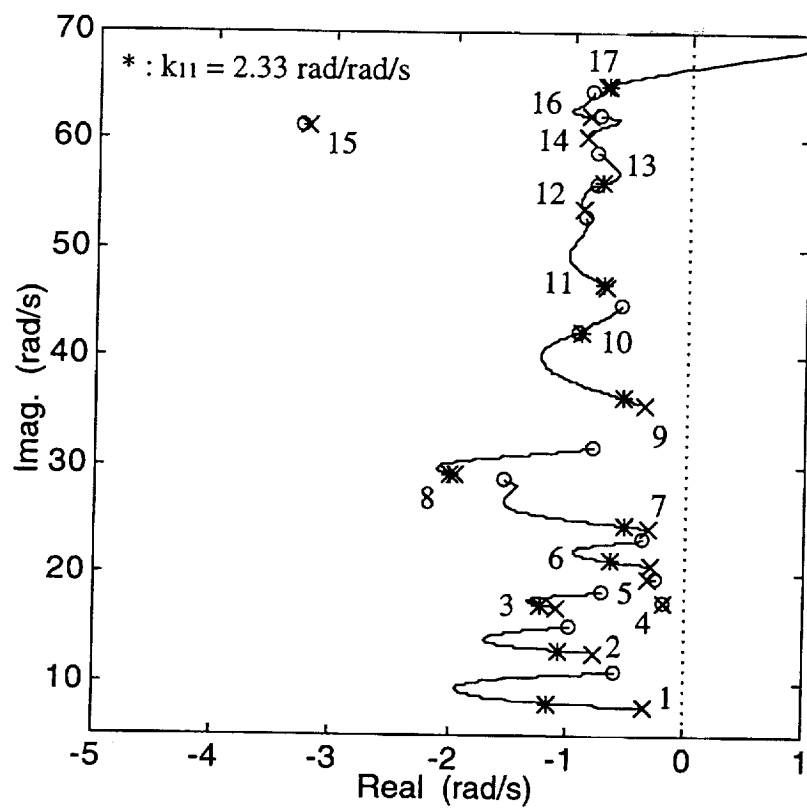


Figure 56. Evans Plot For 400 in Pitch Rate To Vane With Static Compensation

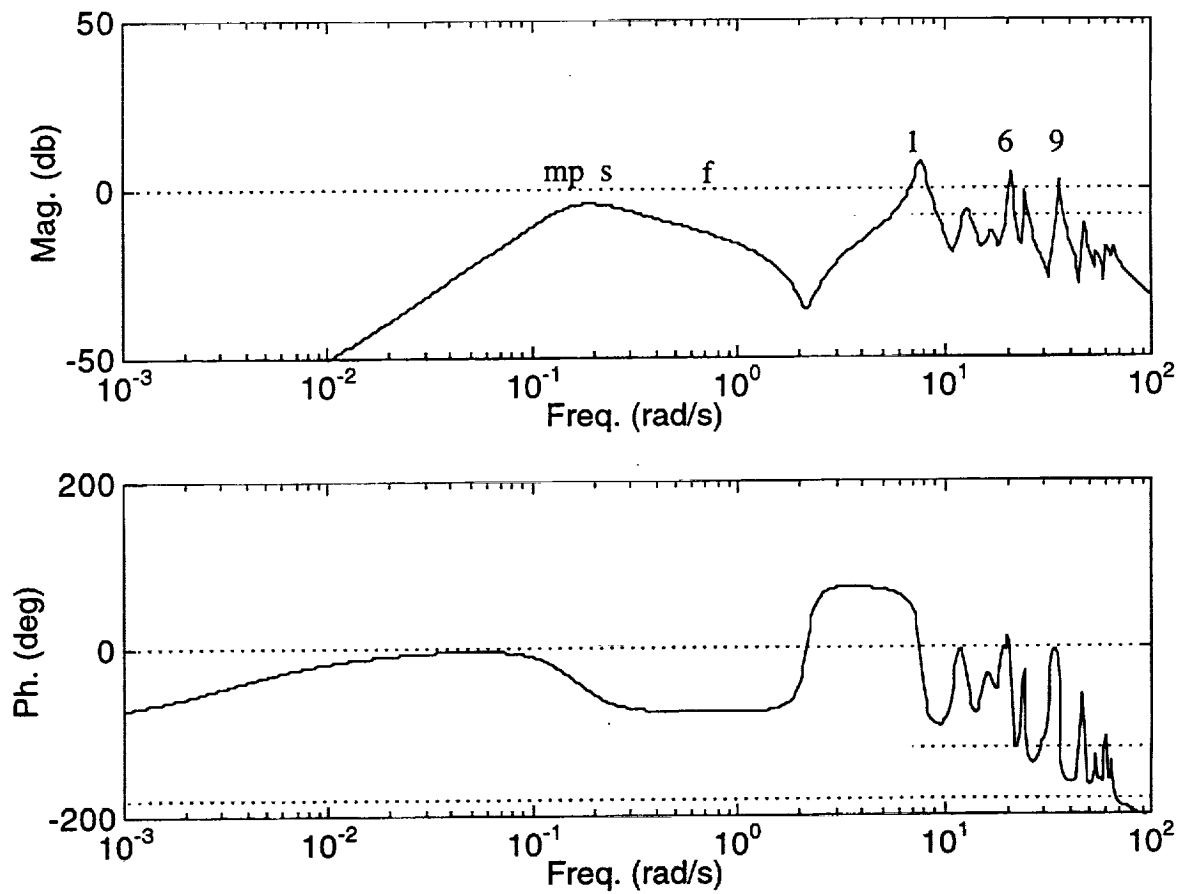


Figure 57. Bode Plot For 400 in Pitch Rate To Vane  
With Static Compensation,  $k_{11} = 2.33 \text{ rad/rad/s}$



Figs. 58-59 show the Evans and Bode characteristics. Several modes have been destabilized towards the imaginary axis. Phase loss from the low pass filter has eliminated the inherent system phase buffer associated with this channel. Multiple -180 deg crossover points occur, preventing significant loop gain increments to augment dampings. For the indicated gain value, mode 9 is riding the 8 db stability margin requirement and the mode 1 damping value is less than that for Fig. 56 ( $\zeta_1 = 0.098$  vs. 0.142). Attempts to restore the lost buffer with additional phase lead terms in Eq. (4.10) were not successful. For these reasons, the low-gain option does not appear to be an attractive solution. The baseline, static compensation results are more desirable than results shown here.

At the other extreme, an aggressive, high-gain option is to boost the inherent phase contour in the region of 25-70 rad/s with a lead-lag filter. With this strategy, the phase buffer will be of sufficient value to satisfy the 60 deg stability margin requirements under significant increments in loop gain. Approximately 40 deg of additional phase is required in the 40-70 rad/s region to achieve the objective. Break points associated with the lead and lag terms to create this phase will extend the control bandwidth considerably. Therefore, this option is considered high risk in the sense current actuation technology may be surpassed. This risk should not be fully equated with susceptibility to modeling errors and resulting instability mechanisms. On the contrary, if the actuator can not deliver the phase lead to high bandwidth, the inherent phase buffer shown in Fig. 57 resurfaces. In this scenario, phase margins would not meet requirement levels, but an inherent lower bound of approximately 20 deg would exist in this channel. Selecting break points at 16 and 100 rad/s, the high-gain option compensator is

$$K_{11}(s) = k_{11} \frac{100}{16} \frac{(s+16)}{(s+100)} \quad (4.11)$$

and Figs. 60-61 show the design characteristics. The upper limit of usable gain is much higher when compared to the baseline, static compensation results. For a gain value double that of the static compensation case, the closed-loop mode 1 damping value is  $\zeta_1 = 0.323$ .

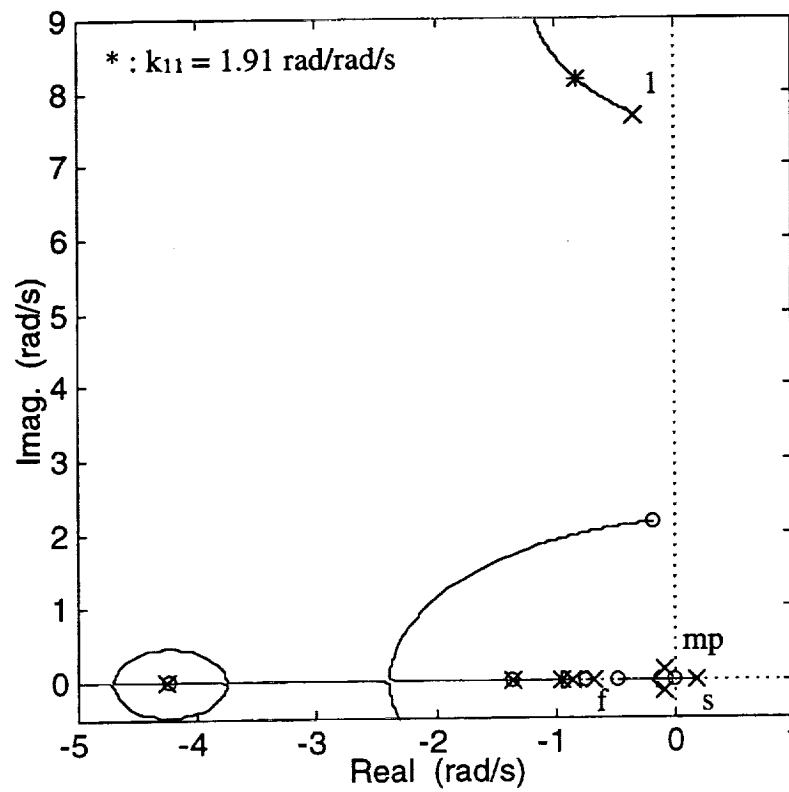
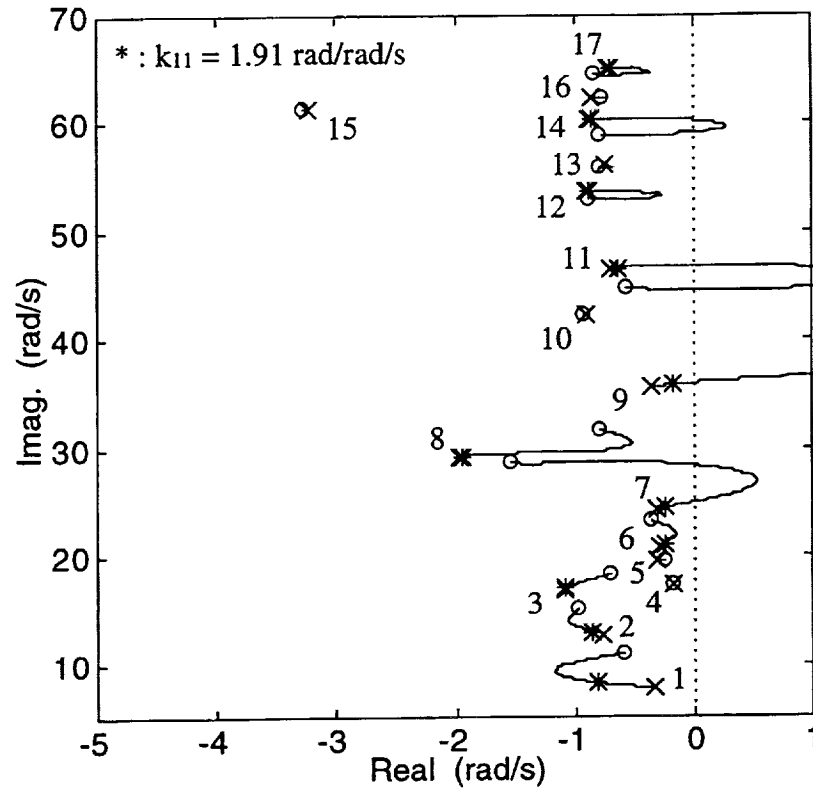


Figure 58. Evans Plot For 400 in Pitch Rate To Vane  
With Low Pass Filter

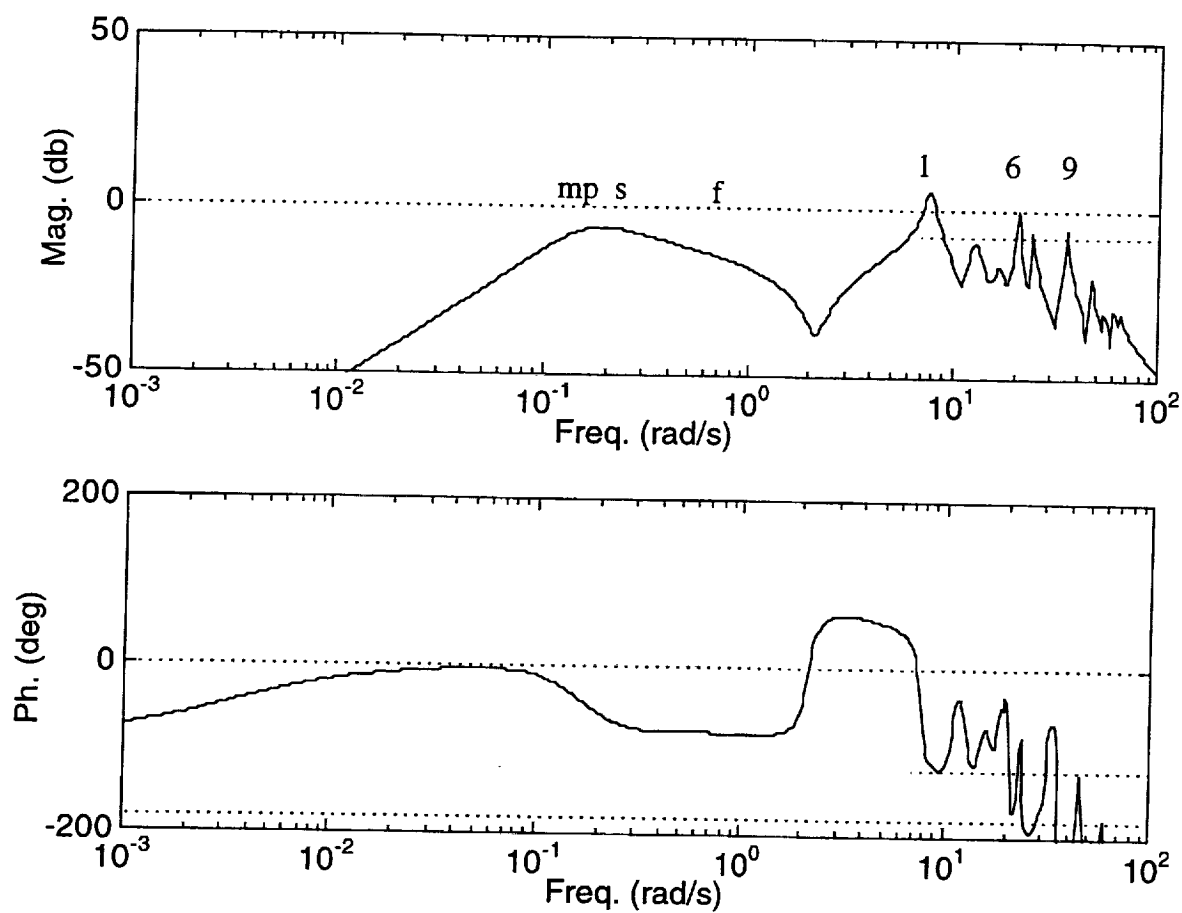


Figure 59. Bode Plot For 400 in Pitch Rate To Vane  
With Low Pass Filter,  $k_{11} = 1.91$  rad/rad/s

A solution falling somewhere in between the previous techniques will incorporate both attenuation and phase lead strategies. In reference to the phase lead approach discussed above, a transition from phase lead to attenuation will be necessary due to eventual airframe-actuator phase crossover and the presence of additional higher frequency modes not included in the design model. With a high authority mode control loop incorporating phase stabilization techniques, the designer must ultimately specify a boundary where modes below the boundary are phase stabilized and above the boundary modes are gain stabilized.

Assessment of the basic magnitude and phase characteristics in Fig. 57 indicate approximately 20 deg of phase lead is needed in the 20-30 rad/s region to meet stability margin requirements, while approximately 40 deg of additional phase is required above this frequency range. Therefore, an eclectic, intermediate-gain strategy is to phase stabilize modes 1-8 leaving modes 9 and up for gain stabilization. Lead-lag behavior will be required in the 20-30 rad/s range. In addition, attenuation of mode 9 is necessary to increase the upper region of usable loop gain. As demonstrated previously (see Fig. 59), first order lag filters are not suitable when applied within a modally dense frequency region. Notching will be considered for mode 9 attenuation.

Consider the intermediate-gain compensator to be

$$K_{11}(s) = k_{11} \frac{40}{15} \frac{(s+15)}{(s+40)} \frac{(s^2+2\{0.01004\}\{35.65\}s+35.65^2)}{(s^2+2\{0.05\}\{35.65\}s+35.65^2)} \quad (4.12)$$

Evans and Bode plots corresponding to Eq. (4.12) are shown in Figs. 62-63. The notch filter attenuates mode 9 by 12 db. The lead-lag filter adds 27 deg of phase at 26.2 rad/s, 20 deg to meet the original phase margin requirement and 7 deg for losses due to the notch filter. The gain value  $k_{11} = 3.00$  rad/rad/s corresponds to a phase margin of 69 deg associated with mode 7. This selected gain value is larger than the baseline value by a factor of 1.3, and further loop gain adjustments are still available since stability margin constraints have yet to be reached. Here, the closed-loop value for damping of mode 1 is  $\zeta_1 = 0.207$ . This level of damping is required for substantial suppression of high frequency transient motions following vehicle excitations. This strategy is considered, to some extent, to be of high risk in the sense notching will require a

premium on design model accuracy, and possibly real-time mode frequency identification when implemented. The intensity of the notch, however, is characterized as mild, rather than aggressive, since the filter only restores margins to acceptable levels. The filter is not heavily relied upon to achieve basic stability, this characteristic is already inherent in the channel. If the notch frequency were in error, the system characteristics would tend to revert back to those of Fig. 57 (minimum of 20 deg phase margin).

In summary, four solutions have been considered for the aeroelastic suppression loop: a baseline system, a low-gain system, an intermediate-gain system, and a high-gain system. The low-gain system, which incorporates low pass logic, has several drawbacks including a restricted region of usable loop gain and little augmentation of modes 1-2. Phase loss is the culprit. The high-gain system, which incorporates a large phase lead element, also has several drawbacks including high bandwidth and reliance on high performance actuators. Only the two remaining candidate solutions warrant further study beyond the confines of this report, one of low risk, the other higher risk. Adoption of gain only compensation for the aeroelastic suppression loop provides reliable mode suppression logic with low sensitivity to modeling inaccuracies. The tradeoff is reduced performance as measured by aeroelastic mode damping ratios. Utilization of combined lead-lag and notch compensation takes a more bold course of action to exploit the full potential of the forward vane and associated feedback loop. Considerable leverage can be applied to the structural modes. However, the trade here is vulnerability to design model uncertainty. As will be shown, this latter strategy still provides good stability robustness characteristics. Thus, the lead-lag and notch strategy will be carried into further design steps in this section.

Design of this mode suppression loop is key to the proposed inner loop architecture described in this section. If this FCS architecture were to be adopted, or some modified version thereof, program activities should invest considerable resources in validating the feasibility and verifying the potential predicted for this loop, as described here in this report. Additionally, further investigations of design issues raised in this subsection are recommended.

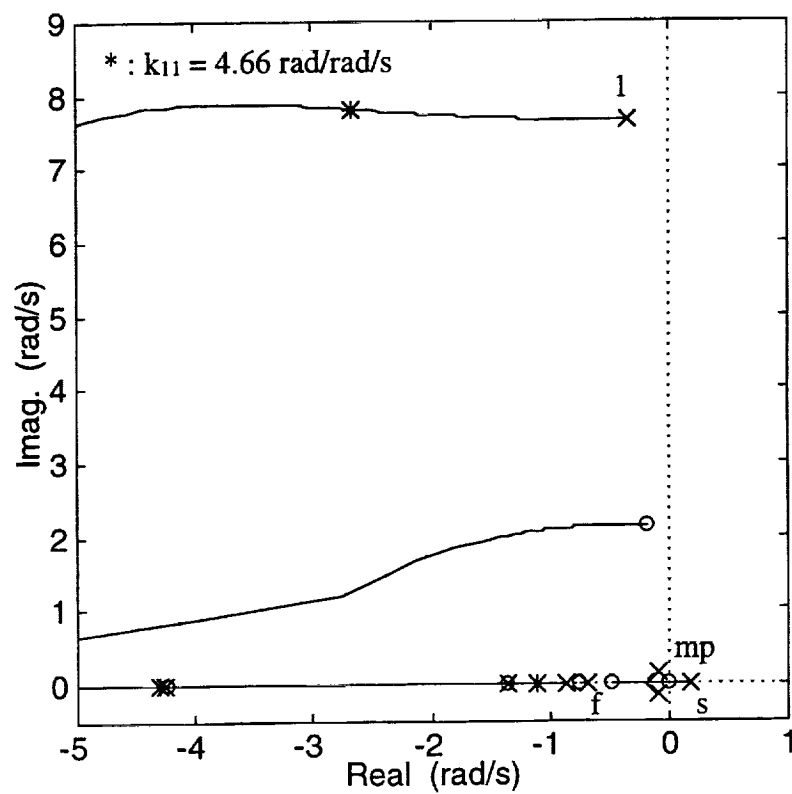
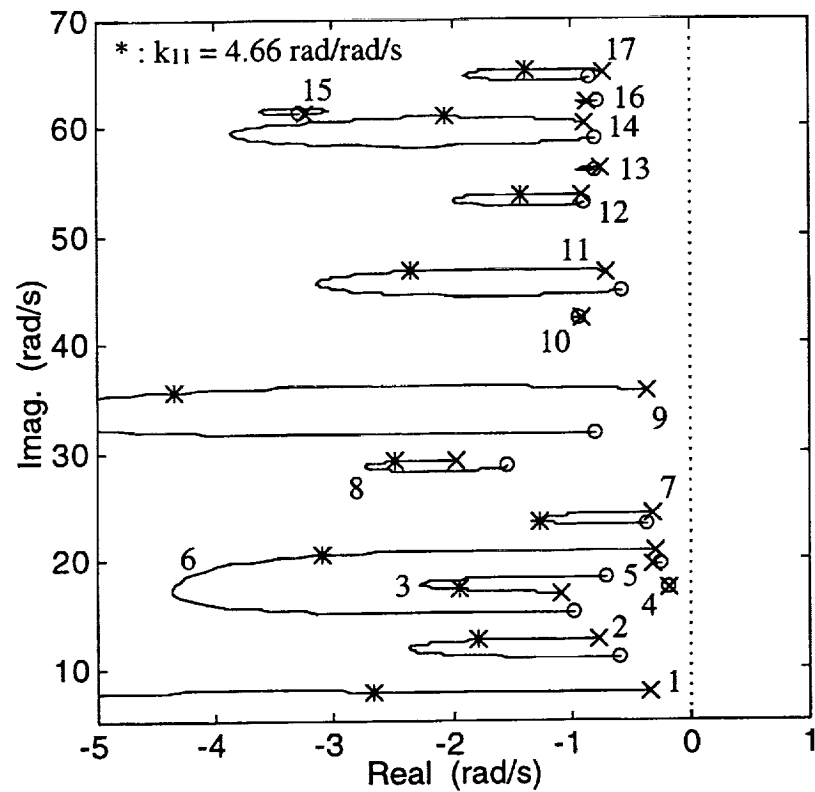


Figure 60. Evans Plot For 400 in Pitch Rate To Vane  
With Phase Lead Filter

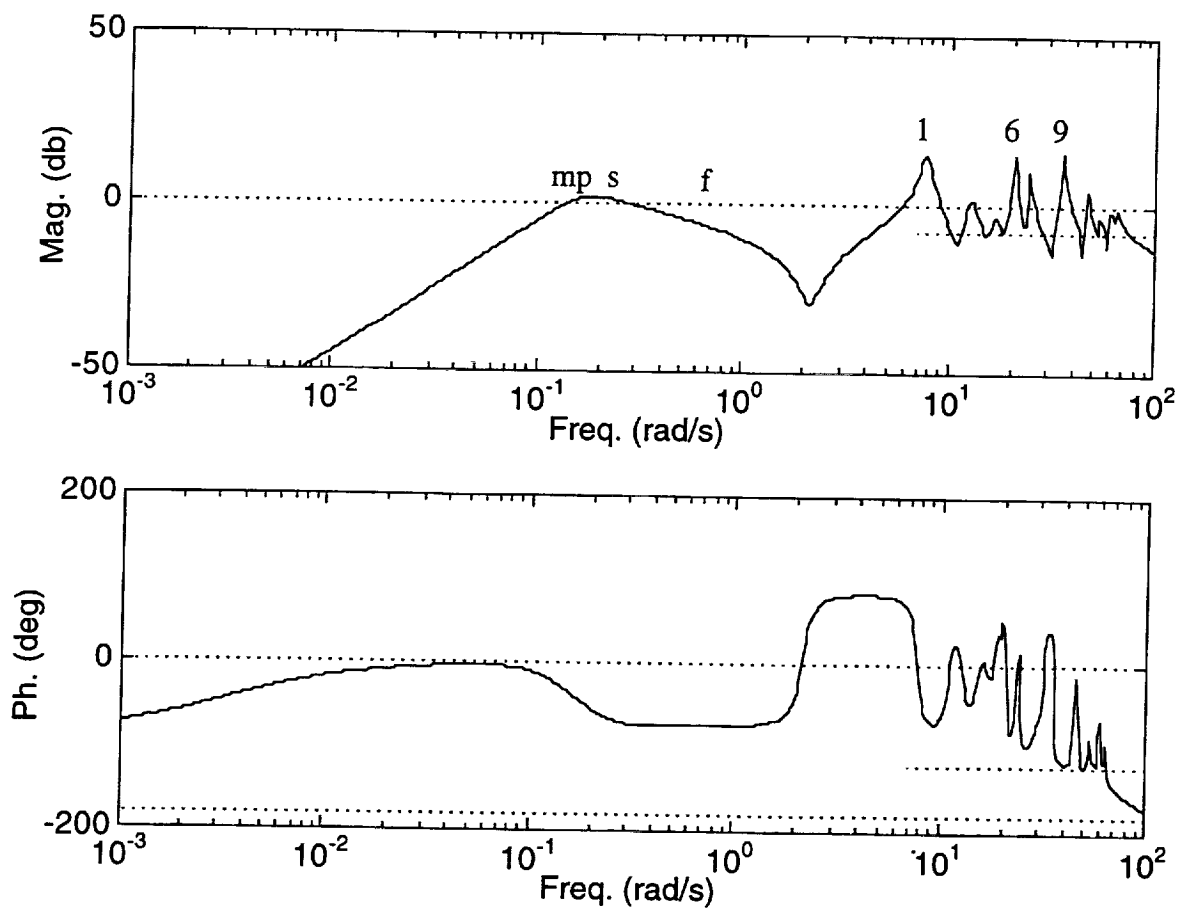


Figure 61. Bode Plot For 400 in Pitch Rate To Vane  
With Phase Lead Filter,  $k_{11} = 4.66$  rad/rad/s

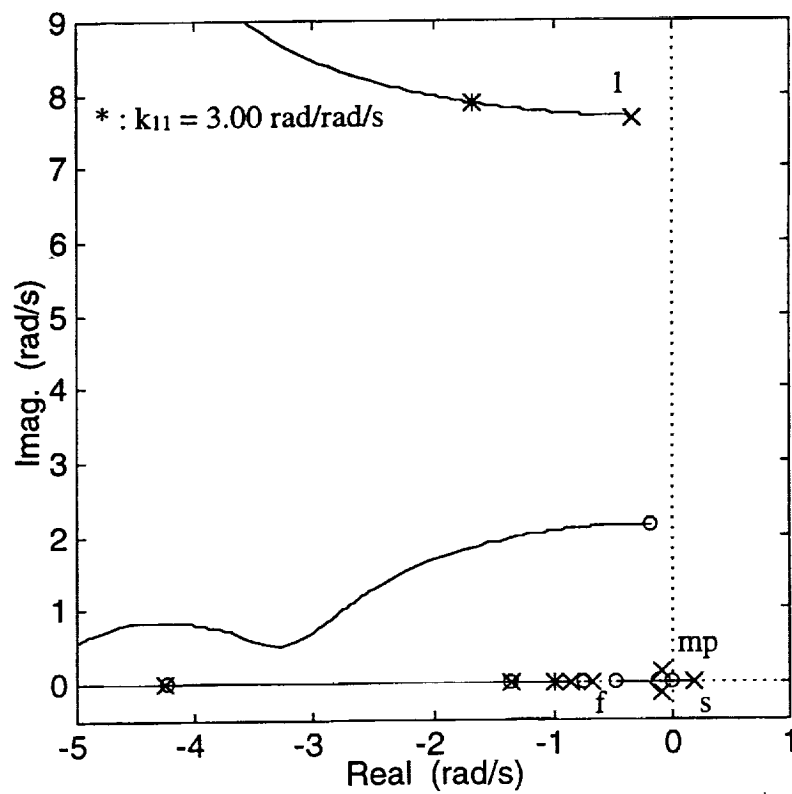
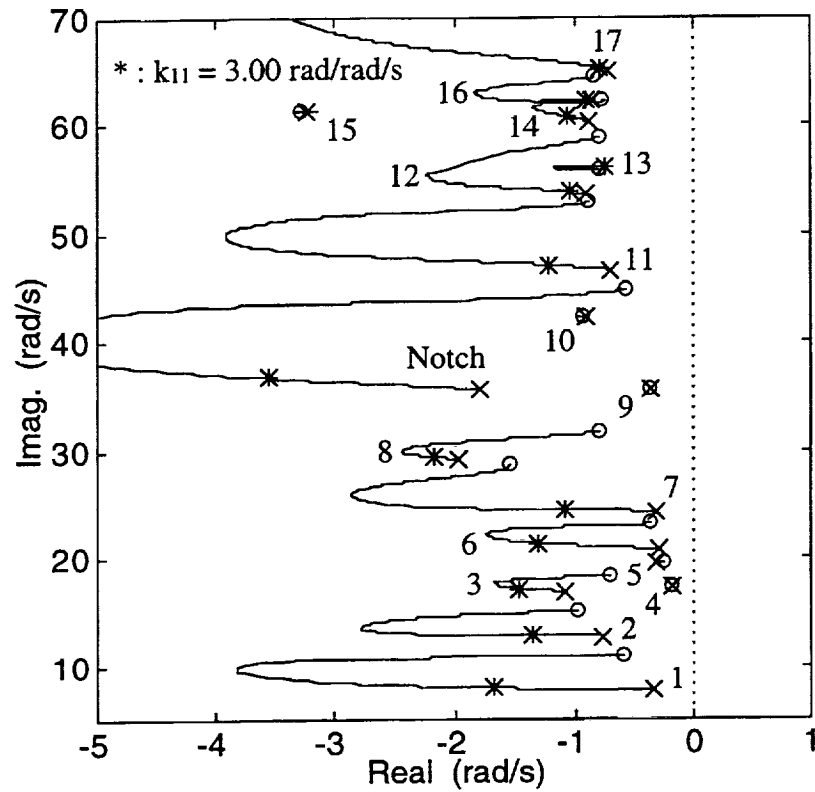


Figure 62. Evans Plot For 400 in Pitch Rate To Vane  
With Phase Lead And Notch Filter



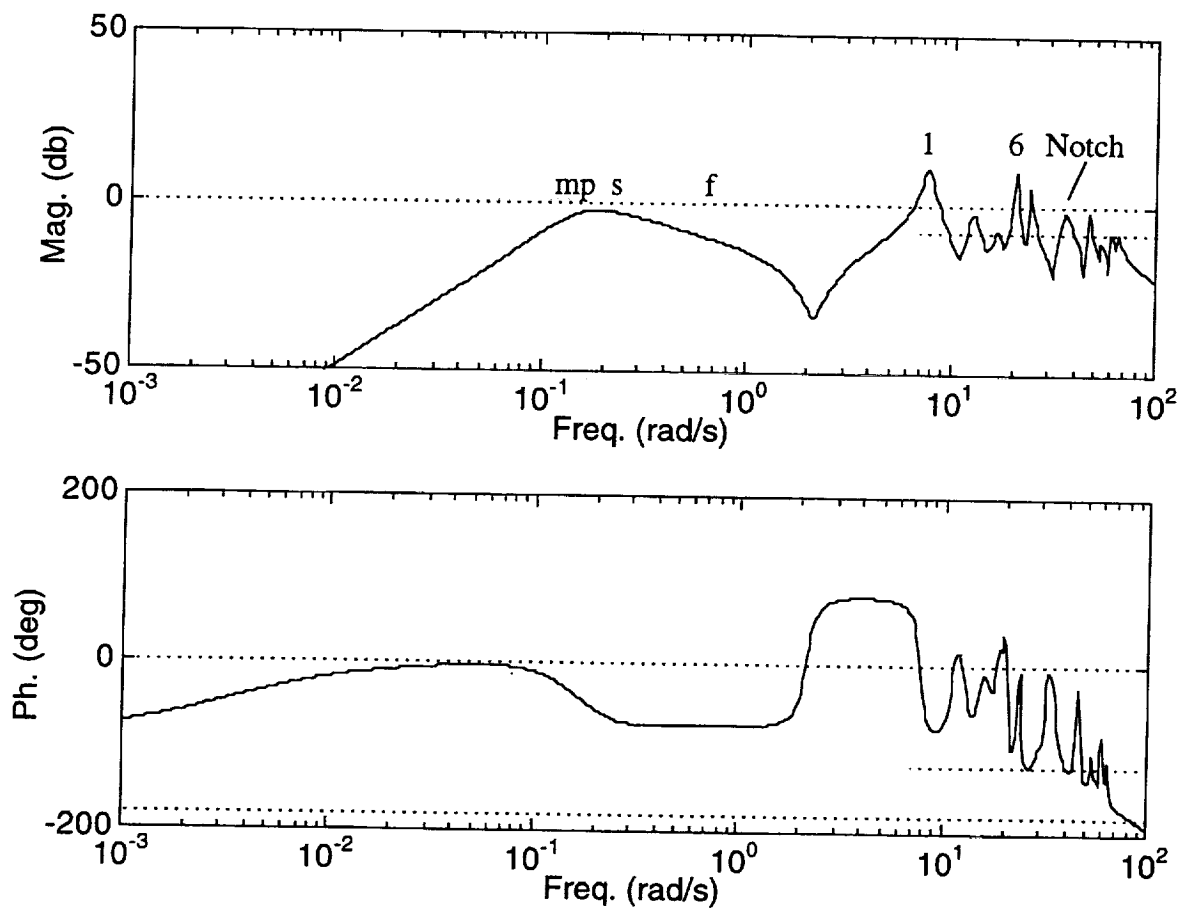


Figure 63. Bode Plot For 400 in Pitch Rate To Vane  
With Phase Lead And Notch Filter,  $k_{11} = 3.00$  rad/rad/s

### C. Coordination Crossfeed

Figs. 64 and 65 show the migration paths for the numerator roots (i.e., zeros) of the  $q_{400}/\delta_E$  and  $a_{z\ 400}/\delta_E$  dynamics corresponding to Eq. (4.5), as the crossfeed gain  $k_{cf}$  (i.e.,  $K_{cf}(s) = k_{cf}$ ) is varied. Note the  $q_{400}/\delta_V$  loop is already closed at this design stage. The SMCS design internal to this analysis is the combined lead-lag/notch compensation described in Eq. (4.12) and Figs. 62-63. Recall the crossfeed path in Fig. 54 is utilized to "bend" the forward portion of the vehicle to oppose elastic deflections arising from pitch commands issued at the aft tail. When translated into the mathematics, the crossfeed is used to eliminate, or reduce, critical nonminimum phase zeros associated with the  $q_{400}/\delta_E$  and  $a_{z\ 400}/\delta_E$  transfer functions. Additionally, the crossfeed is utilized to relocate zeros near critical augmented pole locations from Fig. 62. In Fig. 62, modes 1 and 2 are considered most critical based upon their contribution to the overall responses. These two intermediate pole locations ( $-1.7+j7.9$  and  $-1.4+j12.9$  1/s) are denoted by the "+" symbol in Figs. 64-65. The design strategy of the control architecture in Fig. 54 is now apparent: aeroelastic suppression is achieved by both mode damping (pole augmentation) and dipole "tightening" (zero augmentation).

In Fig. 64, the zero corresponding to mode 1 initiates from well within the right-half plane, and migrates to just inside the left-half plane ( $-0.17+j2.1$  1/s) for large values of  $k_{cf}$ . The right-half plane starting point for this migration path is an inherent characteristic of the non-collocated vehicle  $G_{12}(s)$  transfer function. For a nose down pitch command issued at the tail, an elastic pitch up contribution from mode 1 occurs (see deflection shapes in Fig. 28). This elastic pitch is initially out of phase with the rigid pitch motion. On the other hand, the zero designated with mode 2 starts from well within the left-half plane and migrates towards the imaginary axis ( $-0.58+j11$  1/s) as the gain  $k_{cf}$  increases. Fig. 28 indicates the elastic pitch contribution from mode 2 at this fuselage station is nose down and is initially in phase with the rigid pitch motion. Similar behavior is observed in the  $a_{z\ 400}/\delta_E$  transfer function in Fig. 65, except the mode 1 and mode 2 characteristics are reversed from that in Fig. 64. This reversal of characteristics is due to the inherent nonminimum phase behavior associated with forward station rigid acceleration. For the nose

down pitch command, the 400 in station will initially experience up acceleration from the rigid-body contribution to the overall motion. Acceleration from mode 1 is in phase, and acceleration from mode 2 is out of phase, with respect to this initial rigid motion. Hence, in Fig. 65, migration path 1 originates in the left-half plane while path 2 starts in the right-half plane.

For a crossfeed gearing ratio of  $-0.3 \text{ rad/s/rad}$ , the critical nonminimum phase zeros are reduced, but not fully eliminated. Use of a higher gearing ratio would fully eliminate these right-half plane zeros, but would also result in excessive vane travel and rate activity (see Section V). Excessive vane motions may impact airflow quality over the main wing and at the propulsion inlets. Further, aggressive vane command signals may not be realizable with current actuation hardware technology. Another important issue gleaned from the characteristics in Figs. 64-65 is the fundamental trade between the mode 1 and 2 dipole structures. Consider Fig. 65. For low gearing values (such as  $-0.3 \text{ rad/s/rad}$ ), the crossfeed is tuned to yield a tight dipole for mode 1 (maximum cancellation). This tuning leaves the modal contribution from mode 2 at a high level (i.e., loose dipole for mode 2). Utilization of higher gear ratios would result in opposite dipole characteristics. Similar observations are noted in Fig. 64, but the pitch rate behavior is fundamentally worse because the critical right-half plane migration branch is at a much lower frequency, when compared with corresponding features in Fig. 65.

This conflict between modes 1 and 2 is traceable to the deflection shapes given in Fig. 28. For a pitch command issued at the tail, modes 1 and 2 initially deflect in opposite directions at forward stations. Intentional "bending" of the forward vehicle structure to oppose mode 1 pitch motion inherently amplifies the contribution from mode 2, and vice versa. Due to the close spacing of modes, there is no direct means to independently leverage one mode and not the other. The vane mounting location could be slid back to the mode 2 node point, but significant leverage on mode 1 is lost. For the baseline vane and with static compensation for the  $K_{cf}(s)$  crossfeed block, the only available design freedom is gain adjustment to balance the structural contributions from modes 1 and 2 to the overall response. This balancing leads to unsatisfactory results.

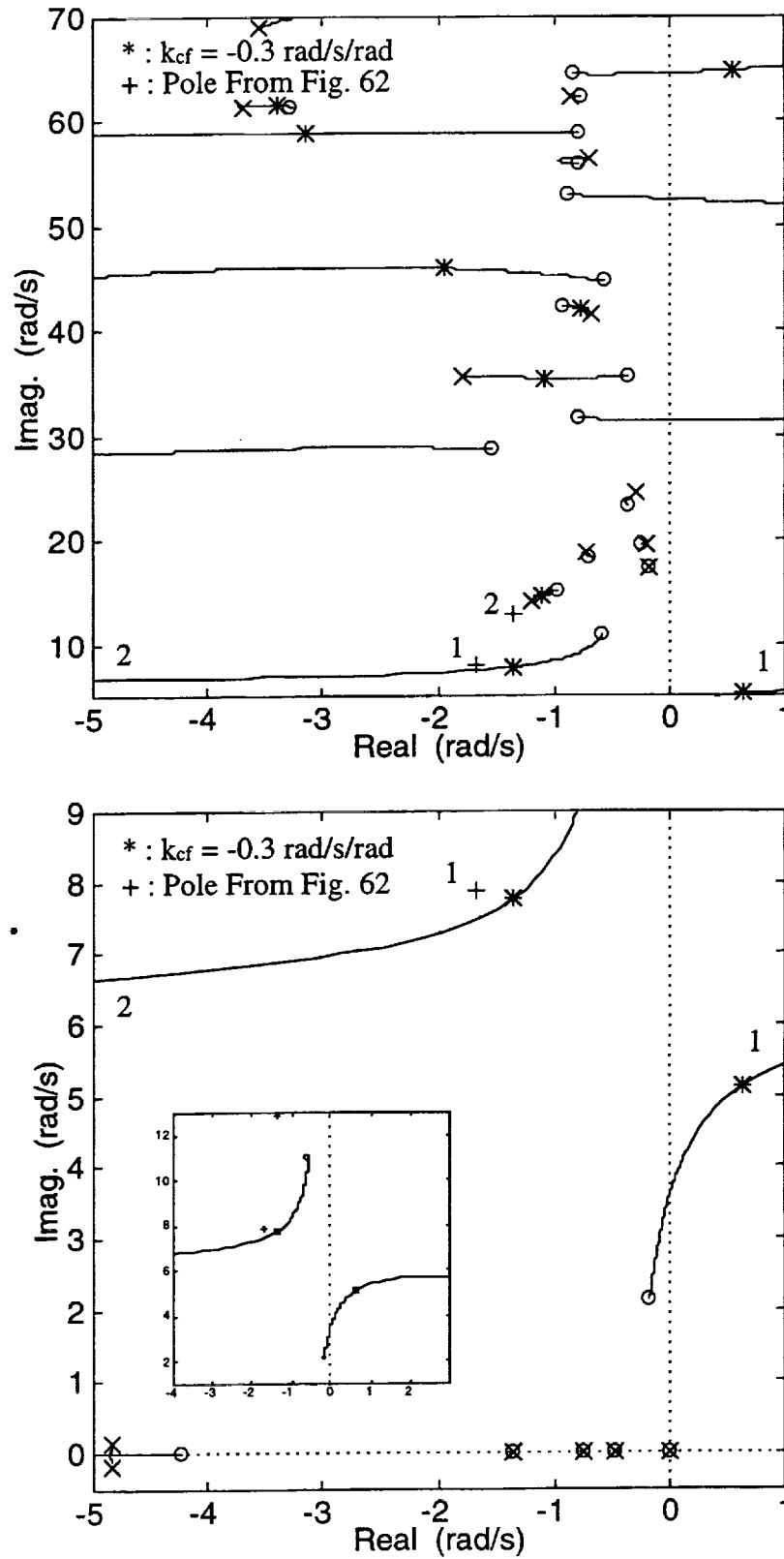


Figure 64. Numerator Migration Plot For 400 in Pitch Rate To Elevator With Static Compensation

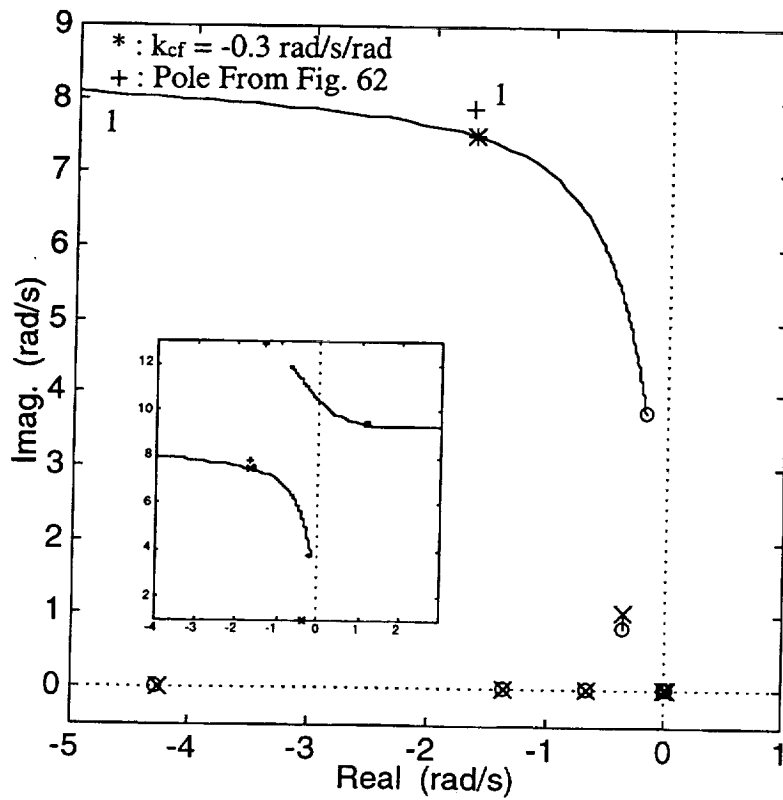
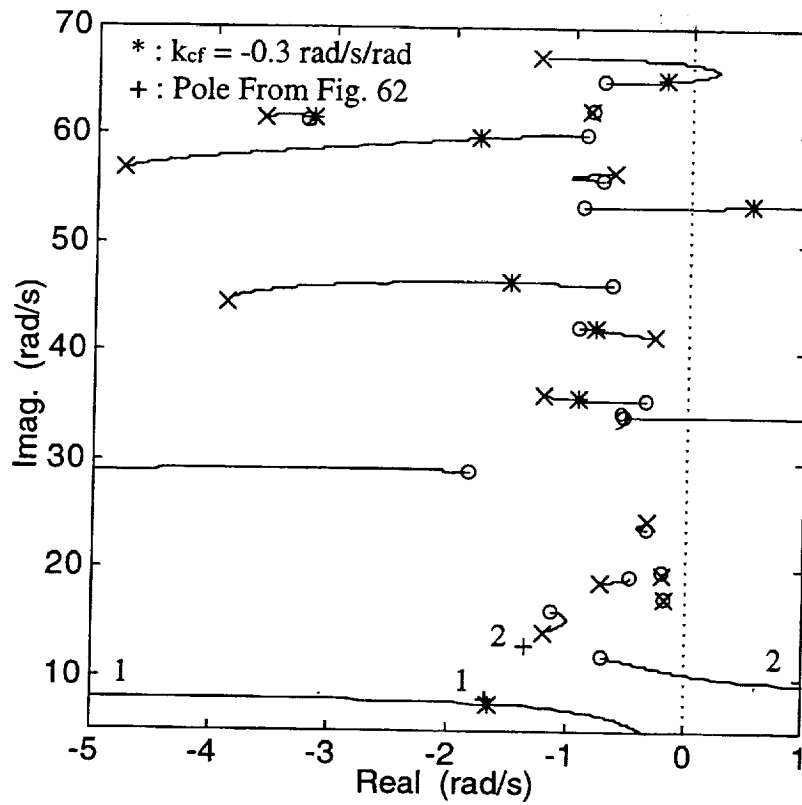


Figure 65. Numerator Migration Plot For 400 in Vertical Acceleration To Elevator With Static Compensation

Utilization of filtering in the crossfeed path has been found to lessen the severity of the trades noted above. Consider a "cliff" filter within the crossfeed block, or

$$K_{cf}(s) = k_{cf} \frac{10^2}{40^2} \frac{(s+40)(s+40)}{(s^2+2\{0.5\}\{10\}s+10^2)} \quad (4.13)$$

This filter consists of two, considerably damped, complex conjugate poles and a pair of real zeros, with break frequencies beyond the denominator natural frequency. The magnitude frequency response shape associated with this filter includes steep (cliff) attenuation beyond the denominator break point and gradual leveling off of magnitude beyond the numerator break points.

Figs. 66-67 show the  $q_{400}/\delta_E$  and  $a_z/400/\delta_E$  numerator migration characteristics corresponding to the dynamic crossfeed  $K_{cf}(s)$  in Eq. (4.13). In both transfer functions, the cliff filter denominator has the effect of introducing a new migration path. This new migration path starts at the cliff filter pole  $-5+j8.7$  1/s and terminates at the points  $-0.17+j2.1$  and  $-0.19+j3.8$  1/s, respectively, in Figs. 66-67. This new path serves as a replacement path for the original mode 1 path (compare the paths labeled "Cliff" in Figs. 66-67 with the paths labeled "1" in Figs. 64-65). An initial assessment of the mode 1 dipole characteristics in Figs. 66-67, relative to the corresponding features in Figs. 64-65, would indicate degraded behavior for the modal contribution to the responses. The mode 1 dipoles in Figs. 66-67 are considerably more open than in Figs. 64-65. However, when both mode 1 and mode 2 dipoles are considered simultaneously, the new characteristics yield notable improvements in the overall modal contributions. A much improved balance between the mode 1 and mode 2 contributions to the responses is obtained with the cliff filter. A value of  $k_{cf} = -0.25$  rad/s/rad provides the "best" balance when monitoring the time responses of the final overall closed-loop system. Another added benefit from the cliff filter is the readjustment of the critical nonminimum phase migration paths to higher frequency regions. Note in Figs. 66-67 the paths originating in the right-half plane labeled "1" and "2" are pushed to a higher frequency when compared with Figs. 64-65.

In terms of the mechanics, this dynamic crossfeed, in response to pitch commands at the tail, will tend to actively control and oppose the out of phase elastic pitch deflections in the

frequency region below 10 rad/s (mode 1), and will respond with reduced authority to the in phase elastic pitch motions occurring above 10 rad/s (mode 2). Under the fixed inner loop architecture given in Fig. 54, there appears to be few other alternative solutions for the crossfeed logic. Crossfeed filters exploiting right-half plane parameters is one alternative, but is not recommended for systems which must be implemented. The two channel control architecture is well suited for augmenting the rigid pitch and lowest frequency structural modes. When the next higher frequency structural mode becomes significant, as in the HSCT configuration, the two channel architecture has limitations to what can be accomplished. Here, these limitations manifest themselves in terms of the crossfeed action impacting modes 1 and 2 in opposing manners, and the resulting residual aeroelastic contamination remaining in the responses. Consideration of a three surface deflection strategy is beyond the scope of study here.

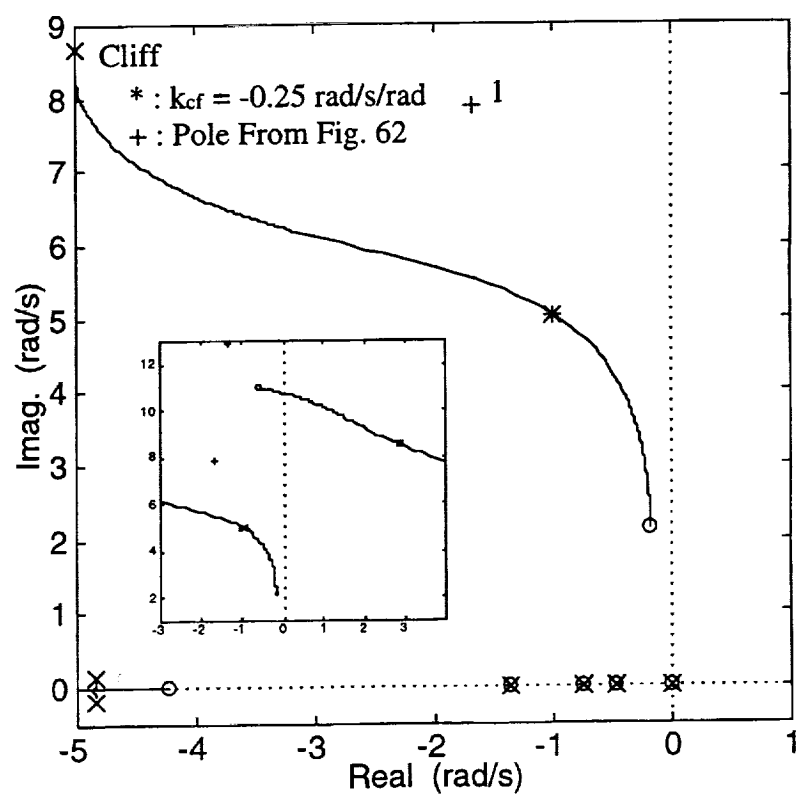
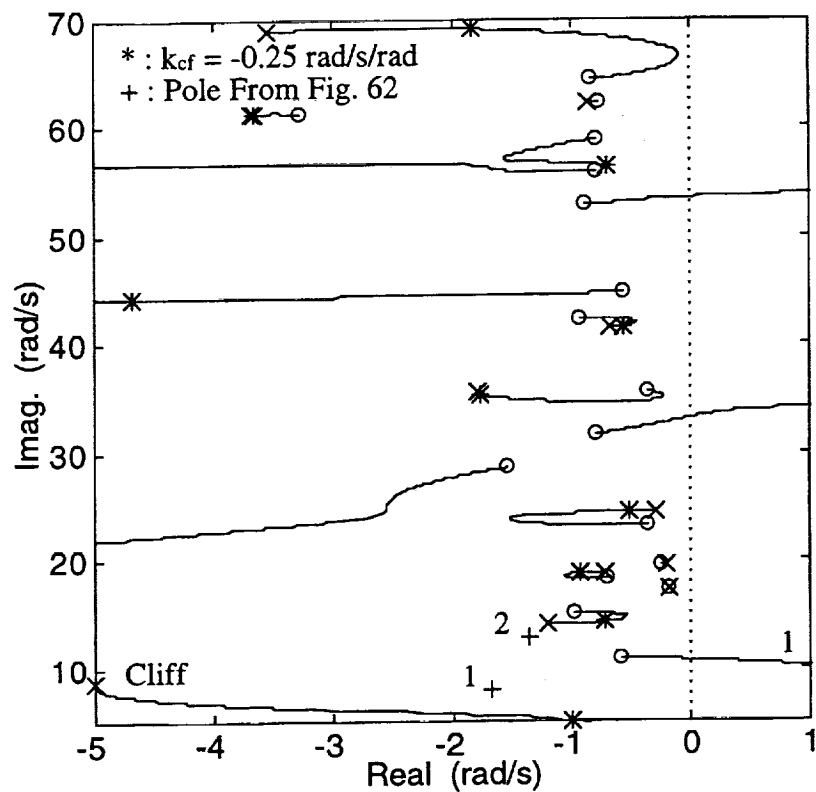


Figure 66. Numerator Migration Plot For 400 in Pitch Rate To Elevator With Cliff Filter



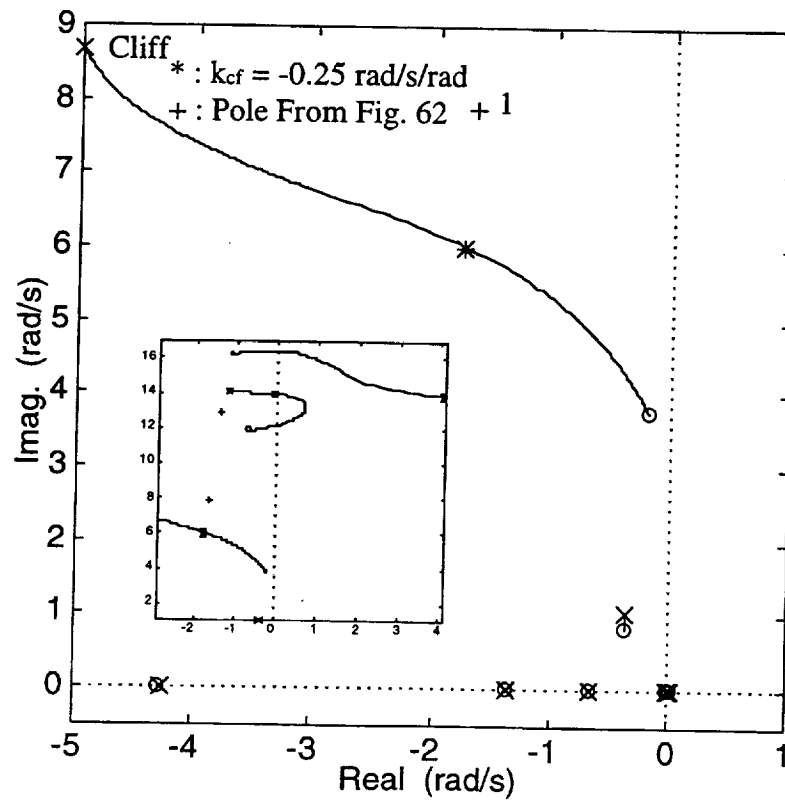
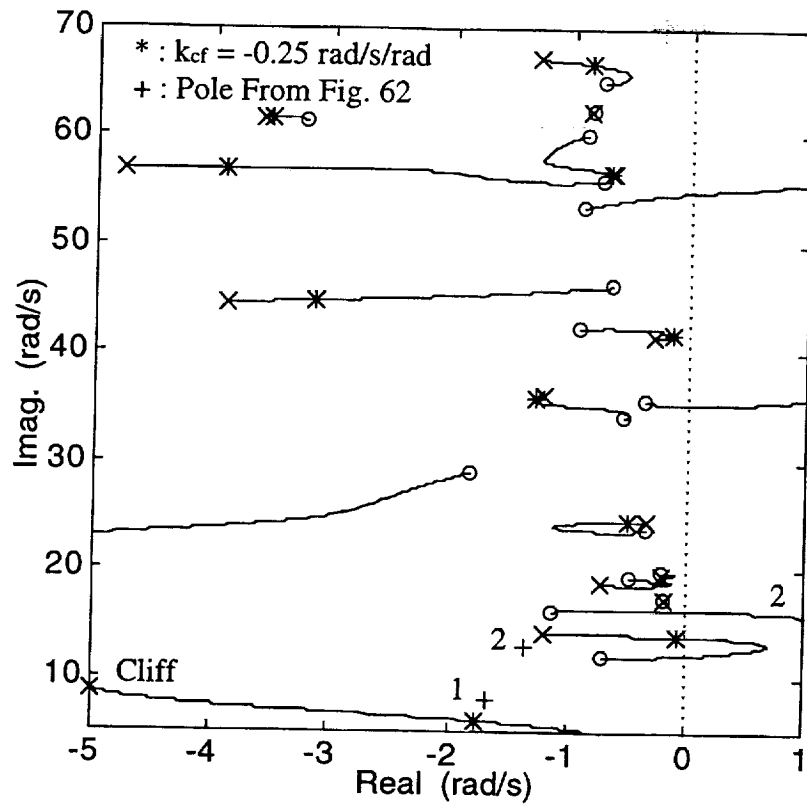


Figure 67. Numerator Migration Plot For 400 in Vertical Acceleration To Elevator With Cliff Filter

#### D. Pitch Augmentation Loop

Consider the traits of the  $q_{1850}/\delta_E$  transfer function Evans plot corresponding to Eq. (4.7) in Fig. 68. In this loop, the baseline controller equalization is proportional-integral (PI) logic, or

$$K_{22}(s) = k_{22} \frac{(s+z)}{s} \quad (4.14)$$

For a relaxed stability airframe (such as the HSCT at low altitude, subsonic flight conditions), PI compensatory manipulation of the pitch rate error signal is a highly effective strategy for stabilization and augmentation of the pitch characteristics. Here, the PI parameter  $z$  will be selected as  $z = 2 \text{ 1/s}$ . Again note the aeroelastic suppression loop with Eq. (4.12), and now the crossfeed with Eq. (4.13), are intrinsic to the system characteristics discussed here. In Fig. 68, observe how the unstable real axis pole is driven into  $1/\tau_{\theta 1}$ , which resides slightly in the left-half plane, and how the mid period mode moves out to become the dominant pitch mode. As expected, the 1<sup>st</sup> aeroelastic pole is accompanied by a closely spaced zero, canceling any effects from this mode in the signal as it travels around the loop, regardless of the loop gain. Focusing on the higher frequency aeroelastic modes, the 1,850 in sensor leads to "out of phase" pick-up of the 2<sup>nd</sup> and 11<sup>th</sup> modes. As the loop gain  $k_{22}$  is increased, these modes lose damping and eventually lead to instabilities. Similar behavior was noted in Ref. 13, but here the aeroelastic suppression loop has already damped these modes, allowing some of the damping to be traded off. The design constraints associated with 1) having a sufficient level of gain for handling qualities, and 2) keeping the gain sufficiently low to preserve aeroelastic stability margins, are significantly less severe when contrasted with similar characteristics observed in Ref. 13 using a SS/SS control architecture.

The closed-loop poles in Fig. 68 are highlighted for a compensator gain of  $k_{22} = -3.07$  rad/rad/s. Fig. 69 shows the corresponding Bode plot. For this gain value, the real axis instability is neutrally stable (note the dc gain of 0 db in Fig. 69 and the closed-loop pole at the origin in Fig. 68). Magnitude crossover occurs at 1.3 rad/s, and is later shown to be satisfactory for pitch damping and frequency, rigid phase margin, and aeroelastic gain margin requirements. The key to

mutual attainment of these various requirements noted in Fig. 69 is the secondary vane loop dedicated to aeroelastic suppression. The vane loop has the fortuitous effect of attenuating the Bode magnitude response peaks in Fig. 69 beyond 6 rad/s. One major deficiency still exists in Fig. 69, however. For the indicated controller gain, note the dc gain in the Bode plot does not meet the low frequency 4.5 db gain margin requirement. In fact, the relaxed stability mode is not fully stabilized with this gain value. A simple solution for this problem will be discussed shortly.

These Evans and Bode features give a qualitative perspective of the much improved tradeoffs (relative to Ref. 13) between rigid-body and aeroelastic characteristics associated with the pitch augmentation loop. For a quantitative description of the tradeoffs, consider Tab. 14 which indicates compliance or non-compliance with several flying quality requirements and metrics, as the loop gain  $k_{22}$  is adjusted. Performance metrics include rigid pitch frequency, damping, control anticipation (CAP), and omega-tau, while stability metrics consist of the rigid low frequency gain margin, rigid high frequency phase margin, and aeroelastic mode 2 gain margin. These metrics are as defined in Refs. 1 and 2. In Fig. 69 note the phase point corresponding to mode 6 is very near -180 deg and the peak magnitude values of mode 6 and mode 2 are nearly equal. Therefore, the computed aeroelastic gain margin for mode 2 also approximately represent margins for mode 6. Shaded boxes in Tab. 14 indicate noncompliance with the requirement.

Before starting the discussion, a few comments are in order. The flying quality requirements spelled out in Refs. 1-2 have not been validated for highly flexible vehicles, and do not fully address important flying quality issues expected with such vehicles.<sup>24</sup> Never the less, there is little else to base flight control decisions on, short of costly piloted simulation tests. Therefore, the requirements are used here, but only to seek ballpark estimates of flying quality levels, not definitive answers. Because of the uncertainty involved, and to reduce computational burdens, the equivalent systems approach was not considered here. Therefore, the numbers in Tab. 14 were calculated by using data taken directly from the full order model, not an equivalent number from a reduced order model. In computing  $\omega_{sp}\tau_{\theta 2}$ ,  $1/z$  was substituted for  $\tau_{\theta 2}$ . Further, the requirements correspond to Class III vehicles in Category C flight.

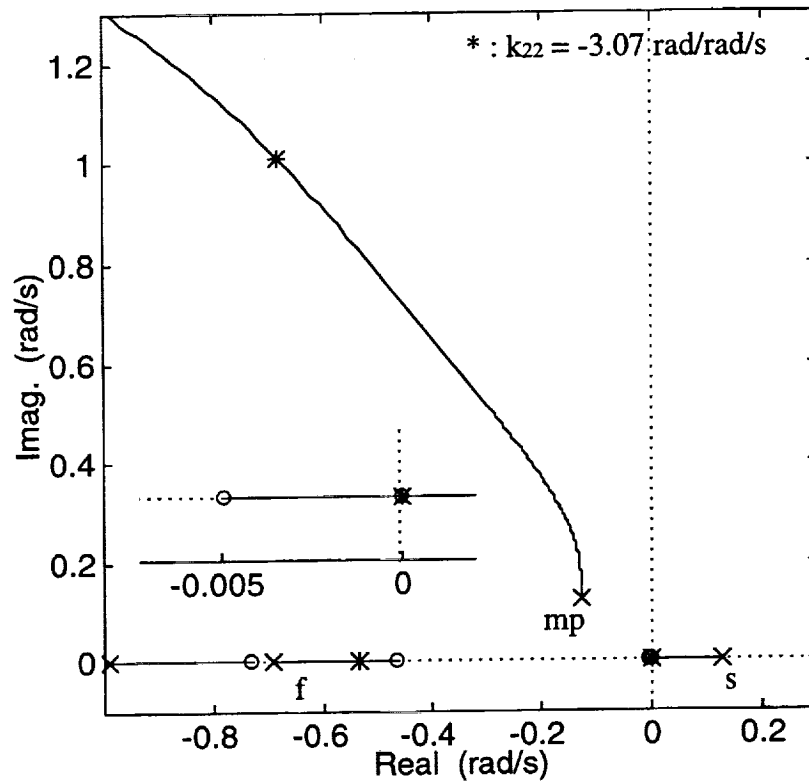


Figure 68. Evans Plot For 1,850 in Pitch Rate To Elevator Without Filtering

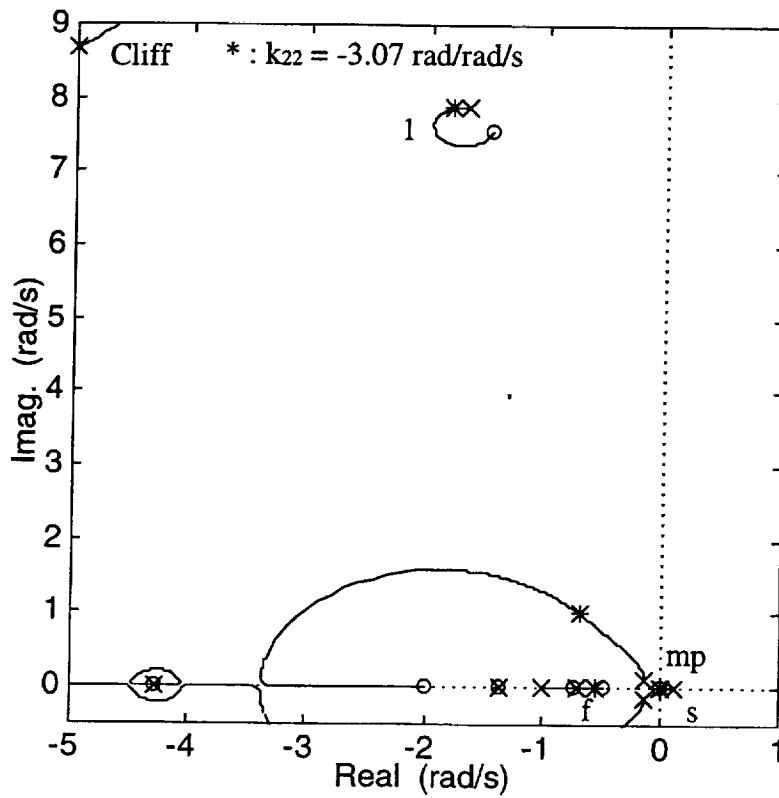
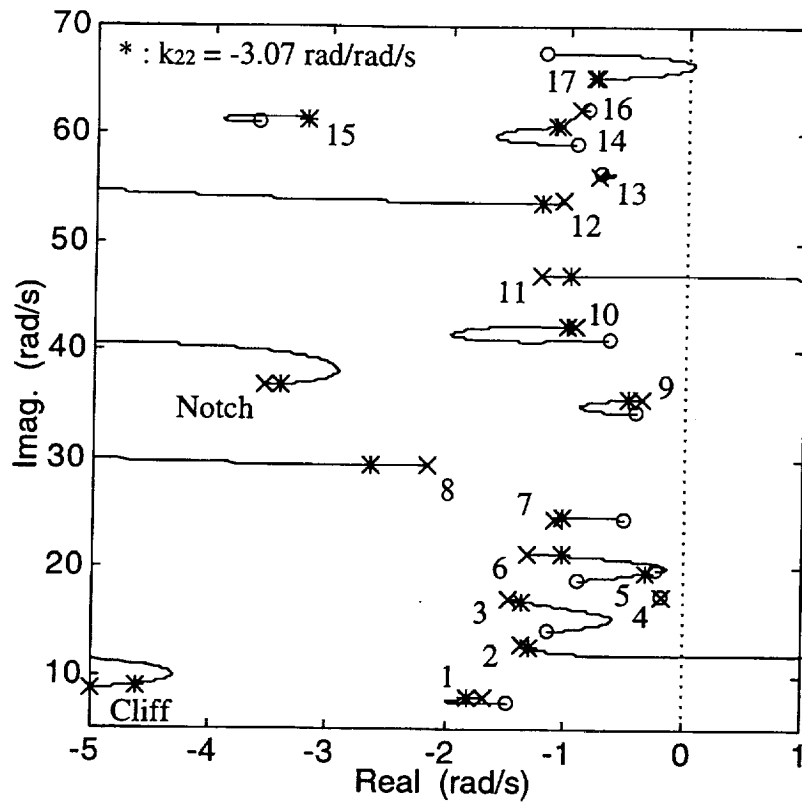


Figure 68. Continued

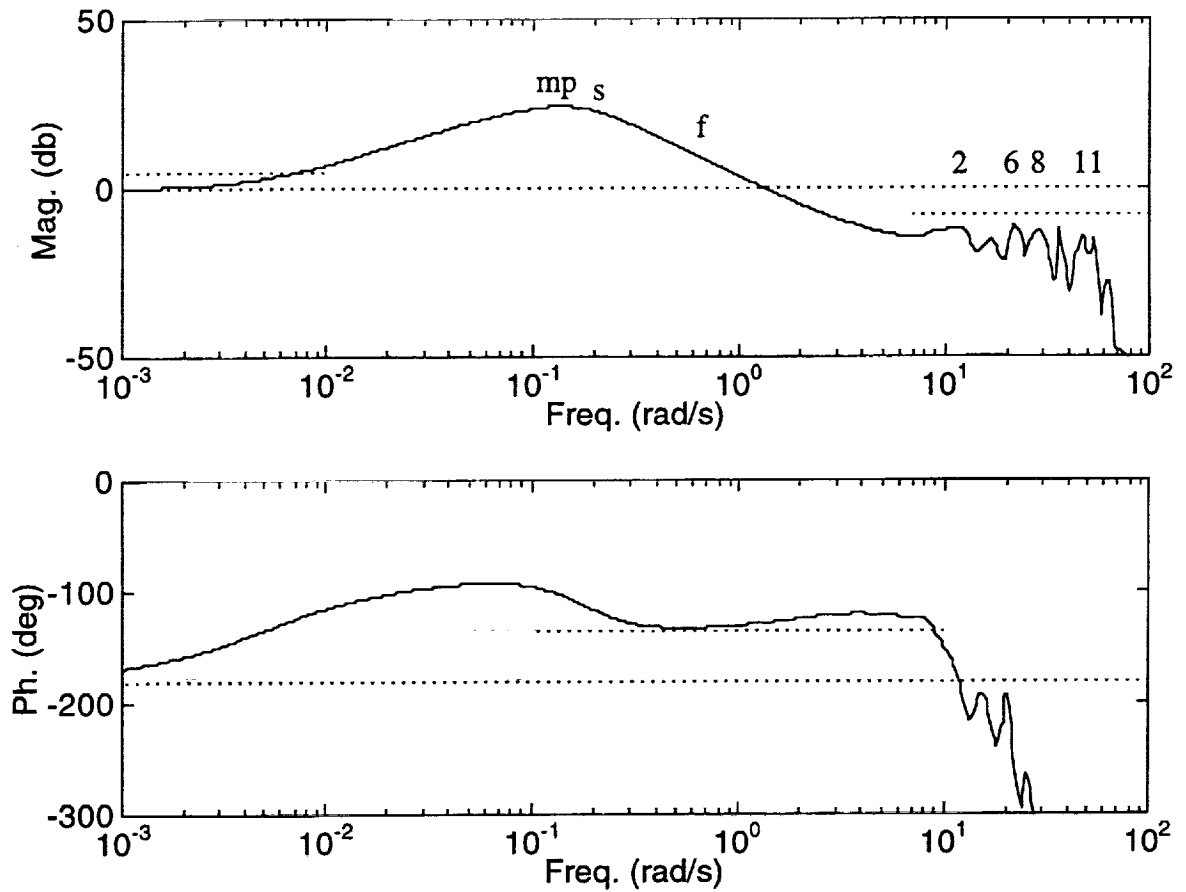


Figure 69. Bode Plot For 1,850 in Pitch Rate To Elevator  
Without Filtering,  $k_{22} = -3.07 \text{ rad/rad/s}$

Table 14. System Characteristics With Gain Adjustment For 1,850 in Pitch Rate To Elevator Without Filtering							
$-k_{22}$ (r/r/s)	$\omega_{sp}$ $\geq 0.7$ (r/s)	$\zeta_{sp}$ $\geq 0.35$ (-)	CAP $\geq 0.16$ (1/g $s^2$ )	$\omega_{sp}\tau_{\theta 2}$ $\geq 1.3$ (-)	GM $_{\omega < .38}$ $\geq 4.5$ (db)	PM $_{\omega > .38}$ $\geq 45$ (deg)	GM $_2$ $\geq 8$ (db)
0.46	0.38	0.47 (min)	0.0087	0.19	-16.49	48.8	28.47
1.12	0.64	0.51	0.025	0.32	-0.76	47.6	20.74
3.07	1.22	0.56	0.089	0.61	0.00	51.6	11.98
5.22	1.66	0.61	0.17	0.83	4.61	55.2	7.37
7.04	1.97	0.66	0.23	0.99	7.21	57.5	4.77
8.84	2.22	0.71	0.30	1.11	9.19	59.1	2.80
10.73	2.45	0.76	0.36	1.23	10.87	59.8	1.11
12.78	2.67	0.81	0.43	1.34	12.39	59.5	-0.41

The entries in Tab. 14 correspond to 0.05 increments in rigid pitch damping, and note that one entry corresponds to the gain previously discussed. Level 1 requirements for short period damping, frequency and control anticipation, as well as requirements for low-end rigid gain margin and high-end rigid phase margin, can all be satisfied with only a small violation in the aeroelastic mode 2 gain margin requirement (for  $k_{22} = -5.22$  rad/rad/s). It should be noted that ratings based on omega-tau do not correlate particularly well with those based on control anticipation. In general (aside from the noted exception), as loop gain is increased, rigid-body performance requirements for predicted Level 1 flying qualities and stability requirements become satisfied just as the aeroelastic mode 2 gain margin violates the 8 db requirement. In Tab. 14, negative gain margin entries imply a margin deficiency beyond neutral stability. Fig. 70 illustrates the situation further. These plots show the CAP vs.  $\zeta_{sp}$  and  $\omega_{sp}\tau_{\theta 2}$  vs.  $\zeta_{sp}$  predicted pilot ratings with aeroelastic gain margin as the parameterization. The 2<sup>nd</sup> aeroelastic mode gain margin is just compromised as good rigid-body flying qualities are attained (based on CAP). These relationships support a high level of confidence in meeting the closed-loop objectives with the proposed inner loop control architecture in Fig. 54.

Refocus attention on stabilization of the relaxed stability mode in Figs. 68-69. This mode is closely tied to the forward speed degree of freedom. One possible solution would be utilization of a speed control loop (either elevator or throttle based) to leverage this unconventional low frequency mode. This solution may add unnecessary control architecture, and may complicate

interfacing issues with a "flight path rate / speed" outer loop control system, the current baseline outer loop architecture for HSCT. Here, utilization of the basic pitch augmentation characteristics previously discussed is recommended. Simple loop gain increments will stabilize the mode. To desensitize the aeroelastic modes to this increased loop gain, a somewhat nonstandard strategy is utilized. The Bode magnitude response above 0.01 rad/s will be attenuated uniformly by the amount approximately needed to stabilize and robustize the relaxed stability mode (4.5 db). This attenuation is achieved from a small lag-lead filter located near 0.01 rad/s. In the critical frequency range, there is virtually no loss of phase from this filter. The low frequency instability is then stabilized, and original crossover bandwidth is recovered, by overall gain adjustment.

The Bode plot for this modified loop design appears very similar to Fig. 69, except the dc magnitude value is now at 4.5 db. Based on criteria already presented, acceptable pitch handling qualities (at the 1,850 in station) and stability margins across the entire frequency spectrum are attainable with the modified loop shape. However, examination of the 400 in pitch rate response due to stick commands reveals an objectionable level of residual structural vibration. In other words, 8 db attenuation of the aeroelastic modes in the 1,850 in loop for stability purposes is not sufficient for performance requirements at other stations. Thus, to further attenuate these modes, a low pass filter with break frequency at 10 rad/s is inserted into the loop design. The low pass filter leads to approximately 6.7 deg of phase loss at the gain crossover point. The overall phase at this same point is 1.2 deg shy of compliance with the 45 deg margin requirement. To recover this margin, an additional small lead-lag circuit is incorporated near 1 rad/s.

The final compensator is

$$K_{22}(s) = k_{22} \frac{(s+2)}{s} \frac{0.01}{0.02} \frac{(s+0.02)}{(s+0.01)} \frac{1.2}{1.1} \frac{(s+1.1)}{(s+1.2)} \frac{10}{(s+10)} \quad (4.15)$$

and Tab. 15 summarizes the design for a gain value of  $k_{22} = -5.08$  rad/rad/s. Also, Figs. 71 and 72 show the final Bode and Evans features. By exploiting the additional filtering in Eq. (4.15), rigid-body stability and performance requirements and aeroelastic stability requirements could all be achieved simultaneously, if a sufficient level of gain is selected. However, a low gain was



intentionally selected ( $k_{22} = -5.08$  rad/rad/s) to keep the residual structural vibrations, in forward station responses, to a "sufficiently small" level. For this gain value, the rigid-body gain crossover only reaches 1.18 rad/s, as seen in Fig. 71. Short period frequency and damping meet Level 1 requirements. However, control anticipation only satisfies the Level 2 requirement (see Tab. 15). Simultaneously, the rigid-body low-end gain margin and high-end phase margin are very near the 4.5 db and 45 deg requirement levels, but do satisfy these requirements. In addition, the aeroelastic mode 1 gain margin is intentionally set well above the 8 db requirement for reasons stated previously. The control anticipation value could easily be boosted to a Level 1 rating with a modest gain increment equivalent to approximately 4 db, still leaving approximately 12 db gain margin for mode 2. However, a more comprehensive assessment, which additionally considers effects on handling qualities from transient response characteristics originating from residual vibrations, would, with high probability, predict a lower rating.

Table 15. Design Summary Of 1,850 in Pitch Rate To Elevator With Filtering,  $k_{22} = -5.08$  rad/rad/s

Metric	Level 1	Level 2	(unit)	Design
$\omega_{sp}$	$\geq 0.7$	$\geq 0.4$	(rad/s)	1.15
$\zeta_{sp}$	$\geq 0.35$	$\geq 0.25$	(-)	0.54
CAP	$\geq 0.16$	$\geq 0.05$	(1/gs <sup>2</sup> )	0.08
$\omega_{sp} \tau_{\theta 2}$	$\geq 1.3$	$\geq 0.75$	(-)	0.58
$GM_{\omega < .38}$	$\geq 4.5$	-	(db)	4.51
$PM_{\omega > .38}$	$\geq 45$	-	(deg)	46.05
$GM_2$	$\geq 8$	-	(db)	16.26

Figs. 73 and 74 show the pitch rate and vertical acceleration responses at the 400 in station for the design summarized in Tab. 15 due to a 1 deg/s nose up command issued at  $y_{2c}$  in Fig. 54. The basic closed-loop response shapes are as expected for such a large airframe with a long lever arm to the cockpit: pitch rate rises with one significant overshoot and settles near the commanded value in approximately 4 s and acceleration generally follows the pitch rate response ( $a_z \sim -x_{B\dot{q}} - Uq$ ). Superimposed on these rigid pitch characteristics, is the residual structural

vibrations that remain even after being actively suppressed. These transients would be even more severe if the pitch loop gain were increased further to satisfy Level 1 CAP requirements. No disagreement will be given concerning the significance of the initial transient motions in these responses (especially for acceleration in Fig. 74) and the impact they may have on compensatory piloting tasks and ride comfort. However, a refined assessment of the features in Figs. 73-74 reveals some attractive characteristics. In direct response to a nose up command, ocular and vestibular cues (both rotational and translational) stimulating the crew would exhibit high initial onset which is in phase with the command signal, and remains so. The observed visual scenery would indeed be rapid nose up motion relative to the horizon. Likewise, the crew would initially receive a solid "kick in the pants" inertial load in the proper direction. The strength of this inertial cue does exhibit transients (approximately 0.02 g or 17% of the steady value, approximately 0.12 g) for about 1.5 s. However, the acceleration cue does not, and does not come close to, direction change ( $\pm$  sign) during these short duration transients. It is quite probable an experienced and sufficiently trained pilot could perform successful closures on such dynamics. Quantification of these effects, through testing and criteria development, for aeroelastic vehicle dynamics and control requires additional work.<sup>24</sup>

The response characteristics in Figs. 73-74 are near optimal, under the proposed architecture and practical constraints discussed in Sections IV-A through IV-D. Each component in the overall multivariable controller is important to, and is tuned for, achieving the dynamic performance levels noted in Figs. 73-74. If any single component is removed, the response characteristics degrade significantly. This sensitivity should not be confused with robustness to unmodeled dynamics and parameter variations. On the contrary, Tab. 15 indicates good gain/phase margins and Section IV-F shows good parameter margins, as well. The response levels in Figs. 73-74 can be improved upon if greater design risks are taken. A more aggressive posture in the aeroelastic suppression loop would damp the residual vibrations seen in Figs. 73-74. This would, in turn, allow for more aggressive augmentation in the pitch loop leading to Level 1 flying qualities (predicted by control anticipation values). A more aggressive filtering strategy in

the crossfeed block would also result in reduced initial transients. The proposed crossfeed is currently tuned to strike a balance between mode 1 and mode 2 contributions to the initial transients, as can be seen in Fig. 74. This report offers several options for the inner control loops for a HSCT class vehicle and shows the tradeoffs between these options. However, program management must ultimately decide the level and aggressiveness of augmentation that is to be undertaken, if this architecture, or a derivative thereof, is adopted.

In Ref. 13, where scalar-loop architectures were considered for both pitch augmentation and aeroelastic suppression simultaneously, a very severe trade between pitch handling characteristics and aeroelastic stability existed. In the multi-loop architecture considered here and implemented with the additional vane loop, this trade becomes one of pitch handling qualities vs. aeroelastic residual vibration, in a performance sense, not a stability sense. Although a significant trade issue remains, it is considerably more appealing than one involving basic stability levels. With the feedback signals fully exploited, the remaining response deficiencies will be resolved with the command signal prefilter.

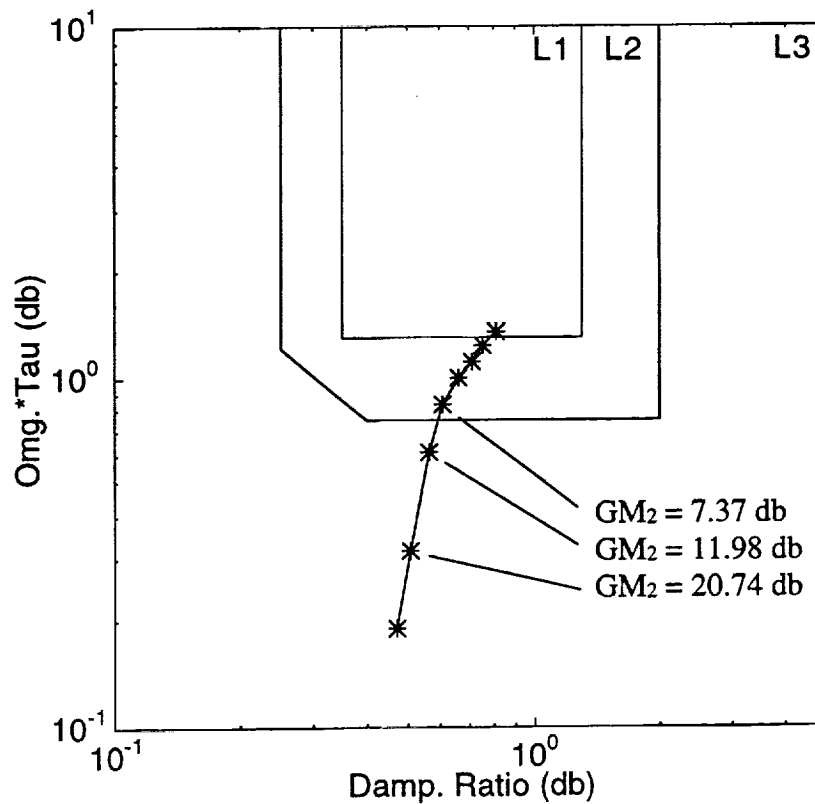
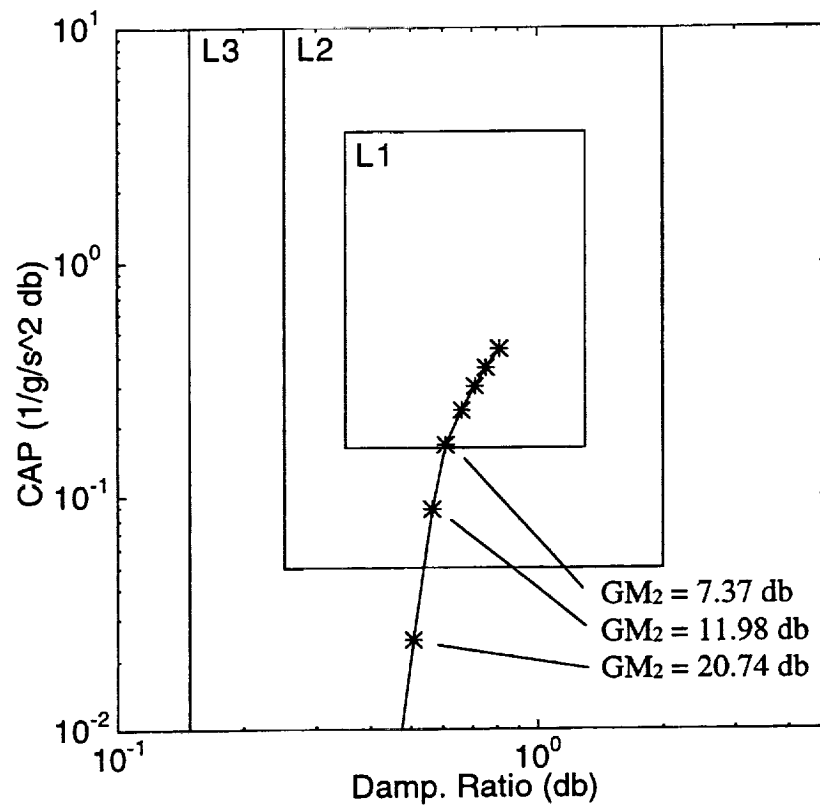


Figure 70. Control Anticipation & Omega-Tau vs. Damping  
For 1,850 in Pitch Rate To Elevator Without Filtering

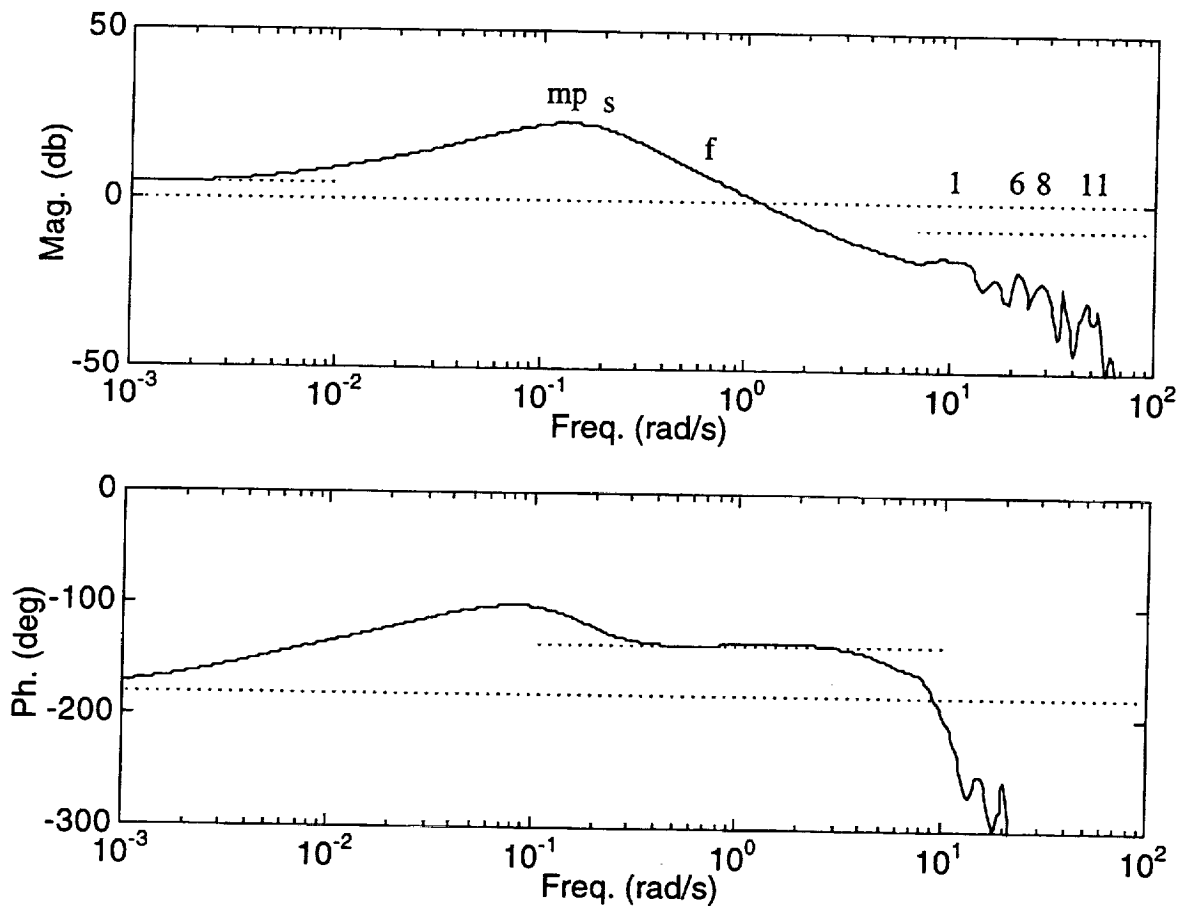


Figure 71. Bode Plot For 1,850 in Pitch Rate To Elevator  
With Filtering,  $k_{22} = -5.08$  rad/rad/s

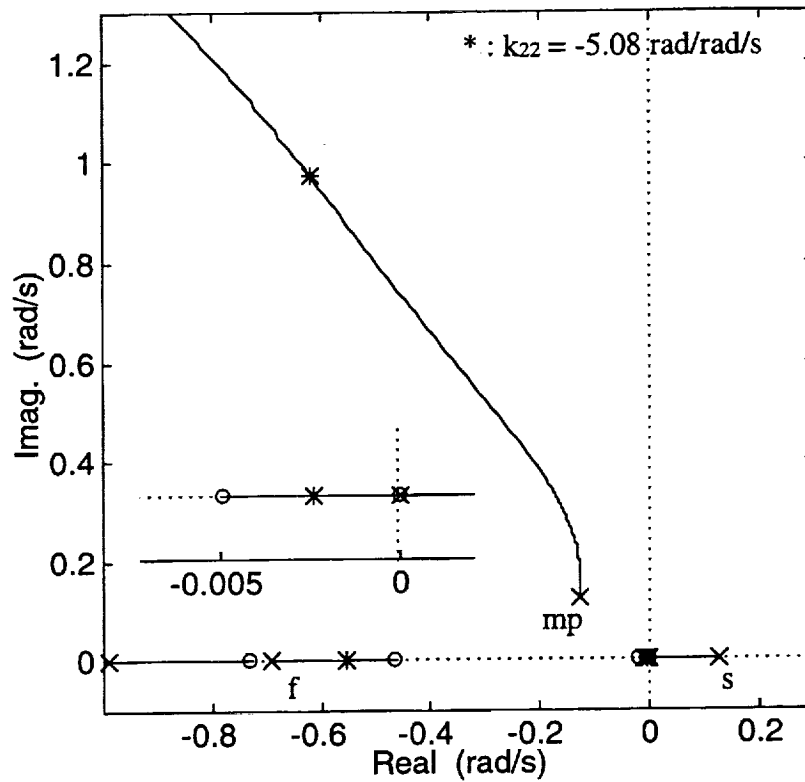


Figure 72. Evans Plot For 1,850 in Pitch Rate To Elevator With Filtering

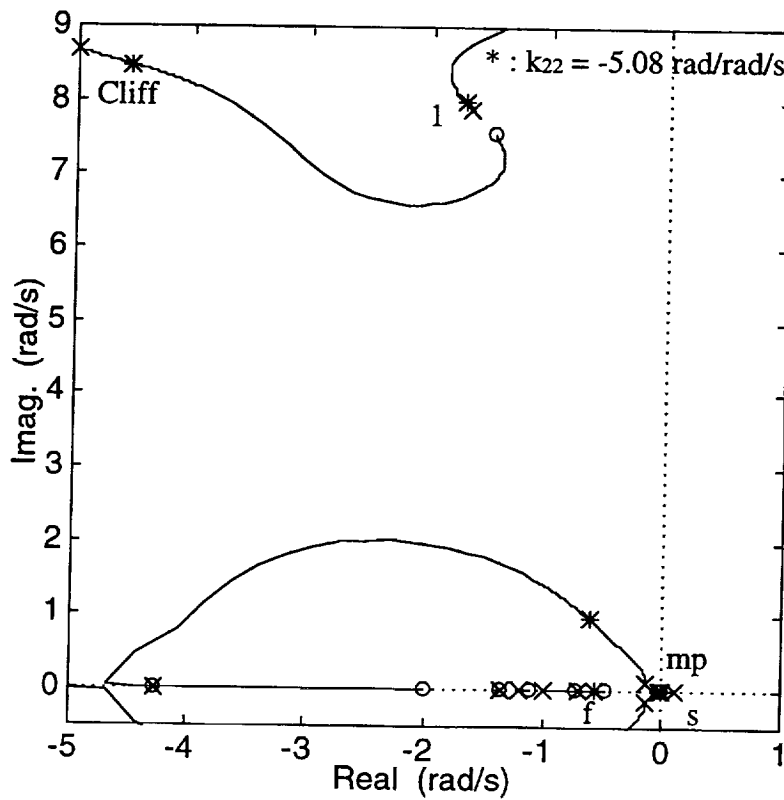
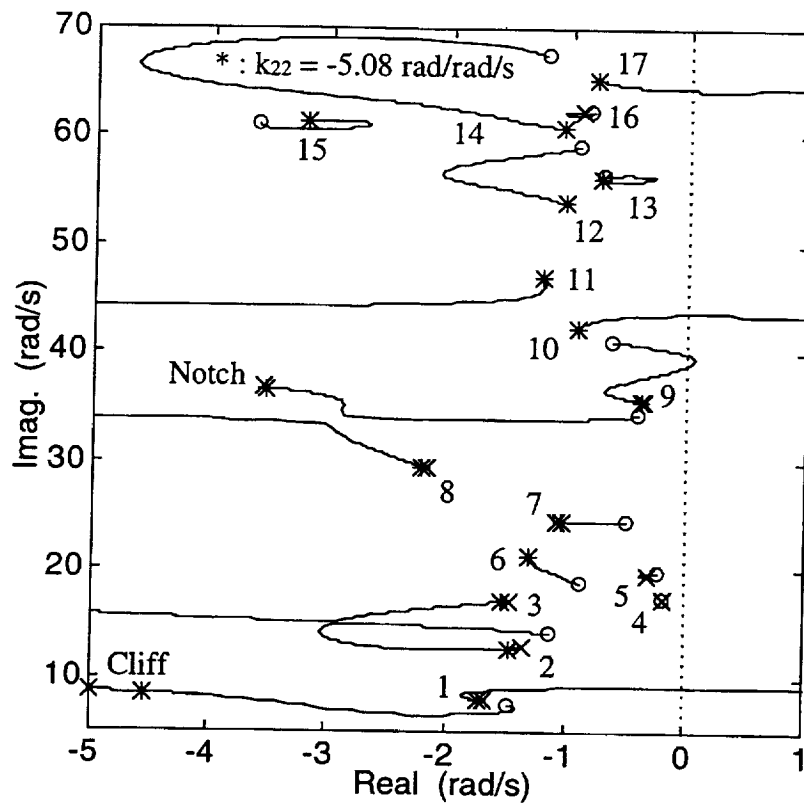


Figure 72. Continued

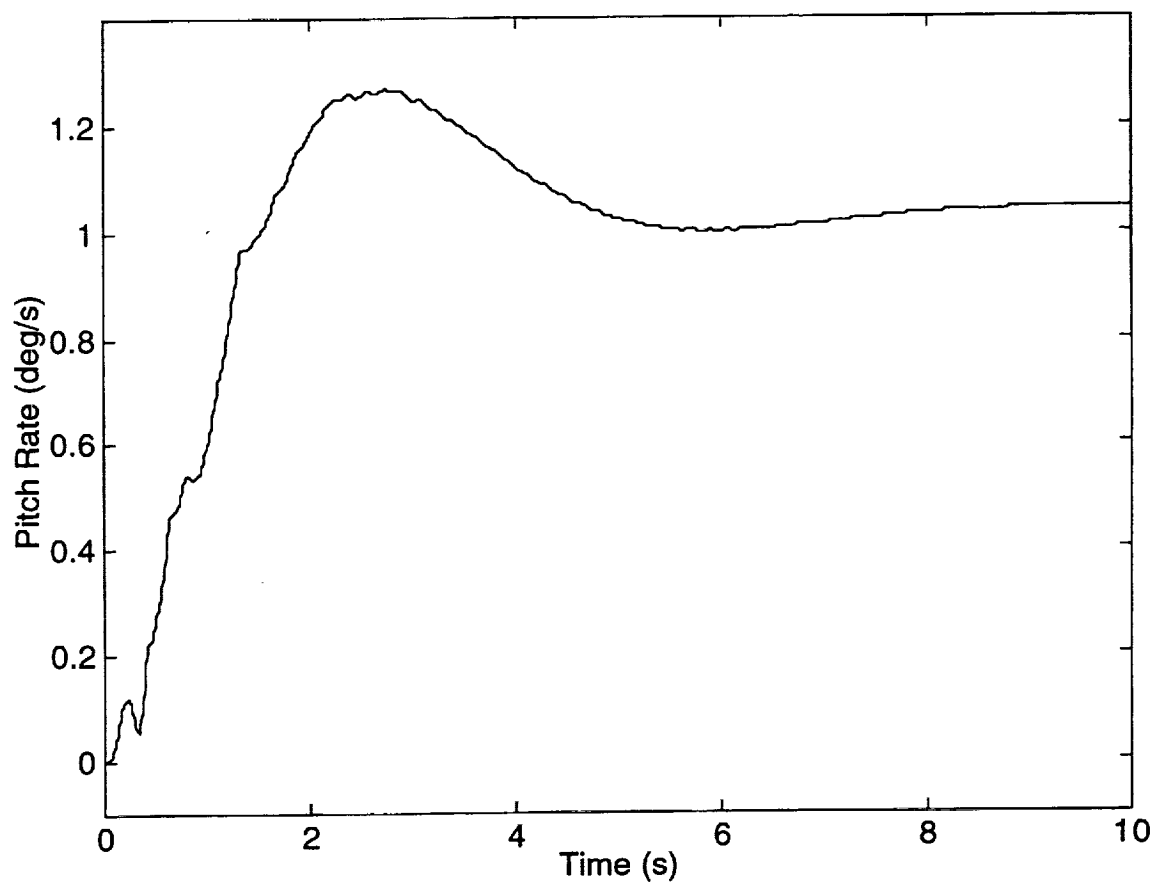


Figure 73. Closed-Loop 400 in Pitch Rate Time Response  
Due To 1 deg/s Command Without Prefilter



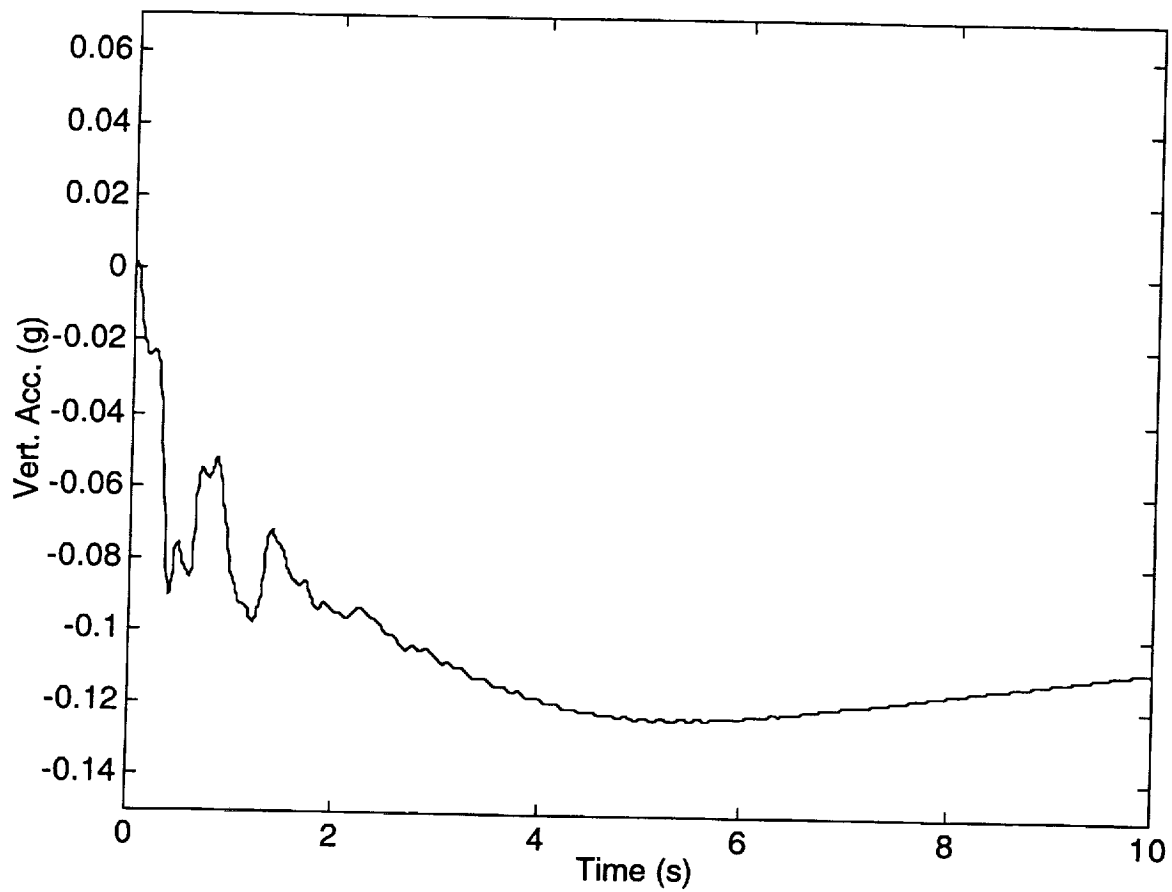


Figure 74. Closed-Loop 400 in Vertical Acceleration Time Response  
Due To 1 deg/s Command Without Prefilter

### E. Command Shaping Prefilter

The residual vibrations noted in Figs. 73-74 can be directly traced to the final closed-loop dipole structures for modes 1 and 2. The closed-loop poles for modes 1 and 2 are shown in Fig. 72. Note these locations are not far removed from the locations indicated in Figs. 66-67. Also observe from Eqs. (4.5) and (4.7) that the closed-loop zeros, after the crossfeed design step and after the pitch loop design step, are identical, aside from any  $K_{22}(s)$  compensator zeros. Therefore, Figs. 66-67 capture the essence of the residual structural vibration problem, and also indicate the required command filtering.

The closed-loop root locations for modes 1 and 2, as computed from the design presented in Section IV-D, are listed in Tab. 16. In Figs. 66-67, these poles are denoted by the "+" symbol, and the zeros by the "\*" symbol. The contribution from each mode to the time response is a function of the modal residue, which in turn is related to the dipole magnitude (distance between pole and zero). Figs. 66-67 illustrate the optimized dipole characteristics, which are highly improved from the basic airframe characteristics, but are still lacking, as evidenced by the responses in Figs. 73-74.

Table 16. Closed-Loop Mode 1 & 2 Root Locations For 400 in Pitch Rate And Vertical Acceleration			
Mode	Poles (1/s)	Zeros-Pitch Rate (1/s)	Zeros-Accel (1/s)
1	$-1.73 \pm j 7.97$	$-0.99 \pm j 5.03$	$-1.75 \pm j 6.01$
2	$-1.48 \pm j 12.75$	$+2.86 \pm j 8.51$	$-0.070 \pm j 13.95$

Screening of selected frequencies by the stick filter is based on the listed root locations in Tab. 16. First note the pitch rate and acceleration zeros associated with mode 2 are located in the right-half plane, or very near to this region. Utilization of left-half plane filter roots rules out any significant screening of mode 2. This is of no great concern, as mode 1 is the largest contributor to the transient motions. Although the mode 1 pole locations are identical for either response channel in Figs. 66-67, the zeros associated with this mode are not. Therefore, some compromise will exist when blocking frequency content in the pitch rate response vs. the acceleration response.

Fortuitously, the cliff filter results in responses with very similar numerator root locations for mode 1.

The prefilter is specified as

$$P_2(s) = \frac{5}{4} \frac{(s+4)}{(s+5)} \frac{5.7^2}{8.1^2} \frac{(s^2+2\{0.21\}\{8.1\}s+8.1^2)}{(s^2+2\{0.26\}\{5.7\}s+5.7^2)} \frac{30}{(s+30)} \quad (4.16)$$

This filter structure consists of quadratic numerator and denominator factors which lead to poles approximately centered between the zeros locations listed above and shown in Figs. 66-67. In addition, a small lead-lag factor is included to effectively increase the closed-loop  $\tau_{\theta 2}$  value in hopes of improving the separation between pitch and flight path responses, and to improve the control anticipation ratings. This lead filter also has the effect of reducing any phase loss from the quadratic factors in the command path. A final component of the prefilter is a low pass element to limit the control bandwidth of the pilot inputs above a specified frequency and to further reduce excitation energy reaching the aeroelastic modes. The prefilter in Eq. (4.16) is mild in the sense that it will not violate physical limitations or possibly saturate limiters and actuators that lie downstream. If the filter is not tuned properly, the stability of the inner loops are not compromised as the prefilter lies outside of these loops. However, stability of the pilot loop closure is dependent upon the tuning accuracy. Since the augmented mode 1 pole and cliff filter zero locations are partially dependent on the specified controller parameters, knowledge of their values should be high, to some extent, allowing accurate tuning. One can even foresee the possibility of a limited, but cockpit adjustable, stick filter to allow pilots to tailor the compromise between screening of initial transients in the pitch rate response vs. vertical acceleration response.

Figs. 75-76 show the pitch rate and vertical acceleration responses at the 400 in station for the design from Section IV-D now including the command shaping prefilter  $P_2(s)$  in Eq. (4.16) due to a 1 deg/s nose up command issued at  $\tilde{y}_{2c}$  in Fig. 54. Additionally, Figs. 77-82 show the responses at several other stations along the vehicle centerline. The effect of the stick filtering is evident when the new responses (Figs. 75-76) are compared with those given in Figs. 73-74. Initial transients in the acceleration response have been greatly reduced and may only register as a

small annoyance that does not impact basic piloting tasks. In addition, the response characteristics illustrated at other stations (Figs. 77-82) will reduce passenger exposure to ride discomfort during maneuvering flight. The small amplitude transients in the 0.5-1.5 s region of the forward station acceleration response (see Fig. 76) can be reduced even further by adjusting the low pass break point from 30 to 10 1/s. However, such a modification leads to large effective time delay. Analysis of the new effective  $\tau_{\theta 2}$  characteristics and the apparent time delay due to the prefilter in Eq. (4.16) are addressed in the next section.

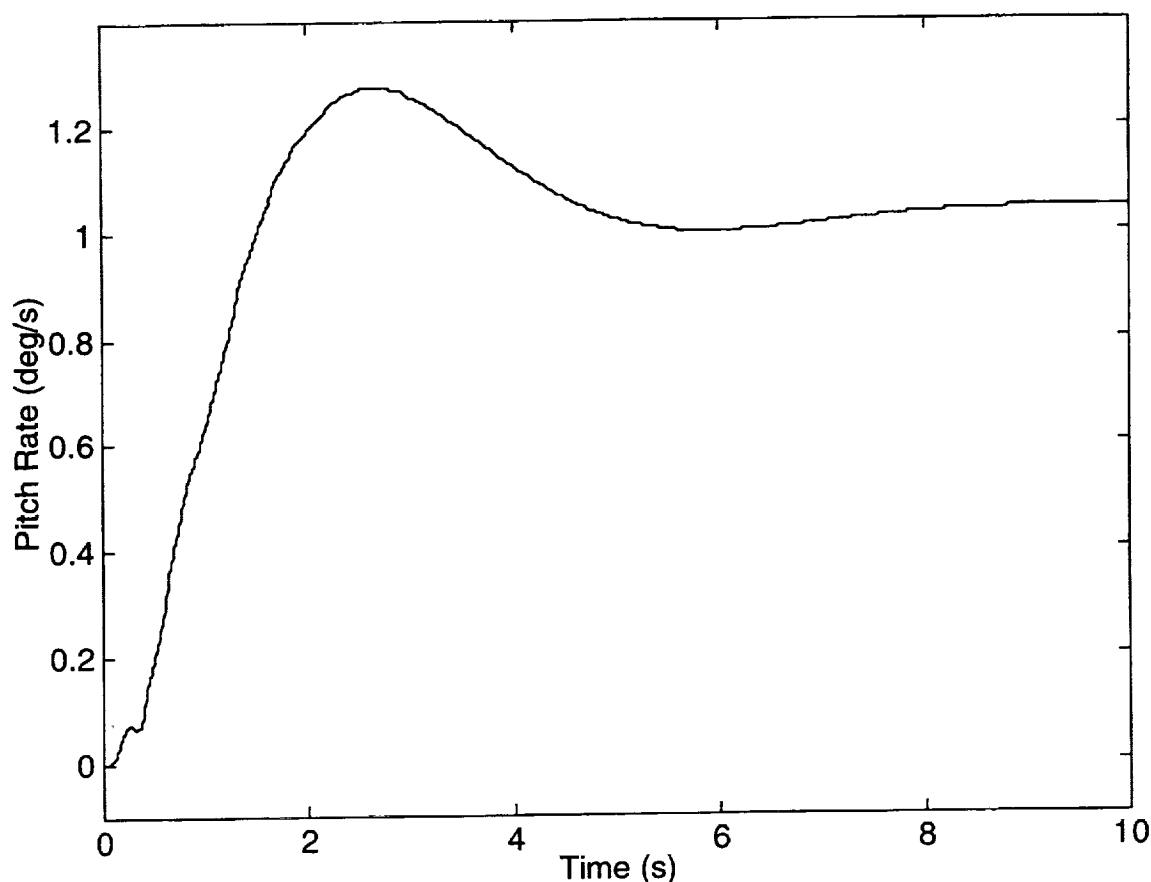


Figure 75. Closed-Loop 400 in Pitch Rate Time Response  
Due To 1 deg/s Command With Prefilter

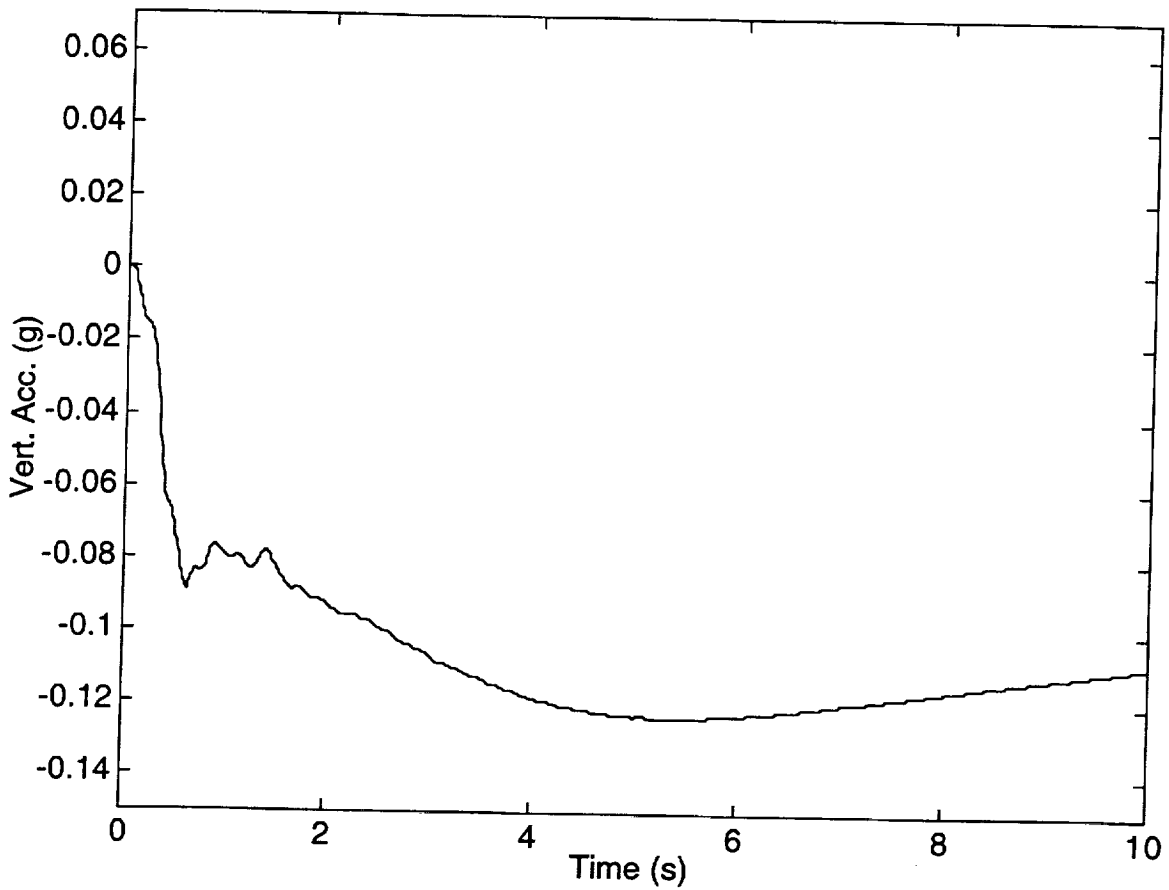


Figure 76. Closed-Loop 400 in Vertical Acceleration Time Response  
Due To 1 deg/s Command With Prefilter

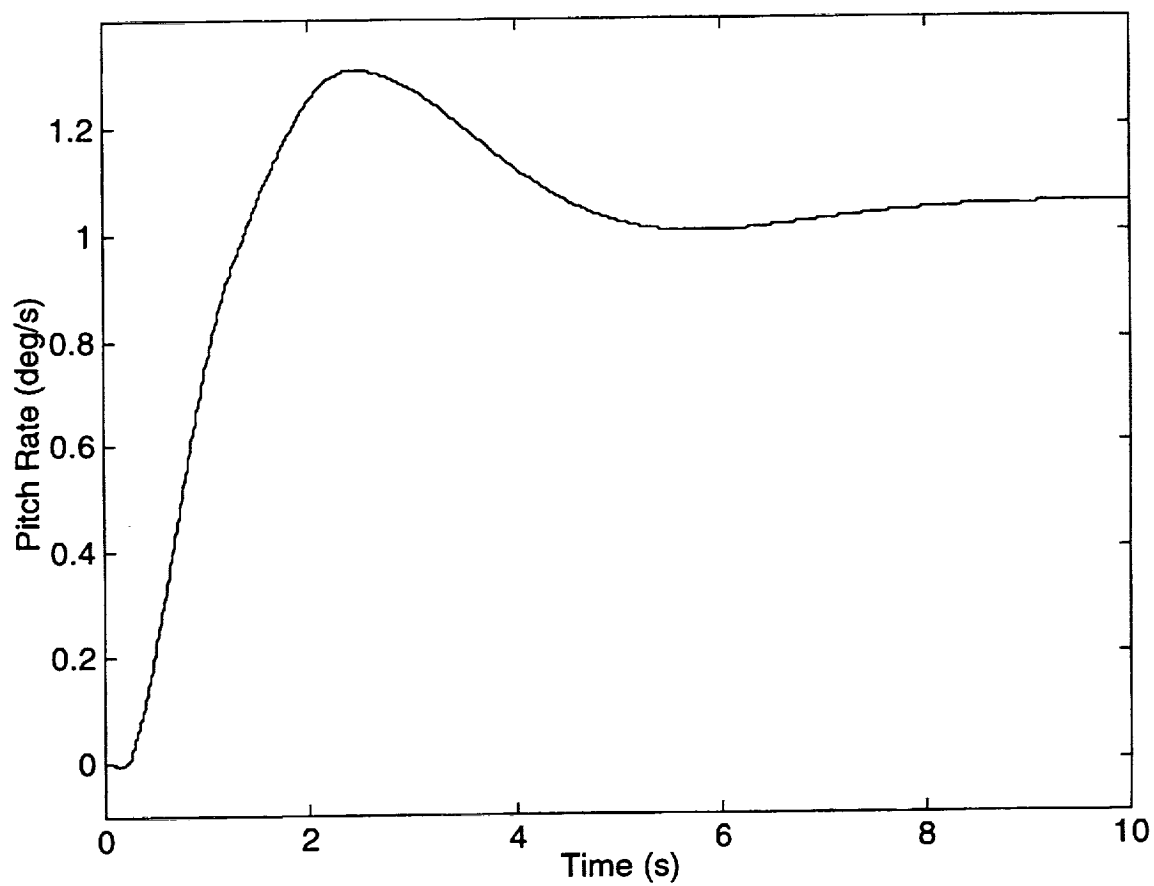


Figure 77. Closed-Loop 1,850 in Pitch Rate Time Response  
Due To 1 deg/s Command With Prefilter

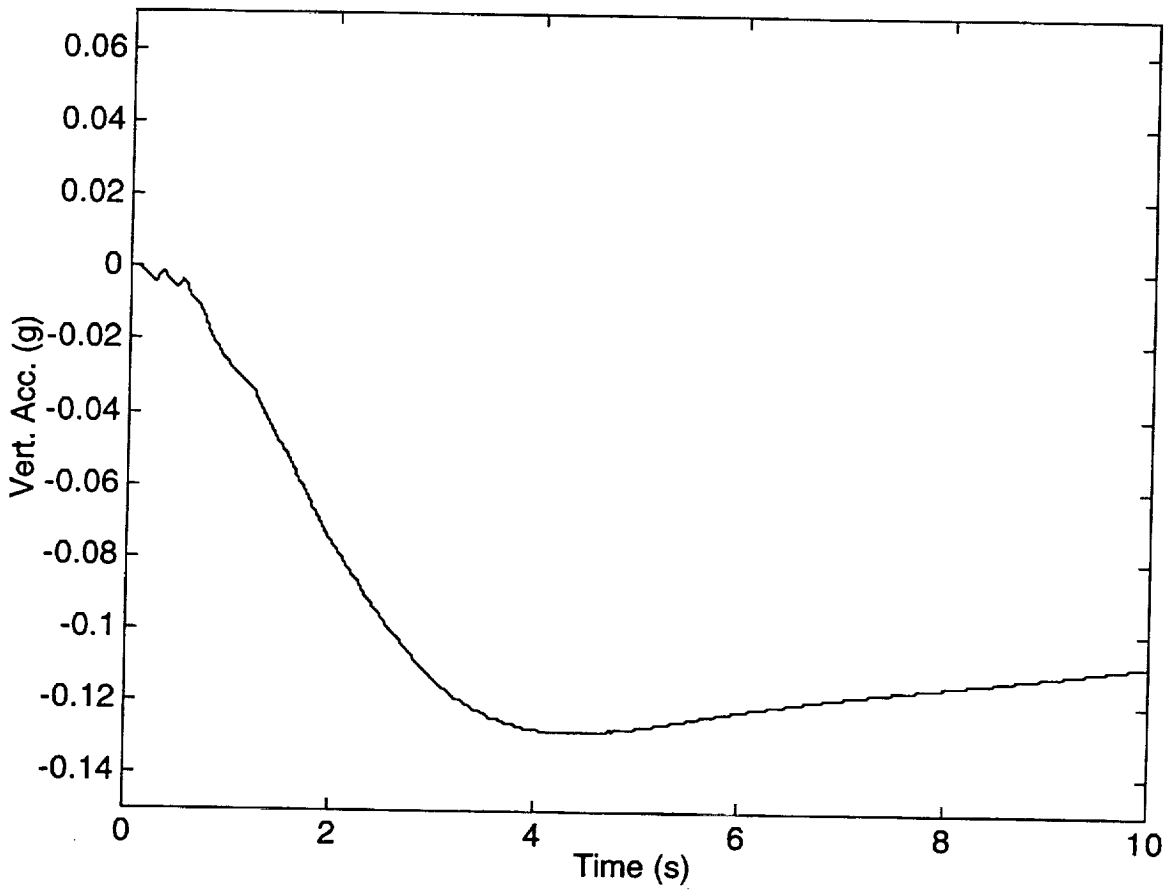


Figure 78. Closed-Loop 1,850 in Vertical Acceleration Time Response  
Due To 1 deg/s Command With Prefilter

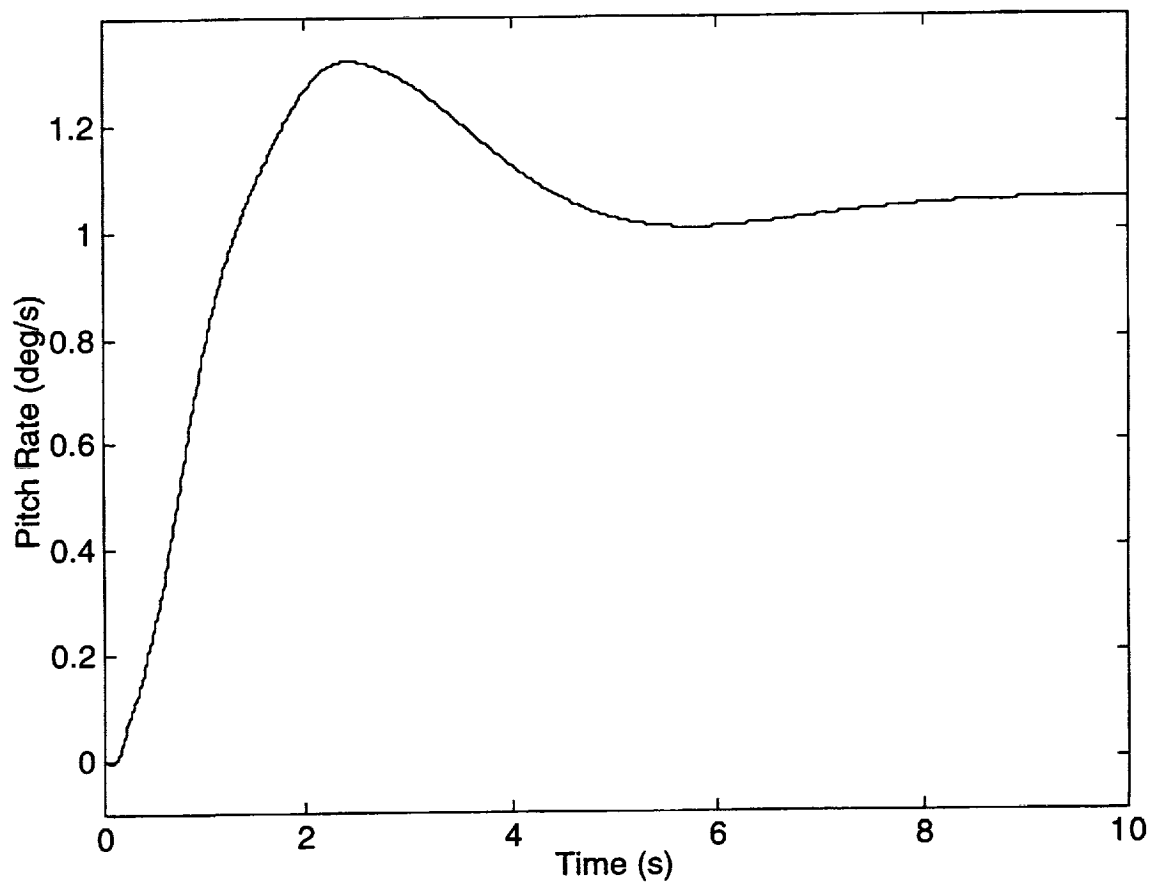


Figure 79. Closed-Loop 2,500 in Pitch Rate Time Response  
Due To 1 deg/s Command With Prefilter



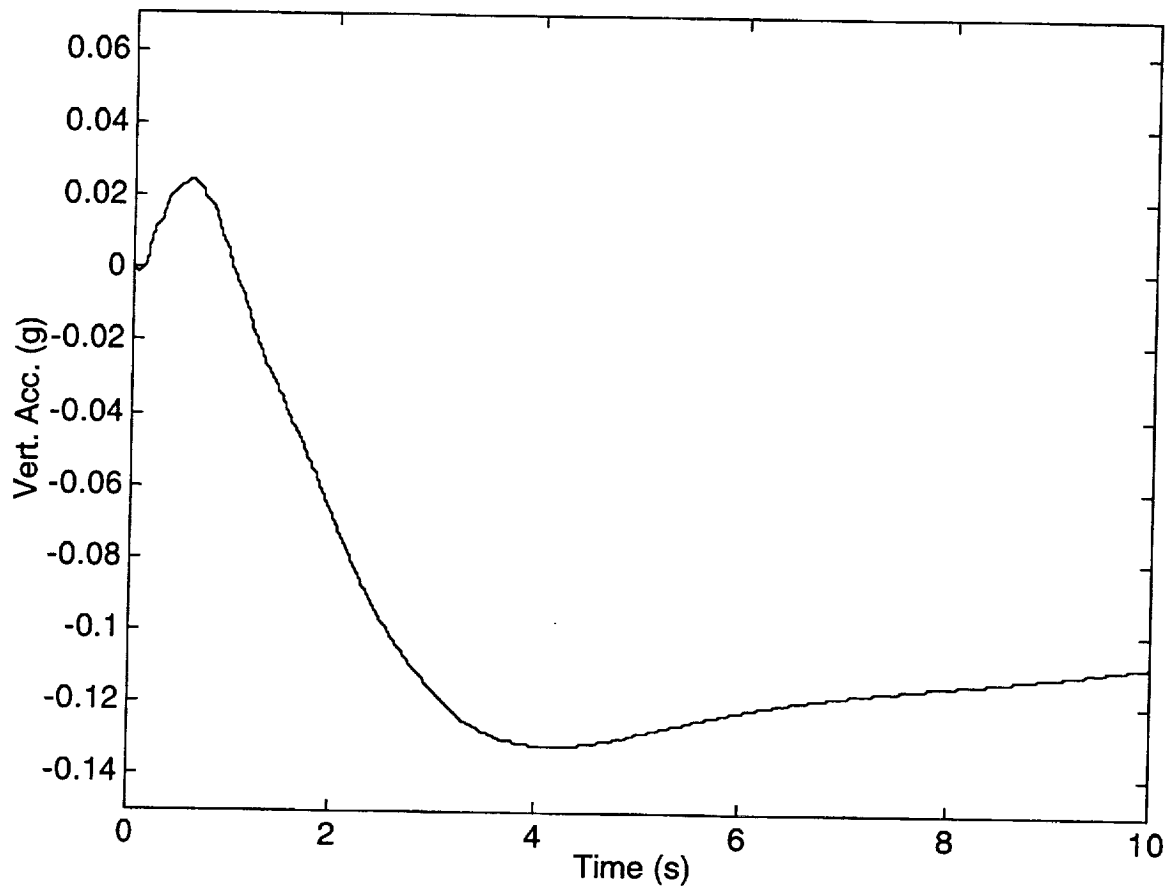


Figure 80. Closed-Loop 2,500 in Vertical Acceleration Time Response  
Due To 1 deg/s Command With Prefilter

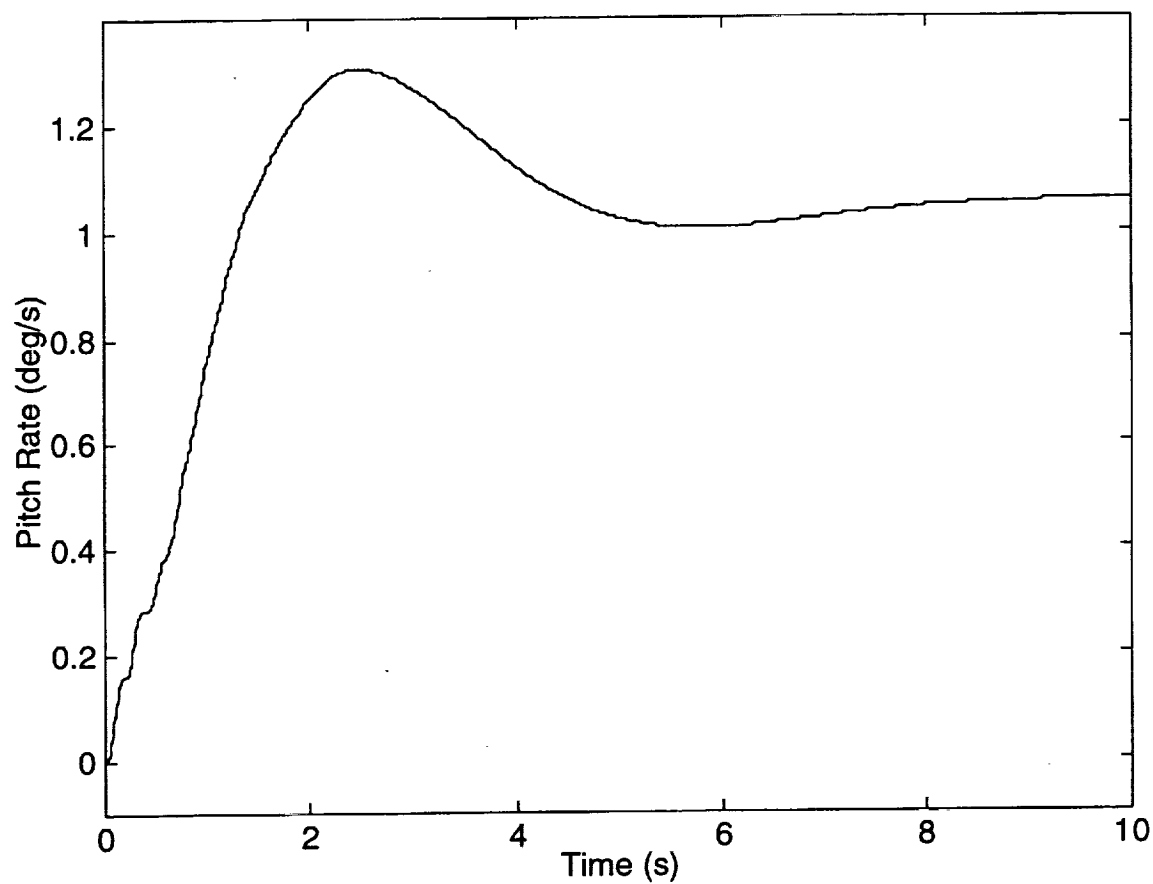


Figure 81. Closed-Loop 3,460 in Pitch Rate Time Response  
Due To 1 deg/s Command With Prefilter

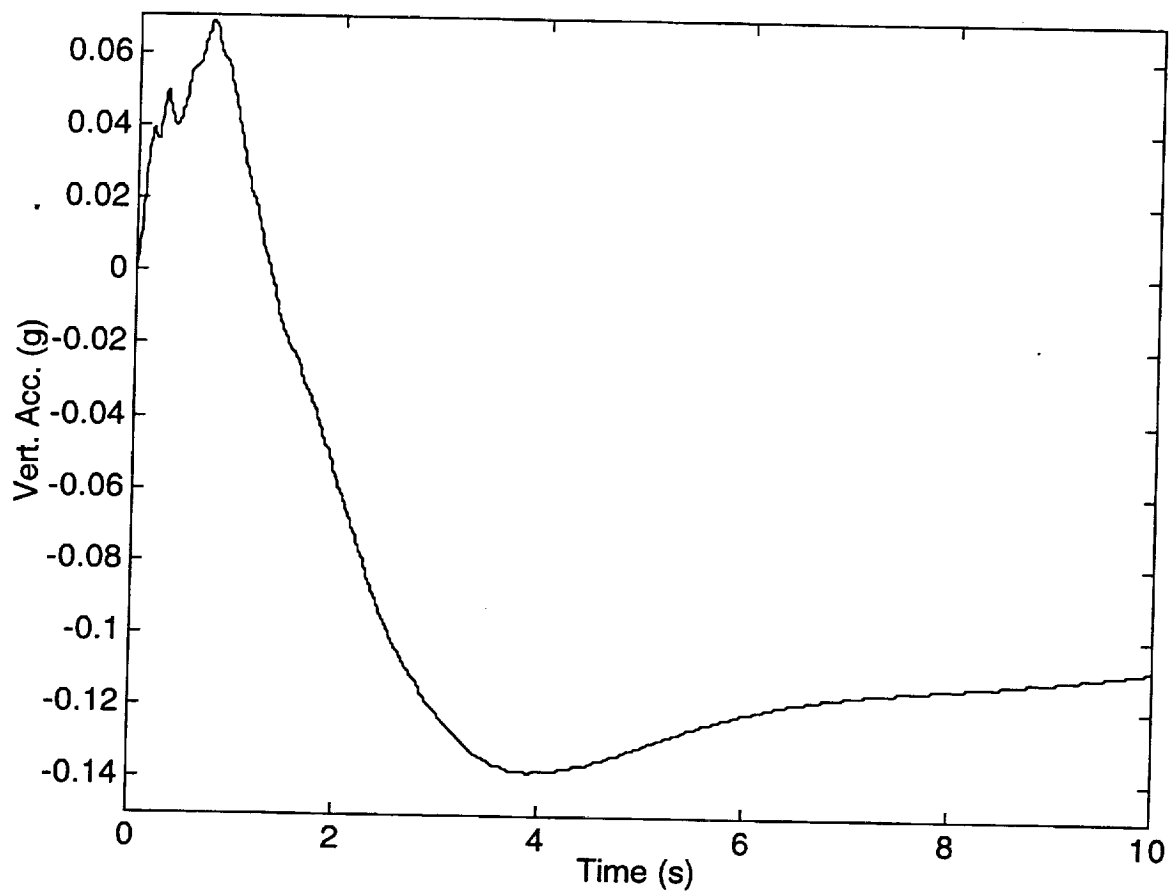


Figure 82. Closed-Loop 3,460 in Vertical Acceleration Time Response  
Due To 1 deg/s Command With Prefilter

## **F. Additional Evaluation of Control Law**

In this section, a more in-depth evaluation of the proposed control law from Section IV-A to IV-E is considered. Basic stability and performance features of the nominal system, as well as limited stability robustness characteristics, were considered in the previous sections to design the control system. Here, evaluation of the closed-loop system will concentrate on the following items:

- **Stability Robustness**
  - Isolated Gain And Phase Variations
  - Simultaneous Gain And Phase Variations
  - Structural Parameter Variations
  - Aerodynamic Parameter Variations
- **Performance**
  - Flying Qualities Based On Equivalent System
  - Gust Ride Discomfort

Finally, several comments are given on Ref. 25, which performed an external analysis of a control law based on an "aggressive" variant of the control system presented here. This reference also developed a new, alternative control law.

## Stability Robustness

### Isolated Gain And Phase Variations

By performing algebraic manipulation, the inner loop architecture in Fig. 54 can be equivalently expressed in standard notation as shown in Fig. 83 where

$$\begin{aligned} K_{12}(s) &= K_{11}(s) K_{cf}(s) K_{22}(s) \\ K_{21}(s) &= 0 \end{aligned} \quad (4.17)$$

Loop transfers obtained by individually breaking the system at the two input signals and the two output signals indicated in Fig. 83 are

$$\begin{aligned} G_{ol@i1}(s) &= \frac{K_{11}G_{11}A_1 + K_{12}G_{21}A_1 + \tilde{K}\tilde{G}_{1-2}A_1A_2}{1 + K_{21}G_{12}A_2 + K_{22}G_{22}A_2} \\ G_{ol@i2}(s) &= \frac{K_{21}G_{12}A_2 + K_{22}G_{22}A_2 + \tilde{K}\tilde{G}_{1-2}A_1A_2}{1 + K_{11}G_{11}A_1 + K_{12}G_{21}A_1} \\ G_{ol@o1}(s) &= \frac{K_{11}G_{11}A_1 + K_{21}G_{12}A_2 + \tilde{K}\tilde{G}_{1-2}A_1A_2}{1 + K_{12}G_{21}A_1 + K_{22}G_{22}A_2} \\ G_{ol@o2}(s) &= \frac{K_{12}G_{21}A_1 + K_{22}G_{22}A_2 + \tilde{K}\tilde{G}_{1-2}A_1A_2}{1 + K_{11}G_{11}A_1 + K_{21}G_{12}A_2} \\ \tilde{K} &= K_{11}K_{22} - K_{12}K_{21} \end{aligned} \quad (4.18)$$

Bode plots corresponding to Eq. (4.18) are shown in Figs. 84-87. Additionally, Tab. 17 lists the gain and phase margins computed at each break point.

Table 17. Isolated Gain And Phase Margins					
Robust. Metric	Spec.	@ u1	@ u2	@ y1	@ y2
$GM^u_{\omega < .38}$	$\geq 4.5$ (db)	N/A	$\infty$	N/A	$\infty$
$GM^l_{\omega < .38}$	$\geq 4.5$ (db)	N/A	7.67	N/A	4.51
$PM_{\omega < .38}$	$\geq 30$ (deg)	127.04	N/A	N/A	N/A
$GM^u_{.38 < \omega < 5}$	$\geq 6$ (db)	18.43	N/A	N/A	N/A
$GM^l_{.38 < \omega < 5}$	$\geq 6$ (db)	$\infty$	N/A	N/A	N/A
$PM_{.38 < \omega < 5}$	$\geq 45$ (deg)	141.60	63.08	N/A	46.05
$GM^u_{5 < \omega}$	$\geq 8$ (db)	18.25	18.73	18.25	16.26
$GM^l_{5 < \omega}$	$\geq 8$ (db)	$\infty$	$\infty$	$\infty$	$\infty$
$PM_{5 < \omega}$	$\geq 60$ (deg)	70.88	N/A	72.30	N/A

N/A: No applicable crossover point exists.

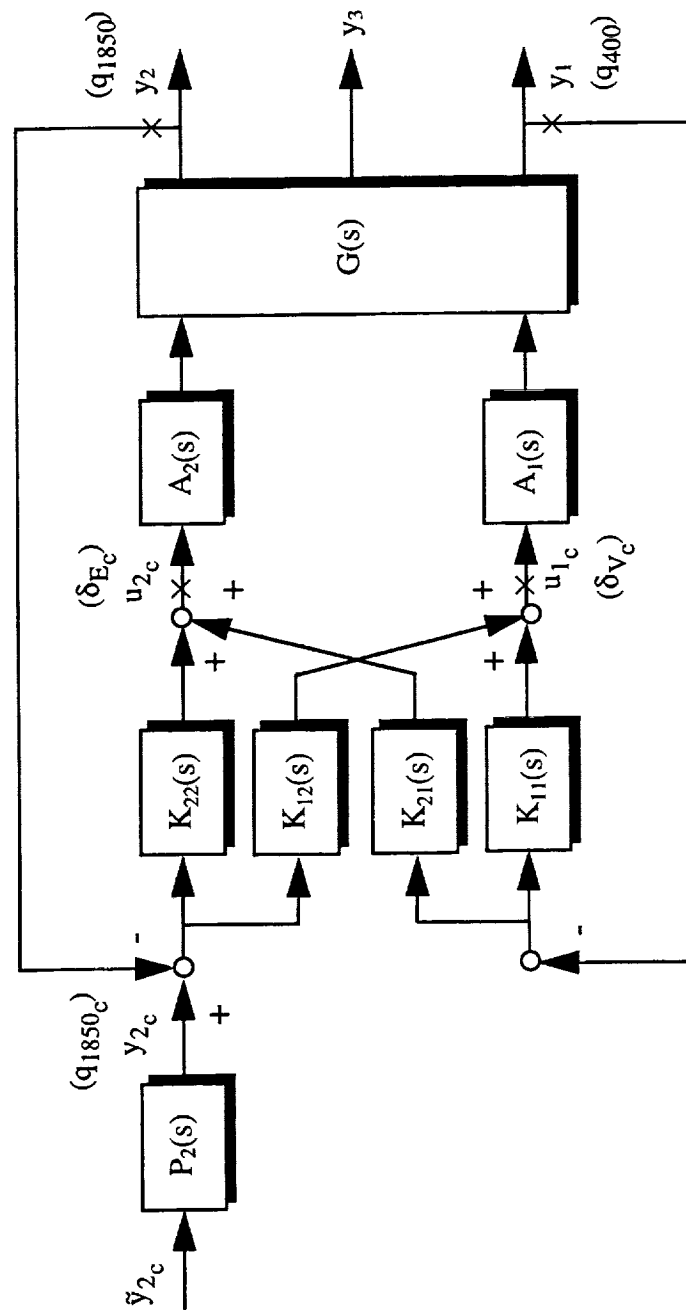


Figure 83. Equivalent Inner Loop Architecture

In Tab. 17, all margin requirements are satisfied. In general, the margins computed at the input and output for a given channel reflect similar values indicating the closed-loop system is "balanced" with respect to robustness. The low frequency gain margins and the high frequency phase margins for the rigid-body modes are riding the requirement limits, while the aeroelastic gain margins are well beyond sufficient levels. These characteristics reflect the superior gain/phase behavior of the vane loop, the pitch loop, and the design strategy to reduce residual structural vibrations. Note Figs. 84 and 86 are similar in appearance to Fig. 63, and thus reflect the vane loop characteristics after the lower frequency pitch loop effects are folded into the system. Also note with  $K_{21}(s) = 0$ , Fig. 87 is identical to Fig. 71.

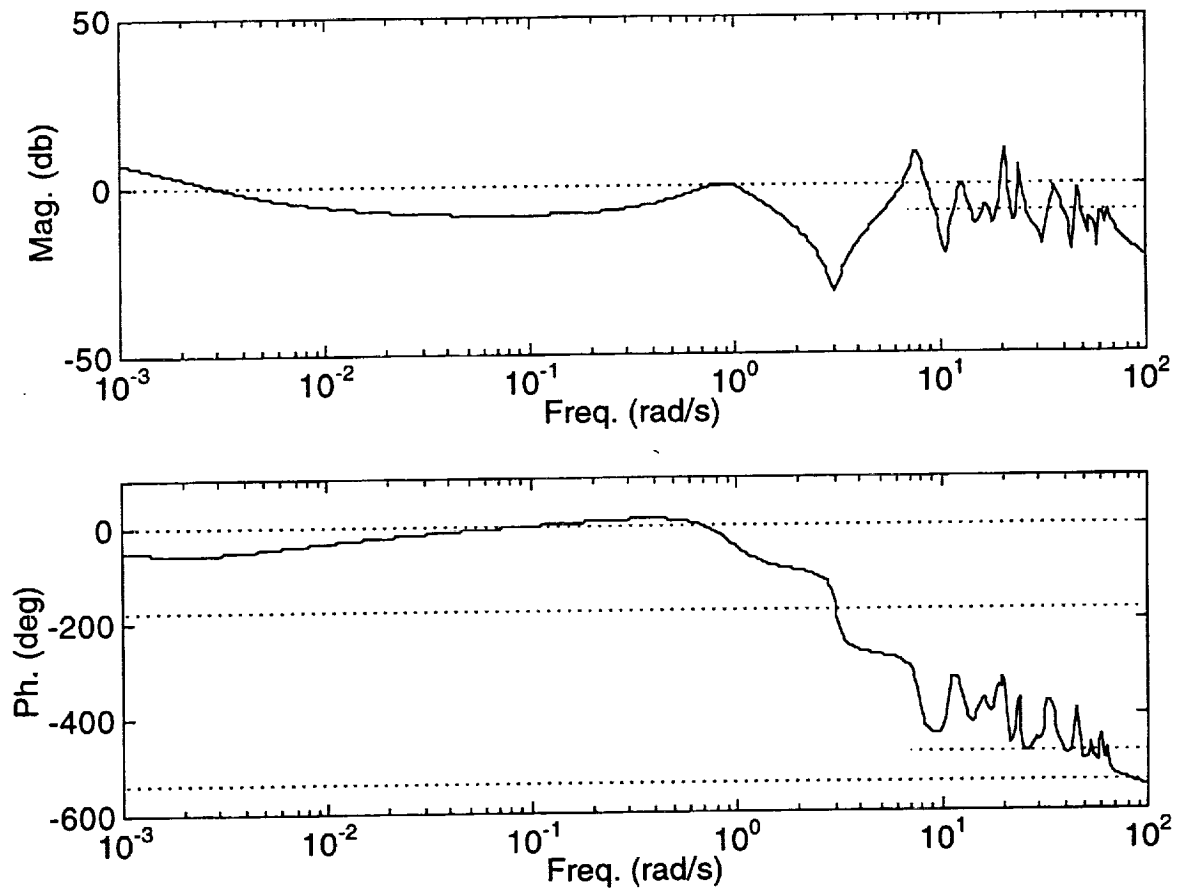


Figure 84. Bode Plot For Input 1 Break Point



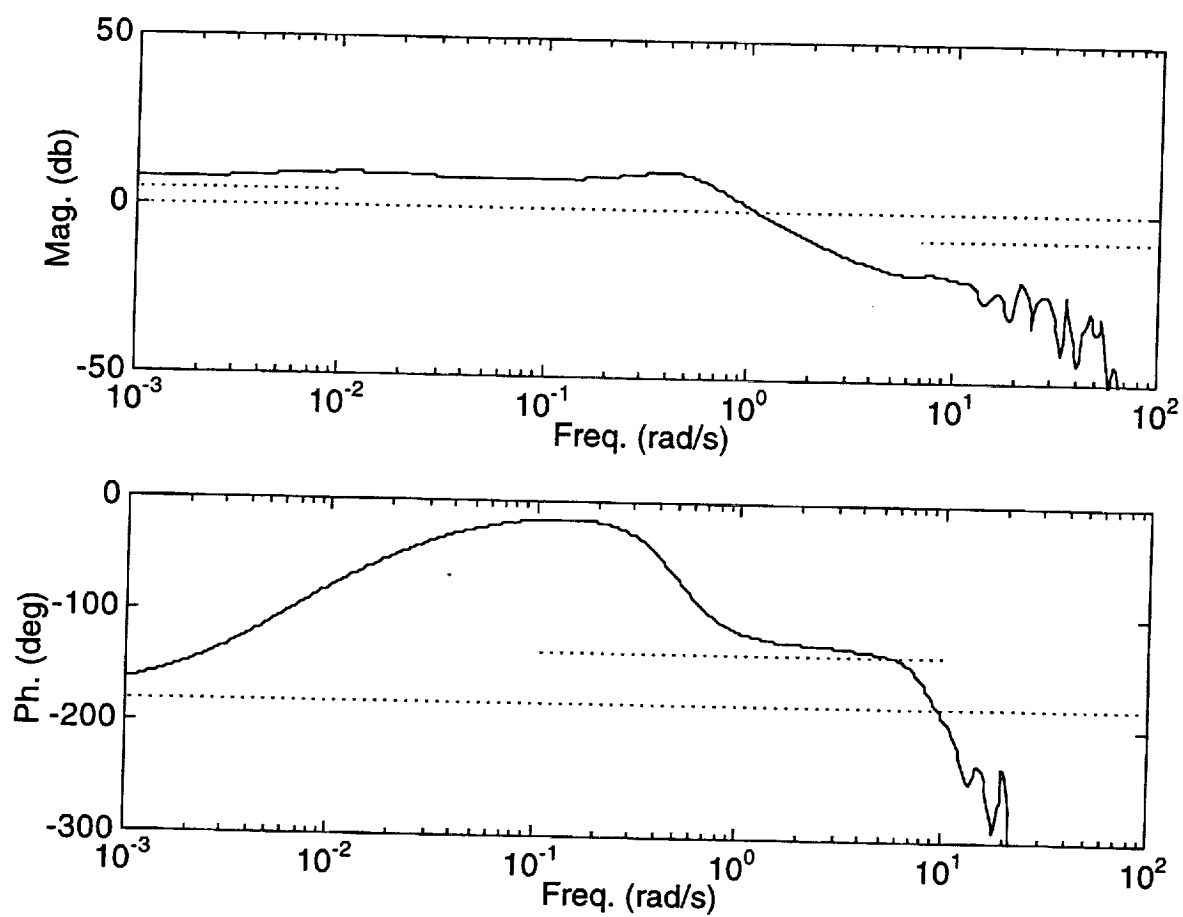


Figure 85. Bode Plot For Input 2 Break Point

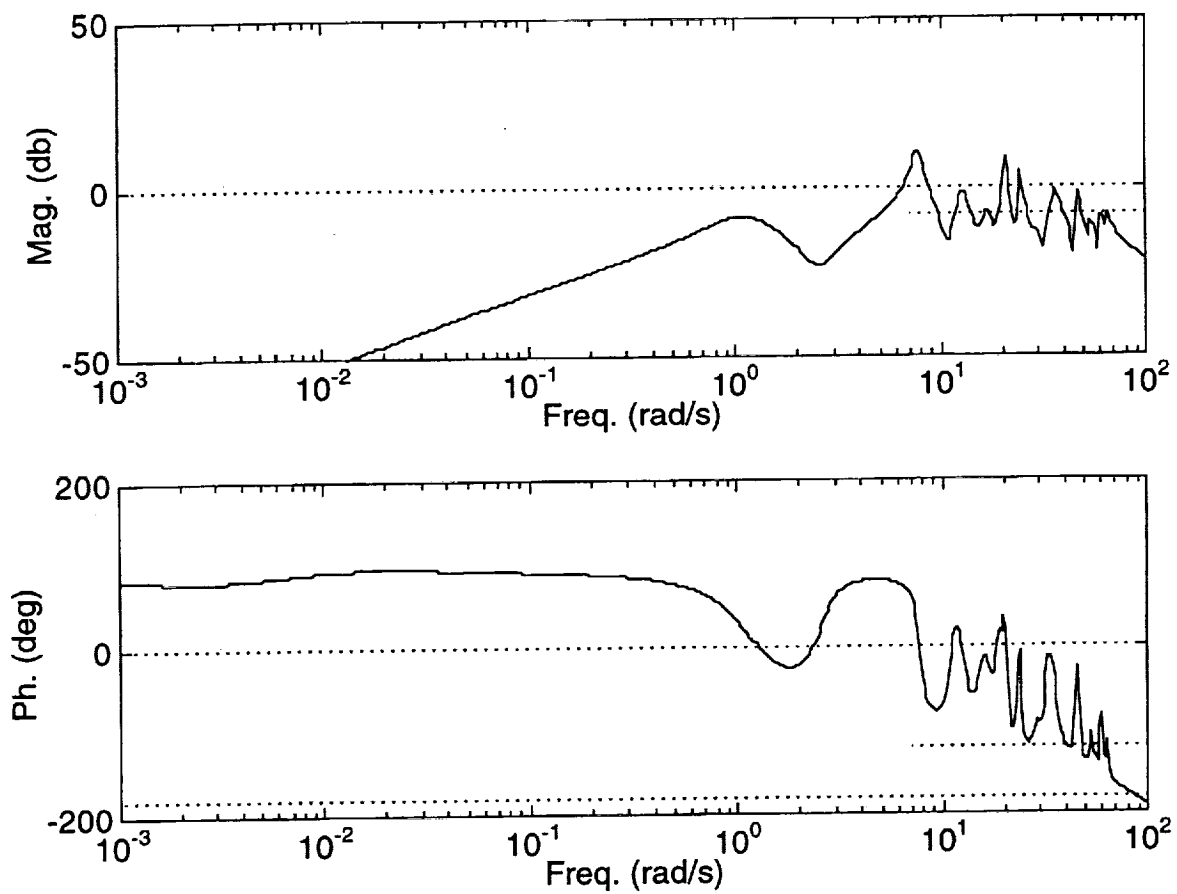


Figure 86. Bode Plot For Output 1 Break Point

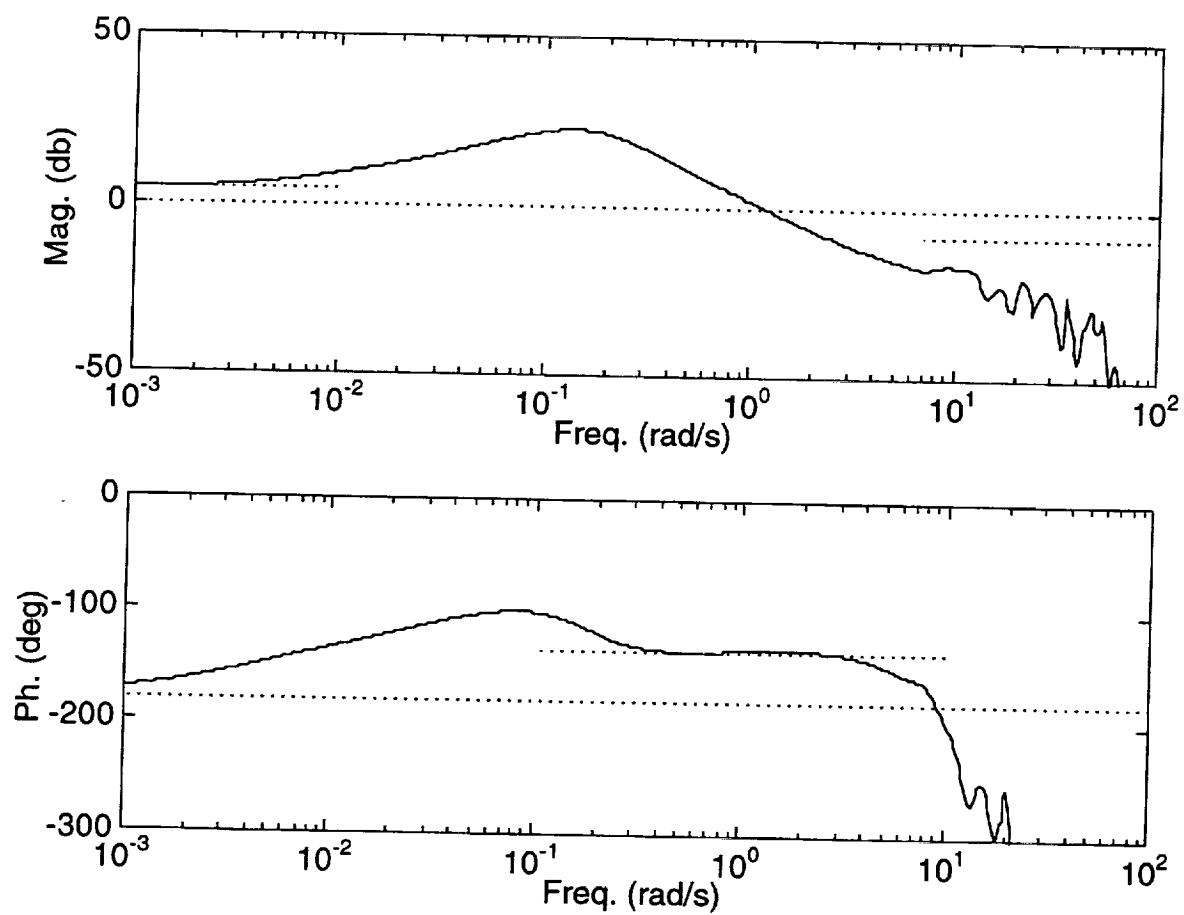


Figure 87. Bode Plot For Output 2 Break Point

## Stability Robustness

### Simultaneous Gain And Phase Variations

Consider the inner loop architecture in Fig. 83 re-expressed with vector notation in Fig. 88 where

$$\begin{aligned} y &= \begin{bmatrix} y_1 \\ y_2 \end{bmatrix}, & u_c &= \begin{bmatrix} u_{1c} \\ u_{2c} \end{bmatrix}, & P &= \begin{bmatrix} 0 \\ P_2 \end{bmatrix} \\ K &= \begin{bmatrix} K_{11} & K_{12} \\ K_{21} & K_{22} \end{bmatrix}, & G &= \begin{bmatrix} G_{11} & G_{12} \\ G_{21} & G_{22} \end{bmatrix}, & A &= \begin{bmatrix} A_1 & 0 \\ 0 & A_2 \end{bmatrix} \end{aligned} \quad (4.19)$$

Fig. 88 also illustrates input and output multiplicative error ( $E_i(s)$  and  $E_o(s)$ ) that is to be considered, albeit separately. Application of stability robustness theory leads to the following inequality relationships:

$$\sigma[I + \{KGA\}^{-1}] > \sigma[E_i] \quad | \quad \sigma[I + \{GAK\}^{-1}] > \sigma[E_o] \quad (4.20a)$$

$$1 > \sigma[\{I + (KGA)^{-1}\}E_i] \quad | \quad 1 > \sigma[E_o\{I + (GAK)^{-1}\}] \quad (4.20b)$$

$$\sigma[I + \{I + (KGA)^{-1}\}^{-1}\varepsilon E_i] > 0 \quad | \quad \sigma[I + \varepsilon E_o\{I + (GAK)^{-1}\}^{-1}] > 0 \quad (4.20c)$$

$$\text{for } 0 \leq \omega \leq \infty \text{ and } 0 \leq \varepsilon \leq 1$$

If Eqs. (4.20a) or (4.20b) are satisfied, then stability is maintained in the presence of error. Since these two relationships are only sufficient, no conclusions can be drawn when they are violated. However, Eq. (4.20c) is sufficient and necessary for stability robustness. Only Eq. (4.20c) can be utilized to ascertain precise stability margins.

Gain and phase variations of equal strength in each channel will be represented as

$$E_i = (me^{j\theta} - 1)I, \quad E_o = (me^{j\theta} - 1)I \quad (4.21)$$

where  $m$  denotes a magnitude parameter with  $m = 1$  being nominal, and  $\theta$  represents the phase parameter with  $\theta = 0$  giving the nominal system. The parameters  $m$  and  $\theta$  are used to determine the multivariable gain and phase margins for the closed-loop system. Two types of variations are considered here: 1) piecewise uniform variations (with respect to frequency) reflecting the multi-loop MIL-F-87242 margin requirements and 2) uniform variations. Type 1 is utilized to establish compliance with specified design requirements listed in Ref. 2. Type 2 is utilized to determine the actual gain and phase margins for the system.

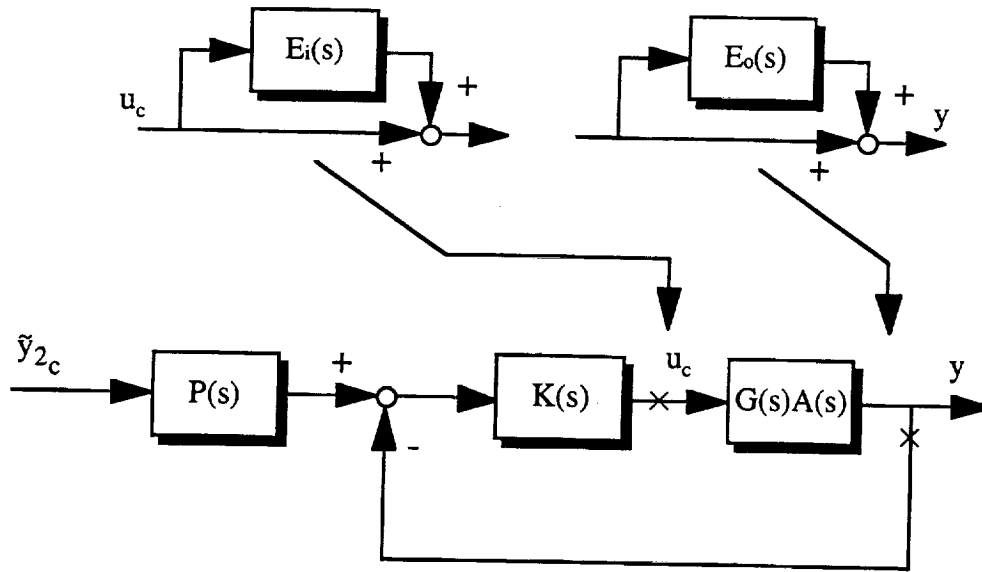


Figure 88. Inner Loop Architecture Expressed With Vector Notation

Figs. 89-90 and 93-94 show the stability robustness characteristics at both input and output locations against the design requirements specified in Ref. 2. Although nearly satisfied across all frequencies, Eqs. (4.20a) and (4.20b) are not satisfied. In these same figures, however, the results corresponding to Eq. (4.20c) are also shown. These results establish that the control law design from Sections IV-A to IV-E meets all multi-loop gain and phase margin requirements. In these figures, note that characteristics at the input and output are quite similar. Magnitude variations indicate that further gain reduction will likely result in a low frequency instability (observe the dc values in Figs. 89 and 93 near 0.2 corresponding to a real axis pole approaching the origin). The relaxed stability airframe and controller form a conditionally stable system which requires a minimum level of feedback gain for stability, and this characteristic is reflected in Figs. 89 and 93. Also based on the robustness curve shape, further gain amplification will likely result in high frequency aeroelastic instabilities. It can also be seen that phase loss strongly influences the short period mode (near 1 rad/s) and further phase loss will destabilize this mode. Phase advance does not significantly influence the closed-loop stability characteristics.

Figs. 91-92 and 95-96 show the precise multivariable uniform gain and phase margins existing with this system at both input and output locations. The non-conservative inequality in

Eq. (4.20c) is utilized to establish these margins. The gain and phase parameters are varied until the minimum singular value becomes zero, as seen in the figures. The upper gain margin is 14 db ( $m = 5.2$ ), while the lower gain margin is 4.3 db ( $m = 0.61$ ). Upper phase margin is 106 deg and the lower phase margin is 44 deg. These margins hold at both the input and output, again reflecting "balanced" robustness properties between input and output. Further, these margins and the corresponding modes that are destabilized correlate strongly with the single-loop isolated margins. The numerical values are quite close (4.3 vs. 4.5 db, 14 vs. 18 db, 44 vs. 46 deg, and 106 vs. 70 deg). The low-end gain margin corresponds to destabilization of the relaxed stability mode (0 rad/s), and the high-end gain margin is associated with the aeroelastic mode 1 (8 rad/s). The phase loss margin drives the short period mode unstable (1 rad/s), and the phase advance margin pushes aeroelastic mode 1 to the right-half plane (8 rad/s).

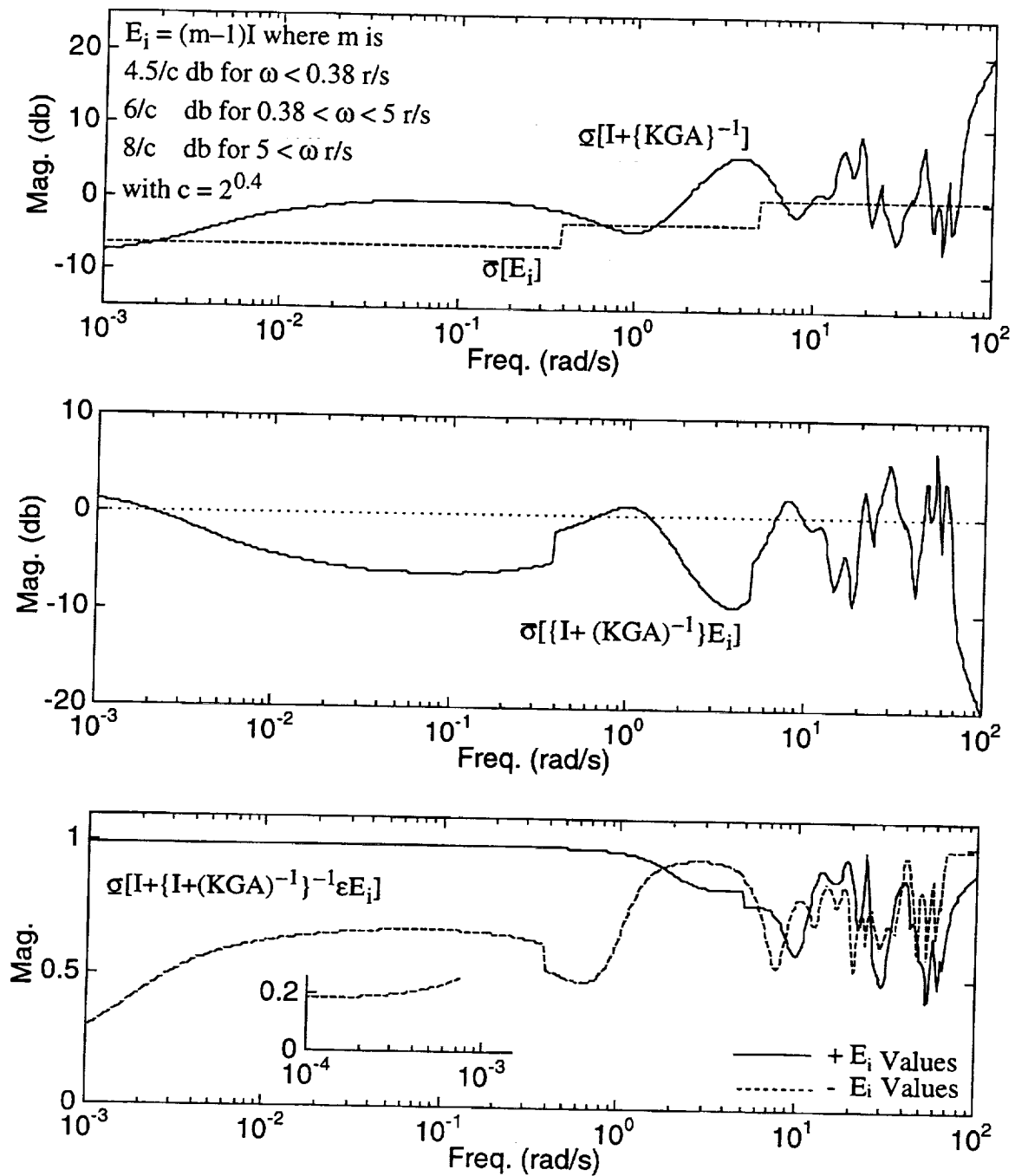


Figure 89. Singular Value Robustness Against Multi-Loop MIL-F-87242 Gain Requirement At Input

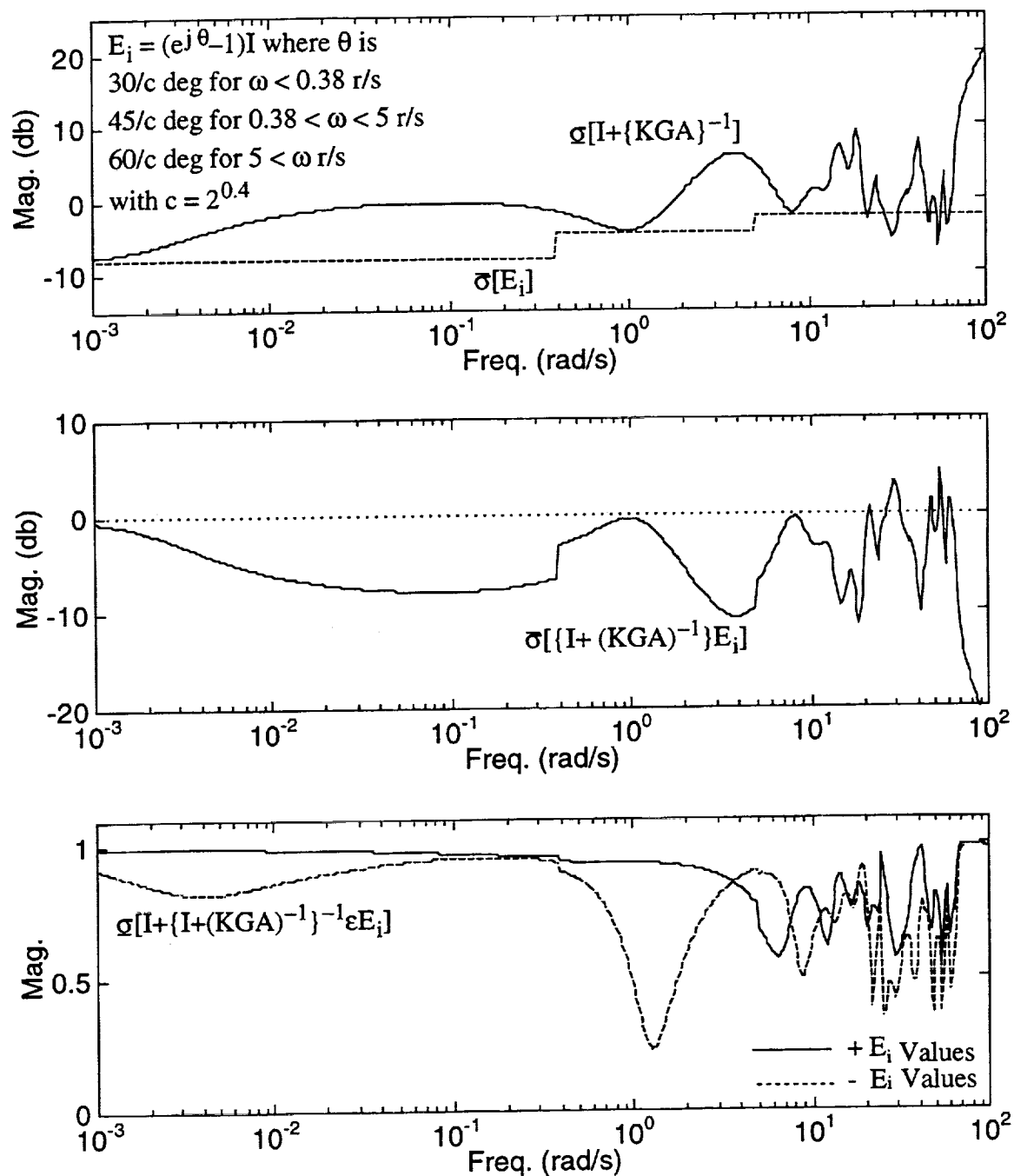


Figure 90. Singular Value Robustness Against Multi-Loop MIL-F-87242 Phase Requirement At Input



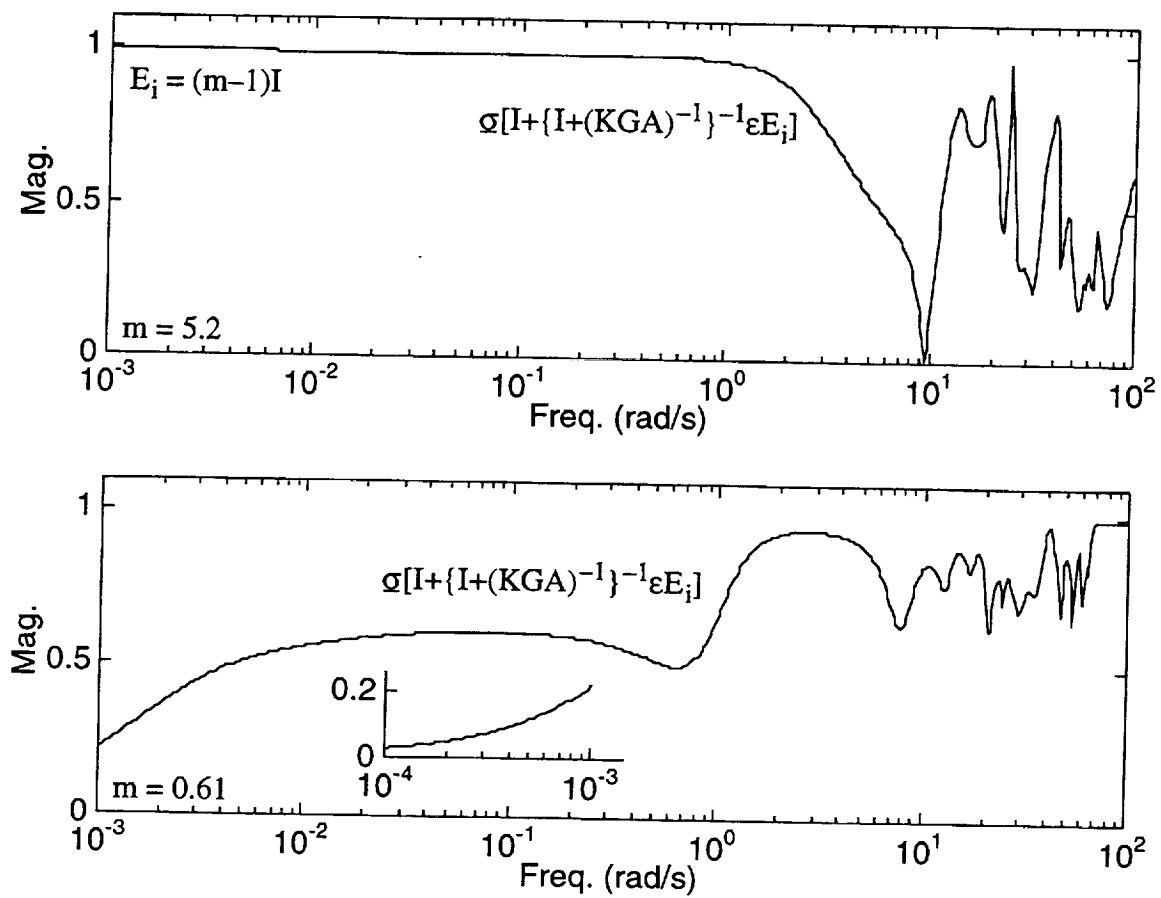


Figure 91. Singular Value Robustness Against Uniform Gain At Input

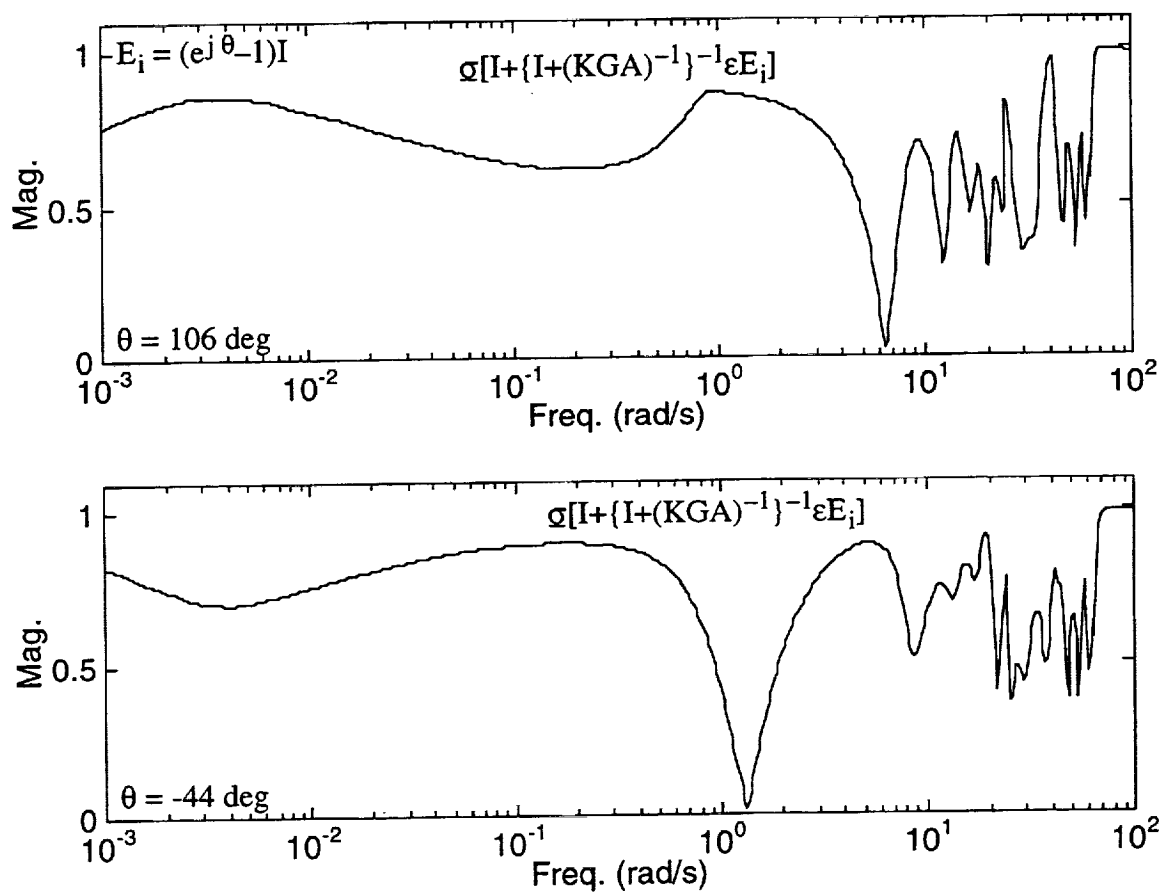


Figure 92. Singular Value Robustness Against Uniform Phase At Input

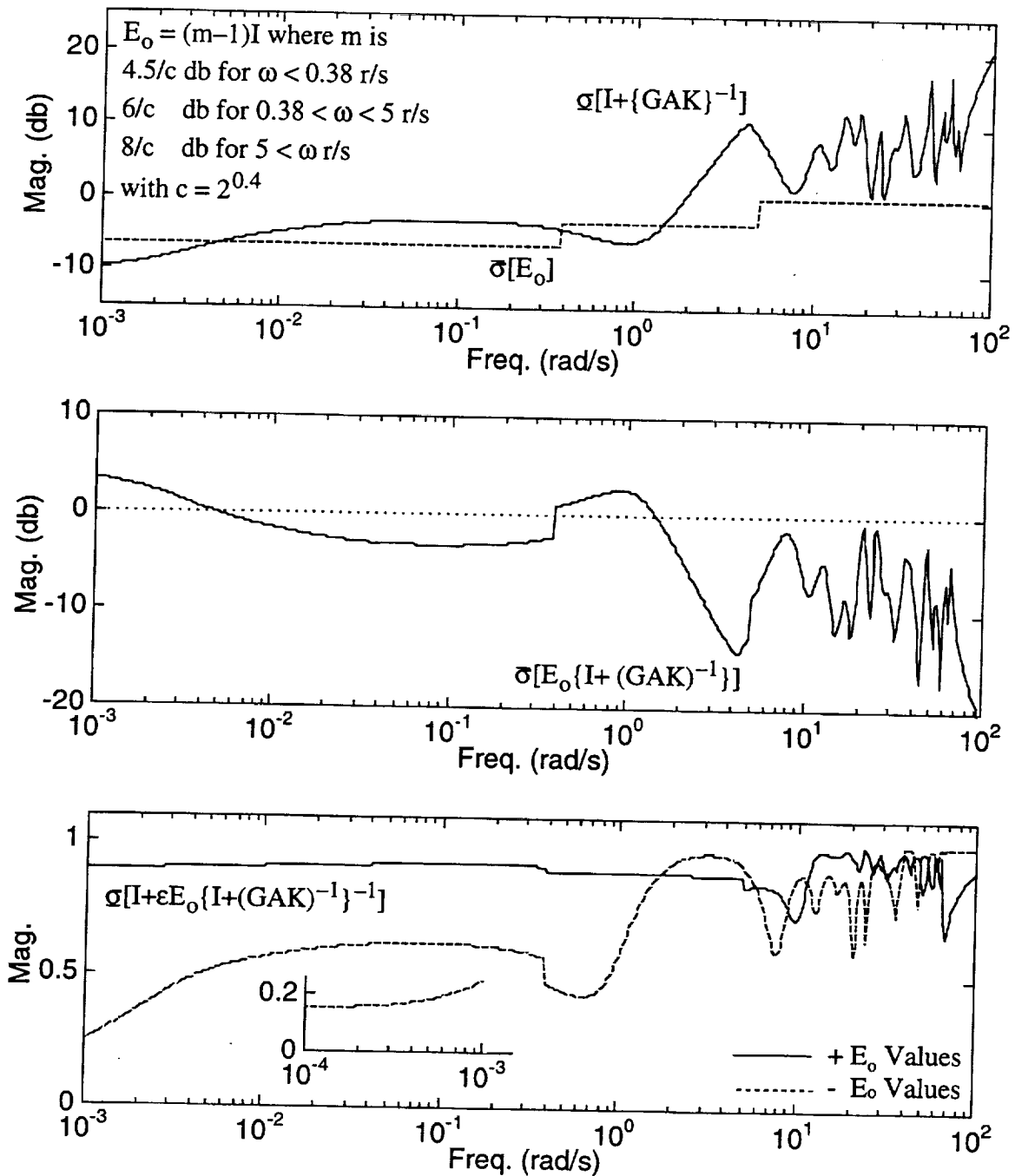


Figure 93. Singular Value Robustness Against Multi-Loop MIL-F-87242 Gain Requirement At Output

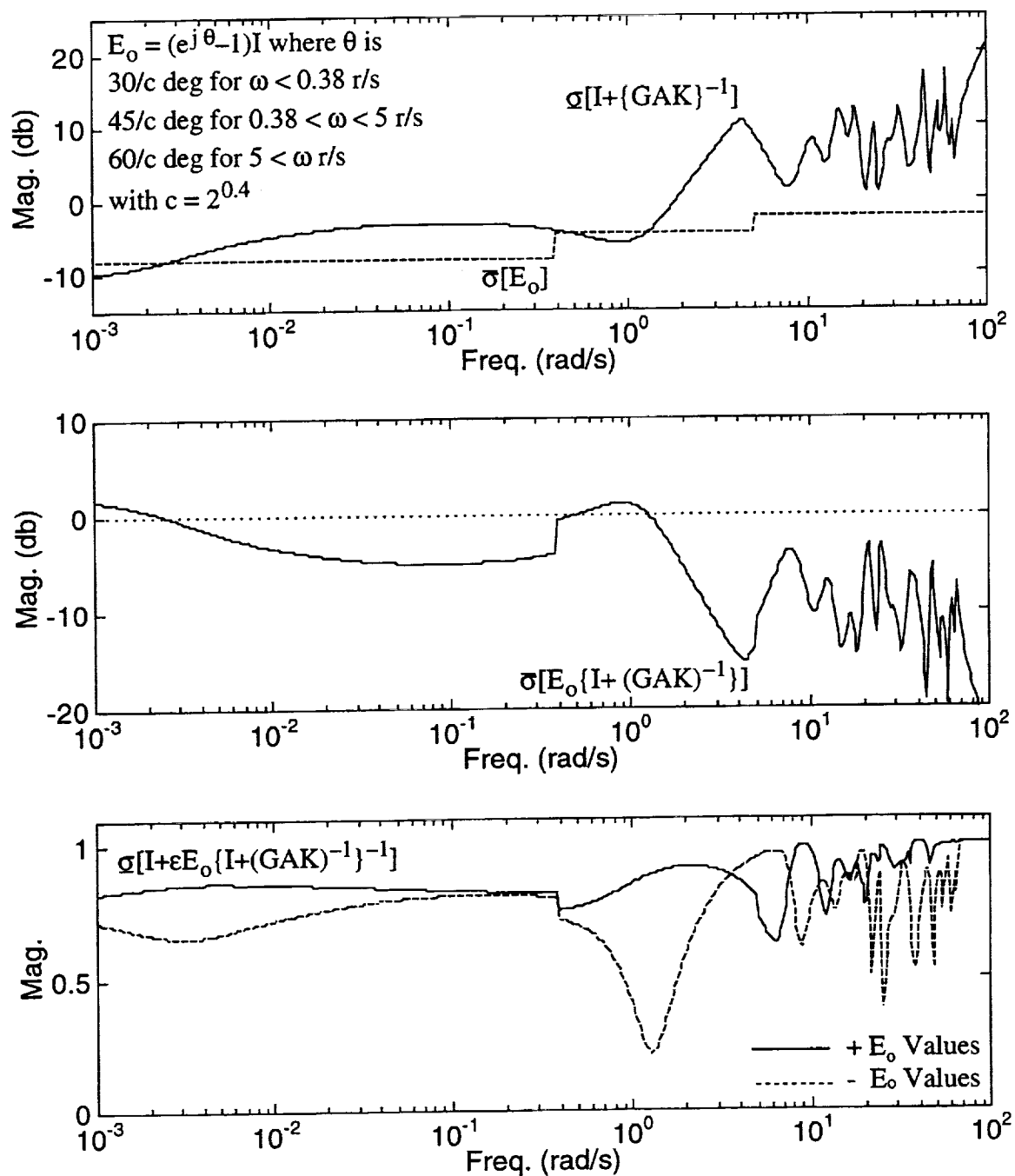


Figure 94. Singular Value Robustness Against Multi-Loop MIL-F-87242 Phase Requirement At Output

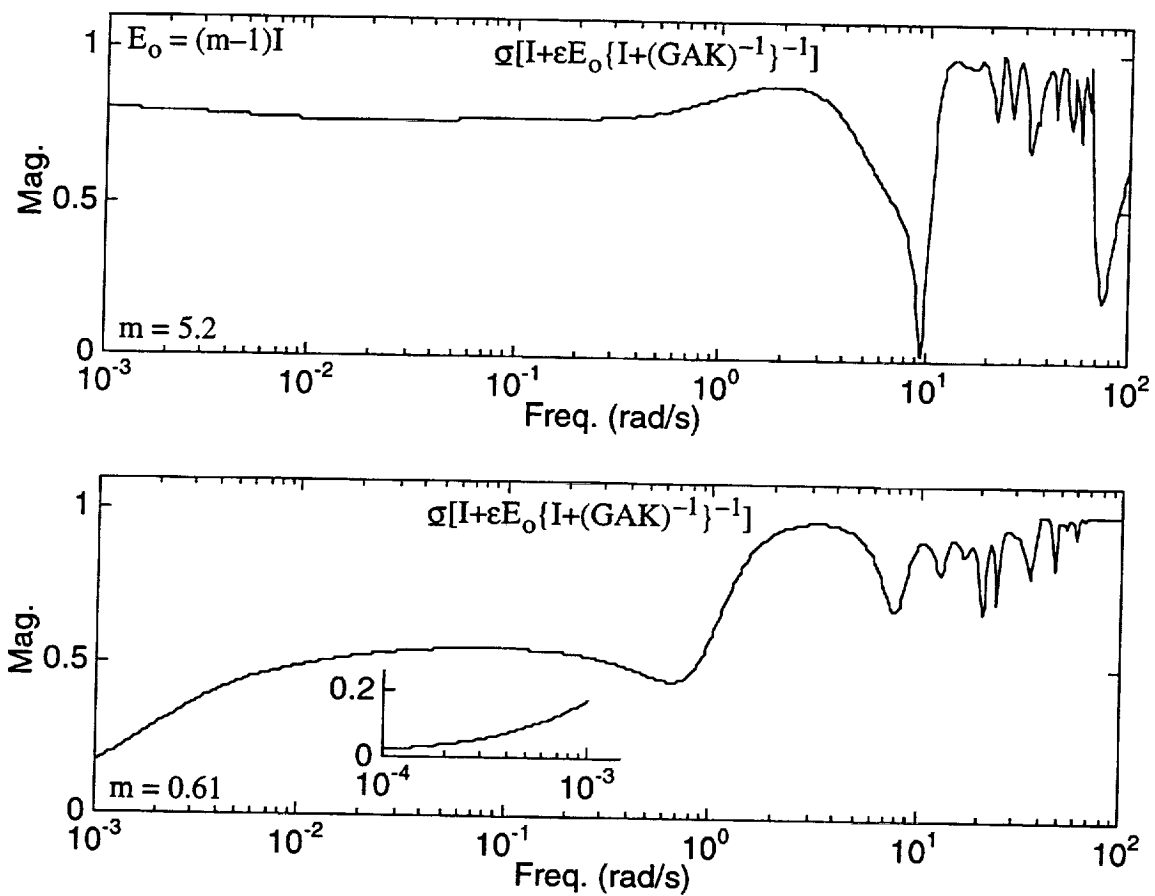


Figure 95. Singular Value Robustness Against Uniform Gain At Output

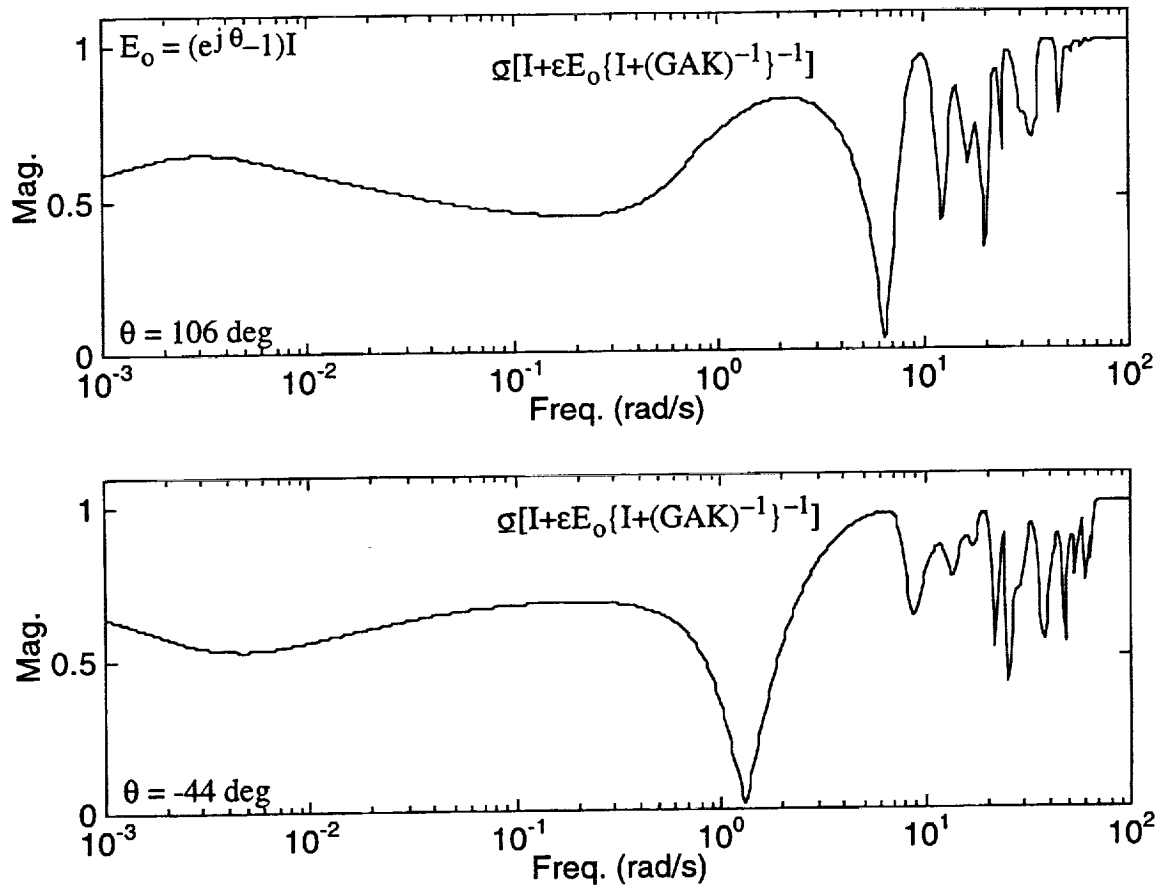


Figure 96. Singular Value Robustness Against Uniform Phase At Output

## Stability Robustness

### Structural Parameter Variations

Consider the inner loop architecture in Fig. 88 re-expressed such that the internal parameter structure of  $G(s)$  is explicit as shown in Fig. 97. This formulation is governed by

$$\begin{bmatrix} y \\ z_i \end{bmatrix} = \begin{bmatrix} M_{11} & M_{12} \\ M_{21} & M_{22} \end{bmatrix} \begin{bmatrix} y_c \\ z_o \end{bmatrix} \quad (4.22)$$

$$z_o = \Delta z_i$$

where  $\Delta$  represents variations in the system parameters of interest. The variables  $z_i$  and  $z_o$  denote the input and output signals for  $\Delta$ , and  $M_{ij}(s)$  represents the corresponding transfer matrices between  $y$ ,  $z_i$  and  $y_c$ ,  $z_o$ . The matrices  $M_{ij}(s)$  are functions of  $K(s)$  and internal components of  $G(s)$ . Application of stability robustness theory leads to the following inequality relationship:

$$\sigma[I - \epsilon \Delta M_{22}] > 0 \quad (4.23)$$

for  $0 \leq \omega \leq \infty$  and  $0 \leq \epsilon \leq 1$

Eq. (4.23) is sufficient and necessary to maintain stability in the presence of error and can be utilized to establish precise stability margins.

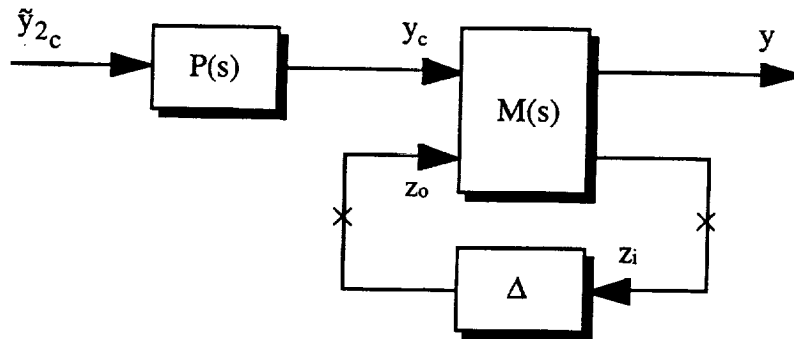


Figure 97. Inner Loop Architecture With Internal Parameter Variations

Variations in structural damping ratios will be considered initially. Suppose the vehicle-actuator state space model from Eq. (2.8) is manipulated such that

$$x = \begin{bmatrix} x_1 & x_2 \end{bmatrix}^T \quad (4.24)$$

$x_1$  = all remaining states

$$x_2 = \begin{bmatrix} \eta_1 & \eta_2 & \dots \end{bmatrix}^T$$

$$\begin{bmatrix} \dot{x}_1 \\ \dot{x}_2 \end{bmatrix} = \begin{bmatrix} A_{11} & A_{12} \\ A_{21} & A_{22} \end{bmatrix} \begin{bmatrix} x_1 \\ x_2 \end{bmatrix} + \begin{bmatrix} B_1 \\ B_2 \end{bmatrix} u_c$$

$$y = \begin{bmatrix} C_1 & C_2 \end{bmatrix} \begin{bmatrix} x_1 \\ x_2 \end{bmatrix}$$

where  $x_2$  represents the generalized coordinate rates  $\eta_i$  for the aeroelastic modes and  $x_1$  represents all other states. The partition  $A_{22}$  is

$$A_{22} = \begin{bmatrix} -(2\zeta_1\omega_1 - F_{1\eta_1}) & F_{1\eta_2} & \dots \\ F_{2\eta_1} & -(2\zeta_2\omega_2 - F_{2\eta_2}) & \\ \vdots & & \ddots \end{bmatrix} \quad (4.25)$$

where  $\zeta_i$  denotes the structural damping ratios and other parameters are defined in Eq. (2.12) or later in this subsection. The variation in damping will be represented as

$$\Delta\zeta_i = (m - 1)\zeta_i \quad (4.26)$$

where  $m$  denotes a scaling parameter with  $m = 1$  being nominal. These variations induce a perturbation for  $A_{22}$ , or

$$\Delta A_{22} = \begin{bmatrix} -2\Delta\zeta_1\omega_1 & 0 & \dots \\ 0 & -2\Delta\zeta_2\omega_2 & \\ \vdots & & \ddots \end{bmatrix} \quad (4.27)$$

For the structural damping ratio variations, the matrices  $M_{22}$  and  $\Delta$  in Eq. (4.23) are

$$M_{22} = \{sI - A'_{22} - A'_{21}(sI - A'_{11})^{-1}A'_{12}\}^{-1} \quad (4.28)$$

$$A'_{11} = A_{11} - B_1KC_1 \quad A'_{12} = A_{12} - B_1KC_2$$

$$A'_{21} = A_{21} - B_2KC_1 \quad A'_{22} = A_{22} - B_2KC_2$$

$$\Delta = \Delta A_{22}$$

Nominal values for all  $\zeta_i$  are 0.02 and Tab. 18 lists the nominal values for  $\omega_i$ .

Fig. 98 shows the stability robustness characteristics against structural damping ratio variations. The non-conservative inequality in Eq. (4.23) is utilized to establish parameter margins. The scaling parameter has been varied until the minimum singular value becomes zero. As expected, the upper parameter margin is essentially unbounded ( $m \approx +\infty$ ). Fig. 98 shows the characteristics for  $m = 10$ , but this is only an example. Significantly larger values for  $m$  yield



similar results. Variations in this direction push the airframe aeroelastic poles into the left-half plane away from instability and the singular value in Fig. 98 does not approach zero. The lower parameter margin is equivalent to a 52% reduction in damping ( $m = 0.48$ ). As seen from Fig. 98, this variation pushes aeroelastic mode 4 into the right-half plane (17 rad/s).

Table 18. Nominal Structural Natural Frequencies

Mode	$\omega_i$ (rad/s)	Mode	$\omega_i$ (rad/s)	Mode	$\omega_i$ (rad/s)
1	7.83	7	24.39	13	56.51
2	12.61	8	29.90	14	60.82
3	16.94	9	36.28	15	62.40
4	17.30	10	43.55	16	64.24
5	19.60	11	47.30	17	65.29
6	21.05	12	54.46		

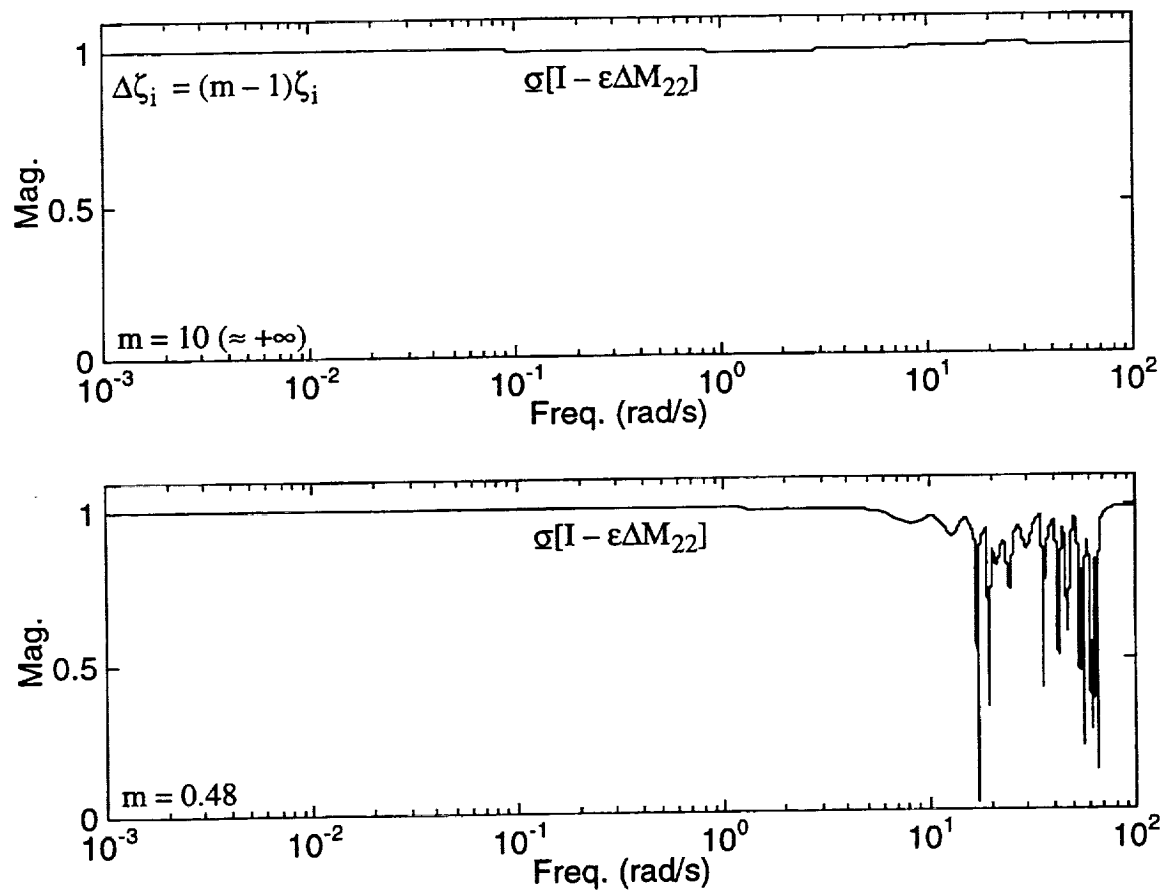


Figure 98. Singular Value Robustness Against Structural Damping Ratio

Variations in structural natural frequencies are considered next. Under this type of variation, the partitioned vehicle-actuator state space model becomes

$$\begin{aligned}
 \mathbf{x} &= \begin{bmatrix} x_1 & x_2 & x_3 \end{bmatrix}^T & x_1 &= \text{all remaining states} \\
 x_2 &= \begin{bmatrix} \eta_1 & \eta_2 & \dots \end{bmatrix}^T & x_3 &= \begin{bmatrix} \dot{\eta}_1 & \dot{\eta}_2 & \dots \end{bmatrix}^T \\
 \begin{bmatrix} \dot{x}_1 \\ \dot{x}_2 \\ \dot{x}_3 \end{bmatrix} &= \begin{bmatrix} A_{11} & A_{12} & A_{13} \\ A_{21} & A_{22} & A_{23} \\ A_{31} & A_{32} & A_{33} \end{bmatrix} \begin{bmatrix} x_1 \\ x_2 \\ x_3 \end{bmatrix} + \begin{bmatrix} B_1 \\ B_2 \\ B_3 \end{bmatrix} u_c \\
 y &= \begin{bmatrix} C_1 & C_2 & C_3 \end{bmatrix} \begin{bmatrix} x_1 \\ x_2 \\ x_3 \end{bmatrix}
 \end{aligned} \tag{4.29}$$

Here,  $x_2$  will denote the generalized coordinate positions for the aeroelastic modes and  $x_3$  denotes the corresponding rates. Partitions  $A_{32}$  and  $A_{33}$  are of interest here.

$$A_{32} = \begin{bmatrix} -(\omega_1^2 - F_{1\eta_1}) & F_{1\eta_2} & \dots \\ F_{2\eta_1} & -(\omega_2^2 - F_{2\eta_2}) & \\ \vdots & & \ddots \end{bmatrix} \quad A_{33} = \begin{bmatrix} -(2\zeta_1\omega_1 - F_{1\eta_1}) & F_{1\eta_2} & \dots \\ F_{2\eta_1} & -(2\zeta_2\omega_2 - F_{2\eta_2}) & \\ \vdots & & \ddots \end{bmatrix} \tag{4.30}$$

In Eq. (4.30),  $\omega_i$  denotes the structural natural frequencies. Variation in frequency will be represented as

$$\Delta\omega_i = (m-1)\omega_i \tag{4.31}$$

The corresponding state space parameter variation matrices  $\Delta A_{32}$  and  $\Delta A_{33}$  are

$$\Delta A_{32} = \begin{bmatrix} -(2\omega_1\Delta\omega_1 + \Delta\omega_1^2) & 0 & \dots \\ 0 & -(2\omega_2\Delta\omega_2 + \Delta\omega_2^2) & \\ \vdots & & \ddots \end{bmatrix} \quad \Delta A_{33} = \begin{bmatrix} -2\zeta_1\Delta\omega_1 & 0 & \dots \\ 0 & -2\zeta_2\Delta\omega_2 & \\ \vdots & & \ddots \end{bmatrix} \tag{4.32}$$

Finally, the matrices  $M_{22}$  and  $\Delta$  become

$$M_{22} = \begin{bmatrix} M_{22_{11}} & M_{22_{12}} \\ M_{22_{21}} & M_{22_{22}} \end{bmatrix}, \quad \Delta = \begin{bmatrix} \Delta A_{32} & 0 \\ 0 & \Delta A_{33} \end{bmatrix} \tag{4.33}$$

$$M_{22_{11}} = \{sI - A''_{22}\}^{-1} A''_{23} \{sI - A''_{33}\}^{-1}$$

$$M_{22_{12}} = \{sI - A''_{22}\}^{-1} A''_{23} \{sI - A''_{33}\}^{-1}$$

$$M_{22_{21}} = \{sI - A''_{33}\}^{-1}$$

$$M_{22_{22}} = \{sI - A''_{33}\}^{-1}$$

$$\begin{aligned}
A''_{22} &= A''_{22} + A''_{23}\{sI - A''_{33}\}^{-1}A''_{32} & A''_{33} &= A''_{33} + A''_{32}\{sI - A''_{22}\}^{-1}A''_{23} \\
A''_{22} &= A'_{22} + A'_{21}\{sI - A'_{11}\}^{-1}A'_{12} & A''_{23} &= A'_{23} + A'_{21}\{sI - A'_{11}\}^{-1}A'_{13} \\
A''_{32} &= A'_{32} + A'_{31}\{sI - A'_{11}\}^{-1}A'_{12} & A''_{33} &= A'_{33} + A'_{31}\{sI - A'_{11}\}^{-1}A'_{13} \\
A'_{11} &= A_{11} - B_1KC_1 & A'_{12} &= A_{12} - B_1KC_2 & A'_{13} &= A_{13} - B_1KC_3 \\
A'_{21} &= A_{21} - B_2KC_1 & A'_{22} &= A_{22} - B_2KC_2 & A'_{23} &= A_{23} - B_2KC_3 \\
A'_{31} &= A_{31} - B_3KC_1 & A'_{32} &= A_{32} - B_3KC_2 & A'_{33} &= A_{33} - B_3KC_3
\end{aligned}$$

Fig. 99 shows the stability robustness characteristics against structural natural frequency variations. The scaling parameter  $m$  is again varied until the minimum singular value indicates neutral stability. Results in Fig. 99 show the closed-loop system can tolerate a 50% reduction ( $m = 0.5$ ) and a 31% enlargement ( $m = 1.31$ ) of the frequency values. On the low-end, the aeroelastic modes cluster in the 4 to 40 rad/s region and all are close to instability (mode 3 initially goes unstable at 8.6 rad/s). Although not readily apparent from Fig. 99 for  $m = 0.5$ , it is interesting to note the rigid pitch mode is damped further, through coupling effects, under this variation. This behavior can be inferred from basic root migration rules (i.e., poles repel poles). As the structural modes migrate in a direction towards the origin under the natural frequency variation, they tend to push the rigid pitch mode to the left resulting in higher damping values. On the high-end, the aeroelastic modes are again destabilized, to some extent (small singular value in the 20-90 rad/s region). However, the initial instability that occurs under this variation is the relaxed stability mode which migrates back towards the right-half plane (0 rad/s). Recall structural natural frequencies influence the vehicle transfer functions through the dc term in the denominator polynomial, which directly influences the generalized Bode magnitude values near 0 rad/s.

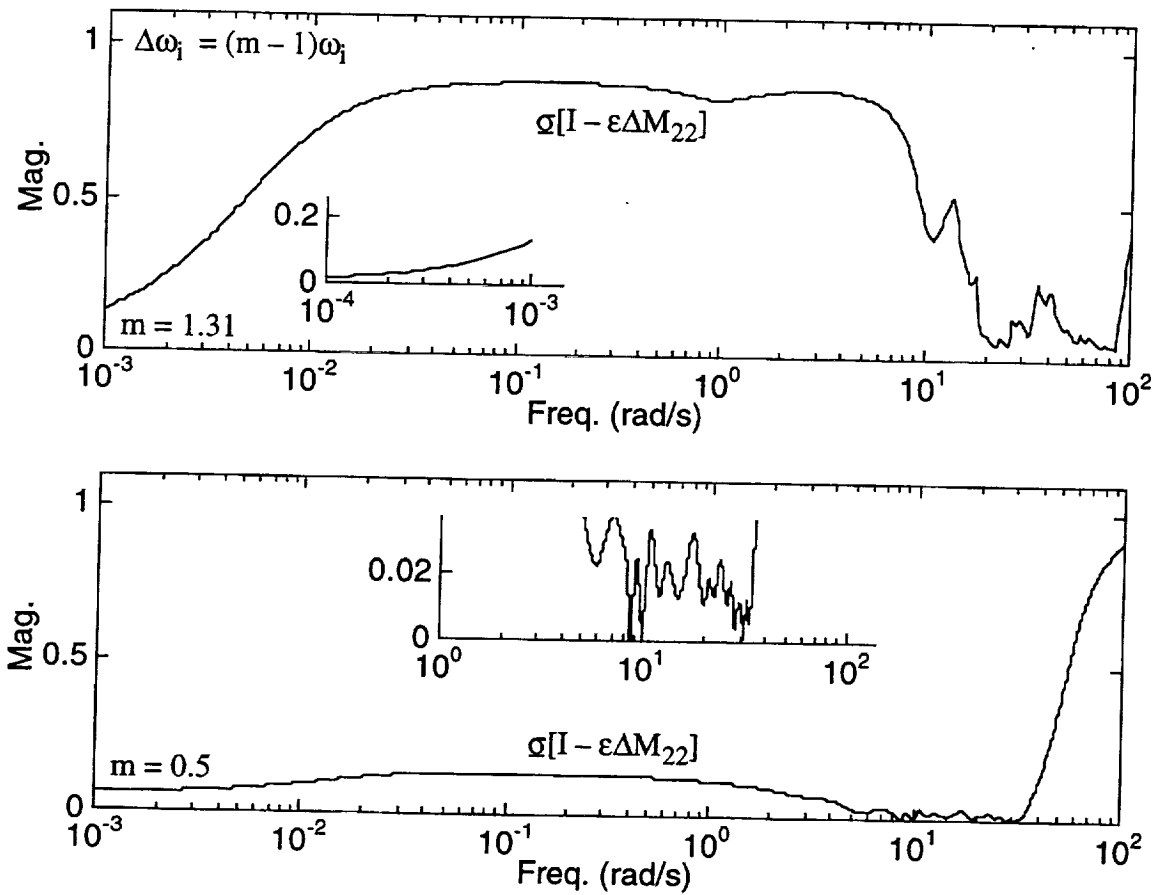


Figure 99. Singular Value Robustness Against Structural Natural Frequency

The final structural variation to be considered is mode shapes. The total variation will be decomposed into two separate variations influencing 1) input and output terms and 2) internal state terms. Mode shape variations associated with the input and output terms are considered first. The vehicle-actuator state space model is partitioned similar to Eq. (4.29), but with different state variable assignments. Here,  $x_2$  denotes the generalized coordinate rates, while  $x_3$  will denote the control surface positions, rates, and accelerations, or

$$x_2 = \begin{bmatrix} \dot{\eta}_1 & \dot{\eta}_2 & \dots \end{bmatrix}^T \quad x_3 = \begin{bmatrix} \delta_j & \dot{\delta}_j & \ddot{\delta}_j & \dots \end{bmatrix}^T \quad (4.34)$$

where  $j = E, V$

Partitions  $A_{23}$  and  $C_2$  are functions of the mode shapes with the following structure,

$$A_{23} = \begin{bmatrix} F_{1\delta_j} & F_{1\dot{\delta}_j} & F_{1\ddot{\delta}_j} & \dots \\ F_{2\delta_j} & F_{2\dot{\delta}_j} & F_{2\ddot{\delta}_j} & \\ \vdots & & & \ddots \end{bmatrix} \quad C_2 = \begin{bmatrix} -\phi_1' & -\phi_2' & \dots \\ \vdots & & \ddots \end{bmatrix} \quad (4.35)$$

$$F_{i\delta_j} = \frac{\bar{q}\bar{S}_k\phi_i}{m_i} C_{L\alpha}^k \varepsilon_{\delta_j} \quad F_{i\dot{\delta}_j} = \frac{\bar{q}\bar{S}_k\phi_i}{m_i} C_{L\alpha}^k \varepsilon_{\delta_j} \quad F_{i\ddot{\delta}_j} = \frac{\bar{q}\bar{S}_k\phi_i}{m_i} C_{L\alpha}^k \varepsilon_{\delta_j}$$

where  $k = H, V$

where  $\phi_i$  denotes the structural mode shapes,  $\varepsilon_{\delta_j}$  denotes control effectiveness ( $\partial\alpha/\partial\delta_j$ ), and other parameters are defined in Section II-C. No attempt is made to include dependency on mode shape through the modal mass terms  $m_i$ . Nominal mode shape values can be obtained from the data given in Appendix C. Variation in deflection shape will be represented as

$$\Delta\phi_i = (m-1)\phi_i \quad (4.36)$$

The corresponding state space parameter variation matrices  $\Delta A_{23}$  and  $\Delta C_2$  are

$$\Delta A_{23} = \begin{bmatrix} \frac{F_{1\delta_j}}{\phi_1} \Delta\phi_1 & \frac{F_{1\dot{\delta}_j}}{\phi_1} \Delta\phi_1 & \frac{F_{1\ddot{\delta}_j}}{\phi_1} \Delta\phi_1 & \dots \\ \frac{F_{2\delta_j}}{\phi_2} \Delta\phi_2 & \frac{F_{2\dot{\delta}_j}}{\phi_2} \Delta\phi_2 & \frac{F_{2\ddot{\delta}_j}}{\phi_2} \Delta\phi_2 & \\ \vdots & & & \ddots \end{bmatrix} \quad \Delta C_2 = \begin{bmatrix} -\Delta\phi_1' & -\Delta\phi_2' & \dots \\ \vdots & & \ddots \end{bmatrix} \quad (4.37)$$

Finally, the matrices  $M_{22}$  and  $\Delta$  become

$$M_{22} = \begin{bmatrix} M_{22_{11}} & M_{22_{12}} \\ M_{22_{21}} & M_{22_{22}} \end{bmatrix}, \quad \Delta = \begin{bmatrix} \Delta A_{23} & 0 \\ 0 & \Delta C_2 \end{bmatrix} \quad (4.38)$$

$$\begin{aligned} M_{22_{11}} &= \{sI - A'''_{33}\}^{-1} A'''_{32} \{sI - A'''_{22}\}^{-1} & M_{22_{12}} &= -\{sI - A'''_{33}\}^{-1} B'''_3 K \\ M_{22_{21}} &= \{sI - A'''_{22}\}^{-1} & M_{22_{22}} &= -\{sI - A'''_{22}\}^{-1} B'''_2 K \\ A'''_{22} &= A''_{22} + A''_{23} \{sI - A''_{33}\}^{-1} A''_{32} & A'''_{33} &= A''_{33} + A''_{32} \{sI - A''_{22}\}^{-1} A''_{23} \\ B'''_2 &= B''_2 + A''_{23} \{sI - A''_{33}\}^{-1} B''_3 & B'''_3 &= B''_3 + A''_{32} \{sI - A''_{22}\}^{-1} B''_2 \\ A''_{22} &= A'_{22} + A'_{21} \{sI - A'_{11}\}^{-1} A'_{12} & A''_{23} &= A'_{23} + A'_{21} \{sI - A'_{11}\}^{-1} A'_{13} \\ A''_{32} &= A'_{32} + A'_{31} \{sI - A'_{11}\}^{-1} A'_{12} & A''_{33} &= A'_{33} + A'_{31} \{sI - A'_{11}\}^{-1} A'_{13} \\ B''_2 &= B_2 + A'_{21} \{sI - A'_{11}\}^{-1} B_1 & B''_3 &= B_3 + A'_{31} \{sI - A'_{11}\}^{-1} B_1 \\ A'_{11} &= A_{11} - B_1 K C_1 & A'_{12} &= A_{12} - B_1 K C_2 & A'_{13} &= A_{13} - B_1 K C_3 \\ A'_{21} &= A_{21} - B_2 K C_1 & A'_{22} &= A_{22} - B_2 K C_2 & A'_{23} &= A_{23} - B_2 K C_3 \\ A'_{31} &= A_{31} - B_3 K C_1 & A'_{32} &= A_{32} - B_3 K C_2 & A'_{33} &= A_{33} - B_3 K C_3 \end{aligned}$$

Fig. 100 shows the stability robustness characteristics against structural mode shape variations related to the input and output terms. The scaling parameter  $m$  is again varied until the minimum singular value indicates neutral stability. Results in Fig. 100 show the closed-loop system can tolerate a 79% reduction ( $m = 0.21$ ) and a 167% enlargement ( $m = 2.67$ ) of the shape values. On the low-end, the relaxed stability mode migrates back to the right-half plane (0 rad/s) under the parameter variation. On the high-end, this same trend occurs. In addition, aeroelastic mode 1 moves to the right-half plane (9 rad/s). This aeroelastic instability is the initial instability. Note the overall magnitude values in Fig. 100 are much smaller when compared to Figs. 98-99. In Fig. 100, the curves approach a value of 1 at higher frequencies, but in the region of interest, the values are very small. This feature suggests all modes are destabilized uniformly, in a gross sense. Vastly different units for  $\Delta A_{23}$  and  $\Delta C_2$  may also be a contributor to this behavior. Scaling for units was not considered. As a final point, uniform variation of mode shapes theoretically should have no influence on dynamic characteristics, since deflection shapes are nonunique. The large parameter margins reflect this observation, however, the implemented variation is an approximation to exact uniform variations.

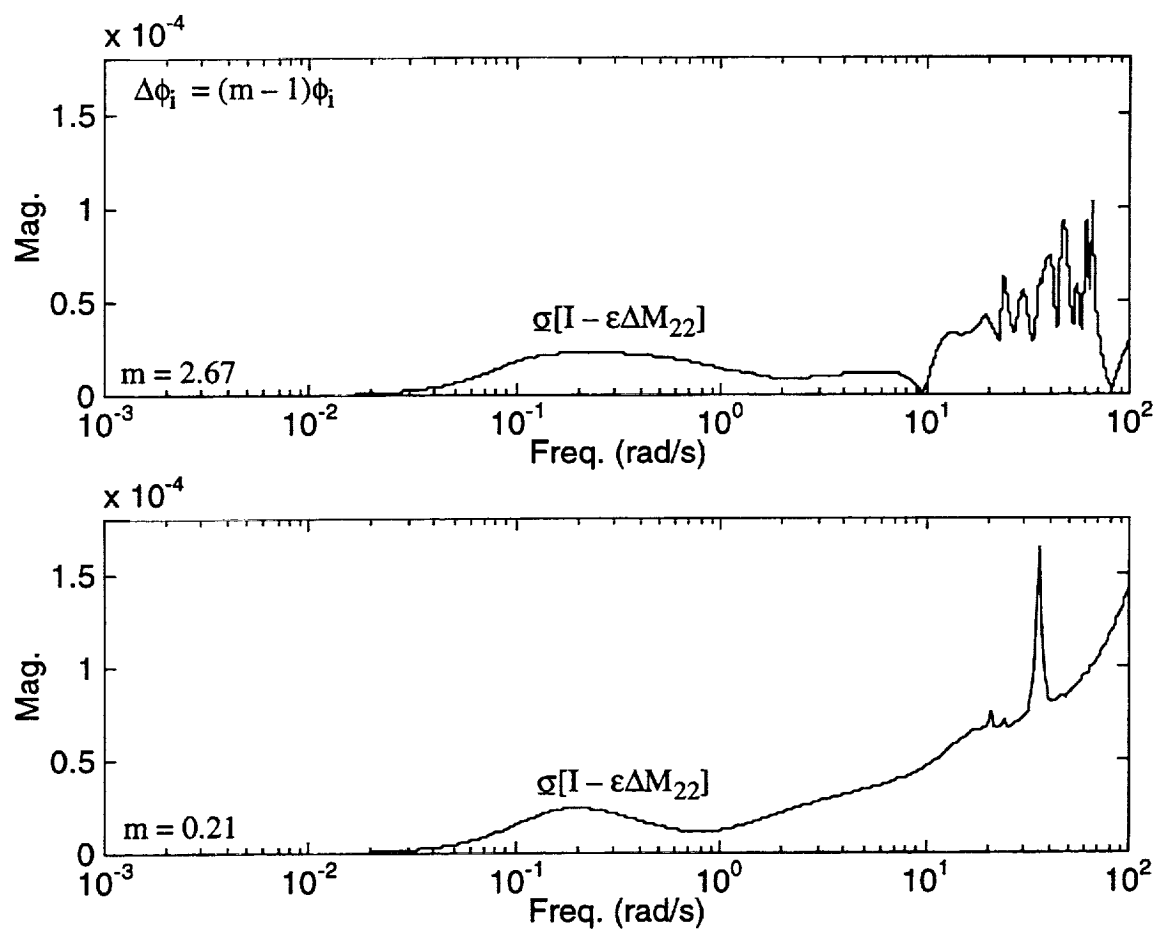


Figure 100. Singular Value Robustness Against Structural Mode Shape - Input And Output



Now consider the second type of mode shape variation associated with internal state terms. The vehicle-actuator state space model is again partitioned as in Eq. (4.29), but here the state variable assignments are

$$x_2 = [\eta_1 \ \eta_2 \ \dots]^T \quad x_3 = [w \ q \ \dot{\eta}_1 \ \dot{\eta}_2 \ \dots]^T \quad (4.39)$$

In Eq. (4.39),  $x_2$  denotes the generalized coordinate positions and  $x_3$  will denote the downward speed, pitch rate, and generalized coordinate rates. Partitions  $A_{32}$  and  $A_{33}$  depend on the mode shapes with the following structure.

$$A_{32} = \begin{bmatrix} Z_{\eta_1} & Z_{\eta_2} & \dots \\ M_{\eta_1} & M_{\eta_2} & \\ -(\omega_1^2 - F_{1\eta_1}) & F_{1\eta_2} & \\ F_{2\eta_1} & -(\omega_2^2 - F_{2\eta_2}) & \\ \vdots & & \ddots \end{bmatrix} \quad (4.40)$$

$$A_{33} = \begin{bmatrix} Z_w & U+Z_q & Z_{\eta_1} & Z_{\eta_2} & \dots \\ M_w & M_q & M_{\eta_1} & M_{\eta_2} & \\ F_{1w} & F_{1q} & -(2\zeta_1\omega_1 - F_{1\eta_1}) & F_{1\eta_2} & \\ F_{2w} & F_{2q} & F_{2\eta_1} & -(2\zeta_2\omega_2 - F_{2\eta_2}) & \\ \vdots & & & & \ddots \end{bmatrix}$$

$$Z_w = \frac{\bar{q}\bar{S}}{mV_T} \left\{ \sum_k -\frac{\bar{S}_k}{\bar{S}} C_{L\alpha}^k \right\}$$

$$M_w = \frac{\bar{q}\bar{S}\bar{c}}{I_{yy}V_T} \left\{ \sum_k \frac{\bar{S}_k}{\bar{S}} \frac{\bar{c}_k}{\bar{c}} \frac{x_k}{\bar{c}_k} C_{L\alpha}^k \right\}$$

$$Z_{\eta_i} = \frac{\bar{q}\bar{S}}{m} \left\{ \sum_k \frac{\bar{S}_k}{\bar{S}} \phi_i' C_{L\alpha}^k \right\}$$

$$M_{\eta_i} = \frac{\bar{q}\bar{S}\bar{c}}{I_{yy}} \left\{ \sum_k -\frac{\bar{S}_k}{\bar{S}} \frac{\bar{c}_k}{\bar{c}} \frac{x_k}{\bar{c}_k} \phi_i' C_{L\alpha}^k \right\}$$

$$F_{iw} = \frac{\bar{q}\bar{S}\bar{c}}{m_i V_T} \left\{ \sum_k \frac{\bar{S}_k}{\bar{S}} \frac{\bar{c}_k}{\bar{c}} \frac{\phi_i}{\bar{c}_k} C_{L\alpha}^k \right\}$$

$$F_{i\eta_j} = \frac{\bar{q}\bar{S}\bar{c}}{m_i} \left\{ \sum_k -\frac{\bar{S}_k}{\bar{S}} \frac{\bar{c}_k}{\bar{c}} \frac{\phi_i}{\bar{c}_k} \phi_j' C_{L\alpha}^k \right\}$$

$$Z_q = \frac{\bar{q}\bar{S}\bar{c}}{2mV_T} \left\{ \sum_k 2 \frac{\bar{S}_k}{\bar{S}} \frac{x_k}{\bar{c}} C_{L\alpha}^k \right\}$$

$$M_q = \frac{\bar{q}\bar{S}\bar{c}^2}{2I_{yy}V_T} \left\{ \sum_k -2 \frac{\bar{S}_k}{\bar{S}} \frac{\bar{c}_k}{\bar{c}} \frac{x_k}{\bar{c}_k} \frac{x_k}{\bar{c}} C_{L\alpha}^k \right\}$$

$$Z_{\eta_i} = \frac{\bar{q}\bar{S}\bar{c}}{2mV_T} \left\{ \sum_k 2 \frac{\bar{S}_k}{\bar{S}} \frac{\phi_i}{\bar{c}} C_{L\alpha}^k \right\}$$

$$M_{\eta_i} = \frac{\bar{q}\bar{S}\bar{c}^2}{2I_{yy}V_T} \left\{ \sum_k -2 \frac{\bar{S}_k}{\bar{S}} \frac{\bar{c}_k}{\bar{c}} \frac{x_k}{\bar{c}_k} \frac{\phi_i}{\bar{c}} C_{L\alpha}^k \right\}$$

$$F_{iq} = \frac{\bar{q}\bar{S}\bar{c}^2}{2m_i V_T} \left\{ \sum_k -2 \frac{\bar{S}_k}{\bar{S}} \frac{\bar{c}_k}{\bar{c}} \frac{x_k}{\bar{c}_k} \frac{\phi_i}{\bar{c}} C_{L\alpha}^k \right\}$$

$$F_{i\eta_j} = \frac{\bar{q}\bar{S}\bar{c}^2}{2m_i V_T} \left\{ \sum_k -2 \frac{\bar{S}_k}{\bar{S}} \frac{\bar{c}_k}{\bar{c}} \frac{\phi_i}{\bar{c}_k} \frac{\phi_j}{\bar{c}} C_{L\alpha}^k \right\}$$

where  $k = W, H, V$

The parameter  $\phi_i$  again denotes structural mode shapes and other parameters are defined in Section II-C. As can be seen from Eq. (4.40), functional dependency upon mode shapes is more involved here.  $\phi_i$  does not appear as a simple multiplying factor, as in Eq. (4.35). To approximately represent the actual variation occurring in the physical system, the parameter structure indicated in Eq. (4.40) must be utilized. Appendix D develops a least squares solution to estimate the component lift curve slopes, assuming all other geometric and inertial data is known. Nominal mode shape values can be obtained from the data given in Appendix C and variations in deflection shape are modeled as in Eq. (4.36). All generalized mass values  $m_i$  equal 1 "slinch", as defined in Ref. 12. The corresponding state space parameter variation matrices  $\Delta A_{32}$  and  $\Delta A_{33}$  are

$$\Delta A_{32} = \begin{bmatrix} \Delta Z_{\eta_1} & \Delta Z_{\eta_2} & \cdots \\ \Delta M_{\eta_1} & \Delta M_{\eta_2} & \\ \Delta F_{1\eta_1} & \Delta F_{1\eta_2} & \\ \Delta F_{2\eta_1} & \Delta F_{2\eta_2} & \\ \vdots & & \ddots \end{bmatrix} \quad \Delta A_{33} = \begin{bmatrix} 0 & 0 & \Delta Z_{\eta_1} & \Delta Z_{\eta_2} & \cdots \\ 0 & 0 & \Delta M_{\eta_1} & \Delta M_{\eta_2} & \\ \Delta F_{1w} & \Delta F_{1q} & \Delta F_{1\eta_1} & \Delta F_{1\eta_2} & \\ \Delta F_{2w} & \Delta F_{2q} & \Delta F_{2\eta_1} & \Delta F_{2\eta_2} & \\ \vdots & & & & \ddots \end{bmatrix} \quad (4.41)$$

$$\Delta Z_{\eta_i} = \frac{\bar{q}\bar{S}}{m} \left\{ \sum_k \frac{\bar{S}_k}{\bar{S}} \Delta\phi_i' C_{L\alpha}^k \right\}$$

$$\Delta M_{\eta_i} = \frac{\bar{q}\bar{S}\bar{c}}{I_{yy}} \left\{ \sum_k -\frac{\bar{S}_k}{\bar{S}} \frac{\bar{c}_k}{\bar{c}} \frac{x_k}{\bar{c}_k} \Delta\phi_i' C_{L\alpha}^k \right\}$$

$$\Delta F_{iw} = \frac{\bar{q}\bar{S}\bar{c}}{m_i V_T} \left\{ \sum_k \frac{\bar{S}_k}{\bar{S}} \frac{\bar{c}_k}{\bar{c}} \frac{\Delta\phi_i}{\bar{c}_k} C_{L\alpha}^k \right\}$$

$$\Delta F_{iq} = \frac{\bar{q}\bar{S}\bar{c}^2}{2m_i V_T} \left\{ \sum_k -2 \frac{\bar{S}_k}{\bar{S}} \frac{\bar{c}_k}{\bar{c}} \frac{x_k}{\bar{c}_k} \frac{\Delta\phi_i}{\bar{c}} C_{L\alpha}^k \right\}$$

$$\Delta F_{i\eta_j} = \frac{\bar{q}\bar{S}\bar{c}}{m_i} \left\{ \sum_k -\frac{\bar{S}_k}{\bar{S}} \frac{\bar{c}_k}{\bar{c}} \frac{(\Delta\phi_i\phi_j' + \phi_i\Delta\phi_j' + \Delta\phi_i\Delta\phi_j')}{\bar{c}_k} C_{L\alpha}^k \right\}$$

$$\Delta F_{i\eta_j} = \frac{\bar{q}\bar{S}\bar{c}^2}{2m_i V_T} \left\{ \sum_k -2 \frac{\bar{S}_k}{\bar{S}} \frac{\bar{c}_k}{\bar{c}} \frac{(\Delta\phi_i\phi_j + \phi_i\Delta\phi_j + \Delta\phi_i\Delta\phi_j)}{\bar{c}_k \bar{c}} C_{L\alpha}^k \right\}$$

where  $k = W, H, V$

Matrices  $M_{22}$  and  $\Delta$  are defined as in Eq. (4.33).

Fig. 101 shows the stability robustness characteristics against structural mode shape variations related to internal state terms. The scaling parameter  $m$  is again varied until the minimum singular value indicates neutral stability. Results in Fig. 101 show the closed-loop system can tolerate a 63% reduction ( $m = 0.37$ ) and a 196% enlargement ( $m = 2.96$ ) of the shape values. On

the low-end, the relaxed stability mode migrates back to the right-half plane (0 rad/s) under the parameter variation. On this same plot, results show the pitch mode is also close to instability. On the high-end, this same trend occurs. Both the relaxed stability mode and the pitch mode move towards the right-half plane (0 and 2.3 rad/s). This pitch mode instability is the initial instability. Again, the magnitude values in Fig. 101 are much smaller overall, as in Fig. 100, indicating nearly uniform destabilization of all modes under this uncertainty variation.

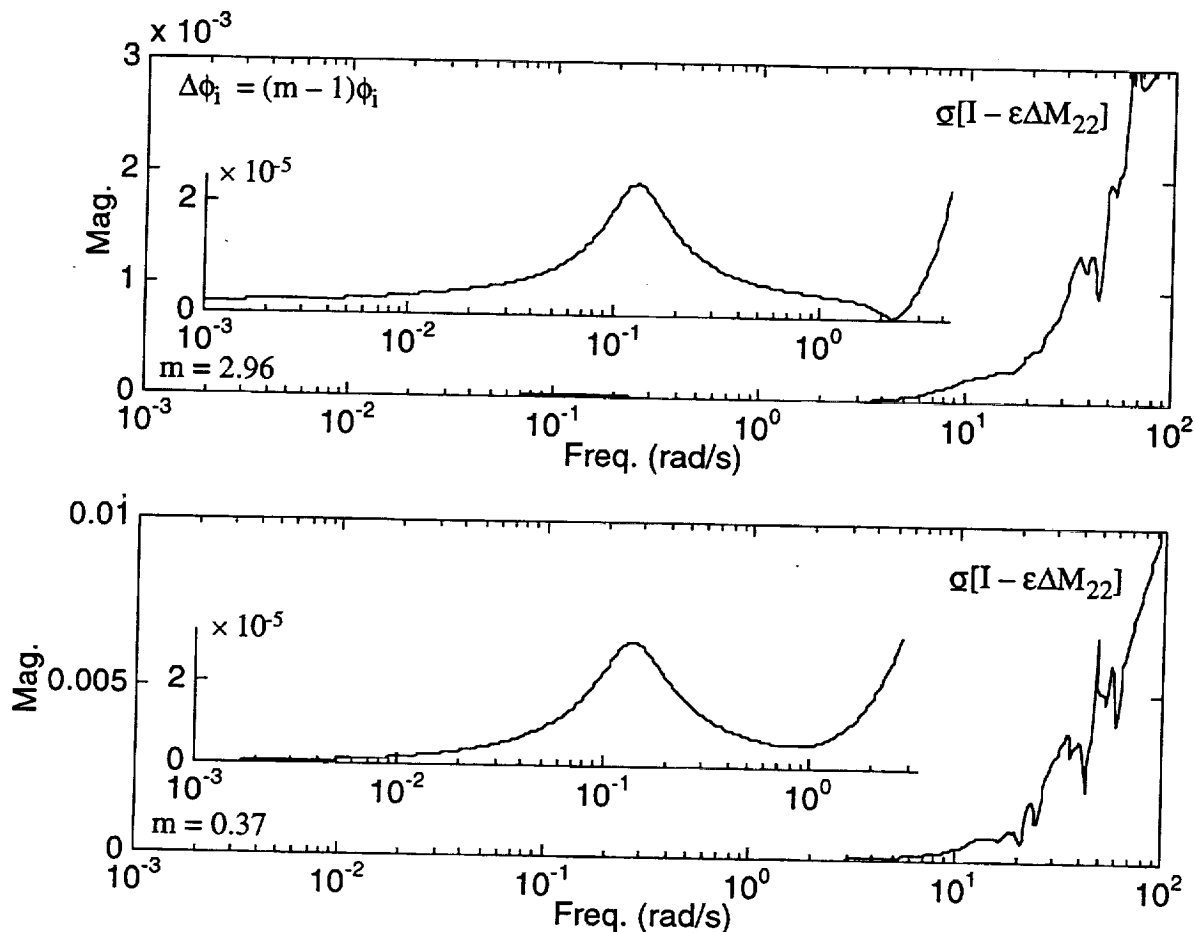


Figure 101. Singular Value Robustness Against Structural Mode Shape - Internal

## Stability Robustness

### Aerodynamic Parameter Variations

Two aerodynamic parameter variations are to be considered. The first aerodynamic variation to be considered is control effectiveness of the elevator and vane. The vehicle-actuator state space model is partitioned as in Eq. (4.29), with yet again different state variable assignments. Here,  $x_2$  denotes the downward velocity, pitch rate, and generalized coordinate rates, while  $x_3$  denotes the control surface positions, rates, and accelerations, or

$$x_2 = [w \ q \ \dot{\eta}_1 \ \dot{\eta}_2 \ \dots]^T \quad x_3 = [\delta_j \ \dot{\delta}_j \ \ddot{\delta}_j \ \dots]^T \quad (4.42)$$

where  $j = E, V$

Partition  $A_{23}$  depends on the control surface effectiveness as follows.

$$A_{23} = \begin{bmatrix} Z_{\delta_j} & Z_{\dot{\delta}_j} & Z_{\ddot{\delta}_j} & \dots \\ M_{\delta_j} & M_{\dot{\delta}_j} & M_{\ddot{\delta}_j} & \\ F_{1\delta_j} & F_{1\dot{\delta}_j} & F_{1\ddot{\delta}_j} & \\ F_{2\delta_j} & F_{2\dot{\delta}_j} & F_{2\ddot{\delta}_j} & \\ \vdots & & & \ddots \end{bmatrix} \quad (4.43)$$

$$Z_{\delta_j} = -\frac{\bar{q}\bar{S}_k}{m} C_{L\alpha}^k \varepsilon_{\delta_j} \quad Z_{\dot{\delta}_j} = -\frac{\bar{q}\bar{S}_k}{m} C_{L\alpha}^k \varepsilon_{\delta_j} \quad Z_{\ddot{\delta}_j} = -\frac{\bar{q}\bar{S}_k}{m} C_{L\alpha}^k \varepsilon_{\delta_j}$$

$$M_{\delta_j} = \frac{\bar{q}\bar{S}_k x_k}{I_{yy}} C_{L\alpha}^k \varepsilon_{\delta_j} \quad M_{\dot{\delta}_j} = \frac{\bar{q}\bar{S}_k x_k}{I_{yy}} C_{L\alpha}^k \varepsilon_{\delta_j} \quad M_{\ddot{\delta}_j} = \frac{\bar{q}\bar{S}_k x_k}{I_{yy}} C_{L\alpha}^k \varepsilon_{\delta_j}$$

$F_{i\delta_j}, F_{i\dot{\delta}_j}, F_{i\ddot{\delta}_j}$  defined in Eq. (4.35)  
where  $k = H, V$

The parameter  $\varepsilon_{\delta_j}$  denotes control effectiveness ( $\partial\alpha/\partial\delta_j$ ), and other parameters are defined in Section II-C. Nominal effectiveness values are estimated from handbook charts and are  $\varepsilon_{\delta_E} = 0.6$  and  $\varepsilon_{\delta_V} = 1$ . Variation in effectiveness will be represented as

$$\Delta\varepsilon_{\delta_j} = (m-1)\varepsilon_{\delta_j} \quad (4.44)$$

The corresponding state space parameter variation matrix  $\Delta A_{23}$  is

$$\Delta A_{23} = \begin{bmatrix} \frac{Z_{\delta_j}}{\epsilon_{\delta_j}} \Delta \epsilon_{\delta_j} & \frac{Z_{\delta_j}}{\epsilon_{\delta_j}} \Delta \epsilon_{\delta_j} & \frac{Z_{\delta_j}}{\epsilon_{\delta_j}} \Delta \epsilon_{\delta_j} & \dots \\ \frac{M_{\delta_j}}{\epsilon_{\delta_j}} \Delta \epsilon_{\delta_j} & \frac{M_{\delta_j}}{\epsilon_{\delta_j}} \Delta \epsilon_{\delta_j} & \frac{M_{\delta_j}}{\epsilon_{\delta_j}} \Delta \epsilon_{\delta_j} & \\ \frac{F_{1\delta_j}}{\epsilon_{\delta_j}} \Delta \epsilon_{\delta_j} & \frac{F_{1\delta_j}}{\epsilon_{\delta_j}} \Delta \epsilon_{\delta_j} & \frac{F_{1\delta_j}}{\epsilon_{\delta_j}} \Delta \epsilon_{\delta_j} & \\ \frac{F_{2\delta_j}}{\epsilon_{\delta_j}} \Delta \epsilon_{\delta_j} & \frac{F_{2\delta_j}}{\epsilon_{\delta_j}} \Delta \epsilon_{\delta_j} & \frac{F_{2\delta_j}}{\epsilon_{\delta_j}} \Delta \epsilon_{\delta_j} & \\ \vdots & & & \ddots \end{bmatrix} \quad (4.45)$$

Finally, the matrices  $M_{22}$  and  $\Delta$  become

$$\begin{aligned} M_{22} &= -\{sI - A'''_{33}\}^{-1} A'''_{32} & \Delta &= \Delta A_{23} \\ A'''_{33} &= A'_{33} + A'_{31}\{sI - A''_{11}\}^{-1} A''_{13} + A'_{32}\{sI - A''_{22}\}^{-1} A''_{23} \\ A'''_{32} &= A'_{32}\{sI - A''_{22}\}^{-1} + A'_{31}\{sI - A''_{11}\}^{-1} A'_{12}\{sI - A'_{22}\}^{-1} \\ A''_{11} &= A'_{11} + A'_{12}\{sI - A'_{22}\}^{-1} A'_{21} & A''_{13} &= A'_{13} + A'_{12}\{sI - A'_{22}\}^{-1} A'_{23} \\ A''_{22} &= A'_{22} + A'_{21}\{sI - A'_{11}\}^{-1} A'_{12} & A''_{23} &= A'_{23} + A'_{21}\{sI - A'_{11}\}^{-1} A'_{13} \\ A'_{11} &= A_{11} - B_1 K C_1 & A'_{12} &= A_{12} - B_1 K C_2 & A'_{13} &= A_{13} - B_1 K C_3 \\ A'_{21} &= A_{21} - B_2 K C_1 & A'_{22} &= A_{22} - B_2 K C_2 & A'_{23} &= A_{23} - B_2 K C_3 \\ A'_{31} &= A_{31} - B_3 K C_1 & A'_{32} &= A_{32} - B_3 K C_2 & A'_{33} &= A_{33} - B_3 K C_3 \end{aligned} \quad (4.46)$$

Fig. 102 shows the stability robustness characteristics against aerodynamic control effectiveness variations for the elevator and vane. The scaling parameter  $m$  is again varied until the minimum singular value indicates neutral stability. Results in Fig. 102 show the closed-loop system remains stable for a 50% reduction ( $m = 0.5$ ) and a 450% enlargement ( $m = 5.5$ ) of the effectiveness values. On the low-end, the relaxed stability mode migrates back to the right-half plane (0 rad/s) under the parameter variation. This trend can be expected since aerodynamic control effectiveness directly impacts loop gain, and this right-half plane airframe mode requires a minimum level of gain for stability. Fig. 102 also indicates pitch stability is compromised (1 rad/s). On the high-end, aeroelastic mode 1 moves to the right-half plane (9.5 rad/s). Variations in this direction are also critical. The system is known to have stability problems when the pitch loop

control bandwidth is set at excessively high values, and Fig. 102 agrees with this behavior. Overall singular value levels are again small when compared with Figs. 98-99.

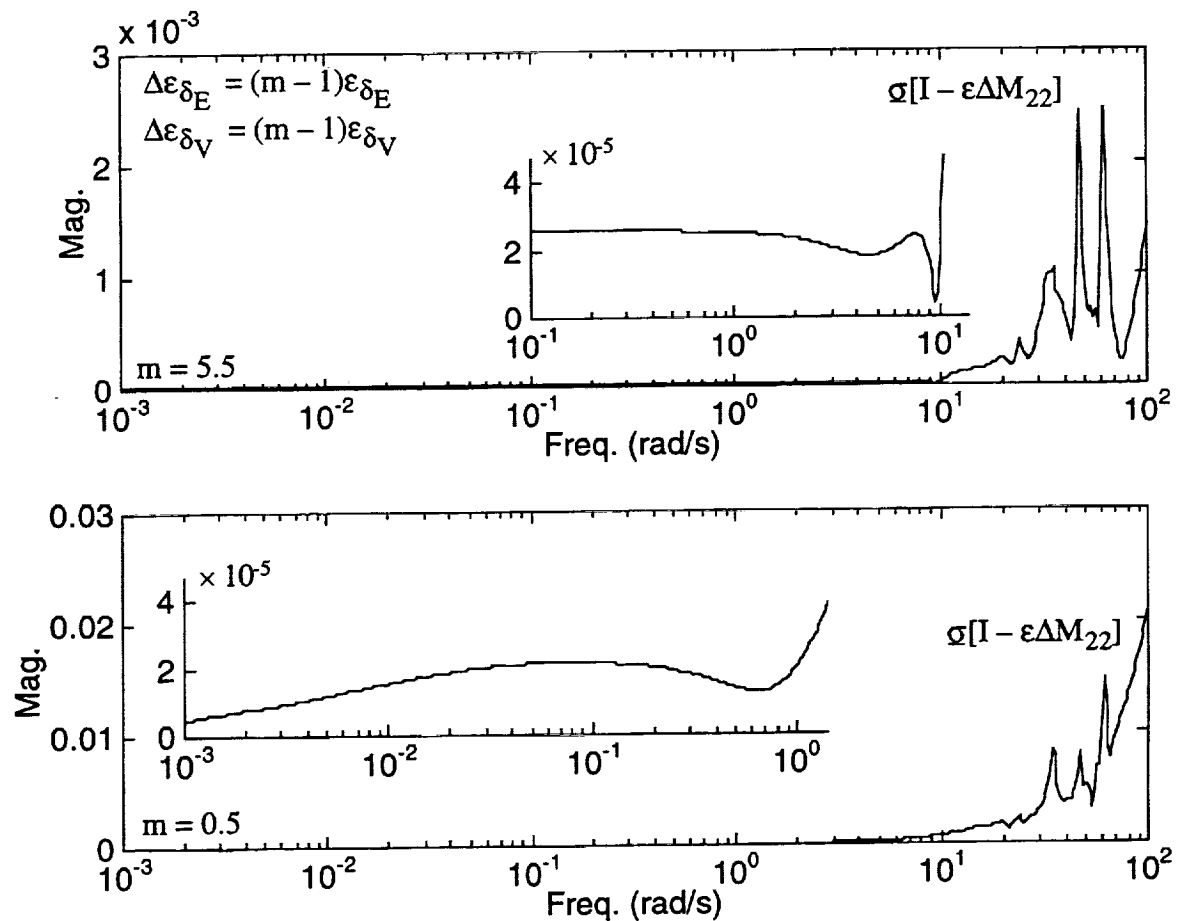


Figure 102. Singular Value Robustness Against Aerodynamic Control Effectiveness

Now consider the second type of aerodynamic parameter variation associated with lift curve slope of the horizontal tail and vane. The vehicle-actuator state space model is partitioned as in Eq. (4.29) with identical state variable assignments as in Eq. (4.39):  $x_2$  denotes the generalized coordinate positions and  $x_3$  denotes the downward speed, pitch rate, and generalized coordinate rates. Partitions  $A_{32}$  and  $A_{33}$  are functions of the lift curve slopes as shown in Eq. (4.40) where  $C_{L\alpha}^k$  denotes the lift curve slopes for the horizontal tail and vane surfaces. Other parameters are defined in Section II-C. As in the internal mode shape analysis, functional dependency upon lift curve slope in Eq. (4.40) is more complex when compared with an overall multiplying factor structure, as in Eq. (4.35) or (4.43). To represent the variation, the parameter structure indicated in Eq. (4.40) must be utilized. Appendix D provides an estimate for the nominal component lift curve slope values:  $C_{L\alpha}^H = C_{L\alpha}^V = 2.073$  1/rad. Variation in lift curve slope is modeled as

$$\Delta C_{L\alpha}^k = (m-1)C_{L\alpha}^k \quad (4.47)$$

The corresponding state space parameter variation matrices  $\Delta A_{32}$  and  $\Delta A_{33}$  are

$$\Delta A_{32} = \begin{bmatrix} \Delta Z_{\eta_1} & \Delta Z_{\eta_2} & \cdots \\ \Delta M_{\eta_1} & \Delta M_{\eta_2} & \\ \Delta F_{1\eta_1} & \Delta F_{1\eta_2} & \\ \Delta F_{2\eta_1} & \Delta F_{2\eta_2} & \\ \vdots & & \ddots \end{bmatrix} \quad \Delta A_{33} = \begin{bmatrix} \Delta Z_w & \Delta Z_q & \Delta Z_{\eta_1} & \Delta Z_{\eta_2} & \cdots \\ \Delta M_w & \Delta M_q & \Delta M_{\eta_1} & \Delta M_{\eta_2} & \\ \Delta F_{1w} & \Delta F_{1q} & \Delta F_{1\eta_1} & \Delta F_{1\eta_2} & \\ \Delta F_{2w} & \Delta F_{2q} & \Delta F_{2\eta_1} & \Delta F_{2\eta_2} & \\ \vdots & & & & \ddots \end{bmatrix} \quad (4.48)$$

$$\begin{aligned} \Delta Z_w &= \frac{\bar{q}\bar{S}}{mV_T} \left\{ \sum_k -\frac{\bar{S}_k}{\bar{S}} \Delta C_{L\alpha}^k \right\} & \Delta Z_q &= \frac{\bar{q}\bar{S}\bar{c}}{2mV_T} \left\{ \sum_k 2 \frac{\bar{S}_k}{\bar{S}} \frac{x_k}{\bar{c}} \Delta C_{L\alpha}^k \right\} \\ \Delta M_w &= \frac{\bar{q}\bar{S}\bar{c}}{I_{yy}V_T} \left\{ \sum_k \frac{\bar{S}_k}{\bar{S}} \frac{\bar{c}_k}{\bar{c}} \frac{x_k}{\bar{c}_k} \Delta C_{L\alpha}^k \right\} & \Delta M_q &= \frac{\bar{q}\bar{S}\bar{c}^2}{2I_{yy}V_T} \left\{ \sum_k -2 \frac{\bar{S}_k}{\bar{S}} \frac{\bar{c}_k}{\bar{c}} \frac{x_k}{\bar{c}_k} \frac{x_k}{\bar{c}} \Delta C_{L\alpha}^k \right\} \\ \Delta Z_{\eta_i} &= \frac{\bar{q}\bar{S}}{m} \left\{ \sum_k \frac{\bar{S}_k}{\bar{S}} \phi_i' \Delta C_{L\alpha}^k \right\} & \Delta Z_{\eta_i} &= \frac{\bar{q}\bar{S}\bar{c}}{2mV_T} \left\{ \sum_k 2 \frac{\bar{S}_k}{\bar{S}} \frac{\phi_i}{\bar{c}} \Delta C_{L\alpha}^k \right\} \\ \Delta M_{\eta_i} &= \frac{\bar{q}\bar{S}\bar{c}}{I_{yy}} \left\{ \sum_k -\frac{\bar{S}_k}{\bar{S}} \frac{\bar{c}_k}{\bar{c}} \frac{x_k}{\bar{c}_k} \phi_i' \Delta C_{L\alpha}^k \right\} & \Delta M_{\eta_i} &= \frac{\bar{q}\bar{S}\bar{c}^2}{2I_{yy}V_T} \left\{ \sum_k -2 \frac{\bar{S}_k}{\bar{S}} \frac{\bar{c}_k}{\bar{c}} \frac{x_k}{\bar{c}_k} \frac{\phi_i}{\bar{c}} \Delta C_{L\alpha}^k \right\} \\ \Delta F_{iw} &= \frac{\bar{q}\bar{S}\bar{c}}{m_i V_T} \left\{ \sum_k \frac{\bar{S}_k}{\bar{S}} \frac{\bar{c}_k}{\bar{c}} \frac{\phi_i}{\bar{c}_k} \Delta C_{L\alpha}^k \right\} & \Delta F_{iq} &= \frac{\bar{q}\bar{S}\bar{c}^2}{2m_i V_T} \left\{ \sum_k -2 \frac{\bar{S}_k}{\bar{S}} \frac{\bar{c}_k}{\bar{c}} \frac{x_k}{\bar{c}_k} \frac{\phi_i}{\bar{c}} \Delta C_{L\alpha}^k \right\} \end{aligned}$$

$$\Delta F_{i\eta_j} = \frac{\bar{q}\bar{S}\bar{c}}{m_i} \left\{ \sum_k -\frac{\bar{S}_k}{\bar{S}} \frac{\bar{c}_k}{\bar{c}} \frac{\phi_i}{\bar{c}_k} \phi_j' \Delta C_{L\alpha}^k \right\} \quad \Delta F_{i\eta_j} = \frac{\bar{q}\bar{S}\bar{c}^2}{2m_i V_T} \left\{ \sum_k -2 \frac{\bar{S}_k}{\bar{S}} \frac{\bar{c}_k}{\bar{c}} \frac{\phi_i}{\bar{c}_k} \frac{\phi_j}{\bar{c}} \Delta C_{L\alpha}^k \right\}$$

where  $k = H, V$

Note perturbations in the control derivative terms due to lift curve slope variations have not been considered here. Matrices  $M_{22}$  and  $\Delta$  are defined as in Eq. (4.33).

Fig. 103 shows the stability robustness characteristics against aerodynamic lift curve slope variations for the horizontal tail and vane surfaces. The scaling parameter  $m$  is again varied until the minimum singular value indicates neutral stability. Results in Fig. 103 show the closed-loop system maintains stability over a 98% reduction ( $m = 0.024$ ) and a 1,100% enlargement ( $m = 11.99$ ) of the lift curve slope values. On the low-end, the relaxed stability mode migrates back to the right-half plane (0 rad/s) under the parameter variation. Note the pitch mode is near instability also (1 rad/s). Horizontal tail lift curve slope contributes directly (through a moment arm) to pitch damping ( $M_q$ ) and pitch stiffness ( $M_w$ ). The low-end variation subtracts from this contribution, yet the pitch augmentation loop is able to compensate for a significant loss. On the high-end, a similar trend occurs but the margin is much larger. This variation is in the noncritical direction and adds to the airframe pitch stiffness and damping characteristics. Further investigation would be required to determine the instability mechanism occurring here. Overall magnitude values in Fig. 103 are again small.



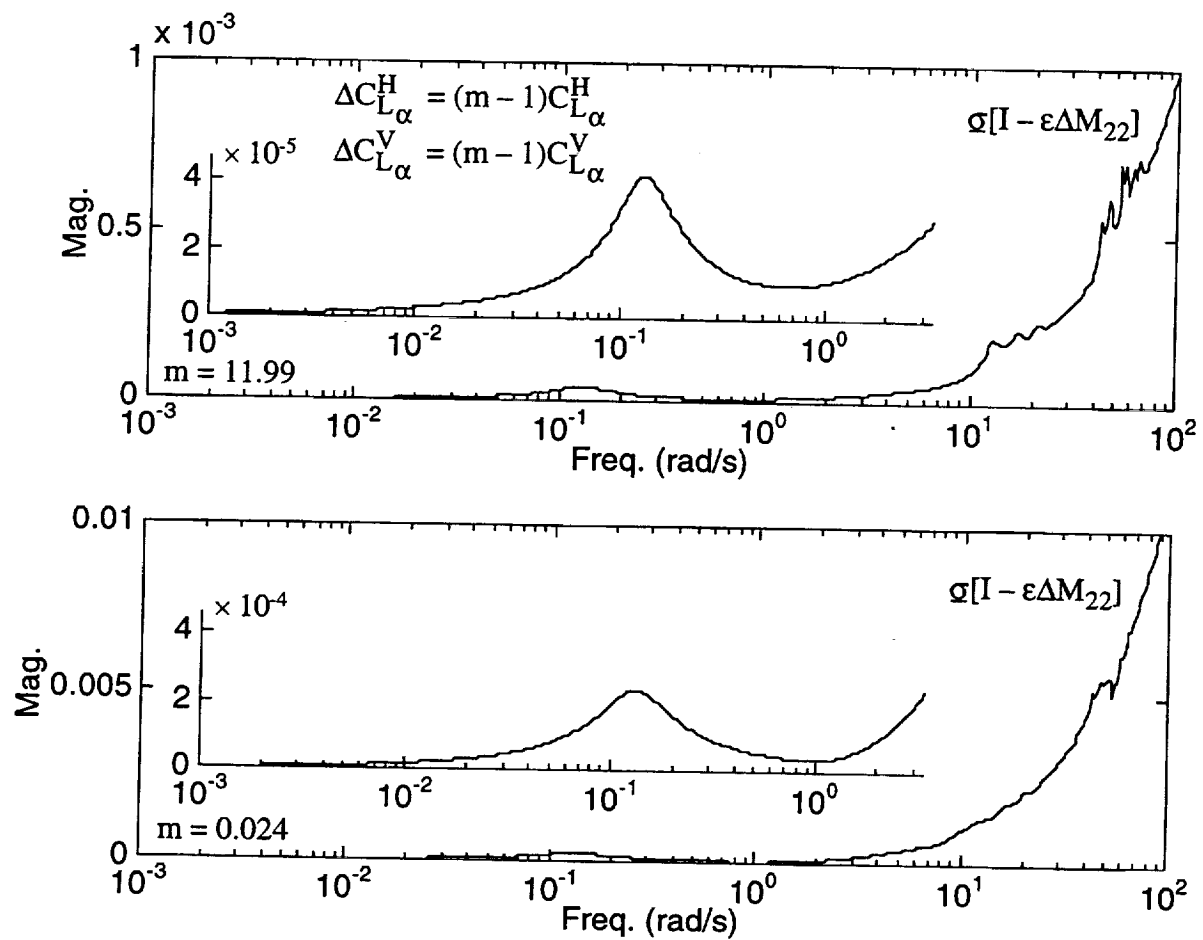


Figure 103. Singular Value Robustness Against Aerodynamic Lift Curve Slope

Tab. 19 summarizes the multivariable stability robustness characteristics of the proposed inner loop control system given in Sections IV-A to IV-E. This table includes modified MIL-F-87242 criteria, as well as gain and phase margins and parameter margins. The stability robustness characteristics of the control system appear quite acceptable. Recall single-loop gain and phase margins were incorporated into the system in a manner which included all significant coupling effects (with the exception of propulsive-aeroelastic coupling). Further, the design strategy avoided steps which would introduce heavy reliance upon model fidelity and associated vulnerability to parameter model uncertainty. A notch filter was utilized in the aeroelastic suppression loop. However, basic system stability did not rely upon this equalization. If the notch frequency was not properly matched to the airframe dynamics, stability characteristics revert back to the inherent features of the collocated vane and rate gyro loop, which is of superior quality (see Figs. 56-57). Therefore, the adequate multi-loop margins in Tab. 19 are expected, to some extent.

Table 19. Summary Of Multivariable Stability Robustness		
Robustness Metric	Upper Margin	Lower Margin
Mod. MIL-F-87242 Gain @ Input	√	√
Mod. MIL-F-87242 Gain @ Output	√	√
Mod. MIL-F-87242 Phase @ Input	√	√
Mod. MIL-F-87242 Phase @ Output	√	√
Uniform Gain @ Input	14.3 (db)	4.3 (db)
Uniform Gain @ Output	14.3 (db)	4.3 (db)
Uniform Phase @ Input	106 (deg)	-44 (deg)
Uniform Phase @ Output	106 (deg)	-44 (deg)
Uniform Structural Damping Ratio	∞ (%)	52 (%)
Uniform Structural Natural Frequency	31 (%)	50 (%)
Uniform Structural Mode Shape - In & Out	167 (%)	79 (%)
Uniform Structural Mode Shape - Internal	196 (%)	63 (%)
Uniform Aerodynamic Control Effectiveness	450 (%)	50 (%)
Uniform Aerodynamic Lift Curve Slope	1100 (%)	98 (%)

√: Compliance with requirement satisfied.

## Performance

### Flying Qualities Based On Equivalent System

Flying quality estimates given in Section IV-D are based on numerical data taken directly from the full order model (excluding the prefilter). For example, full order transfer function root locations were used to obtain short period natural frequency ( $\omega_{sp}$ ) and associated numerator time constant ( $\tau_{\theta_2}$ ) values. The control anticipation metric, in turn, was estimated from these values. Even though aeroelastic motions and other dynamics are included in the design model, their influence upon the predicted pilot ratings is not directly and fully accounted for. Since the criteria do not encompass these effects, the aeroelastic modes and other dynamics (including the prefilter elements) must be folded into the quasi-conventional airframe transfer function parameters utilized in the flying quality predictions. Therefore, a refined handling qualities analysis based on equivalent system concepts is considered next. However, a formal parameter optimization model fitting procedure is not considered in this analysis. Here, conventional model reduction techniques<sup>26</sup> will be utilized.

Suppose the overall closed-loop state space system (including  $P_2(s)$  in Fig. 54) in physical coordinates is

$$\begin{aligned}\dot{x} &= Ax + B\tilde{y}_{2c} \\ y &= Cx + D\tilde{y}_{2c}\end{aligned}\tag{4.49}$$

By performing an eigen decomposition for  $A$ , the model in Eq. (4.49) can be transformed to modal coordinates ( $x = T\chi$ ), or

$$\begin{aligned}\dot{\chi} &= \mathcal{A}\chi + \mathcal{B}\tilde{y}_{2c} \\ y &= C\chi + \mathcal{D}\tilde{y}_{2c}\end{aligned}\tag{4.50}$$

$$\begin{aligned}\mathcal{A} &= T^{-1}AT & \mathcal{B} &= T^{-1}B \\ C &= CT & \mathcal{D} &= D\end{aligned}$$

Consider partitioning the state vector  $\chi$  into three components where  $\chi_2$  represents the two modal states corresponding to the oscillatory pitch mode. Modes with frequency content below the pitch mode will be denoted by  $\chi_1$  and higher frequency modes are represented by  $\chi_3$ .

$$\begin{bmatrix} \dot{\chi}_1 \\ \dot{\chi}_2 \\ \dot{\chi}_3 \end{bmatrix} = \begin{bmatrix} \mathcal{A}_{11} & 0 & 0 \\ 0 & \mathcal{A}_{22} & 0 \\ 0 & 0 & \mathcal{A}_{33} \end{bmatrix} \begin{bmatrix} \chi_1 \\ \chi_2 \\ \chi_3 \end{bmatrix} + \begin{bmatrix} \mathcal{B}_1 \\ \mathcal{B}_2 \\ \mathcal{B}_3 \end{bmatrix} \tilde{y}_{2_c} \quad (4.51)$$

$$y = \begin{bmatrix} C_1 & C_2 & C_3 \end{bmatrix} \begin{bmatrix} \chi_1 \\ \chi_2 \\ \chi_3 \end{bmatrix} + \mathcal{D} \tilde{y}_{2_c}$$

Truncation of the  $\chi_1$  states and residualization of the  $\chi_3$  states leads to the reduced order model below.

$$\begin{aligned} \dot{\chi}_r &= \mathcal{A}_r \chi_r + \mathcal{B}_r \tilde{y}_{2_c} \\ y &= C_r \chi_r + \mathcal{D}_r \tilde{y}_{2_c} \end{aligned} \quad (4.52)$$

$$\begin{aligned} \mathcal{A}_r &= \mathcal{A}_{22} & \mathcal{B}_r &= \mathcal{B}_2 \\ C_r &= C_2 & \mathcal{D}_r &= \mathcal{D} - C_3 \mathcal{A}_{33}^{-1} \mathcal{B}_3 \end{aligned}$$

Recall handling quality predictions given in Section IV-D were based on the 1,850 in station. This station provided an average assessment of the pitch dynamics by lying near the mid fuselage point, and allowed direct comparison with Ref. 13 results. In this section, the order reduction steps listed in Eqs. (4.49)-(4.52) are applied to the  $q_{400}/\tilde{y}_{2_c}$  input-output pair. With this noted change, handling quality predictions will now be based on the resident pitch dynamics imbedded within the manual control loop. This station difference should be noted when comparing results in this section to results in Tab. 15.

After applying the above steps, the resulting low order transfer function is

$$\frac{q_{400}}{\tilde{y}_{2_c}} = \frac{-0.18(s+1.8)(s-4.9)}{(s+0.62 \pm j 0.97)} \text{ rad/s/rad} \quad (4.53)$$

This transfer function is proper (not strictly proper) and thus is not in the appropriate low order form.<sup>1,2</sup> The indicated structure is an inherent consequence of the direct feedthrough matrix generated by the reduction technique. The higher frequency dynamics have been approximated by a steady residual effect in the reduced order dynamics. Even though the original feedthrough matrix is zero ( $D = \mathcal{D} = 0$ ), the reduced feedthrough matrix is nonzero ( $\mathcal{D}_r \neq 0$ ) due to the residual term  $C_3 \mathcal{A}_{33}^{-1} \mathcal{B}_3$  appearing in Eq. (4.52). This lack of a strictly proper transfer structure in Eq. (4.52) turns out to be beneficial for estimating an irrational effective time delay parameter from the

rational polynomial structure. As frequency increases, the phase angle corresponding to the numerator factor  $s-4.9$  varies from  $-180$  to  $-270$  deg, and will be interpreted as pure phase loss (effective time delay) resulting from the higher frequency dynamics. By equating phase loss at 5 rad/s (the recommended cutoff frequency for the equivalent system from Ref. 2), and by preserving gain at 0 rad/s, the low order model in appropriate form is

$$\frac{q_{400}}{\bar{y}_{2c}} = \frac{0.18 \times 4.9(s+1.8)e^{-0.16s}}{(s+0.62 \pm j 0.97)} \text{ rad/s/rad} \quad (4.54)$$

Fig. 104 shows the frequency response comparison between the high order and low order models in the 0.1 to 10 rad/s region. The low order model reflects the gross behavior contained in the high order model and provides an adequate overall match to these characteristics. As expected, the largest mismatch occurs at the higher frequencies where the low order model structure can not fully represent the various modes existing in this region. The magnitude response has a bias error across the entire frequency spectrum, while the phase response has a bias in slope at the higher frequencies. The payoff value is 89 when computed between the frequencies of 0.5 and 5 rad/s. The phase response mismatch in the 2-5 rad/s region could be easily removed by increasing the time delay parameter in Eq. (4.54). Doubling the value of this low order model parameter would lead to significantly lower payoff values. However, flying quality estimates generated from such a model, and based on equivalent time delay, would be unfairly skewed towards poor ratings because other low order model parameters were fixed during this time delay parameter adjustment. In contrast to a quasi-parameter optimization fit, analysis here will rely upon the physical mechanisms inherent in the the high order model, and their mapping into the low order model via the reduction process, to ascertain parameters used to predict handling qualities. These parameters are precisely those indicated in Eq. (4.54). Fig. 105 shows the inherent accuracy in these parameters when the low order frequency responses are uniformly scaled across the frequency spectrum to yield a minimum payoff value (scaling equal to  $me^{j\theta}$ ,  $m = 0.9$ ,  $\theta = -9$  deg). The payoff value here is 37.

Tab. 20 summarizes the predicted flying qualities for the overall closed-loop system (including the prefilter) based on the low order approximation to the 400 in pitch rate dynamics. Tab. 20 includes all metrics considered in Tab. 15, as well as equivalent time delay ( $\tau_e$ ). Short period frequency and damping meet Level 1 requirements. However, control anticipation only satisfies the Level 2 requirement and omega-tau falls just short of the Level 2 boundary. Under the validity of Fig. 105, Tab. 20 indicates equivalent time delay satisfies the Level 2 requirement and is close to the Level 1 boundary.

Note the effect from the lead-lag prefilter element in Eq. (4.16) on the  $1/\tau_{\theta_2}$  zero in Eq. (4.54) with respect to the full order model value (1.8 vs. 2 1/s). Elimination of the lower and higher frequency modes through the order reduction process also influences the low order  $1/\tau_{\theta_2}$  zero location to some extent. This smaller value for  $1/\tau_{\theta_2}$  increases the CAP and  $\omega_{sp}\tau_{\theta_2}$  metrics in Tab. 20 relative to Tab. 15. However, the improvement is not enough to cross the Level 1 boundary. Additional lead behavior in the prefilter can be utilized to address this deficiency with a tradeoff of distorting the small amplitude transients noted in the acceleration response in Fig. 76. Another important prefilter effect to note is the relationship between the equivalent time delay in Tab. 20 and the prefilter low pass break point in Eq. (4.16). As noted in Section IV-E, adjustment of the break point from 30 to 10 1/s will significantly reduce the acceleration transients in Fig. 76. However, the equivalent time delay is very sensitive to this prefilter parameter and will more than double in value under the indicated change.

Under the caveat that criteria in Tab. 20 have not been fully validated for highly flexible vehicles like HSCT, and that efforts here are to explore feasibility of inner loop control architectures and provide first-order estimates of associated handling characteristics, Tab. 20 indicates the low-risk, low-gain closed-loop airframe system has Level 2 dynamics. Basic modal characteristics ( $\omega_{sp}$ ,  $\zeta_{sp}$ ) are well above adequate values, but other characteristics such as pitch-flight path response harmony and initial response delay (CAP,  $\tau_e$ ) are only adequate and may require objectionable piloting work load over sustained periods. As discussed in Section IV-D, the feedback gains for this system are kept intentionally low to reduce residual structural vibration

transients. If a more aggressive posture is considered in the aeroelastic suppression loop and crossfeed path, or if pilot tolerance to vibrational transients is higher than levels assumed in this design, then pitch augmentation can be increased further. Basic Evans and Bode features show that increased pitch augmentation will easily boost CAP to the Level 1 region without compromising hard stability margin requirements. The concern is how much risk should be taken in aeroelastic control augmentation, what are the demands on actuation hardware performance, how applicable are existing flying quality criteria to flexible vehicles, and where do the boundaries between poor, adequate and good flying qualities actually lie.

Table 20. Estimated Flying Qualities Summary Of 400 in Closed-Loop Pitch Rate Dynamics With Prefilter				
Metric	Level 1	Level 2	(unit)	Design
$\omega_{sp}$	$\geq 0.7$	$\geq 0.4$	(rad/s)	1.15
$\zeta_{sp}$	$\geq 0.35$	$\geq 0.25$	(-)	0.54
CAP	$\geq 0.16$	$\geq 0.05$	(1/gs <sup>2</sup> )	0.09
$\omega_{sp}\tau_{\theta 2}$	$\geq 1.3$	$\geq 0.75$	(-)	0.63
$\tau_e$	$\geq 0.15$	$\leq 0.23$	(s)	0.16

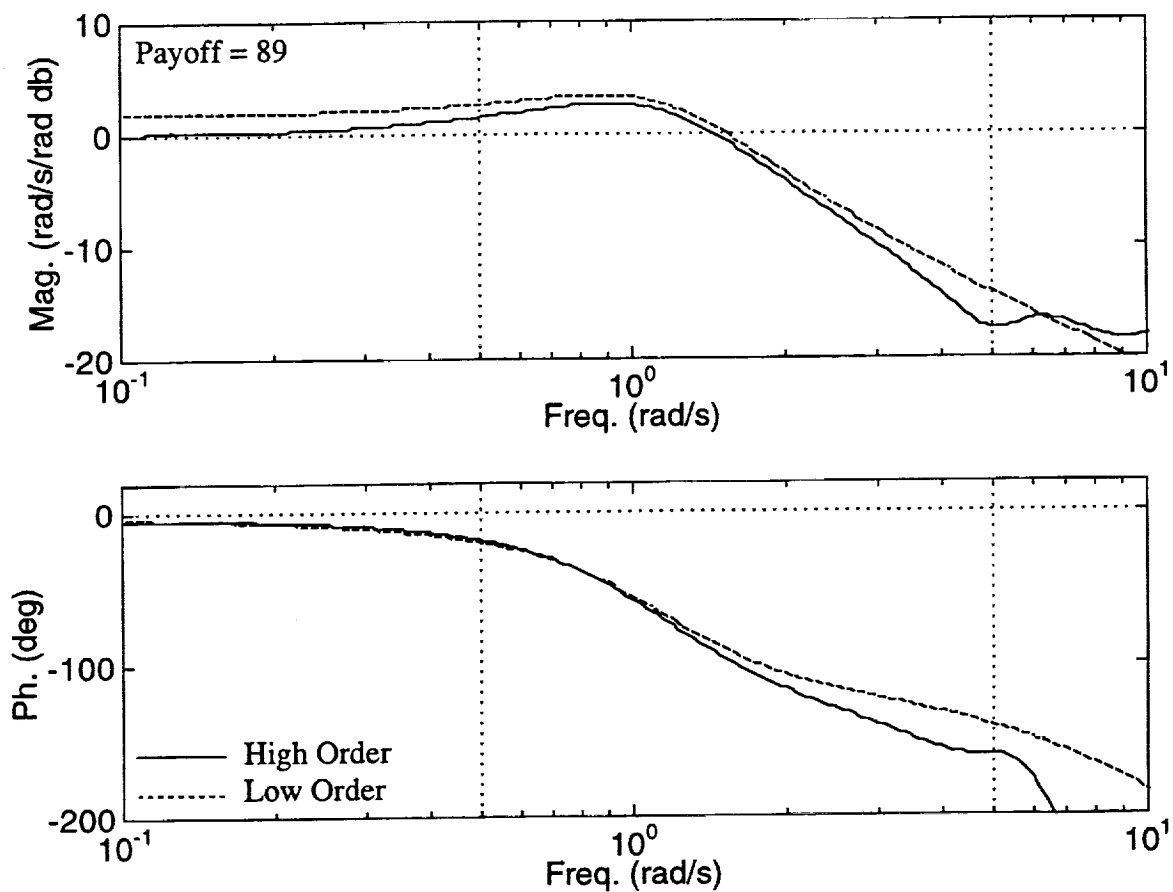


Figure 104. Closed-Loop 400 in Pitch Rate To Stick Command  
Unscaled Frequency Response Comparison



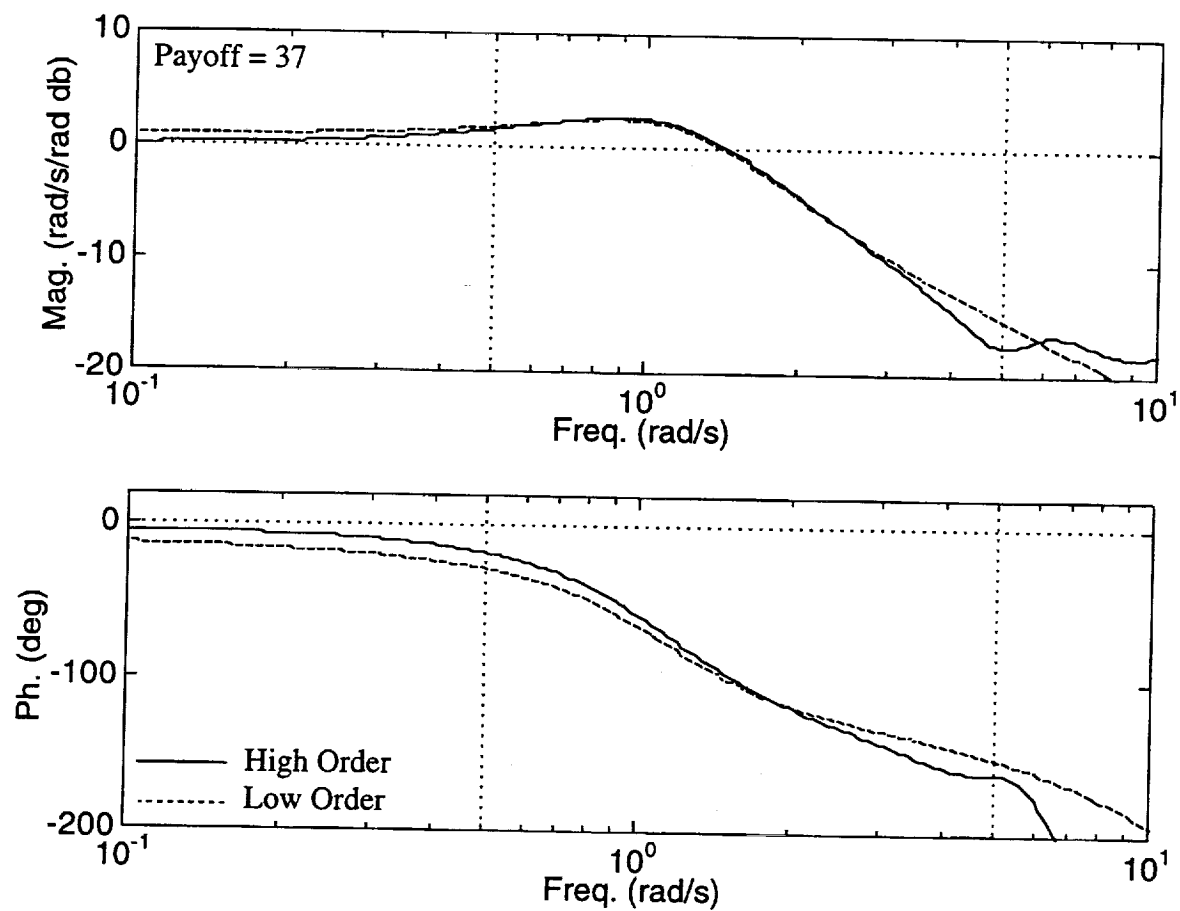


Figure 105. Closed-Loop 400 in Pitch Rate To Stick Command  
Scaled Frequency Response Comparison

## Performance

### Gust Ride Discomfort

Ride quality associated with the closed-loop airframe system presented in Sections IV-A to IV-E will be evaluated with the gust ride discomfort index.<sup>2</sup> This integral frequency response criteria reflects the amount and severity of passenger or crew exposure to vertical acceleration transients during atmospheric gust excitation. The criteria provides emphasis in critical regions where biodynamic sensitivity to transients is high. The ride discomfort index ( $\sigma_{RD}$ ) is computed as

$$\sigma_{RD} = K_{RD} \sigma_{wG} \quad (-) \quad (4.55)$$

$$K_{RD} = \left\{ \int_0^\infty \mathcal{K}_{RD}(\omega) d\omega \right\}^{1/2} \quad (1/\text{ft/s})$$

$$\mathcal{K}_{RD}(\omega) = |T_{RD}(\omega)|^2 |G_{a_z x_s}^{wG}(\omega)|^2 \Phi'_{wG}(\omega) \quad (\text{s/ft}^2/\text{s}^2) \quad (4.55)$$

$$T_{RD}(s) = 113.2 \frac{(s^2 + 4s + 42)}{(s+2.8)(s+5.75)(s+69.9)}, \quad s = j\omega/(2\pi) \quad (1/g)$$

$$G_{a_z x_s}^{wG}(s) = \frac{a_z x_s(s)}{w_G(s)}, \quad s = j\omega \quad (\text{g/ft/s})$$

$$\Phi'_{wG}(\omega) = \frac{\Phi_{wG}(\omega)}{\sigma_{wG}} = \frac{L}{\pi V_T} \frac{1 + \frac{8}{3} (1.339 \frac{L\omega}{V_T})^2}{\{1 + (1.339 \frac{L\omega}{V_T})^2\}^{11/6}} \quad (\text{s})$$

In the above expressions,  $G_{a_z x_s}^{wG}(s)$  denotes the closed-loop transfer function between vertical acceleration at fuselage station  $x_s$  and vertical gust speed  $w_G$ . The gust velocity power spectral density  $\Phi_{wG}(\omega)$  is modeled with the von Karman spectrum and the superscript " ' " denotes a normalized spectrum with respect to gust intensity  $\sigma_{wG}$ .  $T_{RD}(s)$  represents a biodynamic response of the human and plays the role of a weighting filter to emphasize critical frequency regions associated with ride discomfort. The independent frequency variable  $\omega$  should have units of rad/s in the above equations. Note the index can be scaled with turbulence intensity and  $K_{RD}$  denotes the proportionality value.

Ref. 2 provides some guidance on acceptable values for the ride discomfort index. For a turbulence intensity of  $\sigma_{wG} = 3.65 \text{ ft/s}$ , the quality of ride is judged acceptable if  $\sigma_{RD} \leq 0.28$  for

exposure periods of 0.5 hr or less and  $\sigma_{RD} \leq 0.2$  for exposure periods between 0.5 and 1.5 hr. Tab. 21 shows the proportionality constant and ride discomfort index (for  $\sigma_{wG} = 3.65$  ft/s) computed at four representative fuselage stations throughout the vehicle. The estimated ride quality appears to be at adequate levels. Ride quality at three of the four fuselage stations are below the short duration requirement with only a small violation of the long duration requirement at the 1,850 in station. Ride of lesser quality at a mid-fuselage station, relative to an extreme fore or aft station, initially appears counter intuitive. Recall, however, the vane-tail configuration provides high control leverage at the fore and aft extremities, and indirectly controls mid-fuselage stations through structural compliance. Even indirect control provides adequate ride quality, in this case.

Fig. 106 shows the frequency distribution, and component distribution, for the argument  $K_{RD}(\omega)$  of the integral criterion at the 400 in station. The closed-loop airframe trace demonstrates that, even though aeroelastic resonances are well attenuated in the stick command path, the same resonances are vulnerable to high bandwidth turbulence excitations. Note the vane loop damping effect on the 8-20 rad/s modes (rounded peaks), while the higher frequency modes beyond 20 rad/s are still lightly damped (sharp peaks). Note the biodynamic weighting trace can amplify/deamplify individual modes. Fortunately, the trial gust spectrum ( $\sigma_{wG} = 3.65$  ft/s,  $L = 2,500$  ft) does not have sufficient energy content to strongly excite the structural resonances. With the aeroelastic region attenuated 30 db relative to the low frequency overall trace, ride quality performance is influenced primarily by rigid motion characteristics. For other intensity and scale height combinations, however, the ride quality could degrade due to aeroelastic effects.

Table 21. Estimated Ride Quality Of Closed-Loop Airframe		
Fuselage Station (in)	$K_{RD}$ (1/ ft/s)	$\sigma_{RD}$ (-)
400	0.0525	0.192
1,850	0.0813	0.297
2,500	0.0445	0.162
3,460	0.0468	0.171

$\sigma_{wG} = 3.65$  ft/s,  $L = 2,500$  ft

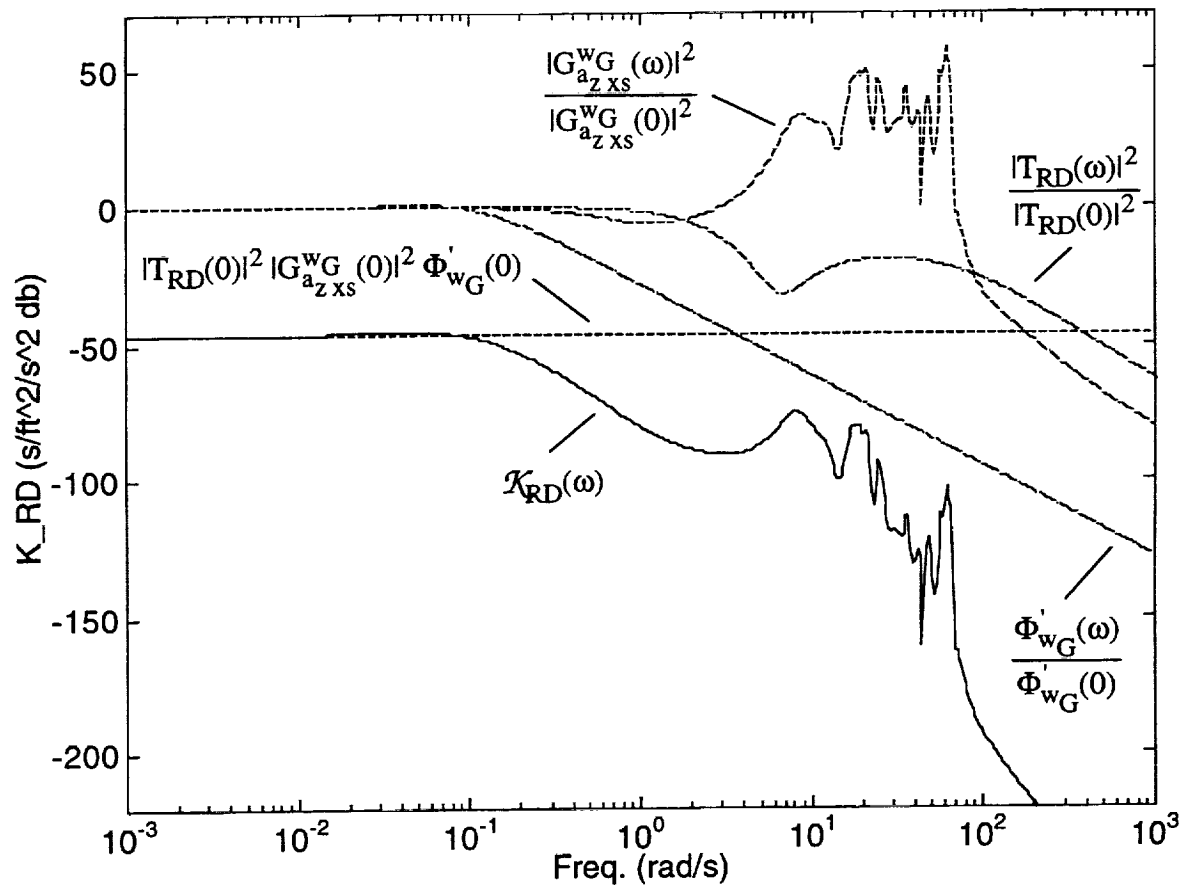


Figure 106. Frequency And Component Distribution For Ride Discomfort Index Integrand At 400 in

## Comments On Reference 25

Ref. 25 conducted an evaluation of a preliminary controller based on the high gain option (Eq. (4.11) ) for the aeroelastic suppression loop. The evaluation emphasized robust stability and performance characteristics based on singular value criteria. The evaluation provided some insight into the strengths and weaknesses of such a controller and considerable descriptive comments were given. In addition, a modified controller was considered to circumvent noted weaknesses in the original controller. Several comments on this evaluation and the modified controller are in order. Note the recommended control law offered in this report does not rely on this high gain option.

Ref. 25 claims a significant weakness of the preliminary controller is high bandwidth in the aeroelastic suppression loop and associated requirements for high performance actuation hardware. From Ref. 25, one reads

"... Second, the aeroelastic suppression loop is a *very* high-bandwidth loop ... is a questionable solution as it amplifies noise and will almost certainly lead to actuator rate saturation ..."

Section IV-B of this report discusses this issue and the risk involved with such a strategy. Equalization of the type in Eq. (4.11) will, without a doubt, place heavy demands on actuator performance. Never the less, high bandwidth in this loop may still be necessary to allow sufficient pitch augmentation bandwidth for Level 1 flying qualities, and to control higher frequency vibrational motion excited by gusts. If such a loop were implemented, and if the hardware could not deliver the demanded performance, the loop, in some sense, would tend to revert back to the collocated static compensation characteristics, which are quite good (see Figs. 56-57). The recommended control law in this report takes a less aggressive stance in the mode suppression loop and the consequence is handling qualities do not quite reach Level 1 ratings.

Ref. 25 also claims another significant drawback of the preliminary controller is insufficient high frequency roll off in the aeroelastic suppression loop and associated stability robustness. From Ref. 25, one also reads

"... Third, there is a more fundamental problem with the aeroelastic suppression loop. It never rolls off! Rather, it relies on *phase* stabilization ... Ultimately, the loop must roll off and be gain stabilized ..."

This statement suggests the authors of Ref. 25 do not fully appreciate the benefits afforded by the Wykes structural mode control paradigm. Collocation provides phase stable behavior and lessens the need for "artificial" controller attenuation. Reliance on "natural" airframe-actuator attenuation characteristics is satisfactory. Refs. 15 and 27 provide strong supporting evidence. The B-1 SMCS loop utilizes acceleration feedback with a  $10/(s+10)$  roll off filter. However, the purpose of this filter is to provide approximate integration to achieve a rate signal for damping purposes. Pitch rate feedback with no roll off filter provides an equivalent system.

Finally, Ref. 25 claims two other drawbacks of the preliminary controller are 1) lack of angle of attack feedback and associated inability to stabilize the phugoid mode, and 2) insufficient low frequency gain to provide good stick command tracking. Ref. 25 states

"... First, the pitch augmentation loop uses only pitch-rate feedback for control. Thus, it cannot stabilize the phugoid mode ... it lacks sufficient gain at low frequency to ensure good command tracking for stick inputs. It could benefit from some angle of attack feedback ..."

This statement also suggests the authors of Ref. 25 do not fully appreciate the benefits of the "superaugmented pitch loop".<sup>28,29</sup> At the flight condition under study, the HSCT airframe does not have a traditional phugoid mode. The aircraft is statically unstable with one stable oscillatory mode (i.e., the "third oscillatory mode") and two aperiodic modes, one stable the other unstable. Pitch rate feedback stabilizes the right-half plane pole by driving it into the  $1/\tau_{\theta_1}$  zero, the left-half plane pole is driven into the  $1/\tau_{\theta_2}$  zero, and the third oscillatory mode becomes the dominant pitch mode. All this is achieved without relying upon aerodynamic-based feedbacks which depend on airdata system calibration and are susceptible to atmospheric disturbances. Ref. 28 provides strong supporting evidence.

Ref. 25 provides a modified controller whose stated objectives are to address only mode 1 and attenuate all others. From Ref. 25, one reads

"... One simple modification to the aeroelastic suppression loop is to phase stabilize only the first mode and gain stabilize remaining modes ... It employs a lag-lead compensator (rather than lead-lag) ..."

Such an objective, for the HSCT airframe model in this report, is naive in many respects. Airframe dynamic characteristics indicate neighboring modes (mode 2, 3, 6 and 7, for example) are significant contributors to the vibrational transients. An inner loop control system that does not address these additional modes will most likely have poor characteristics. For example, consider the 400 in pitch rate response associated with the modified controller in Fig. 3-19, Ref. 25. The response shows considerable frequency content (15 to 25 rad/s) even after 2 s of motion. These transients will be even more severe when gust excitations are considered and no feedforward action is available to counter the gusts. Insertion of lag into the aeroelastic suppression loop spoils inherent collocated phase behavior. Analysis shows that lag severely restricts the usable gain in this loop (see Eq. (4.10), Figs. 58-59 and the associated discussion), and in the end mode 1 can not even be sufficiently damped. Even the controller in this report suffers from such effects because it does not employ the aggressive, high bandwidth strategy. However, the controller recommended in this report is of higher bandwidth, and addresses more modes, than the modified controller offered in Ref. 25.

To summarize, the preliminary controller evaluated by Honeywell staff and reported on in Ref. 25 is on the aggressive, high risk end of the spectrum. Such a controller utilizes high bandwidth and high gain, and will require high performance from actuation hardware. The modified controller offered by Honeywell staff (also in Ref. 25) is on the passive, low risk end of the spectrum. This controller is low bandwidth and low gain, by nature, and does not tax current actuation technologies. The recommended control law offered in this report lies between these two extremes.

## Section V

### Forward Vane Sizing Requirements

#### A. Sizing Strategy Formulation

The inner loop flight control architecture presented in Section IV provides a highly attractive solution for the HSCT airframe. A most critical step in this development is the introduction of a secondary control surface. The additional aerodynamic surface facilitates dedicated control loops focused on structural mode suppression and pitch augmentation, and allows formidable design constraints to be realistically approached. All analysis and synthesis results presented in Section IV are based on the specific vane model documented in Section II-C. This vane model is a "first cut" design based on similarities with other high-speed elastic vehicle geometries (i.e., B-1 and XB-70). This vane model facilitated rapid entry into closed-loop design investigations. However, the vane may be undersized, or oversized, based on such a preliminary model. To address this concern, a vane sizing analysis is provided in this section.

At the most basic level, vane sizing decomposes into specification of the mounting location along the fuselage and the planform surface area. The airframe mechanics and the functional role the vane is targeted to fulfill dictate where desirable mounting locations exist. For a freely constrained elastic body, the characteristic deflection shapes are maximal at body appendage extremities. For the HSCT fuselage, modal data in Fig. 28 confirms this behavior. Fuselage stations associated with large mode shape deflections include well forward and well aft stations. Assuming the primary role of the vane is to provide mode suppression, the mounting location should be well forward to maximize control leverage, yet should not compromise practical considerations like pilot visibility and internal volume availability. A mounting location of 400 in appears to satisfy all these requirements. Therefore, the vane sizing issue boils down to one of specifying planform surface area.



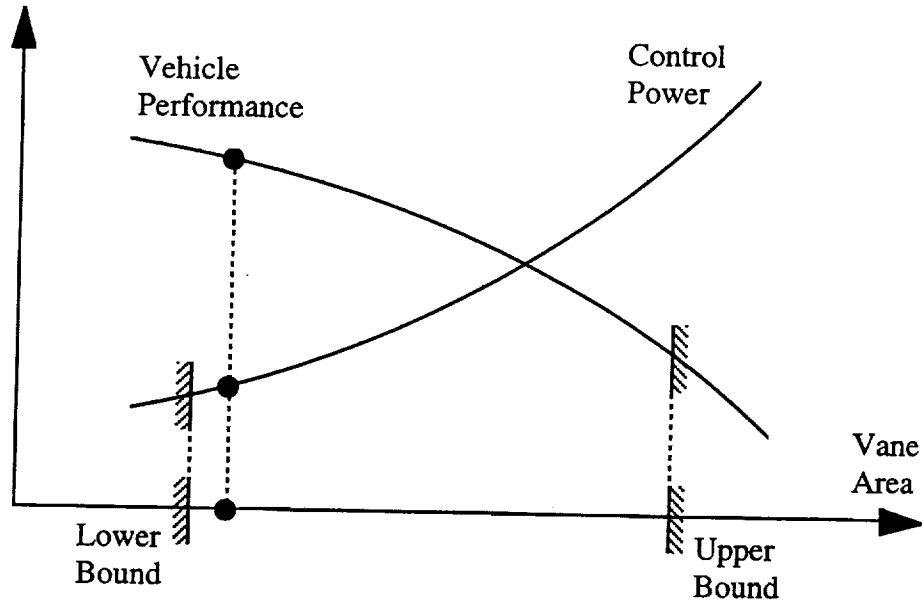


Figure 107. Vane Surface Area Upper And Lower Bounds

Upper and lower bounds, arising from natural design constraints, will influence and ultimately determine the vane surface area requirements. Fig. 107 portrays these bounding limitations. The forward vane will influence static vehicle performance characteristics in numerous ways. Range is one important metric that can be used to illustrate these characteristics. To first order, the Breguet range formula<sup>30</sup> for turbofan systems during cruise indicates how aerodynamic, structural and propulsive characteristics contribute to range  $R$ , or

$$R = \frac{V_T}{c} \frac{C_L}{C_D} \ln \frac{1}{1 - \zeta} \quad (5.1)$$

In Eq. (5.1),  $C_L/C_D$  denotes the vehicle lift to drag ratio,  $\zeta$  denotes the vehicle mass fraction (fuel mass divided by initial total mass) and  $c$  denotes the vehicle thrust specific fuel consumption. Although the vane will add increments to the overall vehicle lift and drag coefficients, the most important aerodynamic influence will most likely be disruption of airflow quality over the main wing. Vortical and downwash impingement on the main wing will degrade the overall lift to drag ratio. In a similar fashion, the flow quality at the propulsion inlets may deteriorate, resulting in reduced propulsive efficiency. Finally, the vane and carry through support structure will decrease the mass fraction. In each case, the range suffers incremental effects, according to Eq. (5.1), and may threaten the vehicle concept viability. Therefore, an upper bound on the vane surface area

naturally arises to limit these performance drops. For such an important issue, nonlinear simulation encompassing all mission flight phases would ultimately be required to obtain accurate estimates. Performance analysis calculations lie outside the scope of this study.

Control power, on the other hand, ultimately sets the lower bound on the vane surface area. Sufficient area is required to maintain vane deflections within acceptable levels during normal and possibly extreme flight conditions. If the surface area is too small, large vane travel will be required to generate the necessary control forces for mode suppression. Excessive vane travel can lead to the presence of nonlinear behavior associated with off-center hydraulic ram positioning and hard stops, as well as separated flow from the vane leading edge. Additionally, these deflections can lead to large vane-fuselage wall gaps and associated nonlinear aerodynamic flow phenomena. Avoidance of operation in these nonlinear regions is highly desirable. If static vehicle performance is paramount to concept viability, the vane would tend to be sized by the lower bound as shown in Fig. 107. In this figure, surface area is selected to just satisfy control power requirements with minimal performance decrements. Estimation of the lower bound is an issue easily addressed in this analysis.

A closed-loop simulation strategy will be utilized to estimate this lower bound for the vane surface area. Fig. 108 summarizes this sizing strategy. The closed-loop system described in Section IV will be excited by various maneuver commands and atmospheric gusts. Vane travel and rate activity will be recorded during the motion transients resulting from such excitations. From each vane response, maximal travel and rate values will be extracted. By contrasting these peak values with design limits on vane travel and vane rate, the lower bound for the vane surface area can be "reverse engineered" from the data. Balancing the vertical load on the baseline vane model with a redesigned vane playing the role of the actual hardware provides the mathematical framework. In Fig. 108, the symbol " ' " denotes a variable associated with the redesigned model. Under the modeling assumption of linear, quasi-static air flow, and assuming the only angle of attack source is vane control deflection, consider balancing these loads at the peak travel.

$$\bar{q} \bar{S}_V C_{L\alpha}^V \delta_{V \max} = F = F' = \bar{q}' \bar{S}_V' C_{L\alpha}^{V'} \delta_{V \max}' \quad (5.2)$$

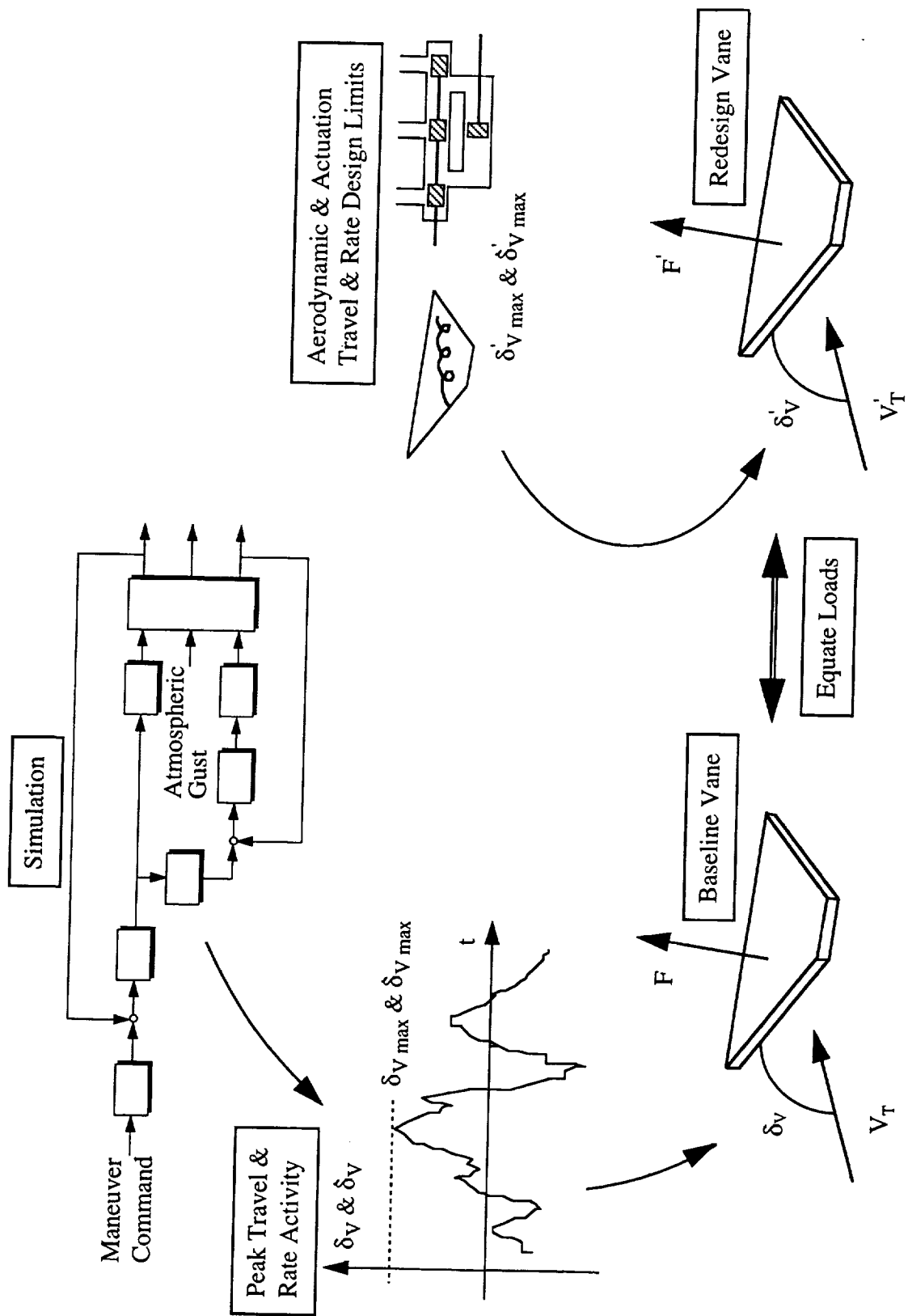


Figure 108. Vane Sizing Summary

Solving for  $\bar{S}'_V$  leads to

$$\bar{S}'_V = \frac{\bar{q}}{\bar{q}'} \frac{C_{L\alpha}^V}{C_{L\alpha}^{V'}} \frac{\delta_{V\max}}{\delta'_{V\max}} \bar{S}_V \quad (5.3)$$

Eq. (5.3) provides the fundamental relationship for backing out the surface area lower bound given appropriate input data. The redesigned surface area plays the role of the lower bound. The ratios of dynamic pressure, lift curve slope and peak vane travel, between the baseline model and the redesigned model, scale the base line area into the redesigned area. Large values for peak vane travel from the baseline simulation, relative to the travel design limit, indicate insufficient surface area and would require enlargement to keep vane operations within acceptable regions. On the other hand, smaller values for this vane travel ratio imply the baseline vane model is grossly oversized with ample control power and could be reduced to lessen the impacts on static vehicle performance (see Fig. 107). By taking the derivative of Eq. (5.2) with respect to time, surface area based on vane rate activity can also be estimated.

$$\bar{S}'_V = \frac{\bar{q}}{\bar{q}'} \frac{C_{L\alpha}^V}{C_{L\alpha}^{V'}} \frac{\delta_{V\max}}{\delta'_{V\max}} \bar{S}_V \quad (5.4)$$

For all computations in this report,  $C_{L\alpha}^V = C_{L\alpha}^{V'}$  and  $\bar{q} = \bar{q}'$  are enforced, but if refined analytical modeling data, or test data, for the lifting or dynamic pressure behavior were to become available, they could be incorporated into Eq. (5.3)-(5.4).

## B. Closed-Loop Simulation Results

Excitation inputs for the simulation runs consist of both maneuver commands and vertical atmospheric gusts. These test inputs should exercise vane motion to a sufficient level, and should represent realistic applications. Three maneuver commands and three atmospheric gusts are considered. The maneuver command inputs consist of a step, sinusoid and square wave applied at the stick input  $\tilde{y}_{2c}$  in Fig. 54. For this system, recall stick inputs command pitch rate. The step input represents a hard nose up or nose down maneuver such as would be executed during go around or for high angle of attack recovery, while the sinusoid input represents some type of tracking task. The square wave input is intended to portray an unexpected adverse pilot-aircraft coupling exchange. The first cycle of this square wave input is a doublet and could also represent a mid-air collision avoidance maneuver. Atmospheric gust inputs consist of a step, sinusoid and turbulence applied at the signal  $w_G$  in Fig. 54. Vertical shear or a periodic thermal updraft are modeled by the step and sinusoid inputs. Turbulence mimics random local atmospheric motions.

These six test inputs are listed in Eq. (5.5).

$$\begin{aligned}
 \tilde{y}_{2c}(t) &= A && \text{(step)} && (5.5) \\
 \text{or} & && && \\
 &= A \sin(\omega t) && \text{(sinusoid)} && \\
 \text{or} & && && \\
 &= \begin{cases} A & \text{for } nT \leq t < (n+\frac{1}{2})T \\ -A & \text{for } (n+\frac{1}{2})T \leq t < (n+1)T \end{cases} \quad n = 0, 1, 2, \dots && \text{(square wave)} && \\
 w_G(t) &= A && \text{(step)} && \\
 \text{or} & && && \\
 &= A \sin(\omega t) && \text{(sinusoid)} && \\
 \text{or} & && && \\
 &= \text{see Eqs. (2.9)-(2.10)} && \text{(turbulence)} &&
 \end{aligned}$$

For the deterministic inputs, unit amplitudes ( $A = 1 \text{ deg/s}$  or  $1 \text{ ft/s}$ ) are used in the simulation, but it should be noted that results can be scaled with input amplitude. The fundamental frequency content of the periodic deterministic inputs is tuned to match the pitch mode natural frequency ( $\omega = 1 \text{ rad/s}$  or  $T = 2\pi \text{ s}$ ). The stochastic input is generated by white noise excitation of the approximate

von Karman turbulence model described in Section II-A and Appendix C. This filter has unit standard deviation gust amplitude ( $\sigma_{w_G} = 1 \text{ ft/s}$ ) and is driven by normally distributed random numbers that have unit standard deviation ( $\sigma_n = 1 \text{ s}^{-1/2}$ ). The discrete simulation utilized in this sizing study can not reproduce continuous time, pure white noise to sufficient accuracy. Therefore, the von Karman filter amplitude was adjusted with a multiplying factor of  $\sqrt{\pi/dt}$  where  $dt$  denotes the simulation time step ( $dt = 0.01 \text{ s}$ ). Appendix E in Ref. 31 provides a concise description and justification for this multiplying factor. At the most basic level, simulation output from the von Karman filter with  $\sigma_{w_G} = 1 \text{ ft/s}$  and with  $\sigma_n = 1 \text{ s}^{-1/2}$  does not result in standard deviation values near  $1 \text{ ft/s}$  when computed from the raw data, and the extra factor corrects for the bias value.

Figs. 109-114 show the detail simulation results for each of the six excitation cases. These figures show responses for the input, pitch rate and vertical acceleration at 400 in, elevator deflection and rate, and vane deflection and rate. The peak travel and rate values are indicated on the vane response plots. Elevator and other variable responses are included for completeness. If comparisons are made between peak elevator and vane responses, one should recall the control architecture from Section IV does not utilize stabilator input.

In each maneuver command case (Figs. 109-111), the vehicle is able to follow the command and execute the maneuver quite well. Note the pitch rate and acceleration responses in Fig. 109 are identical to that in Figs. 75-76. As seen from Fig. 111, the vane response frequency content is primarily concentrated at  $1 \text{ rad/s}$  (command signal and rigid pitch) and  $8 \text{ rad/s}$  (mode 1), with small amounts at higher frequency (other structural modes). As expected, the prefilter and pitch loop attenuate the high frequency content in the excitation signal and very little reaches the structural modes. Some energy at the lower frequency modes gets through and the vane, through the crossfeed path and suppression loop, responds to damp the motion. Note the peak vane motion is coincident with the command signal reversal, rather than during a transient excursion lagging the command change.

The peak vane travel for the sinusoid input (5.3 deg) is almost double that for the step input (3.3 deg). However, when considering peak vane rate, this behavior is reversed, the step input leads to nearly double rate activity when contrasted with that from the sinusoid input (9.2 vs. 5.1 deg/s). Also, note the square wave peak vane travel and rate values are three and two times larger, respectively, compared against the step input values (9.3 vs. 3.3 deg and 18.7 vs. 9.2 deg/s). The square wave command, based on the observed vane motion, appears to be the most severe command of the three.

Response characteristics due to atmospheric gust inputs (Figs. 112-114) appear both similar and different to the maneuver command features. Note for a step gust input (Fig. 112), the control system still maintains pitch rate to the commanded value (zero) in the steady state, and vertical acceleration steady state is a nonzero constant value. This long term behavior is similar to characteristics shown in Fig. 109, however, the transient motion lying between the initial and steady conditions is fundamentally different. The gust excitation impacts the airframe directly and before the vane damping loop has an opportunity to counter the input. The vehicle motion and vane responses show significantly more high frequency activity than in Figs. 109-111. The only vibratory disturbance rejection capability the control architecture of Fig. 54 offers is damping of the structural modes once they are excited. Note the vibrations are significantly damped after approximately 2 s, regardless of this "indirect" approach. Exotic disturbance rejection schemes making use of forward looking laser-based sensors<sup>32</sup> would provide alternative approaches.

For a unit amplitude, the sinusoid gust appears to have the most benign vane response of the three cases. Assuming peak values for the stochastic gust are interpreted as "three sigma" values, the step and turbulence gust inputs lead to similar peak vane activity (0.43 vs. 0.45 deg and 12.1 vs. 9.9 deg/s). The step and turbulence inputs appear to be the most severe, based on resulting vane motion. Also in Figs. 112-114, the peak vane activity tends to occur during a transient following the initial disturbance initiation. This behavior is fundamentally different when compared to the behavior with command maneuver inputs, and is due to the indirect disturbance rejection control scheme discussed above. The structural vibrations lead the initial control action.

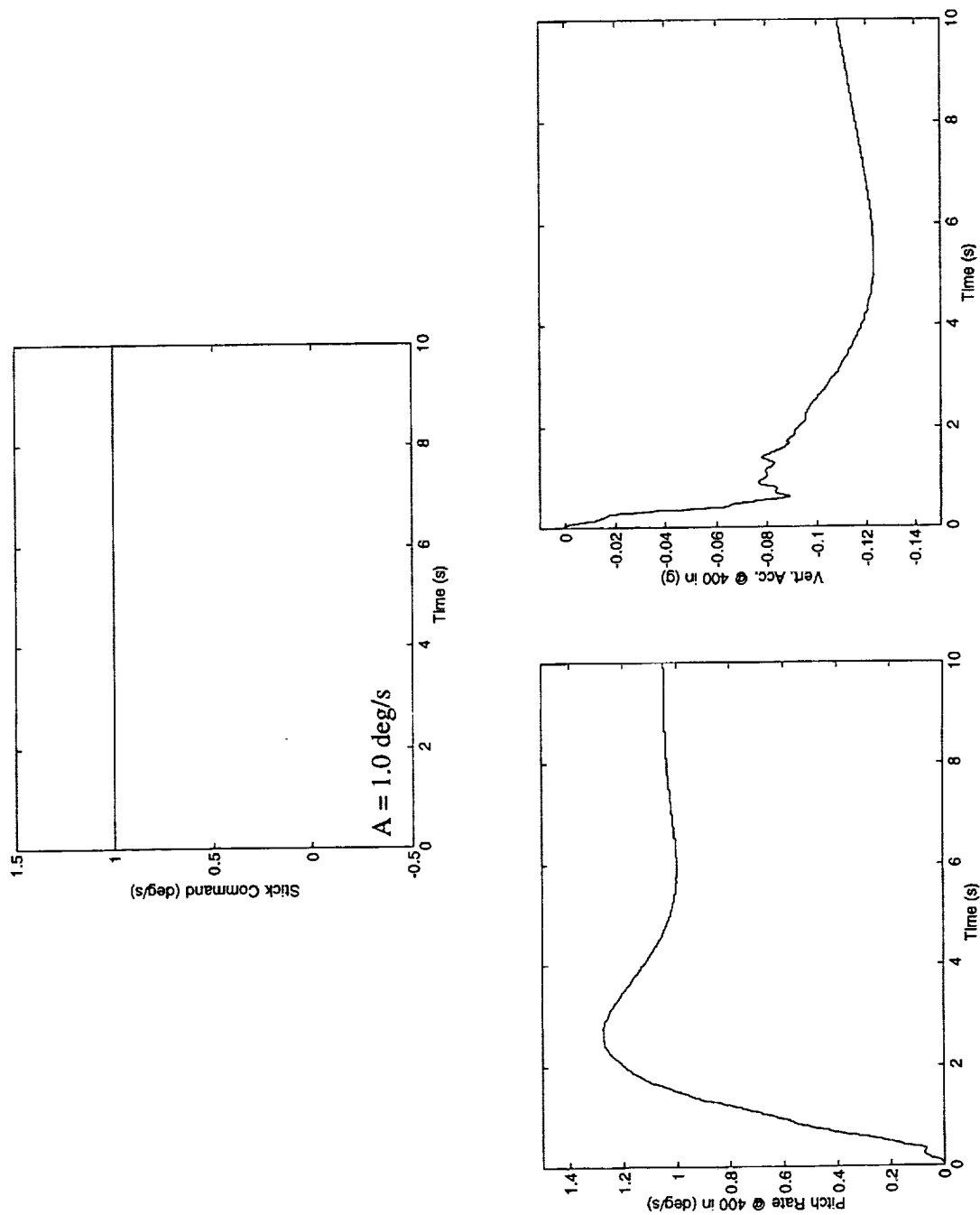


Figure 109. Response Characteristics For Maneuver Command - Step



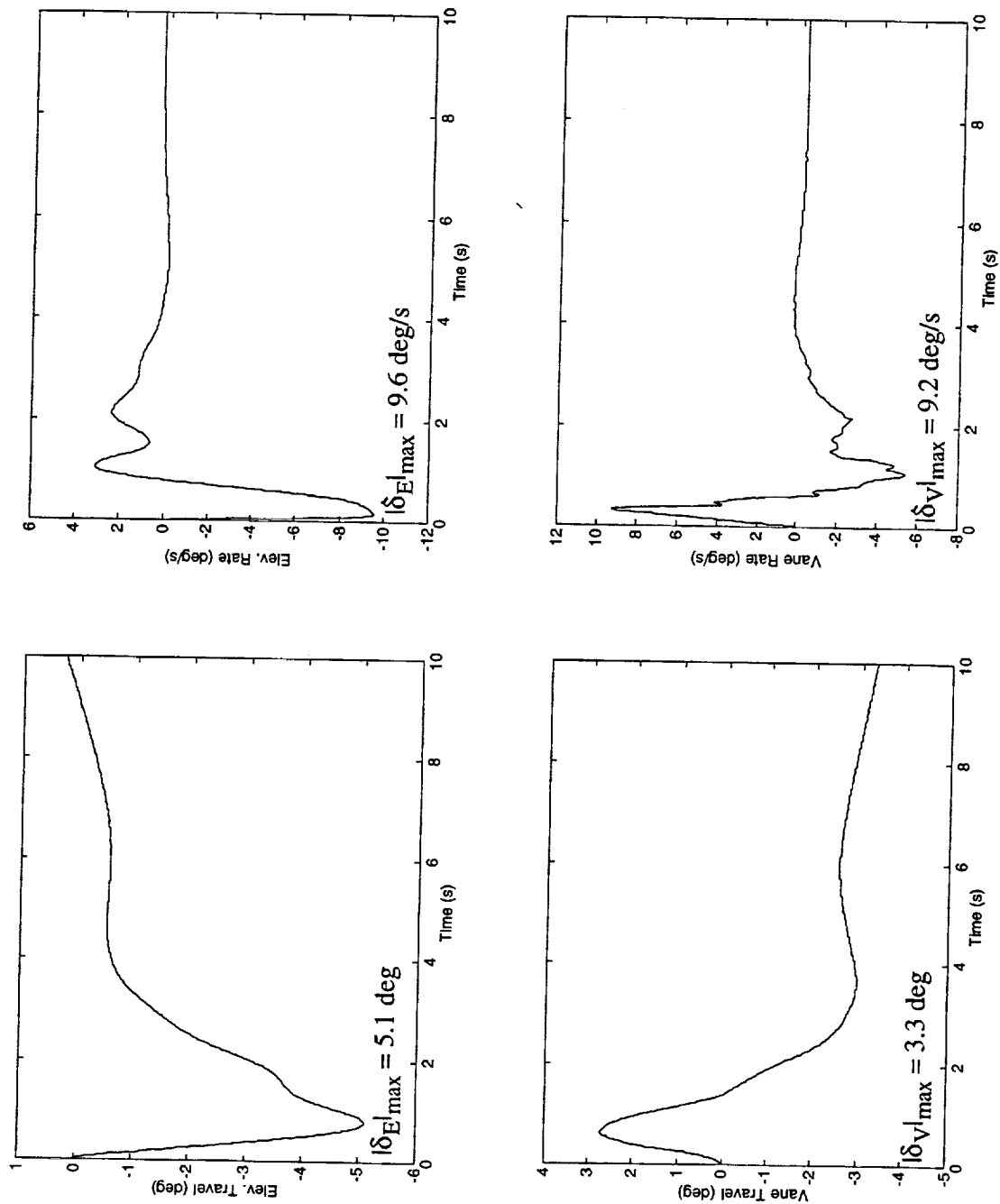


Figure 109. Continued

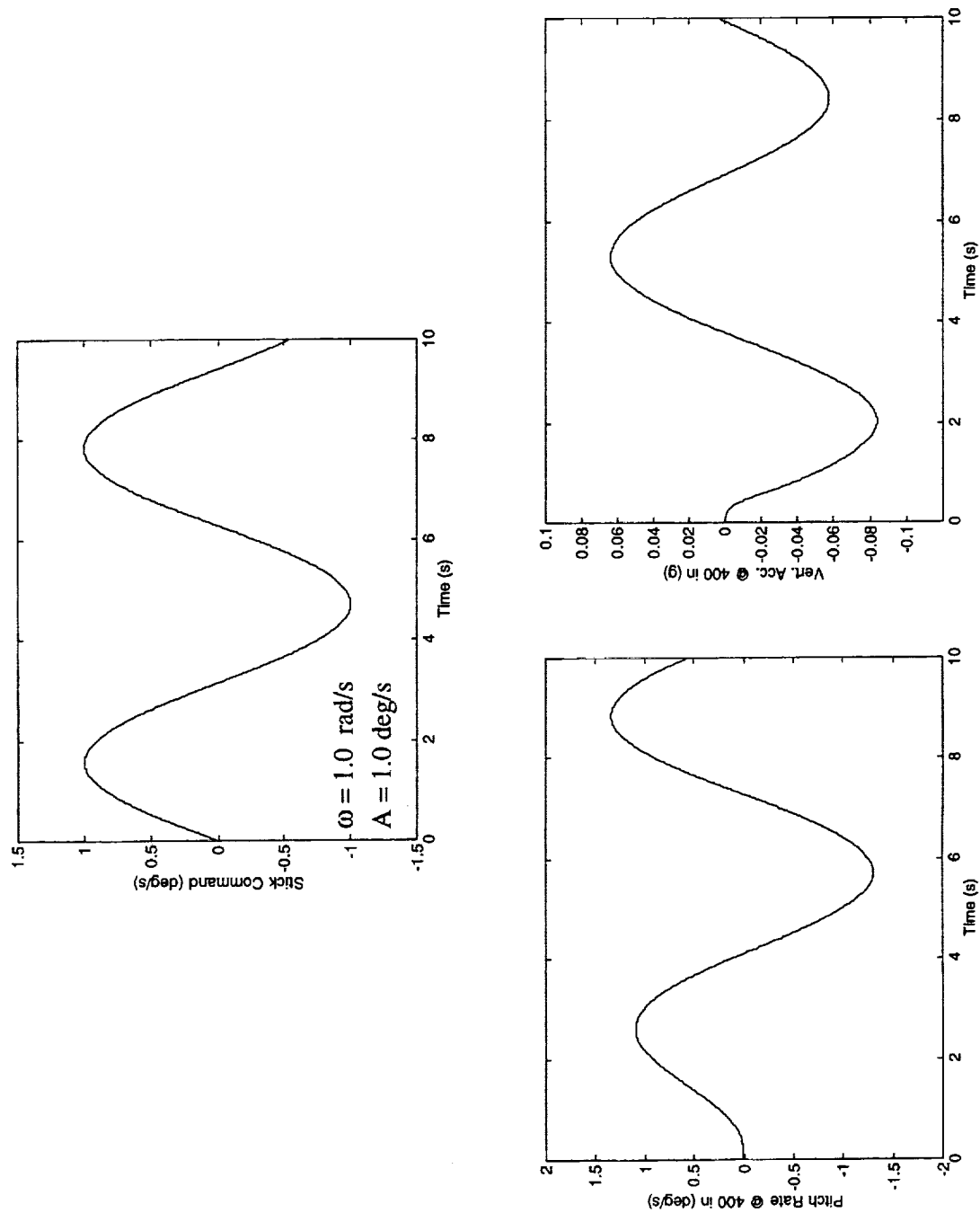


Figure 110. Response Characteristics For Maneuver Command - Sinusoid

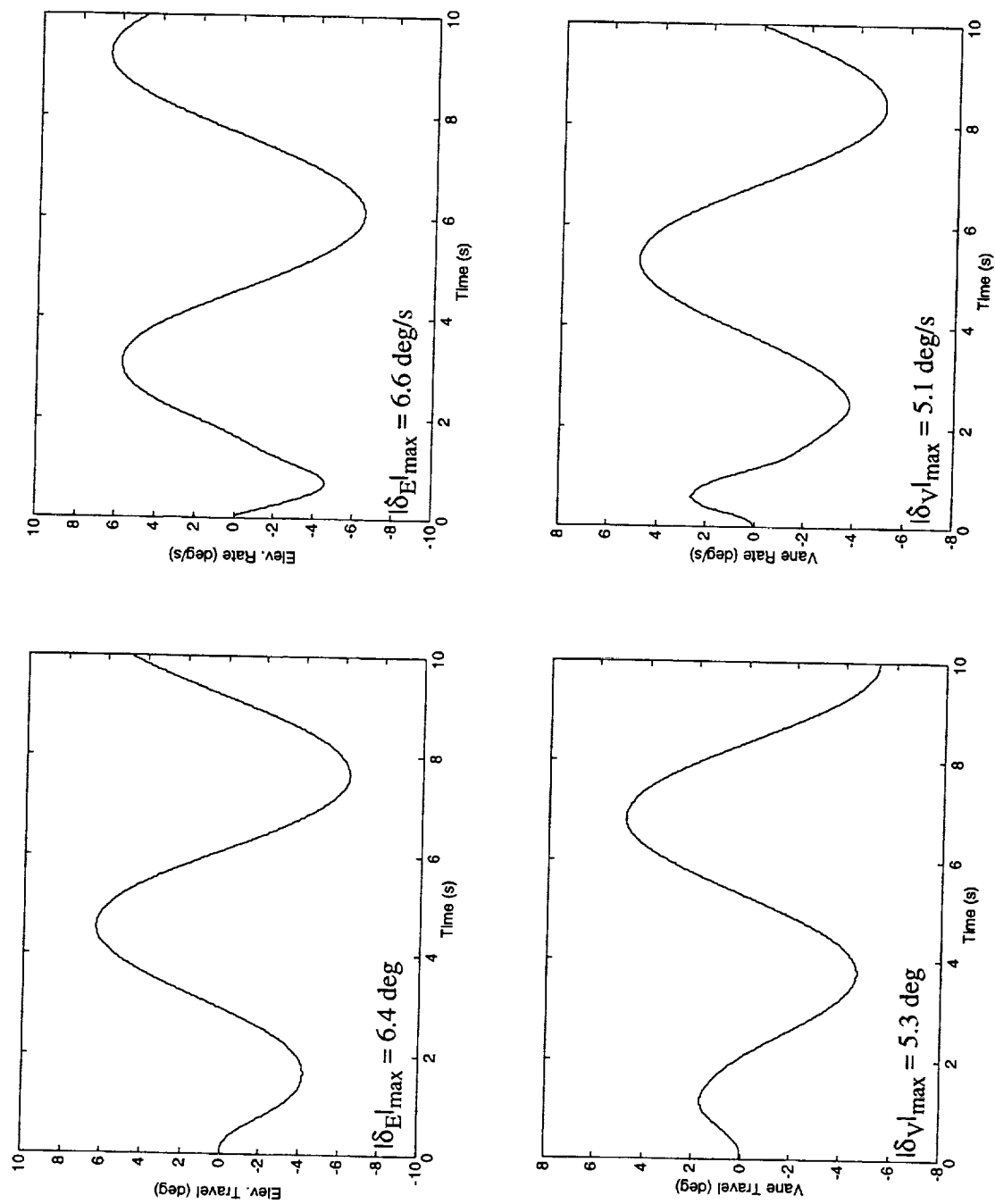


Figure 110. Continued

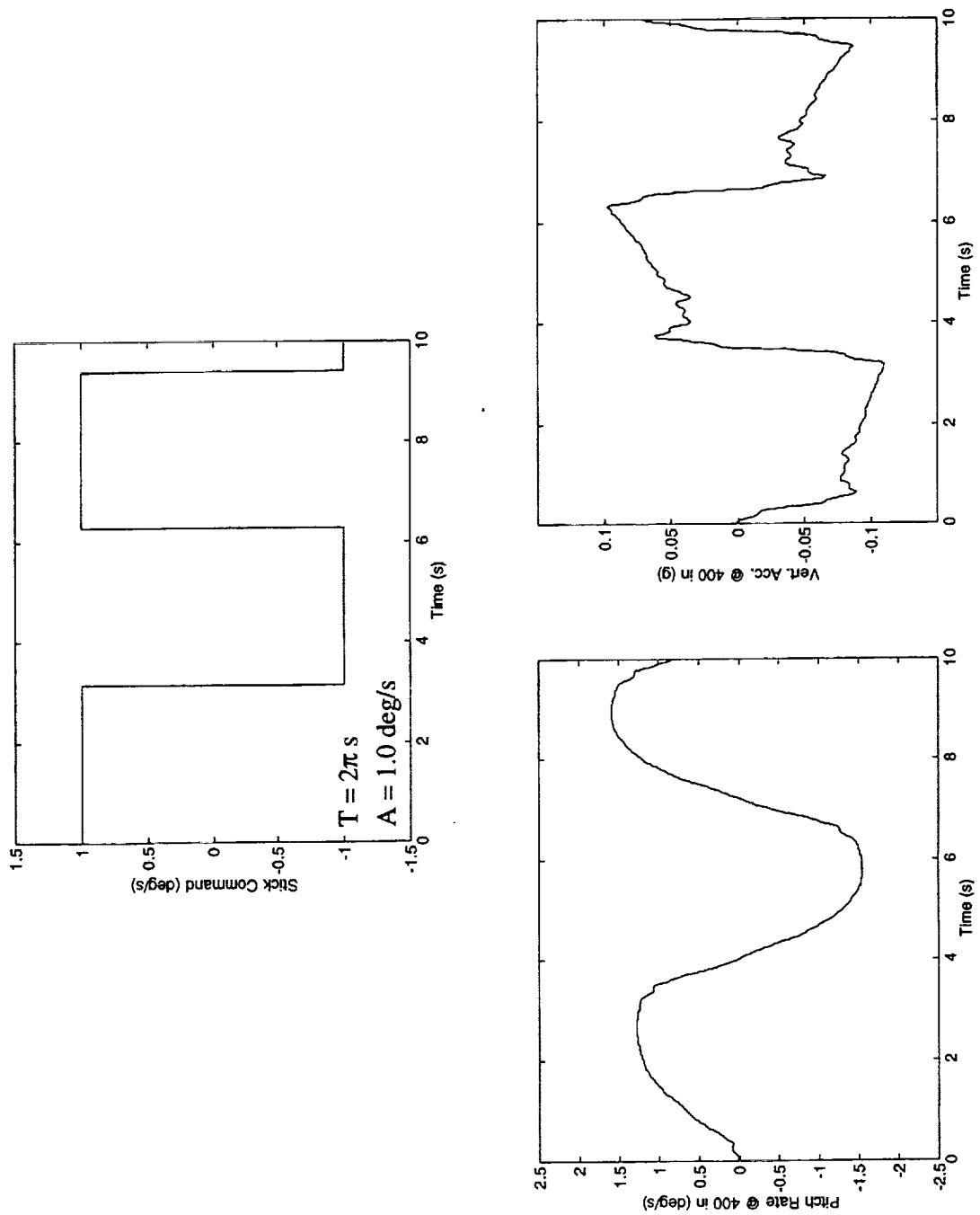


Figure 111. Response Characteristics For Maneuver Command - Square Wave

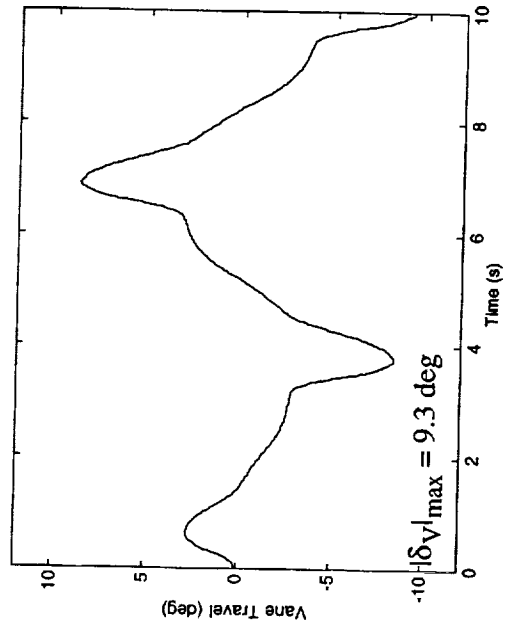
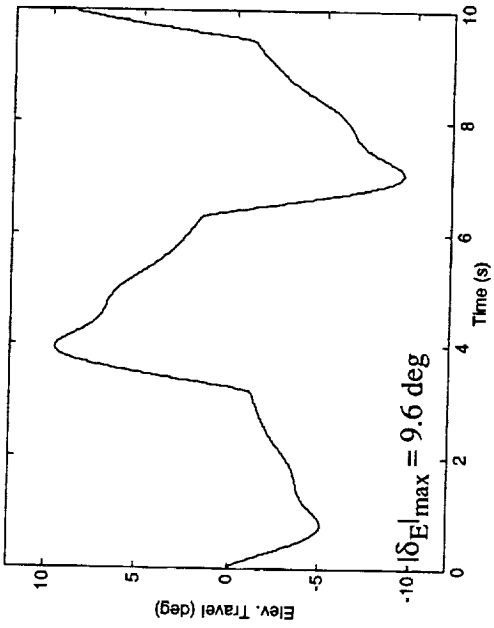
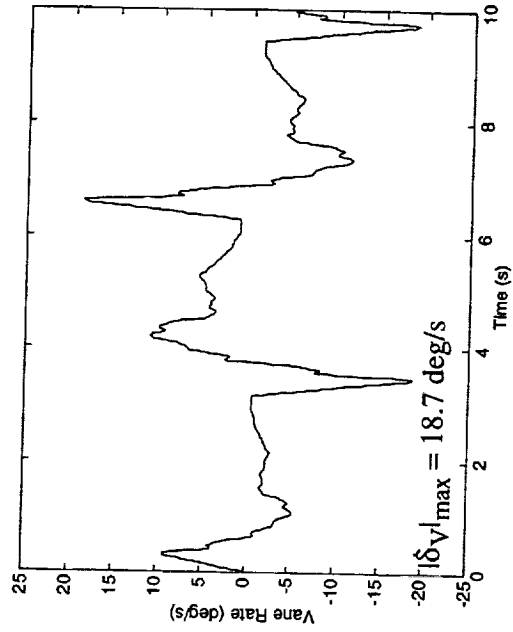
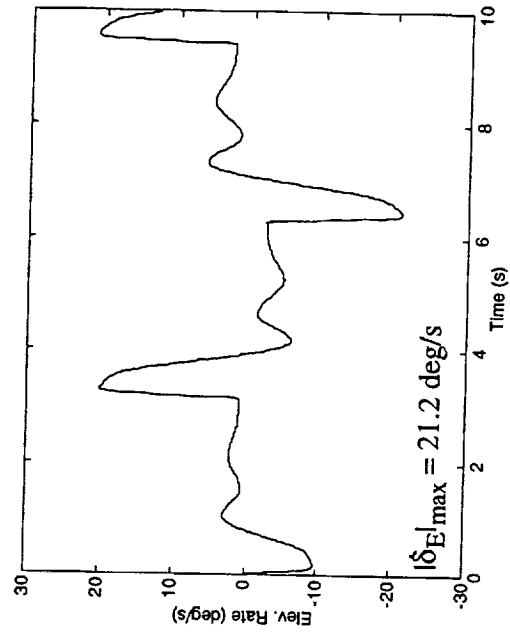


Figure 111. Continued

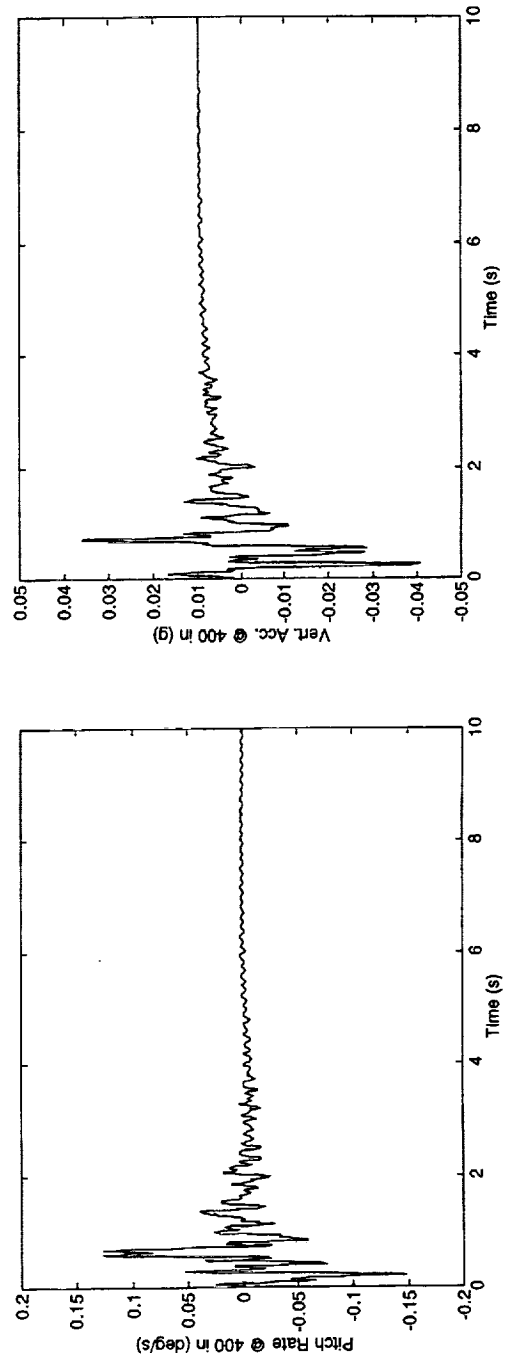
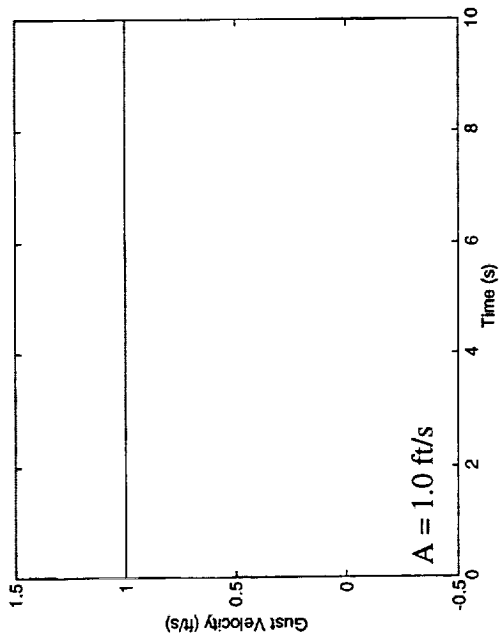


Figure 112. Response Characteristics For Atmospheric Gust - Step

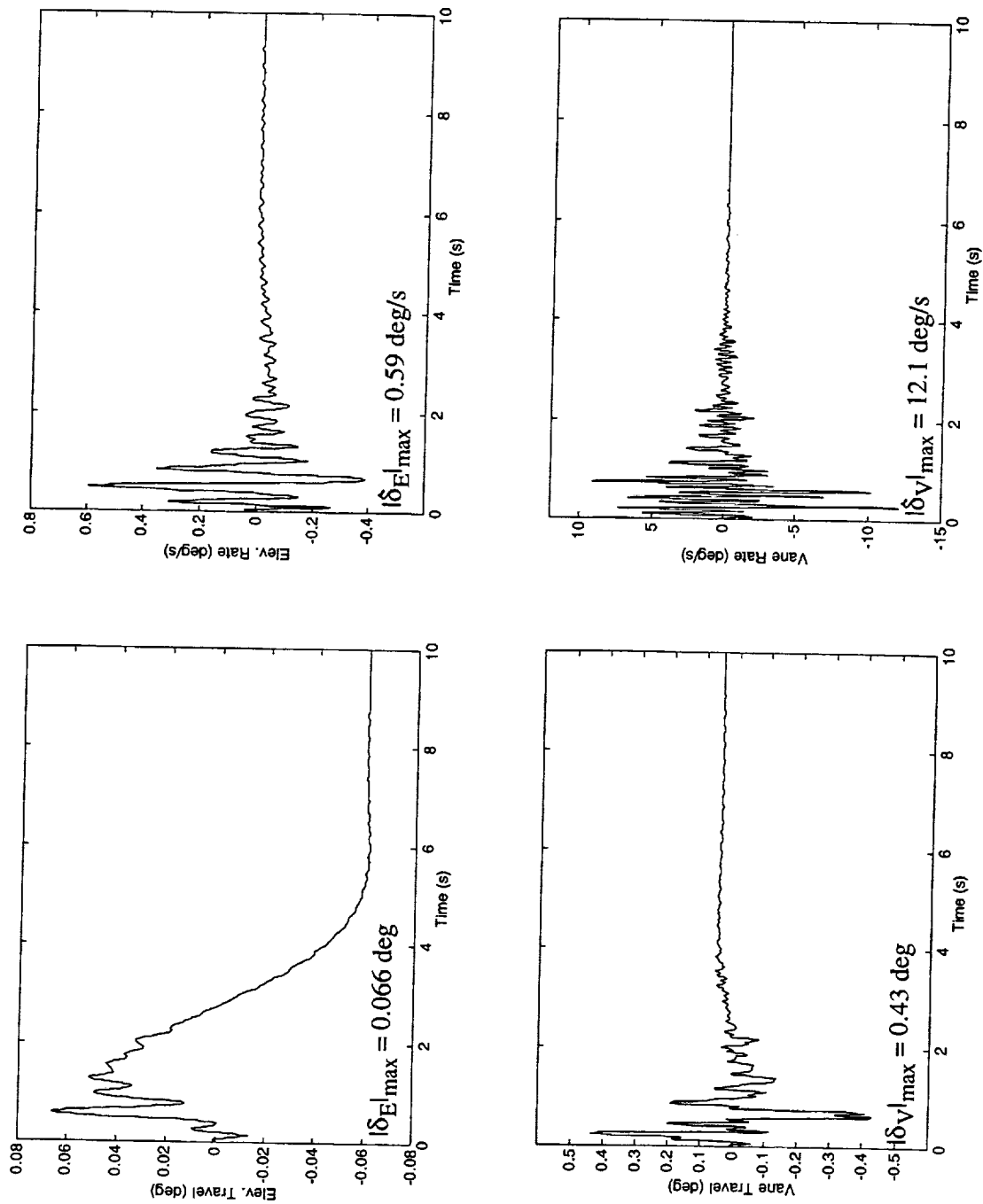


Figure 112. Continued

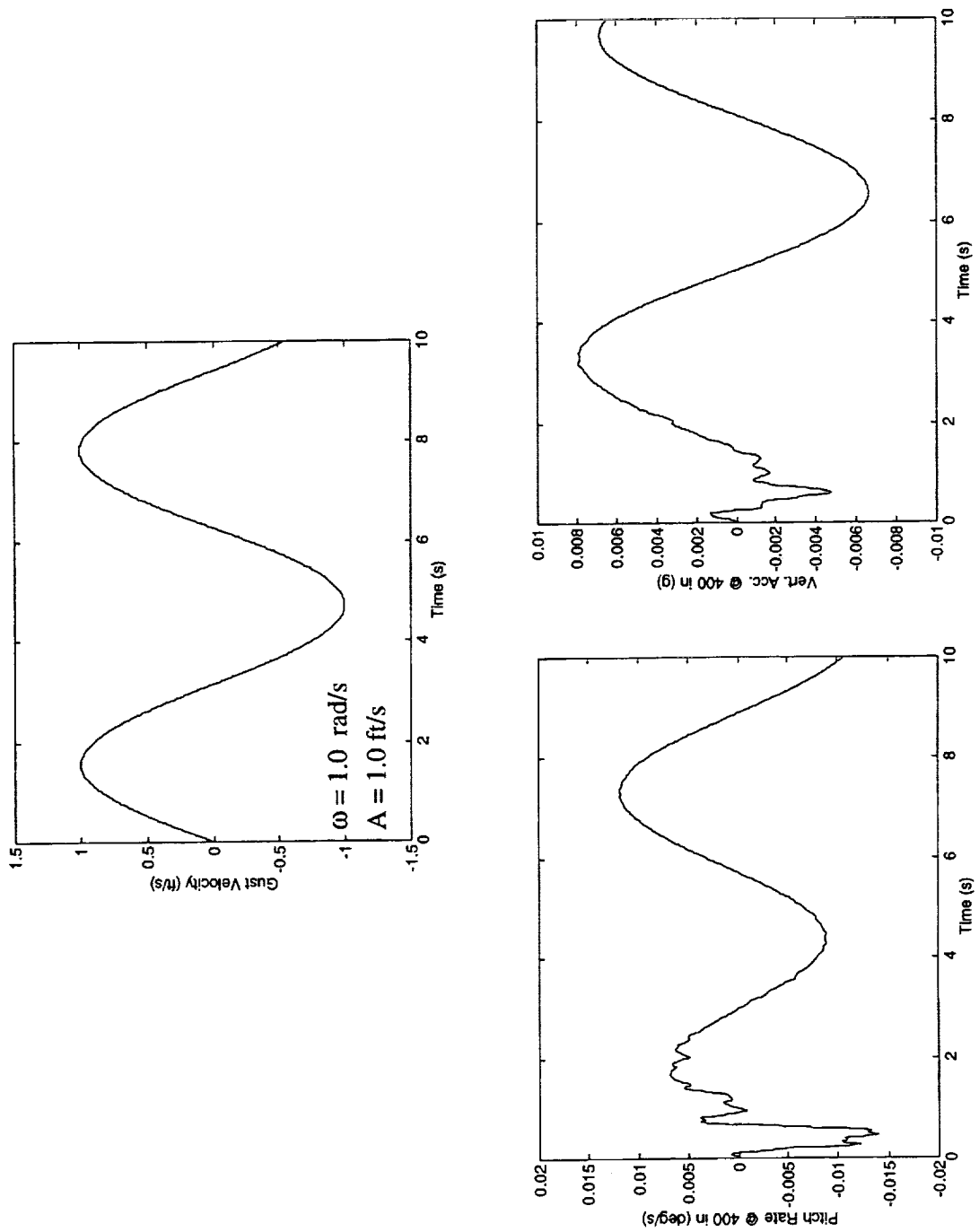


Figure 113. Response Characteristics For Atmospheric Gust - Sinusoid



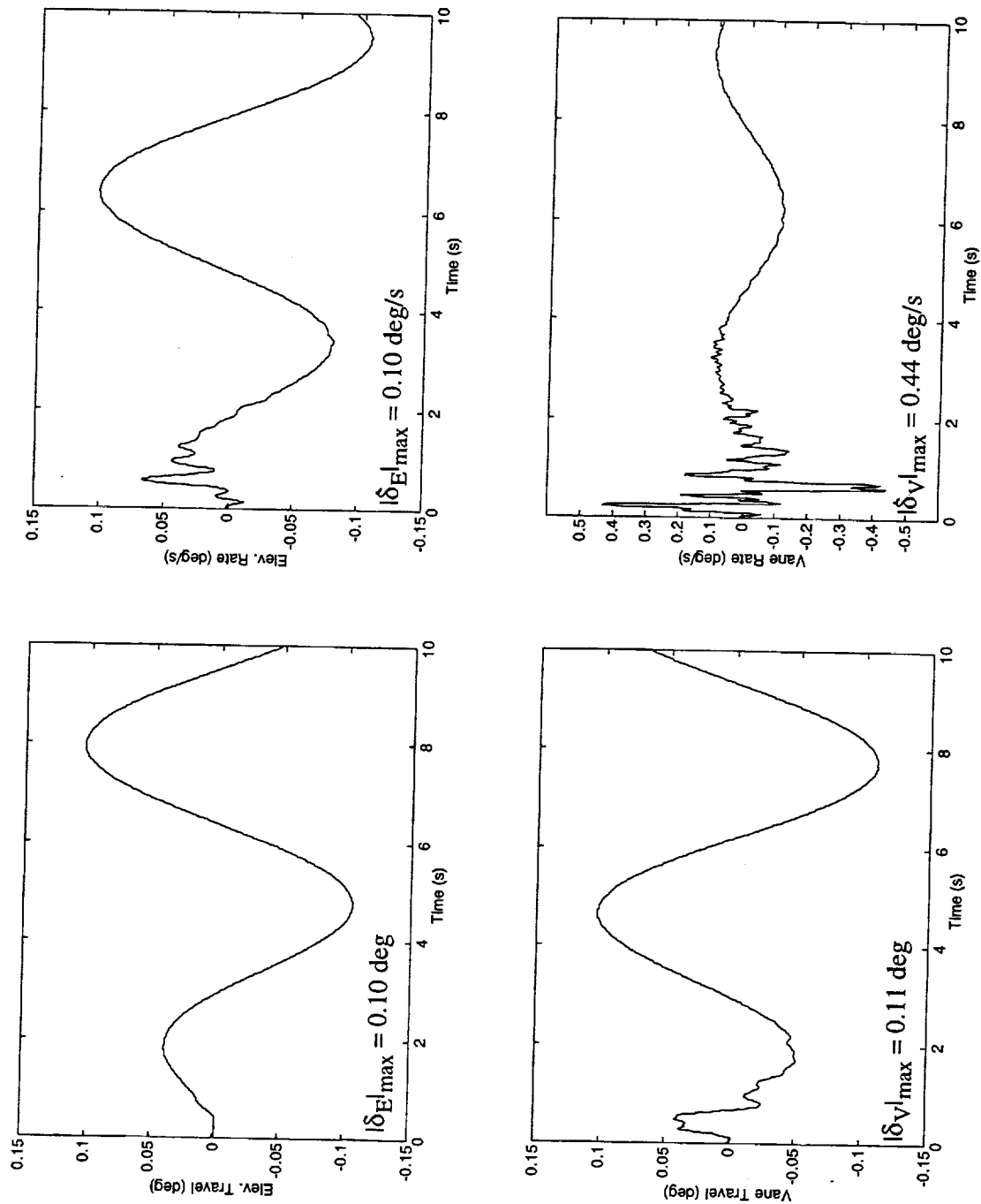


Figure 113. Continued

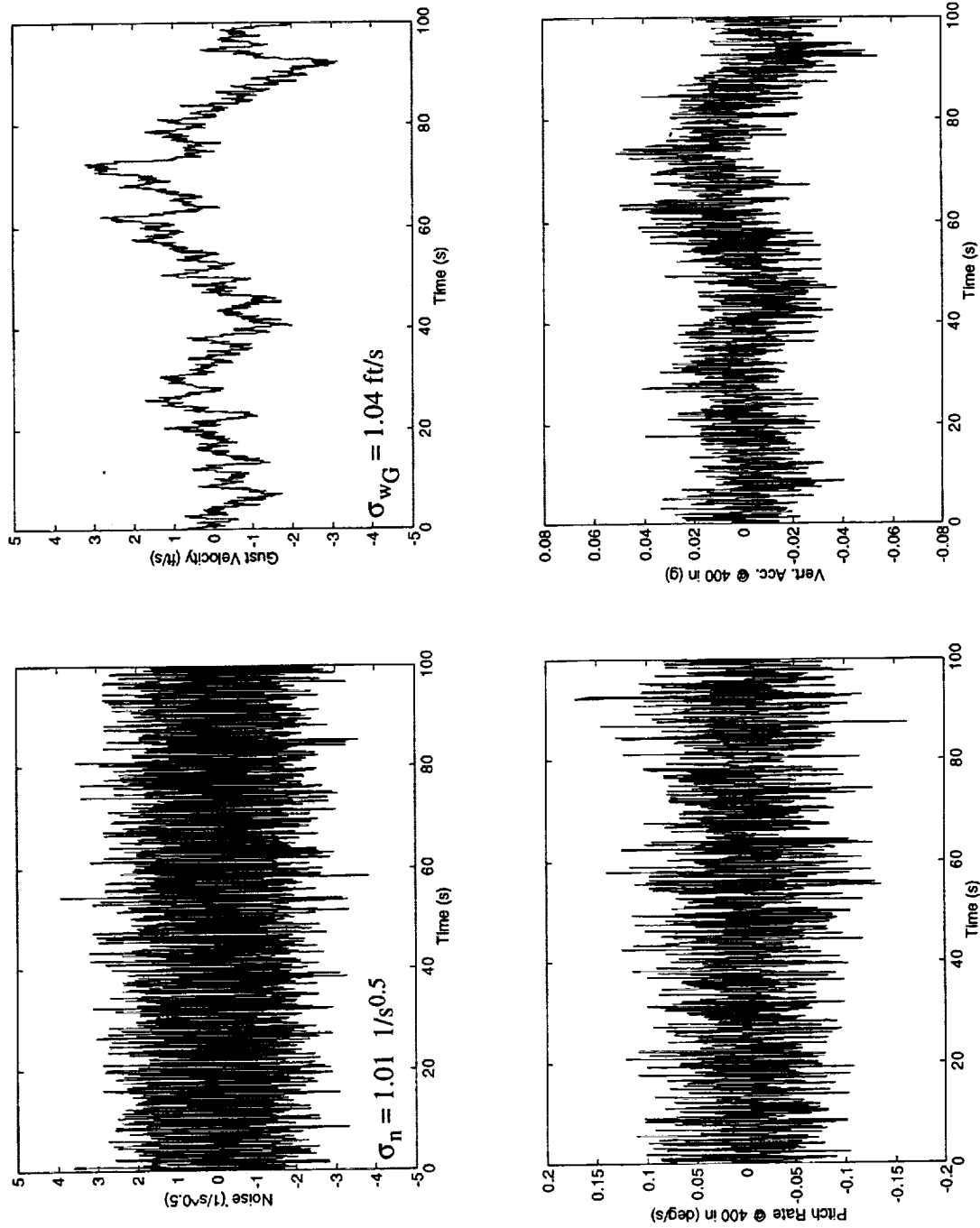


Figure 114. Response Characteristics For Atmospheric Gust - Turbulence

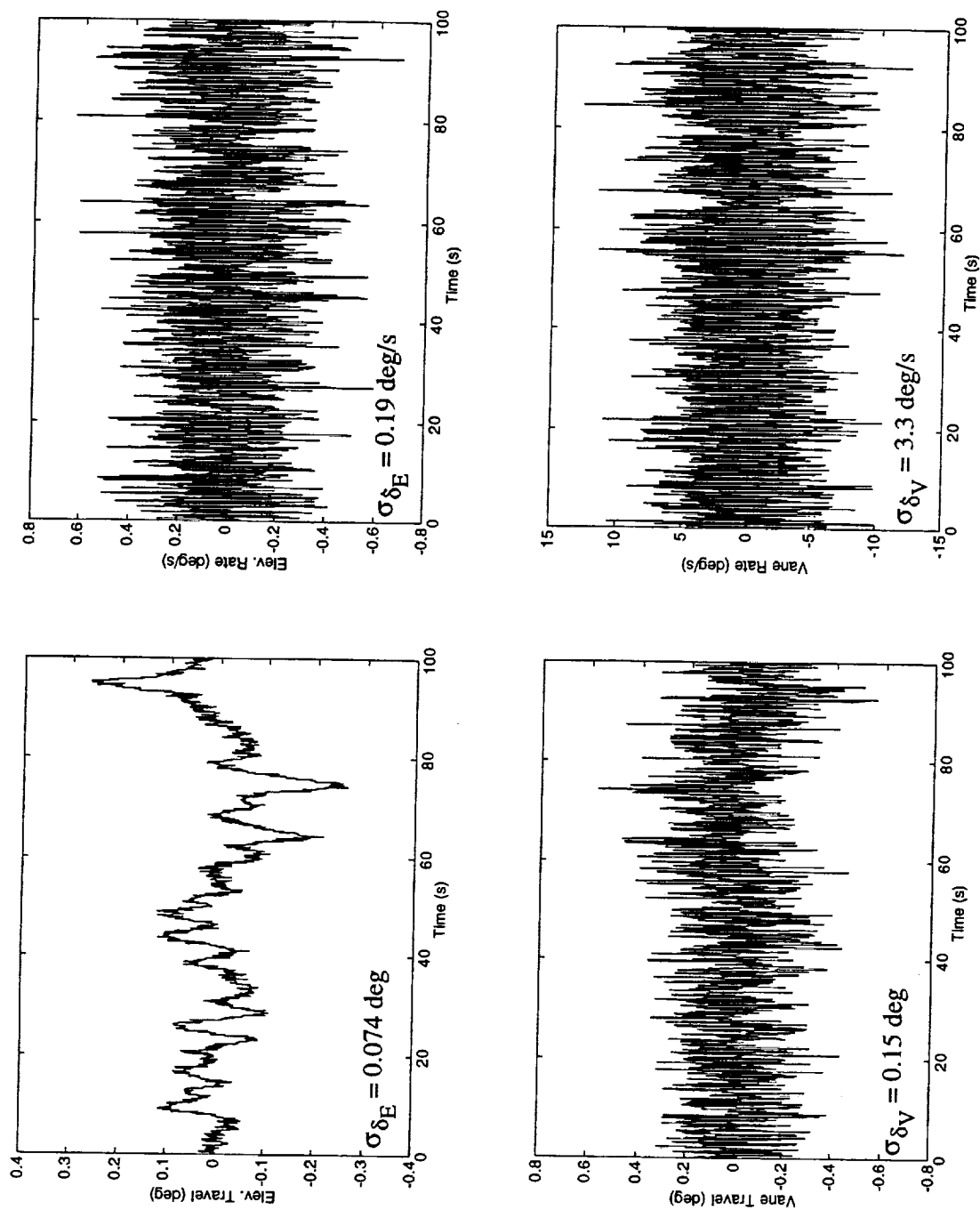


Figure 114. Continued

### C. Discussion of Sizing Results

Tab. 22 summarizes the peak vane activity for all six test cases, and the surface area lower bound necessary to keep vane motion within design limits. These lower bounds are computed from Eqs. (5.3)-(5.4) with travel and rate design limit values of  $\delta'_{V \max} = 20$  deg and  $\dot{\delta}'_{V \max} = 100$  deg/s. Recall these numbers represent the operational range the vane is to be maintained within, not the absolute travel and rate limits which may be substantially higher. The calculations in Tab. 22 are based on a nominal surface area of 177.5 ft<sup>2</sup>. For example, consider the lower bound calculation for the square wave excitation due to travel activity.

$$\begin{aligned}\bar{S}'_V &= (1)(1) \left( \frac{9.3 \text{ deg}}{20 \text{ deg}} \right) (177.5 \text{ ft}^2) \\ &= 83 \text{ ft}^2\end{aligned}\tag{5.6}$$

Table 22. Vane Sizing Results For Unit Excitations				
Excitation Case	$\delta_{V \max}$ (deg)	$\dot{\delta}_{V \max}$ (deg/s)	$\bar{S}'_V$ for $\delta_{V \max}$ (ft <sup>2</sup> )	$\bar{S}'_V$ for $\dot{\delta}_{V \max}$ (ft <sup>2</sup> )
Man. Command - Step	3.3	9.2	29	16
Man. Command - Sinusoid	5.3	5.1	47	9
Man. Command - Sq. Wave	9.3	18.7	83	33
Atmos. Gust - Step	0.43	12.1	4	21
Atmos. Gust - Sinusoid	0.11	0.44	1	1
Atmos. Gust - Turbulence	0.45	9.9	4	18

$$\bar{S}_V = 177.5 \text{ ft}^2, \delta'_{V \max} = 20 \text{ deg}, \dot{\delta}'_{V \max} = 100 \text{ deg/s}$$

From the data in Tab. 22, and based on "unit" excitations for all test cases, the largest required surface area to keep the vane within the design envelope is 83 ft<sup>2</sup>. The associated motion and excitation type are vane travel and square wave maneuver command. This particular case dominates the lower bound estimation. Comparison of the lower bound and baseline value sizing results (83 vs. 177.5 ft<sup>2</sup>) suggests the baseline vane model is oversized by a factor of 2.1 and could be reduced in size.

The lower bound data presented in Tab. 22 is somewhat abstract since it is based on "unit" excitations, and has not been calibrated to specific aggressive maneuvers or high gusts. To

calibrate the loading for the maneuver cases, consider the pitch acceleration requirements given in Ref. 2. Pitch acceleration requirements for go around and high angle of attack recovery can both be satisfied by a value of  $4 \text{ deg/s}^2$ . Using the initial slope of the pitch rate step command response ( $0.67 \text{ deg/s}^2$ ), the input amplitude should be scaled by a factor of 6 in order to obtain an initial pitch acceleration of  $4 \text{ deg/s}^2$ . This scaling of 6 is applied uniformly to all maneuver command input amplitudes. Now to calibrate the gust cases. Vertical drafts associated with moderate weather events can reach standard deviation values of 3 to 4 ft/s, which corresponds to gust levels considered for the ride discomfort index calculations in Section IV-F. Therefore, gust step and sinusoid amplitudes are scaled by a factor of  $3 \times 3.5$  and the turbulence standard deviation is scaled by a factor of 3.5. These calibrations lead to significant airframe loading, but not the rare high load case which occurs once in the airframe life cycle.

Tab. 23 summarizes the peak vane activity under the calibrated excitations and the corresponding lower bounds on surface area to keep vane motions within acceptable design limits. The values in Tab. 23 are obtained from the data in Tab. 22 by the scaling values just prescribed. From Tab. 23, the lower bound on surface area is  $495 \text{ ft}^2$ . Note the square wave command excitation is the critical loading case. This case leads to high vane travel and sets the lower bound on surface area. Also note vertical wind shear (gust step) has a significant impact on vane rate activity, even though it is not the most severe loading case. The results from this study indicate the baseline vane is most likely oversized for common maneuver and gust inputs. However, for large command and gust inputs, the baseline vane surface area will likely result in excursions outside the travel and rate design boundaries, but only for brief periods of time as indicated by Figs. 111-112. This conclusion is drawn under the specified actuation design limits of  $20 \text{ deg}$  and  $100 \text{ deg/s}$ , and the validity of the closed-loop simulation sizing strategy. With the data given in this section, readers can scale the inputs to additional cases and determine the vane excursions and necessary planform area and/or vane motion design limits.

Table 23. Vane Sizing Results For Calibrated Excitations				
Excitation Case	$\delta_{V \max}$ (deg)	$\dot{\delta}_{V \max}$ (deg/s)	$\bar{S}_V$ for $\delta_{V \max}$ (ft <sup>2</sup> )	$\bar{S}_V$ for $\dot{\delta}_{V \max}$ (ft <sup>2</sup> )
Man. Command - Step	19.8	55.2	176	98
Man. Command - Sinusoid	31.8	30.6	282	54
Man. Command - Sq. Wave	55.8	112.2	495	199
Atmos. Gust - Step	4.5	127.1	40	226
Atmos. Gust - Sinusoid	1.2	4.6	11	8
Atmos. Gust - Turbulence	1.6	34.7	14	62

$\bar{S}_V = 177.5 \text{ ft}^2$ ,  $\delta_{V \max} = 20 \text{ deg}$ ,  $\dot{\delta}_{V \max} = 100 \text{ deg/s}$ ,  
Scale factor of 6 (all man. com.), 10.5 (atm. gust - step & sinusoid), and 3.5 (atm. gust - turb.)

Due to the observed large vane travel in the square wave command case, one additional sizing study was considered. This study addressed the sensitivity of peak vane travel to crossfeed gain  $k_{cf}$  in Eq. (4.13). Reconsider the unit square wave command results in Fig. 111 and Tab. 22. These results correspond to a gain value of  $k_{cf} = -0.25 \text{ rad/s/rad}$ . Fig. 115 shows the response behavior when this gain is zeroed out ( $k_{cf} = 0 \text{ rad/s/rad}$ ). In this case, note the peak vane travel is 5.4 deg. When compared with the nominal crossfeed gain case, this new vane travel is considerably less (5.4 vs. 9.3 deg) indicating high sensitivity. The vane motion is nearly halved when the crossfeed path is deleted from the control architecture. However, note the initial 400 in pitch rate response behavior. Initial response reversal is present in the crew station motions and is unacceptable. Thus, a significant trade may exist when sizing the vane and tuning the crossfeed gain: for crew station flying qualities, ample use of crossfeed gain and vane area will eliminate response reversal, while for static vehicle performance, small utilization of crossfeed gain and surface area will lessen main wing/inlet flow impingement effects.

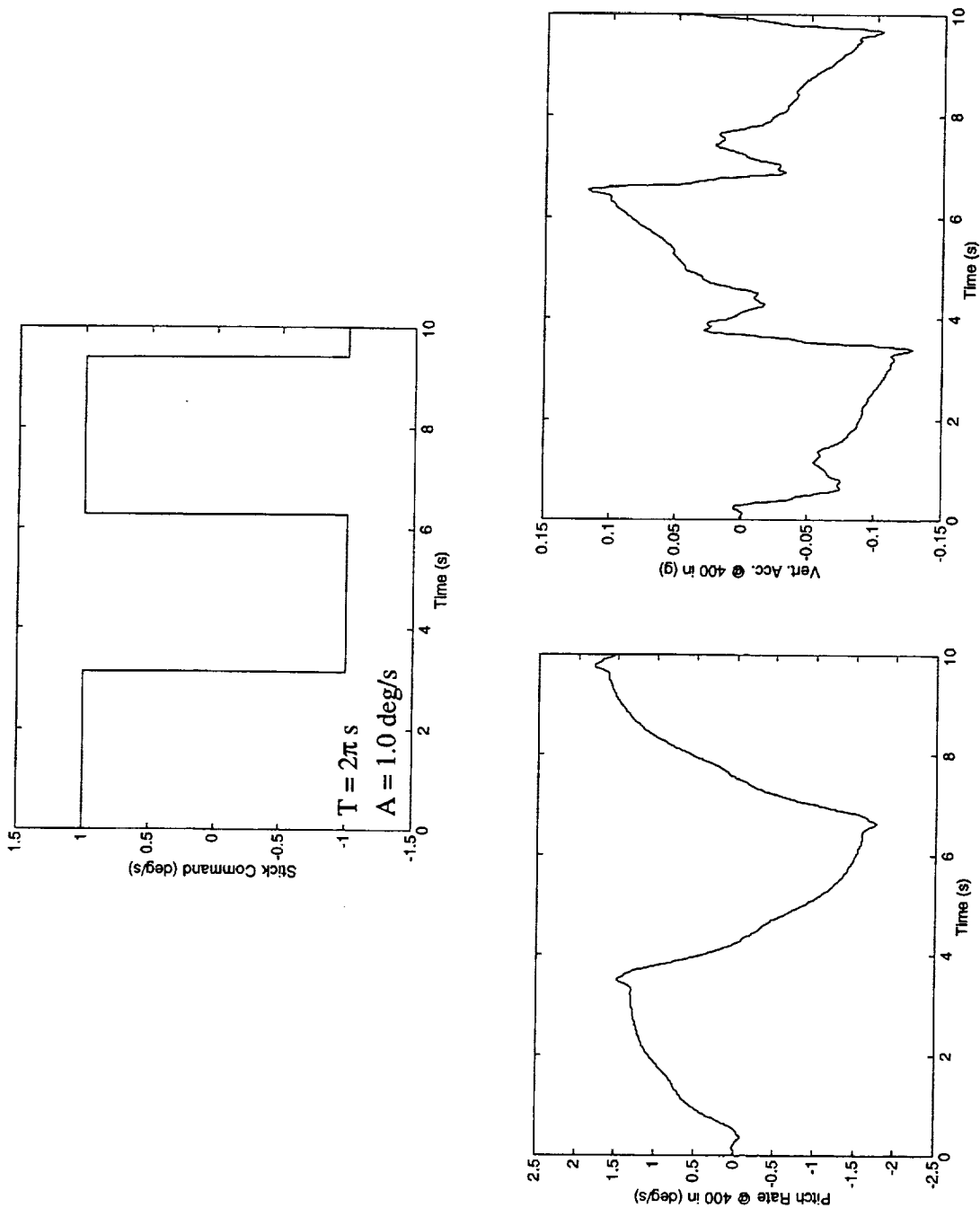


Figure 115. Response Characteristics For Maneuver Command - Square Wave  
With Crossfeed Path Eliminated

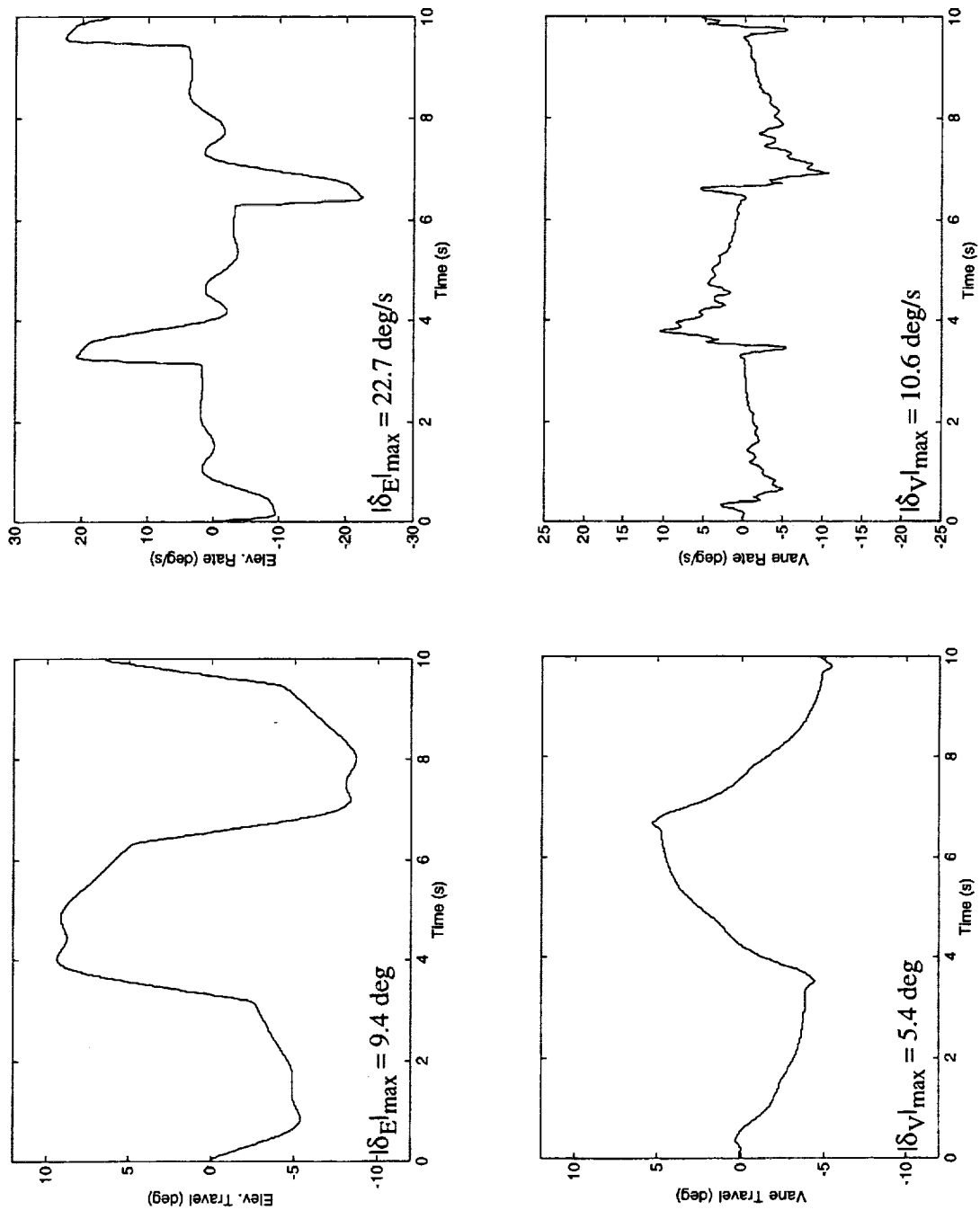


Figure 115. Continued



## Section VI

### Conclusions and Recommendations

One major conclusion drawn from the contract activities is that control architectures based on aft tail only are not well suited for highly flexible, high-speed vehicles such as the HSCT. This conclusion was formulated in Ref. 13, and further analysis in this report supports this important conclusion. The studies performed in Ref. 13 were based on an early dynamic model of the Ref. H HSCT. Analysis here has shown the early model provides an accurate representation of airframe characteristics exhibited in more recently generated models containing refined data. If the single-loop control studies were revisited with the newer models, results would not significantly change. Therefore, the model correlation findings provide further support and justification for this claim of architectural infeasibility. Additional control studies discussed below also provide additional support for this conclusion. The implication from this conclusion is that configuration redesign, possibly addressing control surface alternatives or additional structural stiffening, appears necessary to relax unrealistic and unachievable control design constraints.

Another conclusion that can be formulated from the contract findings concerns the theoretical underpinnings of the original Wykes structural mode control logic utilizing feedback signal differencing schemes. This control logic is based on several assumptions concerning the vehicle dynamic characteristics, and if not satisfied, the control logic can break down leading to mode destabilization. These assumptions include vehicle characteristics that lie below upper limits on structural deflections associated with higher frequency modes and aerodynamic coupling phenomena between these modes, so as not to distort collocated transfer function pole-zero distribution patterns along the imaginary axis. The Ref. H HSCT predicted airframe characteristics violate these basic assumptions. The airframe is modally dense with many significant modes involving the main wing and aft tail surfaces. Further, the dynamic airflow that is present over these surfaces introduces considerable aerodynamic-structural coupling mechanisms between these

modes. Application of the Wykes logic to the HSCT model resulted in destabilizations due to violation of the fundamental assumptions. These new results also strongly support the conclusion drawn above concerning aft tail only control architectures. In spite of this conclusion, a simplified Wykes controller, based on a nondifferenced feedback signal and appropriately located along the fuselage, provided a feasible mode stabilization loop that is discussed below.

The main conclusion arising out of the contractual efforts concerns the development of a two-loop control architecture that utilizes small forward vanes with the aft tail. This multivariable architecture provides a highly attractive and feasible solution to the longitudinal axis control challenges. Pitch augmentation and aeroelastic suppression can be significantly and harmoniously leveraged with a low order, adjustable and implementable architecture. Depending on the severity of airframe dynamic characteristics, the available actuation technology, the design model fidelity, and the aggressiveness of the control augmentation, the vane-tail architecture can provide high levels of stability and performance, robustness, and flying/ride qualities. For the Ref. H HSCT model, and under a conservative design posture, a candidate design is given and is predicted to possess high levels of stability with Level 2 flying qualities. Level 1 flying qualities appear within reach, possibly by trading excess stability margins for improved flying qualities (if only the flying quality boundaries were defined), or by possibly taking more risk in the mode suppression control paths. The importance of this finding is that many of the critical flight dynamics issues resulting from concept viability design constraints, such as aeroelastic contamination of responses due to minimization of structural weight for expanded range/payload and associated economic profit, can be realistically addressed with a "minor" configuration redesign that incorporates forward vanes.

A final conclusion is that the baseline vane model utilized in this report is most likely oversized. The baseline surface area, under normal loading conditions associated with command maneuvering or atmospheric gusts, leads to low travel and rate activity, relative to specified design limits. Such behavior implies the vane is oversized and could be reduced in surface area until the design limits are more closely approached. The implication here is that under most flight conditions, available vane leverage would be maximized. However, for large excitations that occur

infrequently, the baseline vane model would most likely violate the design travel and rate limits. In these situations, available vane leverage would be suboptimal for short duration periods, and the mode suppression function would suffer accordingly.

Recommendations for future activities which are most critical for development of workable inner loop flight control systems for large, high-speed, highly flexible vehicles are listed below.

1. Integration of inner and outer loop systems that are designed independently and possibly under different assumptions. Considerable efforts have already focused on both inner and outer loop systems (pitch rate vs.  $\dot{\gamma}$ /speed command), but under significantly different assumptions (dynamic vs. static aeroelastic) and with little coordination.
2. Creation of a flying and ride qualities data base, applicable to flight vehicles exhibiting significant structural vibration motions, through moving-base piloted simulation test programs. Currently there are little, if any, guidelines and requirements for flight control design of such vehicles.
3. Assessment of the upper limits of stability and performance that can be achieved with contemporary-based multivariable flight control design strategies. Such techniques provide powerful tools for addressing such questions, and would offer alternative architectures to the conventional-based multi-loop system recommended in this report.
4. Investigation of inner loop flight control systems for the lateral-directional axes. Very little attention has been given to this important problem which may provide even more challenging constraints, in some sense, when compared with the longitudinal characteristics.

## References

1. U.S. Dept. of Defense, "Military Standard: Flying Qualities of Piloted Aircraft," MIL-STD-1797A, January, 1990.
2. Rossitto, K., Ray, J., "HSCT Flight Control System Requirements Specification," MDC Report CRAD-9408-TR-2076, NASA Contract NAS1-20220, Task No. 36, Long Beach, California, October, 1997.
3. McRuer, D., Ashkenas, I., and Graham, D., *Aircraft Dynamics and Automatic Control*, Princeton University Press, Princeton, New Jersey, 1973.
4. Kwakernaak, H. and Sivan, R., *Linear Optimal Control Systems*, John Wiley & Sons, New York, New York, 1972.
5. Stevens, B. L. and Lewis, F. L., *Aircraft Control and Simulation*, John Wiley & Sons, New York, New York, 1992.
6. Ray, J. K., Carlin, C. M., and Lambregts, A. A., "High-Speed Civil Transport Flight - and Propulsion - Control Technological Issues," NASA-CR-186015, Dryden Flight Research Facility, Edwards, California, March, 1992.
7. McCarty, C. A., Feather, J. B., Dykman, J. R., Page, M. A., Hodgkinson, J., "Design and Analysis Issues of Integrated Control Systems for High-Speed Civil Transports," NASA-CR-186022, Dryden Flight Research Facility, Edwards, California, May, 1992.
8. Deliverable Item No. 18, Contract NAS1-20220, Task Assignment No. 7, Flight Controls, Langley Research Center, Hampton, Virginia, June, 1995.
9. Zeiler, T., Informal Deliverable Item from Lockheed Martin Engineering & Sciences Co., HSR Program, Langley Research Center, Hampton, Virginia, June-August, 1995.
10. Sotack, R. A., Chowdhry, R. S., and Buttrill, C. S., "High Speed Civil Transport Aircraft Simulation: Reference H Cycle 1 - Matlab Implementation," NASA/TM-1999-209530, Langley Research Center, Hampton, Virginia, December, 1999.
11. Greiner, G. P., "High Speed Civil Transport Aircraft Simulation: Reference H Cycle 3 - Matlab Implementation," To be published.
12. Adams, W. A. and Hoadley, S. T., "ISAC: A Tool for Aeroservoelastic Modeling and Analysis," NASA-TM-109031, Langley Research Center, Hampton, Virginia, December, 1993.
13. Newman, B. and Kassem, A., "Investigation of Inner Loop Flight Control Strategies for High-Speed Research," NASA/CR-1999-209522, Langley Research Center, Hampton, Virginia, December, 1999.

14. Wykes, J. H. and Mori, A. S., "An Analysis of Flexible Aircraft Structural Mode Control," AFFDL-TR-65-190, Air Force Flight Dynamics Laboratory, Wright-Patterson AFB, Ohio, June, 1966.
15. Wykes, J. H., "Structural Dynamic Stability Augmentation and Gust Alleviation of Flexible Aircraft," *Proceedings of the AIAA 5th Annual Meeting and Technical Display*, AIAA Paper No. AIAA-68-1067, Philadelphia, Pennsylvania, October, 1968.
16. Bisplinghoff, R. L. and Ashley, H., *Principles of Aeroelasticity*, Dover Publications, New York, New York, 1962.
17. Swaim, R. L. and Fullman, D. G., "Prediction of Elastic-Airplane Longitudinal Dynamics From Rigid-Body Aerodynamics," *Journal of Aircraft*, Vol. 14, No. 9, September, 1977, pp. 868-873.
18. Waszak, M. R. and Schmidt, D. K., "Flight Dynamics of Aeroelastic Vehicles," *Journal of Aircraft*, Vol. 25, No. 6, June, 1988, pp. 563-571.
19. Arbuckle, P. D., Buttrill, C. S., and Zeiler, T. A., "A New Simulation Model Building Process for Use in Dynamic Systems Interaction Research," *Proceedings of the AIAA Flight Simulation Technologies Conference*, Monterey, California, August, 1987, pp. 96-106.
20. Hoblit, F. M., *Gust Loads on Aircraft: Concepts and Applications*, American Institute of Aeronautics and Astronautics, New York, New York, 1988.
21. Anderson, J. D., *Fundamentals of Aerodynamics*, McGraw-Hill, New York, New York, 1984.
22. Newman, B., "Multivariable Flight Control Design Using Root Locus Techniques," *Proceedings of the AIAA Guidance, Navigation, and Control Conference*, Baltimore, Maryland, August, 1995, pp. 1157-1166.
23. Newman, B. and Schmidt, D. K., "Aeroelastic Vehicle Multivariable Control Synthesis with Analytical Robustness Evaluation," *Journal of Guidance, Control, and Dynamics*, Vol. 17, No. 6, November-December, 1994, pp. 1145-1153.
24. Newman, B., "Proposed Flying Quality Metrics and Simulation Studies for Elastic Vehicles," *Proceedings of the AIAA Atmospheric Flight Mechanics Conference*, San Diego, California, July, 1996, pp. 500-509.
25. Barrett, M. and Elgersma, M., "High Speed Research: Stability and Performance Robustness Analysis for a Flexible HSCT," Honeywell Technology Center, Prepared Under NASA Contract NAS1-20219, Minneapolis, Minnesota, October, 1997.
26. Newman, B. and Schmidt, D. K., "Truncation and Residualization with Weighted Balanced Coordinates," *Journal of Guidance, Control, and Dynamics*, Vol. 17, No. 6, November-December, 1994, pp. 1299-1307.
27. Wykes, J. H., Byar, T. R., MacMiller, C. J., and Greek, D. C., "Analyses and Tests of the B-1 Aircraft Structural Mode Control System," NASA-CR-144887, Dryden Flight Research Facility, Edwards, California, 1980.
28. McRuer, D., Johnston, D., and Myers, T., "A Perspective on Superaugmented Flight Control Advantages and Problems," *Active Control Systems - Review, Evaluation and*

*Projections, AGARD Conference Proceedings No. 384*, Toronto, Canada, October, 1984, pp. 3.1-3.16.

29. Newman, B. and Buttrill, C., "Conventional Flight Control for an Aeroelastic, Relaxed Static Stability High-Speed Transport," *Proceedings of the AIAA Guidance, Navigation, and Control Conference*, Baltimore, Maryland, August, 1995, pp. 717-726.
30. Vinh, N. X., *Flight Mechanics of High-Performance Aircraft*, Cambridge University Press, Cambridge, Great Britain, 1993.
31. Gregory, I. M., Chowdhry, R. S., McMinn, J. D., and Shaughnessy, J. D., "Hypersonic Vehicle Model and Control Law Development Using  $H_\infty$  and  $\mu$  Synthesis," NASA-TM-4562, Langley Research Center, Hampton, Virginia, October, 1994.
32. Arbuckle, P. D., Lewis, M. S., and Hinton, D. A., "Airborne Systems Technology Application to the Windshear Threat," *Proceedings of the 20th Congress of the International Council of the Aeronautical Sciences*, Sorrento, Italy, September, 1996, pp. 1640-1650.

## Appendix A

### Statement of Work for NAS1-19858-93

#### Multivariable Techniques for HSR Flight Control Systems

##### **Technical Objective:**

The High-Speed Civil Transport (HSCT) is projected to have a pitch divergence due to the relaxation of static stability at subsonic speeds. Further, significant interaction between rigid-body and aeroelastic degrees of freedom is expected. Objectives of the inner most loops of the flight control system (FCS) for HSCT will be to artificially supply the stability inherently lacking in the airframe, augment the key responses with crisp, well damped behavior, and to suppress, or lessen, aeroelastic motions in the rigid-body responses. Attainment of these multiple, conflicting closed-loop objectives inherently requires a dexterous FCS architecture, which can sense key motions and apply critical forces/moments simultaneously at multiple points distributed throughout the vehicle. Here, the objectives are three fold: 1) to investigate contemporary multivariable design techniques for meeting the closed-loop objectives and to assess the "theoretically achievable" upper limits of stability/performance, 2) to explore the control benefits derived from an additional, small, forward aerodynamic control surface applicable to preliminary HSCT concepts, and 3) to establish requirements for levels of controllability of rigid and elastic responses that can be used to guide configuration design. This task shall be coordinated with the HSR Flight Controls Task (Task 7 on NAS1-20220), specifically, the subtask entitled "Ref. H Assessment", and is a follow on task to Contract NAS1-19858, Task 71 and NASA-ASEE activities during 1996.

##### **Background & Approach:**

Previous analysis of conventional-based single-loop FCS for HSCT class vehicles indicate several hard conflicting constraints. Results indicate these single-loop FCS architectures do not allow sufficient design freedoms to overcome the constraints. The extreme level of flexibility, and the necessary stability augmentation bandwidth, seen in current HSCT models, points to the need for maximum capability and effectiveness from the FCS. The first task is to explore the potential of contemporary-based multi-loop FCS, such as those designed with LQ and  $H_\infty$  theory, for meeting the numerous closed-loop objectives. An initial activity will focus on revisiting the single-loop FCS architectures using contemporary-based design schemes to determine the upper limits of stability and performance that can be "achieved" with these powerful techniques. An important outcome of this phase will be to define minimum levels of control power that needs to exist for the rigid and elastic modes that are in the pilot and FCS bandwidth. Controller implementation and realizability issues will be given less emphasis in this phase. If stability and performance characteristics, and specific design strategies, look promising, these issues will be given more emphasis. The follow on activity addresses true multi-loop FCS. Conventional-based multi-loop FCS architectures do not typically exploit the full capabilities offered by cross channels and higher order filtering. The follow on thrust will utilize the contemporary-based design techniques with multiple feedback paths. Initially, the studies will consider only existing HSCT surfaces (elevator and wing trailing edge flaps). Follow on activities will consider the forward vane control input from objective 2. Practical considerations for FCS implementation will also be addressed. This task will support further assessment of the baseline configuration, as well as provide feasibility recommendations for FCS development.

The second task concerns the inner loop control power and controllability benefits afforded by a small, forward aerodynamic control surface. In previous preliminary multi-loop FCS studies,

existing HSCT wing trailing edge devices were considered as potential secondary surfaces to perform the aeroelastic suppression role. Results implied these surfaces are not favorably located throughout the vehicle for this role. Feedback loops using these surfaces were characterized by low damping augmentation sensitivity and simultaneous destabilization of elevator driven feedback loops. A forward control surface would appear to overcome these deficiencies and offer an attractive force/moment generator for aeroelastic suppression which works in harmony with the rigid pitch control loops. Inclusion of such capability in existing HSCT models is to be the initial activity. A linear "component build-up" modeling procedure will be used to expand the suite of HSCT control surfaces with a small, forward vane. Additional higher fidelity models supplied by the contracting agency can also be considered. Previous multi-loop FCS milestones will be revisited here using the forward vane. The new surface characteristics will require some modification and tuning of the earlier design. Analysis of merits and/or deficiencies of the new FCS which utilizes the forward surface, relative to the baseline architecture, will be addressed.

Quantifying the merits and/or deficiencies of inner loop FCS strategies will be an integral part of the above tasks. Metrics should address, where available and appropriate, closed-loop features such as augmented damping increments, bandwidth requirements, controllability, robustness levels, modal frequency separations, and handling/ride qualities.

HSCT flight control design activities face hard constraints and challenging hurdles. Conclusions and data from this study may provide valuable insight for future planning and decision making pertaining to HSCT configuration and FCS architecture development and definition.

#### **Deliverables:**

- Preliminary feasibility assessment and preliminary recommendation of selected inner loop FCS architectures presented in an oral briefing at the Aero Performance workshop. To include electronic and paper copies of vugraphs with written commentary in facing page text format. Boundaries and format shall be suitable for inclusion in a NASA CDCP. Feb, 1997
- Feasibility assessment and final recommendation of selected inner loop FCS architectures presented in an oral briefing. To include electronic and paper copies of vugraphs with written commentary in facing page text format. Fall, 1997
- Final report to include documentation of final results and findings in an HSR controlled distribution report suitable for submittal to HSR via the "salmon colored" report tracking card. Shall conform to NASA margin requirements and shall include all HSR-dictated data restriction notices in the margins and on the cover sheet as specified by the HSRPO. Sept, 1997
- Software used to perform analysis. Shall include documentation and preliminary user's guide. Software shall be well commented and legible. Sept, 1997



## Appendix B

### $M = 0.24 / h = 500 \text{ ft}$ Cycle 3.1a Model

This appendix describes the NASA Langley  $M = 0.24$ ,  $h = 500 \text{ ft}$  model generated from the Ref. H Cycle 3.1a Simulation. All variables are expressed with feet, second, and radian units.

Airframe states, inputs, and outputs are listed below.

$$x = \begin{bmatrix} u & w & q & \theta & \dot{\eta}_1 & \dots & \dot{\eta}_{17} & \eta_1 & \dots & \eta_{17} \end{bmatrix}^T$$

$$u = \begin{bmatrix} \delta_S & \delta_E & \delta_{TE1} & \delta_{TE2} & \delta_{TE3} & \delta_{TE4} \end{bmatrix}^T$$

$$y = \begin{bmatrix} q_{358} & q_{1900} & q_{2115} & q_{2152} & q_{2200} & a_{z\ 358} & a_{z\ 1900} & a_{z\ 2115} & a_{z\ 2152} & a_{z\ 2200} \end{bmatrix}^T$$

Actuator model data corresponding to Eq. (2.6) is tabulated below.

Actuator Data	p	$\omega$	$\zeta$
$\delta_S$	19.	190.	0.7071
$\delta_E$	22.	220.	0.7071
$\delta_{TE1}$	20.	200.	0.7071
$\delta_{TE2}$	21.	210.	0.7071
$\delta_{TE3}$	23.	230.	0.7071
$\delta_{TE4}$	24.	240.	0.7071

Note for this model, a single actuator drives left and right symmetric control surfaces. State space matrices listed below are defined in Eqs. (2.1)-(2.8).

A =

Columns 1 through 6

-5.1879e-03	4.9041e-02	-5.3845e+01	-3.1473e+01	-7.3748e-08	-1.4362e-06
-1.2392e-01	-6.1512e-01	2.4483e+02	-6.6932e+00	-6.3126e-05	-2.2454e-03
-2.7399e-04	1.4236e-03	-3.4273e-01	-6.5882e-05	2.6650e-05	-1.4373e-05
4.6810e-08	9.9134e-09	1.0000e+00	-4.8531e-20	0	0
-6.7396e+00	-8.5449e+01	-7.3969e+02	-1.0235e+01	-6.8438e-01	-5.1329e-01
-5.8658e+00	-6.3168e+01	3.7882e+02	-5.2713e+01	-2.8055e-01	-1.3981e+00
-1.3879e+01	-1.1664e+02	-2.8992e+03	-1.7084e+01	-2.1866e-01	-8.5742e-01
4.4919e+00	3.7536e+01	9.5729e+02	5.6363e+00	6.9540e-02	3.0064e-01
-4.7396e+00	-4.5350e+01	-9.6149e+02	-1.0236e+01	-1.1141e-01	-4.2691e-01
-8.2358e+00	-8.5827e+01	-2.2147e+03	-7.2326e+00	-1.8269e-01	-5.9318e-01



0	0	0	0	1.0000e+00	0
0	0	0	0	0	1.0000e+00
0	0	0	0	0	0
0	0	0	0	0	0
0	0	0	0	0	0
0	0	0	0	0	0
0	0	0	0	0	0
0	0	0	0	0	0
0	0	0	0	0	0
0	0	0	0	0	0
0	0	0	0	0	0

Columns 13 through 18

-1.4373e-06	-4.8561e-07	1.1202e-06	5.1881e-08	-5.7428e-07	-2.2825e-07
-2.2526e-03	-6.7780e-04	1.7812e-03	2.6727e-05	-9.0559e-04	-3.3555e-04
-1.7208e-05	3.7888e-05	2.6910e-05	-2.8044e-05	-9.7964e-06	8.9037e-06
0	0	0	0	0	0
1.0579e-01	-9.7756e-01	-3.7932e-01	8.3187e-01	2.5402e-01	-2.5979e-01
5.7349e-01	2.3046e-01	-5.9928e-01	4.3231e-01	6.7507e-01	4.2294e-02
-1.8392e-02	7.6462e-01	-2.0149e-01	-2.8609e-01	1.1816e-02	4.3719e-01
-1.7148e-02	-3.1385e-01	9.6629e-02	1.0135e-01	-2.6500e-02	-1.7164e-01
4.4762e-02	9.1077e-02	-2.1064e-01	1.6865e-01	1.1220e-01	1.3627e-01
-2.3344e-01	-6.9034e-01	-1.6654e-01	6.5012e-01	2.9435e-02	-5.8678e-02
4.9570e-01	5.2710e-01	-2.6899e-01	-1.2434e-01	2.2574e-01	1.6603e-01
1.5877e+00	-1.6502e+00	-1.7014e+00	1.9033e+00	1.3347e+00	-5.3067e-01
-1.4832e+00	-2.3853e-01	1.1583e+00	-2.8168e-01	-5.7538e-01	-2.2432e-01
-4.4625e-01	-2.7138e+00	5.2634e-01	4.9665e-01	-7.5493e-02	-1.0332e+00
7.8448e-02	5.8058e-01	-1.5224e+00	4.2870e-01	3.8731e-01	4.3364e-01
-2.1326e-01	-1.9958e-01	-1.0972e-02	-1.6652e+00	-6.6994e-01	4.8222e-01
-4.2231e-01	-8.6087e-01	4.5571e-01	-2.7499e-01	-2.0326e+00	9.7381e-02
-6.8786e-02	-4.7467e-01	1.0078e-02	1.8859e-01	3.0265e-01	-1.8235e+00
1.0763e-01	-1.0772e-02	1.0216e-01	-1.7664e-01	2.8672e-01	-3.2438e-01
1.3100e+00	2.5447e+00	-8.4031e-01	-6.5124e-01	1.7316e+00	4.4286e-01
-5.3041e-01	-1.1541e+00	2.5930e-01	3.4116e-01	-4.4146e-01	-4.2049e-01
0	0	0	0	0	0
0	0	0	0	0	0
0	0	0	0	0	0
0	0	0	0	0	0
0	0	0	0	0	0
0	0	0	0	0	0
0	0	0	0	0	0
0	0	0	0	0	0
0	0	0	0	0	0
1.0000e+00	0	0	0	0	0
0	1.0000e+00	0	0	0	0
0	0	1.0000e+00	0	0	0
0	0	0	1.0000e+00	0	0
0	0	0	0	1.0000e+00	0
0	0	0	0	0	1.0000e+00
0	0	0	0	0	0
0	0	0	0	0	0
0	0	0	0	0	0
0	0	0	0	0	0

Columns 19 through 24

-6.2233e-07	3.4617e-07	-1.2341e-07	6.3126e-06	-1.8776e-05	-8.1353e-06
-9.8174e-04	4.3410e-04	-1.5184e-04	9.7991e-03	-2.9041e-02	-1.2651e-02
-1.0818e-05	-5.2768e-05	2.0346e-05	2.6204e-05	-2.2952e-05	-4.5754e-05



Columns 31 through 36

253



Columns 7 through 12

255





Columns 7 through 12

Columns 13 through 18

257

0	0	0	0	0	1.0000e+00
0	0	0	-1.3824e+06	-6.5746e+04	-3.6341e+02

B<sub>a</sub> =

0	0	0	0	0	0
0	0	0	0	0	0
685900	0	0	0	0	0
0	0	0	0	0	0
0	0	0	0	0	0
0	2129600	0	0	0	0
0	0	0	0	0	0
0	0	0	0	0	0
0	0	1600000	0	0	0
0	0	0	0	0	0
0	0	0	1852200	0	0
0	0	0	0	0	0
0	0	0	0	0	0
0	0	0	0	2433400	0
0	0	0	0	0	0
0	0	0	0	0	0
0	0	0	0	0	2764800

C =

Columns 1 through 6

0	0	1.0000e+00	0	1.9940e-04	-1.6837e-04
0	0	1.0000e+00	0	-1.1167e-05	3.9885e-05
0	0	1.0000e+00	0	-3.8027e-05	6.1231e-05
0	0	1.0000e+00	0	-3.3775e-05	6.0645e-05
0	0	1.0000e+00	0	-4.1293e-05	6.2995e-05
4.1720e-02	3.1053e-01	-4.3998e+01	1.0222e-02	-2.6491e-03	1.3019e-03
1.4003e-01	8.9444e-01	1.7973e+01	-1.7806e-01	2.4496e-03	5.4952e-05
1.1468e-01	5.8851e-01	2.6451e+01	-2.3320e-01	6.3667e-04	8.3794e-04
1.0788e-01	5.1164e-01	2.7938e+01	-2.4849e-01	2.1842e-04	9.5438e-04
9.9633e-02	4.1771e-01	2.9468e+01	-2.6127e-01	-2.8529e-04	1.1260e-03

Columns 7 through 12

1.6588e-04	-5.4117e-05	-4.6642e-05	-2.8092e-04	2.5860e-04	1.9031e-04
-5.8335e-05	1.8402e-05	1.5809e-05	8.6460e-05	-5.4346e-05	6.1394e-06
-6.0117e-05	1.9030e-05	8.9343e-06	3.4980e-05	2.6039e-05	4.9845e-05
-6.4397e-05	1.9924e-05	1.0797e-05	4.5999e-05	1.4329e-05	4.5521e-05
-6.0888e-05	1.9171e-05	8.0922e-06	2.9043e-05	3.5668e-05	5.5654e-05
-2.0308e-03	6.5161e-04	2.4937e-04	2.1329e-03	-1.9877e-03	-1.1709e-03
-2.2803e-03	8.6985e-04	5.8743e-04	4.8837e-03	-3.9439e-03	-4.6871e-04
-3.2684e-03	1.1553e-03	1.5707e-04	3.0564e-03	-1.7768e-03	-7.5063e-05
-3.4768e-03	1.2119e-03	4.0224e-05	2.5534e-03	-1.2328e-03	-4.0639e-05
-3.6763e-03	1.2614e-03	-1.0029e-04	1.8936e-03	-5.2104e-04	4.8660e-05

Columns 13 through 18

5.6041e-04	-4.2983e-05	5.0418e-04	4.2963e-04	-9.9955e-05	6.1936e-04
1.0603e-04	-3.0990e-05	1.3081e-04	4.1265e-05	-1.1476e-05	-5.9456e-05

1.6499e-04	-3.3396e-05	-2.3558e-05	-1.4266e-04	2.0182e-05	-1.4972e-04
1.7174e-04	-3.9399e-05	7.6347e-06	-1.3048e-04	1.6610e-05	-1.6541e-04
1.6388e-04	-4.2011e-05	-4.5524e-05	-1.5924e-04	1.5578e-05	-1.3664e-04
-4.8267e-03	-5.1457e-04	-2.8675e-03	-2.5673e-03	1.2727e-04	-4.0172e-03
2.1986e-03	2.8161e-03	3.3573e-03	2.2149e-03	8.8810e-04	1.8119e-03
3.5753e-03	-2.0876e-04	2.8654e-03	3.0614e-05	2.1956e-04	-1.8578e-03
3.7285e-03	-9.9576e-04	2.6942e-03	-5.1477e-04	1.8253e-05	-2.7110e-03
3.8431e-03	-1.9299e-03	2.3360e-03	-1.2965e-03	-2.8112e-04	-3.5979e-03

Columns 19 through 24

1.7871e-04	-2.4977e-04	-4.0211e-04	0	0	0
-2.4860e-05	3.8578e-05	2.5607e-05	0	0	0
-1.1269e-05	6.1281e-06	-1.0314e-04	0	0	0
-1.3560e-05	1.6158e-05	-1.0718e-04	0	0	0
-1.4100e-07	1.6653e-07	-1.1658e-04	0	0	0
-1.2753e-03	3.4300e-03	2.1742e-03	-6.8476e-01	9.6879e-01	-1.3706e+00
-5.8451e-04	-6.3503e-03	4.5114e-03	1.8872e-01	-3.4652e-01	1.0303e-01
-1.1430e-03	-1.1783e-03	4.5487e-04	1.5852e-01	-2.1774e-01	-1.8924e-01
-1.2016e-03	2.0701e-04	-6.8132e-04	1.5276e-01	-1.9283e-01	-2.4748e-01
-1.1609e-03	1.9086e-03	-2.0915e-03	1.4463e-01	-1.5949e-01	-3.1990e-01

Columns 25 through 30

0	0	0	0	0	0
0	0	0	0	0	0
0	0	0	0	0	0
0	0	0	0	0	0
0	0	0	0	0	0
4.5641e-01	4.4787e-01	2.9212e+00	-3.1186e+00	-2.7537e+00	-9.3880e+00
-3.4552e-02	5.2653e-02	5.7777e-01	-1.2034e+00	-1.4249e+00	-4.3584e+00
6.2410e-02	1.2124e-01	9.7292e-01	-1.2439e+00	-8.8327e-01	-1.0545e+00
8.1252e-02	1.3248e-01	1.0339e+00	-1.2199e+00	-7.6383e-01	-3.6765e-01
1.0477e-01	1.4486e-01	1.0949e+00	-1.1587e+00	-5.9339e-01	4.8290e-01

Columns 31 through 36

0	0	0	0	0	0
0	0	0	0	0	0
0	0	0	0	0	0
0	0	0	0	0	0
0	0	0	0	0	0
8.1632e-01	-9.5682e+00	-8.3856e+00	2.0152e+00	-1.2911e+01	-3.9200e+00
-6.0565e-01	4.7198e+00	9.8296e+00	-2.2983e+00	7.9594e+00	8.1947e-01
-1.6571e+00	5.9338e+00	4.9768e+00	-1.7926e+00	4.0280e-02	-6.3717e-01
-1.8894e+00	6.0112e+00	3.8323e+00	-1.6385e+00	-1.8695e+00	-8.1443e-01
-2.2045e+00	5.8455e+00	2.1582e+00	-1.4495e+00	-4.0729e+00	-8.9027e-01

Columns 37 through 38

0	0
0	0
0	0
0	0
0	0
6.1415e+00	1.0731e+01
7.4498e-01	7.5462e+00
2.4883e+00	3.5405e+00

```

2.8190e+00  2.1479e+00
3.0854e+00  2.2282e-01

```

$\hat{C} =$

Columns 1 through 6

```

      0      0      0      0      0      0
      0      0      0      0      0      0
      0      0      0      0      0      0
      0      0      0      0      0      0
      0      0      0      0      0      0
-1.1154e+01 -1.1152e-01 -1.6383e-03 -3.2728e-02 -2.0443e-03 -2.7292e-04
-5.3233e-01 -2.3101e-01 -5.2585e-05 -1.3392e-02 -6.8538e-02  1.2170e-03
 3.1653e+00  1.7564e-02  4.2759e-05  4.5331e-01 -1.7756e-02  8.3477e-04
 4.1118e+00  8.6003e-02  1.2533e-04  5.9109e-01 -4.7627e-03  7.4682e-04
 5.3000e+00  1.5797e-01  1.3182e-04  7.4081e-01  8.0151e-03  6.1700e-04

```

Columns 7 through 12

```

      0      0      0      0      0      0
      0      0      0      0      0      0
      0      0      0      0      0      0
      0      0      0      0      0      0
      0      0      0      0      0      0
-1.5100e+00  3.0869e-02  1.0140e-03  5.7530e-01  4.5438e-02 -5.0114e-04
 8.3614e-01 -9.9258e-02  1.5011e-02  1.8640e+00 -1.8093e-01  1.1083e-02
 4.2586e+00  3.3966e-01  1.3923e-02  4.0809e+00  8.9521e-02  9.0245e-03
 4.9639e+00  4.4524e-01  1.3269e-02  4.5329e+00  1.5657e-01  8.3050e-03
 5.8523e+00  5.7529e-01  1.2450e-02  5.1276e+00  2.4004e-01  7.4114e-03

```

Columns 13 through 18

```

      0      0      0      0      0      0
      0      0      0      0      0      0
      0      0      0      0      0      0
      0      0      0      0      0      0
      0      0      0      0      0      0
-9.6688e-01  5.9713e-02 -1.5943e-03  3.5006e-01  6.7356e-02 -1.3184e-03
 1.3990e+00 -2.4834e-01  1.0691e-02  4.9105e-01 -2.0509e-01  7.1067e-03
 6.0328e-01 -1.1992e-01  6.6073e-03 -3.5816e-01 -7.7047e-02  4.1190e-03
 3.9188e-01 -8.2218e-02  5.4741e-03 -5.4671e-01 -4.0823e-02  3.2965e-03
 2.4956e-01 -3.4050e-02  4.1418e-03 -7.5688e-01  1.2773e-03  2.3268e-03

```

## Appendix C

### $M = 0.24 / h = 0 \text{ ft}$ Cycle 1/ISAC Model

This appendix describes the NASA Langley  $M = 0.24$ ,  $h = 0 \text{ ft}$  model generated from the Ref. H Cycle 1/ISAC Simulation. All variables are expressed with feet, second, and radian units except structural axes coordinates and mode shape/slope deflections which utilize inch. Airframe states, inputs, and outputs are listed below.

$$x = \left[ u \ w \ q \ \theta \ \dot{\eta}_1 \ \dots \ \dot{\eta}_{17} \ \eta_1 \ \dots \ \eta_{17} \ z_1 \ \dots \ z_{10} \right]^T$$

$$u = \left[ \delta_S \ \delta_E \ \delta_V \ \delta_{TE1} \ \delta_{TE2} \ \delta_{TE3} \ \delta_{TE4} \right]^T$$

$$d = w_G$$

$$y = \left[ \dots q_{xs} \dots \dots a_{z \ xs} \dots \right]^T$$

Measured pitch rates and vertical accelerations are calculated from

$$q_{xs} = q - \sum_{i=1}^{17} \phi_i'(x_s) \dot{\eta}_i$$

$$a_{z \ xs} = \dot{w} - x_B \dot{q} - Uq - \sum_{i=1}^{17} \phi_i(x_s) \ddot{\eta}_i$$

$$\phi_i(x_s) = C_{\phi_i} \bar{x}_s$$

$$\phi_i'(x_s) = \frac{d \phi_i(x_s)}{dx_s}$$

where  $C_{\phi_i}$  is the  $i^{\text{th}}$  row of  $C_\phi$  and

$$\bar{x}_s = [x_s^{10} \ x_s^9 \ \dots \ x_s \ 1]^T$$

$C_\phi$  represents a polynomial curve fit to the mode shapes ( $\phi_i$ ) which allows pitch rates and vertical accelerations to be computed at any point along the fuselage centerline. The state space C, D, D', D'', and  $D_d$  matrices can be easily constructed from the above description. In the above expressions, the sensor is mounted at the body axes location  $x_B$ , and U denotes the forward body

axes trimmed flight speed component. Actuator model data corresponding to Eq. (2.6), and gust turbulence model data corresponding to Eq. (2.9), is tabulated below.

Actuator Data	p	$\omega$	$\zeta$
$\delta_S$	19.	190.	0.7071
$\delta_E$	22.	220.	0.7071
$\delta_V$	22.	220.	0.7071
$\delta_{TE1}$	20.	200.	0.7071
$\delta_{TE2}$	21.	210.	0.7071
$\delta_{TE3}$	23.	230.	0.7071
$\delta_{TE4}$	24.	240.	0.7071

Gust Turbulence Data	$\sigma_{wG}$	L	$V_T$	k	$z_1$	$z_2$	P1	P2	P3
wG	1.	2500.	267.9	0.4079	0.04094	0.8257	0.05145	0.1302	1.194

Note for this model, a single actuator drives both left and right symmetric control surfaces. State space matrices defined in Eqs. (2.1)-(2.10) and  $C_\phi$  are listed below.

A =

Columns 1 through 6

5.9489e-04	2.1308e-02	-4.1438e+01	-3.1782e+01	0	0
-1.4249e-01	-1.0812e+00	2.5063e+02	0	4.4062e-04	-2.3471e-03
-1.5018e-04	-1.8238e-02	-8.3968e-02	0	-7.1923e-07	-1.2275e-05
0	0	1.0000e+00	0	0	0
0	-5.8016e+01	-2.1366e+02	0	-3.1696e-01	7.9866e-01
0	-7.8996e+01	-3.3229e+03	0	4.5412e-01	-1.2659e+00
0	-1.4208e+02	-2.3133e+02	0	1.3484e-02	-1.0384e+00
0	-4.7866e+01	-1.8416e+02	0	1.0231e-02	-3.5376e-01
0	2.6580e+01	2.0421e+03	0	-1.1230e-01	3.9269e-01
0	-2.8096e+01	-7.0839e+03	0	3.3803e-01	-3.2240e-01
0	-4.1414e+01	-3.5274e+03	0	1.2018e-01	6.9592e-02
0	2.3729e+00	-2.1190e+03	0	-1.0035e-01	1.8198e-01
0	-3.5075e+01	2.6666e+03	0	-7.5154e-03	-6.7766e-01
0	2.5373e+02	6.8524e+03	0	-5.1365e-02	3.3286e-01
0	-1.1031e+02	-5.6936e+03	0	-2.6779e-01	5.6236e-01
0	2.5193e+02	6.6340e+03	0	1.0339e-01	-3.7091e-01
0	9.8379e+00	4.5101e+03	0	2.6557e-01	-5.6127e-01
0	9.8179e+00	-3.2552e+03	0	-2.7956e-02	-1.2971e-01
0	1.3641e+01	5.1642e+02	0	-1.1640e-02	2.6579e-01
0	-9.5650e+01	-3.9555e+03	0	3.4232e-01	-3.0837e-01
0	1.9257e+01	2.6607e+03	0	-2.0758e-01	1.6640e-01
0	0	0	0	1.0000e+00	0
0	0	0	0	0	1.0000e+00
0	0	0	0	0	0
0	0	0	0	0	0
0	0	0	0	0	0
0	0	0	0	0	0
0	0	0	0	0	0

0	0	0	0	0	0
0	0	0	0	0	0
0	0	0	0	0	0
0	0	0	0	0	0
0	0	0	0	0	0
0	0	0	0	0	0
0	0	0	0	0	0
0	0	0	0	0	0
0	0	0	0	0	0
0	0	0	0	0	0
0	5.0274e-01	-8.4015e+00	0	1.0870e-02	1.9733e-02
0	8.6196e-01	3.2999e+02	0	-1.6020e-01	-3.7630e-01
0	-6.1473e+01	-7.0734e+02	0	-1.0947e-01	3.0905e-01
0	2.8760e+02	3.7594e+03	0	4.9659e-01	-3.6739e-01
0	-1.8644e+02	4.0003e+03	0	2.2756e-01	-1.2203e+00
0	-3.5938e+02	-6.7843e+03	0	5.4455e-01	-1.2685e-01
0	-1.2347e+02	-2.3769e+03	0	5.1268e-01	7.2126e-01
0	-7.9291e+02	-2.6798e+04	0	3.6005e+00	-1.1180e+00
0	-2.6492e+02	-7.1313e+04	0	3.9221e+00	4.8925e+00
0	-2.6749e+03	9.3293e+02	0	4.8022e+00	2.2209e-01

Columns 7 through 12

0	0	0	0	0	0
-1.0441e-03	-4.7593e-04	5.1136e-04	1.9860e-04	3.1024e-04	1.7113e-02
-8.7379e-06	-4.4627e-06	2.5422e-06	2.7352e-06	-9.2798e-07	3.8823e-04
0	0	0	0	0	0
-8.6001e-02	-1.1747e-02	-1.3371e-01	1.9847e-01	-2.0533e-01	-1.2101e+00
-1.2424e+00	-4.7972e-01	4.6727e-01	-2.5850e-02	3.7041e-01	1.9978e+00
-1.7683e+00	-5.4009e-01	5.6387e-01	-1.7793e-01	1.6647e-01	1.1044e+00
-5.0591e-01	-5.3792e-01	1.9920e-01	-6.2051e-02	6.1967e-02	3.8293e-01
5.5670e-01	2.0653e-01	-6.1257e-01	8.0879e-02	-1.3786e-01	-2.1587e-01
-5.6630e-01	-1.9822e-01	2.0739e-01	-5.1239e-01	1.6298e-01	2.4959e-01
4.5862e-02	2.2505e-02	-5.4231e-02	1.0083e-01	-6.2477e-01	-6.4407e-02
-2.9916e-01	-1.0243e-01	-5.2085e-02	3.8312e-01	-4.0457e-03	-3.8735e+00
2.9587e-02	-6.2427e-03	1.5925e-02	1.1216e-01	1.6338e-01	1.0872e+00
4.9384e-01	1.7775e-01	-5.8308e-02	-2.7323e-01	2.0244e-01	-1.3912e+00
1.1313e-01	5.4052e-02	-4.4141e-02	-6.5123e-02	-1.8631e-01	-3.2109e-02
2.2069e-01	7.3669e-02	1.8528e-02	-1.5453e-01	1.3154e-01	-1.3084e+00
-1.2922e-01	-5.3835e-02	1.0181e-01	-1.0495e-01	1.2720e-01	1.3976e+00
-2.8710e-01	-1.0301e-01	6.8673e-02	6.1879e-02	-9.5318e-02	-1.1410e+00
1.5704e-01	7.1691e-02	-3.6605e-02	-1.4852e-01	-3.5587e-02	-9.5331e-02
-8.1519e-01	-2.4968e-01	2.9102e-01	-4.9902e-01	-1.3954e-01	6.7767e-02
4.5076e-01	1.4709e-01	-1.3978e-01	1.4064e-01	7.0221e-02	3.3394e-01
0	0	0	0	0	0
0	0	0	0	0	0
1.0000e+00	0	0	0	0	0
0	1.0000e+00	0	0	0	0
0	0	1.0000e+00	0	0	0
0	0	0	1.0000e+00	0	0
0	0	0	0	1.0000e+00	0
0	0	0	0	0	1.0000e+00
0	0	0	0	0	0
0	0	0	0	0	0
0	0	0	0	0	0
0	0	0	0	0	0
0	0	0	0	0	0
0	0	0	0	0	0
0	0	0	0	0	0
0	0	0	0	0	0

0	0	0	0	0	0
0	0	0	0	0	0
0	0	0	0	0	0
-6.4576e-02	-2.3055e-02	-4.6117e-03	4.6993e-02	3.3040e-02	-5.1215e-02
5.2193e-01	1.6784e-01	4.6369e-02	-1.6794e-01	2.1601e-01	1.0131e+00
3.1263e-01	1.3671e-01	6.1207e-02	-6.2795e-01	-1.0173e+00	-1.0026e+00
-1.0992e+00	-3.9282e-01	-3.8935e-01	1.9763e+00	2.6149e+00	6.6115e+00
6.7413e-01	1.5754e-01	1.5947e-01	-1.1183e+00	-2.9486e-01	9.9624e+00
6.6493e-01	2.1482e-01	2.2968e-01	-1.5844e+00	-1.4616e+00	1.0493e+00
-1.8519e-01	-3.0157e-02	-4.1860e-03	5.5422e-02	-5.2063e-01	-2.1455e+00
1.1693e+00	3.3250e-01	2.6711e-01	-4.3147e+00	-1.7979e+00	7.7710e+00
-2.8950e+00	-8.6880e-01	-1.6836e-01	1.6101e+00	-9.6289e-01	-2.0033e+00
-1.7876e-01	-2.2370e-01	-4.6449e-03	-6.6874e-01	-1.0274e+00	8.9590e+01

Columns 13 through 18

0	0	0	0	0	0
1.1027e-02	-2.5255e-05	-1.8455e-03	-4.0819e-05	1.3165e-03	-4.4495e-04
2.4990e-04	1.3435e-05	-4.1450e-05	-5.6930e-06	6.5372e-06	-8.2031e-06
0	0	0	0	0	0
-3.6008e-01	-3.6091e-01	5.4676e-01	-7.1170e-01	-6.8539e-01	2.0149e-01
1.7375e+00	-7.8333e-01	-1.1729e+00	2.1551e-01	1.1214e+00	1.3059e-01
1.4137e+00	-1.5363e+00	-7.0810e-01	-3.6274e-01	6.3973e-01	6.4425e-01
5.0333e-01	-5.6495e-01	-2.7067e-01	-1.2692e-01	2.3196e-01	2.4071e-01
-2.7864e-01	4.5395e-01	3.4951e-01	-5.4146e-02	-3.1855e-01	-2.1185e-01
-7.7151e-02	2.6398e-02	-3.6480e-01	3.1348e-01	3.1993e-01	5.8684e-02
-3.6986e-01	3.1838e-01	2.2034e-01	1.9451e-03	-1.1567e-01	-1.6427e-01
-1.6003e+00	-1.8150e+00	1.8118e+00	-2.0429e+00	-1.3320e+00	5.4609e-01
-1.8244e-01	-6.6307e-02	6.8710e-01	-3.7381e-01	-1.2738e-01	-2.5683e-01
-8.2364e-01	-1.9287e+00	-1.7325e-02	-2.6702e-01	-4.4797e-01	8.0945e-01
-4.2677e-02	-8.3157e-02	-1.4315e+00	5.0515e-01	8.8786e-02	3.6394e-01
-1.0984e+00	-1.7216e-01	3.8865e-01	-1.7471e+00	-5.2257e-01	4.1052e-01
6.5880e-01	3.3540e-01	9.7539e-02	-3.7913e-01	-1.4876e+00	5.7409e-02
-6.1120e-01	3.3119e-02	1.4459e-01	6.5507e-02	3.6151e-01	-1.6276e+00
-2.1812e-01	7.3373e-02	-6.1991e-02	1.8913e-01	-3.7677e-01	3.3479e-01
-5.2127e-01	9.5078e-01	3.9049e-01	2.1628e-01	-9.3815e-01	-2.2041e-02
5.0908e-01	-4.0322e-01	-1.3048e-01	-1.0723e-01	1.2635e-01	2.1247e-01
0	0	0	0	0	0
0	0	0	0	0	0
0	0	0	0	0	0
0	0	0	0	0	0
0	0	0	0	0	0
0	0	0	0	0	0
0	0	0	0	0	0
0	0	0	0	0	0
0	0	0	0	0	0
0	0	0	0	0	0
1.0000e+00	0	0	0	0	0
0	1.0000e+00	0	0	0	0
0	0	1.0000e+00	0	0	0
0	0	0	1.0000e+00	0	0
0	0	0	0	1.0000e+00	0
0	0	0	0	0	1.0000e+00
0	0	0	0	0	0
0	0	0	0	0	0
0	0	0	0	0	0
0	0	0	0	0	0
4.3539e-02	-4.2040e-02	-3.8771e-02	-5.0614e-02	-1.0846e-02	-1.2448e-02
3.0797e-02	-1.3013e-01	2.1032e-02	6.1924e-01	5.9149e-01	3.1094e-02
-1.0921e+00	5.9243e-01	3.7703e-01	-2.4342e-01	-6.8003e-01	5.2032e-01
4.9573e+00	1.2436e+00	-1.3153e-02	4.3299e-01	1.2582e+00	-2.8783e+00



6.9899e+00	-2.5719e+00	-4.6741e-01	-5.4233e-01	9.0328e-01	7.0160e-02
2.6866e-01	-1.4613e+00	-1.7574e-01	-1.1025e-01	-5.6022e-01	1.1310e+00
-1.9129e+00	8.1748e-01	7.3412e-02	-3.7964e-02	3.5500e-02	-4.1469e-01
6.5650e+00	-1.7105e+00	-1.7710e+00	-7.4774e-01	-1.7037e+00	-2.9915e-02
-2.8062e+00	4.7038e-01	-1.1856e-01	-9.3840e-01	-1.9088e+00	2.1388e-01
5.5113e+01	4.2794e+00	-7.1330e+00	-2.1585e+00	2.6753e+00	-5.3698e+00

Columns 19 through 24

0	0	0	0	0	0
1.6807e-03	1.1113e-02	-3.1438e-03	-9.8583e-03	-2.1697e-02	-7.2984e-03
1.6594e-05	1.5379e-04	-3.8848e-05	-2.7333e-05	2.0741e-05	1.3973e-05
0	0	0	0	0	0
-1.7635e-01	-9.3520e-01	2.2755e-01	-5.7663e+01	6.0515e+00	1.5702e+00
2.6618e-01	4.2018e+00	-1.4793e+00	1.0686e+00	-1.6057e+02	-5.6484e+00
-1.9271e-02	3.8112e+00	-1.4936e+00	-1.6858e+00	-7.3223e+00	-2.8754e+02
-2.1648e-02	1.3618e+00	-5.4393e-01	-5.1485e-01	-2.3028e+00	-1.2878e-01
6.0821e-02	-1.2279e+00	5.5189e-01	2.4891e-01	2.0718e+00	2.3343e+00
-3.1355e-02	7.6798e-01	-4.0551e-01	-1.6557e-01	-2.6304e+00	-7.6076e+00
2.1078e-01	-9.2006e-02	1.1018e-01	-1.2525e-01	-8.9143e-01	-3.2016e+00
4.7959e-02	4.9430e-02	-1.7825e-01	1.1737e+00	-1.7185e+00	1.7030e+00
5.7806e-01	1.0317e+00	-1.1023e-01	-1.2318e+00	-5.7637e+00	-1.1473e+00
-1.1473e+00	-1.9839e+00	6.7291e-02	2.2538e+00	6.6065e+00	7.3587e+00
-5.8636e-01	-1.1038e+00	9.3810e-02	-1.3009e+00	3.5619e+00	2.4416e+00
1.3384e-02	-2.5068e-01	-8.8919e-02	1.7902e-01	-2.7795e+00	2.5919e+00
1.7264e-01	6.3917e-02	-2.5121e-02	1.9066e-01	-6.3177e+00	-3.1861e+00
4.5334e-01	9.2548e-01	4.5209e-02	-1.4366e+00	-2.3622e+00	-2.1640e+00
-2.0152e+00	-2.3122e+00	4.5187e-01	3.3039e-01	5.4742e-02	-3.3008e-01
-8.0078e-01	-6.1749e+00	1.5019e+00	-1.4475e+00	-1.6717e+01	-1.6499e+01
-2.7941e-03	1.0419e+00	-1.7889e+00	4.6019e-01	5.9492e+00	7.9800e+00
0	0	0	0	0	0
0	0	0	0	0	0
0	0	0	0	0	0
0	0	0	0	0	0
0	0	0	0	0	0
0	0	0	0	0	0
0	0	0	0	0	0
0	0	0	0	0	0
0	0	0	0	0	0
0	0	0	0	0	0
0	0	0	0	0	0
0	0	0	0	0	0
0	0	0	0	0	0
0	0	0	0	0	0
0	0	0	0	0	0
0	0	0	0	0	0
0	0	0	0	0	0
0	0	0	0	0	0
0	0	0	0	0	0
1.0000e+00	0	0	0	0	0
0	1.0000e+00	0	0	0	0
0	0	1.0000e+00	0	0	0
1.9768e-02	1.2190e-01	-7.5640e-02	0	0	0
1.7947e-01	1.0697e+00	-1.8981e-01	0	0	0
-5.4807e-01	-2.7616e+00	1.1847e+00	0	0	0
1.2436e+00	1.0950e+00	2.9058e-01	0	0	0
1.3966e+00	8.0582e+00	-2.8129e+00	0	0	0
-2.8869e-03	2.5204e+00	-1.6530e+00	0	0	0
-1.5214e-01	-2.8884e+00	1.3550e+00	0	0	0
8.1616e-01	4.8504e+00	-3.5551e+00	0	0	0
-1.0261e+00	-8.9203e-01	-1.2996e+00	0	0	0
3.8606e+00	2.2522e+01	-2.7545e+00	0	0	0

[illegible][illegible][illegible][illegible]

Columns 37 through 42

267

Columns 43 through 48

268

$$\hat{A} =$$

-4.1790e-01	0	0	-4.2796e-01	0	0
-1.3286e+01	-3.6235e-01	-4.8357e-03	-2.1582e+00	2.1105e-02	-1.2991e-03
-3.0693e-01	-1.1966e-02	-1.8788e-04	-7.0595e-02	-1.2823e-03	-2.2137e-05
0	0	0	0	0	0
-4.7762e+03	-5.0626e+02	-7.5876e+00	-4.0604e+03	-1.3613e+02	-1.2154e+00
2.3340e+03	3.3359e+02	3.9252e+00	2.5850e+03	8.5826e+01	8.9500e-01
-2.4924e+03	-2.3854e+02	-3.6136e+00	-2.0286e+03	-5.5991e+01	-9.3193e-01
-8.3934e+02	-8.0728e+01	-1.2421e+00	-6.8974e+02	-1.9360e+01	-3.0839e-01
-1.9137e+02	-4.8321e+01	-5.1339e-01	-3.4643e+02	-1.3904e+01	-9.3009e-02
1.2119e+03	2.3652e+02	2.9854e+00	1.8715e+03	6.6480e+01	6.7954e-01
-2.5900e+02	-1.2235e+01	-3.4601e-01	-1.9086e+02	-5.8778e+00	3.7657e-02
8.9196e+02	-1.0457e+03	-1.7381e+01	-1.0736e+04	-4.3033e+02	-2.9172e+00
3.6815e+03	-1.1053e+02	-2.5297e+00	-1.8711e+03	-9.2314e+01	-6.7493e-01
9.4767e+03	1.1436e+02	6.1831e-02	-3.1457e+02	-9.7201e+01	4.5704e-01
-1.0263e+04	-2.6955e+02	-1.8775e+00	-1.0017e+03	5.3107e+01	-5.2362e-01
1.2935e+04	3.0306e+02	2.8879e+00	1.8563e+03	-8.6922e+01	4.0814e-01
7.6461e+03	2.2724e+02	2.1756e+00	1.7076e+03	-4.0999e+01	4.5612e-02
-2.2164e+03	-3.3292e+01	-3.5436e-01	-5.9616e+02	3.4254e+01	2.1683e-01
-1.8539e+01	7.3433e-01	-7.6920e-03	1.5631e-01	1.4049e+00	1.5519e-02
-2.9351e+02	2.2380e+01	-4.6192e-01	-9.1487e+01	9.4009e+00	-1.9353e-01
-1.8225e+01	-4.9810e+01	-3.4997e-01	-7.2696e+01	-2.6935e+01	-1.7156e-01
0	0	0	0	0	0
0	0	0	0	0	0

0	0	0	0	0	0
0	0	0	0	0	0
0	0	0	0	0	0
0	0	0	0	0	0
0	0	0	0	0	0
0	0	0	0	0	0
0	0	0	0	0	0
0	0	0	0	0	0
0	0	0	0	0	0
0	0	0	0	0	0
0	0	0	0	0	0
0	0	0	0	0	0
0	0	0	0	0	0
0	0	0	0	0	0
0	0	0	0	0	0
0	0	0	0	0	0
0	-6.0022e+00	0	0	-4.9040e+00	0
0	3.1817e+01	0	0	2.8501e+01	0
0	4.3841e+01	0	0	2.7036e+01	0
0	-4.8896e+01	0	0	3.4873e+01	0
0	-1.0344e+02	0	0	-1.4355e+02	0
0	-1.9748e+01	0	0	-1.2306e+02	0
0	2.9647e+01	0	0	2.6433e+01	0
0	-1.3342e+02	0	0	-2.3578e+02	0
0	2.1818e+02	0	0	-1.6747e+02	0
0	2.4946e+02	0	0	-1.8617e+02	0

Columns 7 through 12

0	0	0	2.8499e-01	0	0
-2.4285e+00	0	0	-7.2392e+00	-8.2180e-02	-8.6334e-03
9.6527e-02	0	0	1.9046e-02	1.1132e-02	-2.0913e-04
0	0	0	0	0	0
-3.7183e+03	0	0	2.2386e+03	2.3225e+02	-1.2552e+00
-1.9350e+03	0	0	-1.1406e+03	1.2703e+02	-6.7353e+00
1.4492e+03	0	0	7.7170e+02	7.7893e+01	2.8020e+00
4.6036e+02	0	0	2.7788e+02	3.1669e+01	8.0396e-01
3.5372e+02	0	0	4.9169e+02	-1.5562e+01	1.4263e+00
-1.9682e+03	0	0	-1.8882e+03	1.9397e+01	-5.6312e+00
-1.5374e+03	0	0	-3.9015e+02	6.5101e+01	-2.4882e+00
-8.2493e+02	0	0	-3.5020e+02	6.6446e+01	-2.7240e+00
1.8122e+03	0	0	-2.2351e+03	-1.2986e+02	-1.4544e+00
5.4043e+01	0	0	-1.2966e+03	-1.5998e+02	-4.1089e+00
9.1599e+02	0	0	2.0641e+03	9.7938e+01	3.7692e+00
4.1833e+02	0	0	-1.3780e+03	-1.5029e+02	-1.9263e+00
-1.0465e+02	0	0	-1.6814e+03	-6.5638e+01	-2.9720e+00
5.1265e+02	0	0	7.7960e+02	5.2839e+01	2.5710e+00
-1.8079e+02	0	0	1.5133e+02	2.5919e-01	3.8916e-01
2.1740e+02	0	0	-8.8359e+02	6.9505e+01	-1.5553e+00
3.7251e+02	0	0	-7.7078e+01	-6.6315e+01	-2.3912e-01
0	0	0	0	0	0
0	0	0	0	0	0
0	0	0	0	0	0
0	0	0	0	0	0
0	0	0	0	0	0
0	0	0	0	0	0
0	0	0	0	0	0
0	0	0	0	0	0
0	0	0	0	0	0
0	0	0	0	0	0

Columns 13 through 18

271

Columns 19 through 21

272



0	1.4187e+02	0
0	-5.8025e+02	0
0	-1.3681e+02	0
0	-1.8836e+03	0

A<sub>a</sub> =

Columns 1 through 6

0	1.0000e+00	0	0	0	0
0	0	1.0000e+00	0	0	0
-6.8590e+05	-4.1205e+04	-2.8770e+02	0	0	0
0	0	0	0	1.0000e+00	0
0	0	0	0	0	1.0000e+00
0	0	0	-1.0648e+06	-5.5244e+04	-3.3310e+02
0	0	0	0	0	0
0	0	0	0	0	0
0	0	0	0	0	0
0	0	0	0	0	0
0	0	0	0	0	0
0	0	0	0	0	0
0	0	0	0	0	0
0	0	0	0	0	0
0	0	0	0	0	0
0	0	0	0	0	0
0	0	0	0	0	0
0	0	0	0	0	0
0	0	0	0	0	0
0	0	0	0	0	0
0	0	0	0	0	0
0	0	0	0	0	0
0	0	0	0	0	0
0	0	0	0	0	0

Columns 7 through 12

0	0	0	0	0	0
0	0	0	0	0	0
0	0	0	0	0	0
0	0	0	0	0	0
0	0	0	0	0	0
0	0	0	0	0	0
0	1.0000e+00	0	0	0	0
0	0	1.0000e+00	0	0	0
-1.0648e+06	-5.5245e+04	-3.3312e+02	0	0	0
0	0	0	0	1.0000e+00	0
0	0	0	0	0	1.0000e+00
0	0	0	-8.0000e+05	-4.5656e+04	-3.0280e+02
0	0	0	0	0	0
0	0	0	0	0	0
0	0	0	0	0	0
0	0	0	0	0	0
0	0	0	0	0	0
0	0	0	0	0	0
0	0	0	0	0	0
0	0	0	0	0	0
0	0	0	0	0	0
0	0	0	0	0	0
0	0	0	0	0	0
0	0	0	0	0	0
0	0	0	0	0	0
0	0	0	0	0	0

Columns 13 through 18

0	0	0	0	0	0
0	0	0	0	0	0
0	0	0	0	0	0
0	0	0	0	0	0
0	0	0	0	0	0
0	0	0	0	0	0
0	0	0	0	0	0
0	0	0	0	0	0
0	0	0	0	0	0
0	0	0	0	0	0
0	0	0	0	0	0
0	0	0	0	0	0
0	1.0000e+00	0	0	0	0
0	0	1.0000e+00	0	0	0
-9.2610e+05	-5.0336e+04	-3.1790e+02	0	0	0
0	0	0	0	1.0000e+00	0
0	0	0	0	0	1.0000e+00
0	0	0	-1.2167e+06	-6.0380e+04	-3.4830e+02
0	0	0	0	0	0
0	0	0	0	0	0
0	0	0	0	0	0

Columns 19 through 21

0	0	0
0	0	0
0	0	0
0	0	0
0	0	0
0	0	0
0	0	0
0	0	0
0	0	0
0	0	0
0	0	0
0	0	0
0	0	0
0	0	0
0	0	0
0	0	0
0	0	0
0	0	0
0	0	0
0	0	0
0	1.0000e+00	0
0	0	1.0000e+00
-1.3824e+06	-6.5745e+04	-3.6340e+02

B<sub>a</sub> =

Columns 1 through 6

0	0	0	0	0	0
0	0	0	0	0	0
685900	0	0	0	0	0
0	0	0	0	0	0
0	0	0	0	0	0
0	1064800	0	0	0	0
0	0	0	0	0	0

Column 7

1382400

0  
-4.3896e-01  
5.6003e-04  
0  
6.1206e+01  
-4.7001e+01  
-9.3017e+01  
-2.9828e+01  
3.6810e+01  
-7.3090e+01  
-4.2771e+01  
-2.0382e+01  
-2.1966e+01  
1.3646e+02  
2.4884e+01  
1.6344e+01

O  
O  
O  
O  
O  
O  
O  
O  
O  
O  
O  
O  
O  
O  
O

```

0      1.0000e+00      0
0      0      1.0000e+00
-7.9999e-03 -2.2361e-01 -1.3756e+00

```

```

0
0
1.3787e-02

```

1.0000e+00    2.5638e+01    2.9585e+01

8.301178827425707e-34      -1.628205748844804e-29      1.372050144741868e-25

-2.398928391363306e-33	4.662240659331708e-29	-3.898454783095921e-25
1.342072644023924e-33	-2.677490587747102e-29	2.305578482397280e-25
3.850432764857099e-34	-7.813945368338021e-30	6.843513575502914e-26
-1.963479938062043e-34	3.660842849003138e-30	-2.884792821599977e-26
2.321413566600321e-33	-4.339565823294105e-29	3.450383194480395e-25
4.257802949572939e-33	-8.121718645683212e-29	6.622321268387818e-25
-2.267898739006242e-33	4.575126810693514e-29	-3.973056863177187e-25
7.249585328273933e-34	-2.132736930516789e-29	2.448435142364401e-25
9.072253334064948e-33	-1.703686978576889e-28	1.373064220090287e-24
6.028655379747041e-33	-1.213630117564197e-28	1.039534282710865e-24
1.922605490436470e-32	-3.678958283513847e-28	3.006061662155286e-24
-5.870450637124765e-33	1.068456013403474e-28	-8.265522840062014e-25
1.040214506043362e-32	-1.799464456343366e-28	1.285724637503218e-24
3.348252214624320e-33	-7.080201621374685e-29	6.466473618011492e-25
-4.318617393445473e-33	8.753879778190511e-29	-7.660137379414326e-25
-1.869271183568359e-32	3.590055065528789e-28	-2.949062769632514e-24

Columns 4 through 6

-6.493847391884795e-22	1.895471016168797e-18	-3.532953569423090e-15
1.837303892407005e-21	-5.374777001222165e-18	1.013210552541857e-14
-1.123098351334804e-21	3.408010645860328e-18	-6.676209575354410e-15
-3.389160564784808e-22	1.044621459178714e-18	-2.075297522373345e-15
1.246561273458546e-22	-3.210790649610812e-19	5.060025717682157e-16
-1.521043064722067e-21	4.071698253438240e-18	-6.859042744061461e-15
-3.016381246776095e-21	8.435403115019250e-18	-1.505531875480730e-14
1.945691949230662e-21	-5.905573641859421e-18	1.146910095017845e-14
-1.478513590435617e-21	5.195854771890724e-18	-1.092956970269888e-14
-6.221206575217577e-21	1.744625264237110e-17	-3.142828269436613e-14
-4.917122799575414e-21	1.395372410240261e-17	-2.421233114683359e-14
-1.368982003807542e-20	3.808337642460932e-17	-6.688208951097880e-14
3.544902509832968e-21	-9.229227045609213e-18	1.504995705893585e-14
-4.851169714776445e-21	1.014078301136427e-17	-1.078756356653300e-14
-3.335837037790087e-21	1.066669395464222e-17	-2.182253366054936e-14
3.779179903909866e-21	-1.151334156460765e-17	2.229248043125178e-14
1.352711227004220e-20	-3.795438606009239e-17	6.711470812386572e-14

Columns 7 through 9

4.231977558046239e-12	-3.235210022883074e-09	1.484477170328078e-06
-1.234711312059186e-11	9.461791423740360e-09	-4.347749184020776e-06
8.429018454008999e-12	-6.630072292507173e-09	3.122020870755360e-06
2.650918654307225e-12	-2.104013523188491e-09	9.983665152445943e-07
-4.963417182550160e-13	3.186611573992679e-10	-1.174118333556579e-07
7.397936800440352e-12	-5.168923263858147e-09	2.143881970626828e-06
1.738080415484061e-11	-1.287950534870085e-08	5.700672224538596e-06
-1.418466681299844e-11	1.085652641225680e-08	-5.021734586274730e-06
1.358184007546555e-11	-9.723879002892494e-09	4.364205352515888e-06
3.655585861229349e-11	-2.692210773525070e-08	1.198255811391400e-05
2.527387646003088e-11	-1.547709300721408e-08	5.941983554895076e-06
7.446838195795083e-11	-5.208540729522832e-08	2.265954712531172e-05
-1.539951953408894e-11	9.795566956470702e-09	-3.895900709599346e-06
3.149438359462759e-12	3.559241522527517e-09	-2.238424562839060e-06
2.843633993115569e-11	-2.271896811515770e-08	1.022038750791463e-05
-2.718039707464994e-11	1.988756080858650e-08	-7.780924980610234e-06
-7.429765335428279e-11	4.934494574729768e-08	-1.773247183959827e-05

Columns 10 through 11

-1.649928463329068e-04	-1.714144973581012e-01
1.242985311858461e-03	-2.421376062331806e-01
-9.566985396961361e-04	1.976883320295947e-01
-3.086682702701979e-04	6.385455089960489e-02
-2.593063624493261e-05	2.959438630187768e-02
-1.842734637995300e-04	-1.398074976582409e-01
-1.082542200183630e-03	-2.853290283859677e-02
1.455841953123610e-03	-2.351407200599648e-01
-1.700837991114923e-03	4.119840791531642e-01
-2.932427686002768e-03	3.045095434920225e-01
-1.872685208384877e-03	3.715979485180754e-01
-5.959395497990053e-03	7.491437286730505e-01
9.884841700727579e-04	-1.299428985931198e-01
-3.696568865405928e-04	2.913210178558300e-01
-2.162407817896708e-03	1.343530200145992e-01
1.181455141826400e-03	1.603551176169710e-02
2.585657292403225e-03	7.583766854844444e-03

## Appendix D

### Estimation of Component Lift Curve Slopes

This appendix provides a simple least squares estimate for the component lift curve slopes needed to implement the structural mode shape (internal terms) and aerodynamic lift curve slope parameter variations in Section IV-F. The framework for the estimation is based on linear, first order component build-up procedures utilized in preliminary aircraft dynamic analyses.

Assuming only wing (W), horizontal tail (H), and vane (V) components, the overall airframe lift and pitch moment dimensionless derivatives with respect to angle of attack and pitch rate, in terms of component geometry and lifting surface characteristics are

$$\begin{aligned}
 C_{L\alpha} &= \frac{\bar{S}_W}{\bar{S}} C_{L\alpha}^W + \frac{\bar{S}_H}{\bar{S}} C_{L\alpha}^H + \frac{\bar{S}_V}{\bar{S}} C_{L\alpha}^V \\
 C_{Lq} &= -2 \frac{\bar{S}_W}{\bar{S}} \frac{x_W}{\bar{c}} C_{L\alpha}^W - 2 \frac{\bar{S}_H}{\bar{S}} \frac{x_H}{\bar{c}} C_{L\alpha}^H - 2 \frac{\bar{S}_V}{\bar{S}} \frac{x_V}{\bar{c}} C_{L\alpha}^V \\
 C_{M\alpha} &= \frac{\bar{S}_W}{\bar{S}} \frac{x_W}{\bar{c}} C_{L\alpha}^W + \frac{\bar{S}_H}{\bar{S}} \frac{x_H}{\bar{c}} C_{L\alpha}^H + \frac{\bar{S}_V}{\bar{S}} \frac{x_V}{\bar{c}} C_{L\alpha}^V \\
 C_{Mq} &= -2 \frac{\bar{S}_W}{\bar{S}} \frac{x_W^2}{\bar{c}^2} C_{L\alpha}^W - 2 \frac{\bar{S}_H}{\bar{S}} \frac{x_H^2}{\bar{c}^2} C_{L\alpha}^H - 2 \frac{\bar{S}_V}{\bar{S}} \frac{x_V^2}{\bar{c}^2} C_{L\alpha}^V
 \end{aligned}$$

where

$$\begin{aligned}
 C_{L\alpha} &= -\frac{mV_T}{\bar{q}\bar{S}} Z_w & C_{Lq} &= -\frac{2mV_T}{\bar{q}\bar{S}\bar{c}} Z_q \\
 C_{M\alpha} &= \frac{I_{yy}V_T}{\bar{q}\bar{S}\bar{c}} M_w & C_{Mq} &= \frac{2I_{yy}V_T}{\bar{q}\bar{S}\bar{c}^2} M_q
 \end{aligned}$$

Inherent assumptions associated with these equalities include no interference effects, neglect of drag terms, small angle assumption, and linear aerodynamic characteristics only. The above parameters and variables are defined as

- $\bar{S}$  - vehicle reference area
- $\bar{c}$  - vehicle reference chord
- $\bar{S}_k$  - component reference area ( $k = W, H, V$ )

- $C_{L\alpha}^k$  - component lift curve slope ( $k = W, H, V$ )  
 $x_k$  - body x axis component aerodynamic center location ( $k = W, H, V$ )  
 $m$  - vehicle mass  
 $I_{yy}$  - vehicle pitch moment of inertia  
 $V_T$  - total velocity  
 $\bar{q}$  - dynamic pressure  
 $C_{L_i}$  - vehicle dimensionless lift stability derivative ( $i = \alpha, q$ )  
 $C_{M_i}$  - vehicle dimensionless pitch stability derivative ( $i = \alpha, q$ )  
 $Z_i$  - vehicle dimensional z axis translational stability derivative ( $i = w, q$ )  
 $M_i$  - vehicle dimensional y axis rotational stability derivative ( $i = w, q$ )

In the above relationships, all geometric and inertial data and aerodynamic center location data are assumed known leaving only the component lift curve slopes as unknown variables to be solved for. Since the vane planform is an identically scaled duplicate of the horizontal tail planform, the associated lift curve slopes are assumed equal, or

$$C_{L\alpha}^V = C_{L\alpha}^H$$

Also note the  $C_{L_q}$  and  $C_{M_\alpha}$  equalities suggest these derivatives are related as  $C_{L_q} = -2C_{M_\alpha}$ . The vehicle numerical data does not adhere precisely to this assumed structure. Therefore, the above equalities represent four independent equations in two unknowns. In matrix notation, these equalities are expressed as

$$\begin{bmatrix}
 \frac{\bar{S}_W}{\bar{S}} & \frac{\bar{S}_H + \bar{S}_V}{\bar{S}} \\
 -2\frac{\bar{S}_W}{\bar{S}} \frac{x_W}{\bar{c}} & -2\frac{\bar{S}_H x_H + \bar{S}_V x_V}{\bar{S}\bar{c}} \\
 \frac{\bar{S}_W}{\bar{S}} \frac{x_W}{\bar{c}} & \frac{\bar{S}_H x_H + \bar{S}_V x_V}{\bar{S}\bar{c}} \\
 -2\frac{\bar{S}_W}{\bar{S}} \frac{x_W^2}{\bar{c}^2} & -2\frac{\bar{S}_H x_H^2 + \bar{S}_V x_V^2}{\bar{S}\bar{c}^2}
 \end{bmatrix}
 \begin{bmatrix} C_{L\alpha}^W \\ C_{L\alpha}^H \end{bmatrix} = \begin{bmatrix} C_{L\alpha} \\ C_{L_q} \\ C_{M_\alpha} \\ C_{M_q} \end{bmatrix}$$

$A \quad x = b$

The least squares solution for the unknown lift curve slopes is

$$x = (A^T A)^{-1} A^T b$$

Numerical data necessary for the above solution is listed below.



$$\bar{S} = 7,100 \text{ ft}^2$$

$$\bar{c} = 86.02 \text{ ft}$$

$$\bar{S}_W = 7,100 \text{ ft}^2$$

$$x_{s \text{ ac}}^W = 2,280 \text{ in}$$

$$\bar{S}_H = 700 \text{ ft}^2$$

$$x_{s \text{ ac}}^H = 3298.55 \text{ in}$$

$$\bar{S}_V = 177.5 \text{ ft}^2$$

$$x_{s \text{ ac}}^V = 400 \text{ in}$$

$$m = 11,960 \text{ slug}$$

$$I_{yy} = 4.395 \times 10^7 \text{ slug ft}^2$$

$$x_{s \text{ cm}} = 2152.55 \text{ in}$$

$$V_T = 267.95 \text{ ft/s}$$

$$\bar{q} = 85.33 \text{ lbf/ft}^2$$

$$Z_w = -1.081 \text{ 1/s}$$

$$Z_q = -17.32 \text{ ft/s}$$

$$M_w = -0.01824 \text{ 1/ft s}$$

$$M_q = -0.08397 \text{ 1/s}$$

The variables  $x_{s \text{ cm}}$  and  $x_{s \text{ ac}}^k$  denote the vehicle mass center and component aerodynamic center locations in the structural axes (i.e.,  $x_k = x_{s \text{ cm}}^k - x_{s \text{ ac}}^k$ ).

With the above outline, the component lift curve slope estimates are

$$C_{L\alpha}^W = 5.943 \text{ 1/rad}$$

$$C_{L\alpha}^H = 2.073 \text{ 1/rad}$$

$$C_{L\alpha}^V = 2.073 \text{ 1/rad}$$

and the accuracy of the least squares solution is given below.

$$Ax = \begin{bmatrix} 6.200 \\ 1.745 \\ -0.8727 \\ -0.9837 \end{bmatrix}$$

$$b = \begin{bmatrix} 5.720 \\ 2.131 \\ -4.121 \\ -0.4412 \end{bmatrix}$$

REPORT DOCUMENTATION PAGE			Form Approved OMB No. 0704-0188	
Public reporting burden for this collection of information is estimated to average 1 hour per response, including the time for reviewing instructions, searching existing data sources, gathering and maintaining the data needed, and completing and reviewing the collection of information. Send comments regarding this burden estimate or any other aspect of this collection of information, including suggestions for reducing this burden, to Washington Headquarters Services, Directorate for Information Operations and Reports, 1215 Jefferson Davis Highway, Suite 1204, Arlington, VA 22202-4302, and to the Office of Management and Budget, Paperwork Reduction Project (0704-0188), Washington, DC 20503.				
1. AGENCY USE ONLY (Leave blank)	2. REPORT DATE December 1999	3. REPORT TYPE AND DATES COVERED Contractor Report		
4. TITLE AND SUBTITLE Multivariable Techniques for High-Speed Research Flight Control Systems		5. FUNDING NUMBERS C NAS1-19858 TA 93 WU 537-07-24-23		
6. AUTHOR(S) Brett A. Newman				
7. PERFORMING ORGANIZATION NAME(S) AND ADDRESS(ES) Old Dominion University Department of Aerospace Engineering Norfolk, VA 23529		8. PERFORMING ORGANIZATION REPORT NUMBER		
9. SPONSORING/MONITORING AGENCY NAME(S) AND ADDRESS(ES) National Aeronautics and Space Administration Langley Research Center Hampton, VA 23681-2199		10. SPONSORING/MONITORING AGENCY REPORT NUMBER NASA/CR-1999-209528		
11. SUPPLEMENTARY NOTES Langley Technical Monitor: Carey S. Buttrill				
12a. DISTRIBUTION/AVAILABILITY STATEMENT Unclassified-Unlimited Subject Category 08 Availability: NASA CASI (301) 621-0390			12b. DISTRIBUTION CODE	
13. ABSTRACT (Maximum 200 words) This report describes the activities and findings conducted under contract NAS1-19858-93 with NASA Langley Research Center. Subject matter is the investigation of suitable multivariable flight control design methodologies and solutions for large, flexible high-speed vehicles. Specifically, methodologies are to address the inner control loops used for stabilization and augmentation of a highly coupled airframe system possibly involving rigid-body motion, structural vibrations, unsteady aerodynamics, and actuator dynamics. Design and analysis techniques considered in this body of work are both conventional-based and contemporary-based, and the vehicle of interest is the High-Speed Civil Transport (HSCT). Major findings include 1) control architectures based on aft tail only are not well suited for highly flexible, high-speed vehicles, 2) theoretical underpinnings of the Wykes structural mode control logic is based on several assumptions concerning vehicle dynamic characteristics, and if not satisfied, the control logic can break down leading to mode destabilization, 3) two-loop control architectures that utilize small forward vanes with the aft tail provide highly attractive and feasible solutions to the longitudinal axis control challenges, and 4) closed-loop simulation sizing analyses indicate the baseline vane model utilized in this report is most likely oversized for normal loading conditions.				
14. SUBJECT TERMS HSCT; HSR; Flight controls; Inner loop; Stability augmentation; Handling qualities; Aeroelastic; Modeling			15. NUMBER OF PAGES 294	
			16. PRICE CODE A13	
17. SECURITY CLASSIFICATION OF REPORT Unclassified	18. SECURITY CLASSIFICATION OF THIS PAGE Unclassified	19. SECURITY CLASSIFICATION OF ABSTRACT Unclassified	20. LIMITATION OF ABSTRACT UL	